DEVELOPMENT OF NEW AFM BASED METHODOLOGIES FOR THE QUANTITATIVE MAGNETIC CHARACTERIZATION OF NANOPARTICLES FOR BIOMEDICAL APPLICATIONS

Thèse en cotutelle
Doctorat en génie des matériaux et de la métallurgie

Livia Angeloni

Université Laval
Québec, Canada
Doctorat (Ph. D.)

et

Sapienza University
Rome, Italy
Doctorat (Ph. D.)

DEVELOPMENT OF NEW AFM BASED METHODOLOGIES FOR THE QUANTITATIVE MAGNETIC CHARACTERIZATION OF NANOPARTICLES FOR BIOMEDICAL APPLICATIONS

Thèse en cotutelle
Doctorat en génie des matériaux et de la métallurgie

Livia Angeloni

Sous la direction de:

Diego Mantovani, directeur de recherche

Marco Rossi, directeur de cotutelle

Resumé

L'objectif du projet de doctorat est le développement d'une procédure innovante de mesure et post-traitement des données pour obtenir des informations quantitatives sur les paramètres magnétiques de nanoparticules magnétiques individuelles par l'utilisation de la Microscopie à Force Magnétique (MFM).

Les nanoparticules magnétiques (MNP), grâce à leurs propriétés magnétiques particulières (monodomaine, superparamagnétisme, etc.) et leur taille nanométrique, conviennent à plusieurs applications biomédicales, telles que les systèmes d'administration de médicaments, les traitements de hyperthermie magnétique, l'étiquetage cellulaire, les agents de contraste pour l'imagerie a résonance magnétique (IRM). La conception de ces techniques requiert une connaissance détaillée des propriétés magnétiques des nanomatériaux utilisès, comme l'aimantation de saturation M_s, le champ magnétique de saturation H_s, la coercivité H_c. Les techniques standard, comme les dispositifs supraconducteurs à interférence quantique (SQUID) ou la magnétomètrie à échantillon vibrant (VSM), permettent la détection des propriétés magnétiques globales des populations de nanoparticules. Mais la détection des propriétés magnétiques des particules isolées n'est pas possible et l'évaluation de ces propriétés en fonction de la taille des particules n'est pas explicite. Grâce à sa résolution latérale nanométrique et sa capacité à détecter des champs magnétiques faibles, MFM est un outil puissant pour la caractérisation de dimensions de nanoparticules isolées, ainsi que leurs propriétés magnétiques. Cependant, une méthodologie pour obtenir des informations quantitatives sur les caractéristiques magnétiques de nanoparticules isolées par MFM n'a pas été individualisée, principalement en raison de i) la complexité des interactions pointe-échantillon qui affectent les mesures MFM et qui produisent également des phénomènes non magnétiques (par exemple, des interactions électrostatiques), et ii) l'absence d'un modèle théorique décrivant les interactions magnétiques entre la pointe et une nanoparticule de manière cohérente avec les données expérimentales détectées. Pour exploiter toutes le potentialités de la technique MFM en tant qu'instrument de nanométrologie magnétique, la stratégie proposée et suivie dans ce projet est organisée en 4 phases:

1) a vérification théorique et expérimentale et la rationalisation des problemes ouvertes limitant l'applicabilité de la MFM à la caractérisation magnétique quantitative des NP individuels; Dans cette phase, la présence d'artefacts

électrostatiques a été individualisée comme principale limite responsable de l'incohérence entre les données expérimentales et les modèles théoriques décrivant les interactions tip-NP.

2) le développement d'un appareil instrumental et d'une procédure de mesure pour évaluer et éliminer les contributions non magnétiques (électrostatiques) affectant quantitativement les données MFM;

3) l'individuation d'un modèle théorique décrivant l'interaction magnétique pointe-NP, cohérente avec les données expérimentales, et capable d'établir une relation précise entre les données mesurées et les paramètres physiques à déterminer (magnétisation dans le cas spécifique);

4) le développement d'une procédure pour mesurer quantitativement les propriétés magnétiques, et eventuellement d'autres paramètres, de nanoparticules isolées par MFM.

Les résultats obtenus avec les procédures et les méthodologies présentées dans cette thèse ont démontré la possibilité de réaliser des mesures magnétiques quantitatives sur des NP magnétiques individuelles par la plateforme technologique MFM.

Abstract

The objective of the PhD project is the development of a innovative measurement procedure and a data post-processing method to obtain quantitative information about the magnetic parameters of single magnetic nanoparticles through the use of the Magnetic Force Microscopy (MFM) technique.

Magnetic nanoparticles (MNPs), thanks to their particular magnetic properties (single domains, superparamagnetism, etc.) and their nanometric size, are thought to be suitable for several biomedical applications, such as drug delivery systems, magnetic hyperthermia treatments, cell labelling, contrast agents for Magnetic Resonance Imaging (MRI). The design of these techniques requires a detailed knowledge on the magnetic properties of the adopted nanomaterials, like the saturation magnetization M_S, the saturation magnetic field H_S, the coercivity H_C. Standard techniques, like Superconducting Quantum Interference Devices (SQUID) or Vibrating Sample Magnetometer (VSM), to allow the detection of global magnetic properties of nanoparticles populations. Nevertheless, the detection of magnetic properties of single particles is not possible and the evaluation of the particle size dependence is not explicit. Thanks to its nanometric lateral resolution and its capability to detect weak magnetic fields, MFM is a potential powerful tool for the characterization of single nanoparticles dimensions, together with their magnetic properties. However, a methodology to extract quantitative information about the magnetic characteristics of single nanoparticles through MFM has not been individuated, mainly because of the complexity of tip-sample interactions affecting MFM measurements, which produces also non magnetic phenomena (e.g. electrostatic interactions), and the lack of a theoretical model describing the magnetic tip-NP interactions consistently with the detected experimental data.

In order to exploit all the potential capabilities of MFM as a magnetic nanometrology tool, the strategy proposed and followed in this project is organized in the following four phases:

1) the theoretical and experimental verification and rationalization of the open issues and the problems limiting the applicability of MFM to the quantitative magnetic characterization of single NPs; in this phase the presence of electrostatic artifacts has been individuated as the main limitation responsible for the inconsistency

between experimental data and theoretical models describing the tip-NP interactions.

2) the development of an instrumental apparatus and a measurement procedure to evaluate and eliminate the non-magnetic (electrostatic) contributions quantitatively affecting the MFM data;
3) the individuation of a theoretical model describing the magnetic tip-NP magnetic interaction, coherent with the experimental data, and able to establish a precise relationship between the measured data and the physical parameters desired to be determined (magnetization in the specific case);
4) the development of a procedure to quantitatively measure the magnetic properties, and eventually other parameters, of single nanoparticles by MFM.

The results obtained with the procedures and methodologies presented in this thesis demonstrated the possibility of performing quantitative magnetic measurements on single magnetic NPs by MFM technology platform.

Riassunto

L'obiettivo del progetto di dottorato è lo sviluppo di una procedura di misura innovativa e di un metodo di elaborazione dei dati al fine di ottenere informazioni quantitative sui parametri magnetici di singole nanoparticelle magnetiche attraverso l'uso della Microscopia a Forza Magnetica MFM. Le nanoparticelle magnetiche (MNPS), grazie alle loro particolari proprietà magnetiche (singolo dominio, superparamagnetismo, etc.) e le loro dimensioni nanometriche, stanno recentemente trovando grande applicazione in diverse tecniche in campo biomedico, come i sistemi di somministrazione mirata di farmaci, trattamenti di tumori tramite ipertermia magnetica, l'etichettatura cellulare, gli agenti di contrasto per la risonanza magnetica nucleare (MRI). Il design e l'ottimizzazione di queste tecniche richiede una conoscenza dettagliata delle proprietà magnetiche dei nanomateriali adottati, come la magnetizzazione di saturazione M_S, il campo magnetico di saturazione H_s, la coercitività H_c. Le tecniche standard, come i Superconducting Quantum Interference Devices (SQUID) o i magnetometro a vibrazione del campione (VSM), consentono il rilevamento delle proprietà magnetiche globali di numerose popolazioni di nanoparticelle. Ma il rilevamento delle proprietà magnetiche di singole particelle non è possibile e la valutazione di queste proprietà in dipendenza della dimensione delle particelle non è esplicito. Grazie alla risoluzione laterale nanometrica e la sua capacità di rilevare i campi magnetici deboli, la tecnica MFM rappresenta uno strumento ad elevato potenziale per la caratterizzazione delle proprietà magnetiche di singole nanoparticelle, insieme alle loro dimensioni. Tuttavia, un metodo per estrarre informazioni quantitative sulle caratteristiche magnetiche di singole nanoparticelle attraverso la tecnica MFM non è stato individuato, soprattutto a causa della complessità delle interazioni punta-campione che interessano le misurazioni e che possono dare luogo anche a contributi non magnetici (ad esempio interazioni elettrostatiche), e alla mancanza di un modello teorico in grado di descrivere le interazioni magnetiche punta-NP in modo coerente con i dati sperimentali rilevati.

Al fine di individuare e superare i limiti della tecnica MFM che ne limitano l'utilizzo come strumento nanometrologico magnetico, la strategia proposta e seguita in questo progetto di dottorato è organizzata nelle seguenti 4 fasi:

1) la verifica teorica e sperimentale e la razionalizzazione delle problematiche che limitano l'applicabilità della tecnica MFM alla caratterizzazione magnetica quantitativa di singole NP; in questa fase la presenza di artefatti elettrostatici è

stato individuata come il principale limite responsabile per la riscontrata l'inconsistenza tra i dati sperimentali e modelli teorici che descrivono le interazioni tip-NP.

2) lo sviluppo di un apparato strumentale e una procedura miosura per la valutazione ed eliminazione dei contributi elettrostaticie non magnetici che influiscono quantitativamente sui dati MFM;
3) l'individuazione di un modello teorico che descrive l'interazione magnetica punta-NP coerentemente con i dati sperimentali, e in grado di stabilire una relazione precisa tra i dati misurati e i parametri fisici che si desiderano misurare (magnetizzazione nel caso specifico);
4) lo sviluppo di un procedimento per misurare quantitativamente le proprietà magnetiche, ed eventualmente altri parametri, di singole nanoparticelle tramite MFM.

I risultati ottenuti con le procedure e le metodologie presentate in questa tesi hanno dimostrato la possibilità di effettuare misure magnetiche quantitative su singole NP magnetiche facendo uso della piattaforma tecnologica MFM.

TABLE OF CONTENTS

LIST OF FIGURES

To my mother and my father

ACKNOWLEDGEMENTS

I wish to express my deepest gratitude to my supervisors, Prof. Marco Rossi and Prof. Diego Mantovani, that gave me the opportunity to work under their joint supervision, which has greatly enriched me from both a professional and a personal point of view. I thank them for having been for me a guide and a reference point in these four years, giving me the possibility to travel and live this doctoral experience in a dynamic and highly multicultural environment, to see and test different ways of working and doing research, different means, different approaches and methodologies. I had the possibility to collaborate and interact with many people, experts in different fields, having different cultures and coming from different parts of the world. This allowed me to acquire very diverse competences, to open my mind, to acquire autonomy and critical spirit, as well as to learn tolerance and respect for different ideas, beliefs and habits, qualities that I consider essential for a researcher.

My heartfelt thanks go to my "scientific father", Daniele Passeri. He was and still is for me a guide, a patient teacher and a true friend. I thank him for having welcomed me into his lab and always made me feel at home, for having conveyed his curiosity and passion for research to me, for having transferred his skills to me with generosity, for his never-ending patience, for having teached me to work seriously and honestly, but also with humor and critical spirit.

A special thanks goes to the professional researchers and post-doc researchers of LBB in Quèbec with whom I have had the luck and the honor to work for long or short periods: Pascale, Stephane, Carlo, Ranna, Vanessa. I wish to thank them for their patient teachings and for the skills and competences they shared with me every day, with generosity and professionalism, and for the enthusiasm and energy that they put every day in their work. Their example motivated me during the last four years and will be forever a model for me to be followed.

I wish to thank wholeheartedly all the people with whom, over the years, I shared the daily life, always in a peaceful and welcoming environment: the PhD students in Rome and Quèbec. I would like to thank Melania, because the laughs we had during our long days in front of the AFM will be one of the best memories of this experience. And I

would like to thank all the students of LBB, which are too numerous to be listed, but to which I am deeply grateful for having welcomed, supported and tolerated me every day, for having taught me, for having given me the opportunity to open my eyes to different cultures and habits, for having made me feel at home when I was far from home.

I wish to thanks with all my heart my parents, to whom I dedicate this thesis. They have made this experience possible, supporting and encouraging me in every moment and in every possible way. Thank you for having been always present and for never showing sadness because of the distance, but always joy and pride. Thanks for having left the computer on continuously for 4 years and have always answered to my calls, in all circumstances and at any time. Thanks for teaching me the universal and fundamental rules of life, such as courtesy, discretion, and respect for the others, which allowed me to integrate myself and be accepted in any place in the world. Thank you for having accompanied me in these (many) years of study, for giving me the energy and the motivation to not give up, even when everything was difficult.

I wish to thank Arnaud, for having been with me in every moment of these wonderful four years, for having taken care of me, and having always encouraged and supported me. I'm sure that this doctorate is just the first of many successes we will achieve together.

PREFACE

The development and optimization of a novel material require, in general, the use of metrological tools for the measurement and tuning of its functional properties (e.g. mechanical, magnetic, electrical, thermal, etc.). In the case of nanomaterials (materials having one or more dimensions smaller than 100 nm), due to the small involved characteristic sizes, conventional measurement techniques at the macro- and microscopic scale are not effective. This is reason why the development of nanomaterials and the advancements in nanotechnology field are strictly related to the development of new, appropriate technologies and methodologies for the characterization at the nanoscale.

Since today, the remarkable outbreak of nanotechnologies has been allowed by the invention and the continuous improvement of different techniques and instrumentations for the imaging of materials and systems at the nanoscale, such as Scanning Electron Microscopy (SEM), Transmission Electron Microscopy (TEM) and Scanning Probe Microscopies (SPM). Nevertheless, the definition of standard and reliable techniques and methodologies for the quantitative measurement of physical parameters of nanomaterials is still an open issue.

Scanning Probe Microscopy, thanks to its working principle, which is based not on "seeing" the sample but on detecting the interaction forces between the probe and the scanned surface, is a technology platform potentially able to provide information about not only the morphology of a surface (through the detection of Van der Waals forces), which represents, currently, its main application, but also information about a wide number of functional properties, such as mechanical, electric, electromechanical, magnetic, thermal, chemical, of both articificial and biological materials, with high sensitivity and nanometric lateral resolution.

Nevertheless, despite the important advancements in the last decades and the continuous development of tools for the map and measurement of specific materials properties at the nanoscale, the use of Scanning Probe Microscopy techniques as a really quantitative metrological instrument is still limited. Only Atomic Force Microscopy, based on the detection of Van der Waals interactions between the probe and the sample, is considered as a reliable quantitative technique for the dimensional measurements at the nanoscale and it is known to provide accurate results. Contrariwise, other physical measuring and mapping modes, such as AFM based mechanical characterization techniques (AFM-

nanoindentation, CR-AFM, and TH-AFM), magnetic characterization techniques (MFM), "biological-AFM" techniques, as well as electric, chemical and thermal modes, despite the great efforts of researchers to find appropriate methodologies and solutions, are still mainly used to produce only qualitative or semi-quantitative (differential maps) results, with no direct relation to absolute values.

This can be mainly ascribed to the complexity of the nanoscale tip-sample interactions, which can contain many different components and can be dependent on several factors, such as geometrical, chemical and physical properties of both the tip and the sample, making difficult the individuation of precise relationships between the measured data and the physical parameter which is desired to be measured.

In general, the main problems that still are limiting the use of SPM techniques for the measurement of quantitative parameters at the nanoscale can be summarized as:

1) Lack of standard methodologies (strategies for probes calibration and characterization, definition of appropriate reference samples, measurements procedures, etc.) to facilitate the correlation between measured data and quantitative values of the parameters of interest;
2) Lack of standard and appropriate models that will consider all the tip-sample interactions and define accurate relationships between measured data and absolute quantitative values of the parameters of interest.

In this context, the general objective of the PhD project is to bring a contribution to the development of AFM techniques, allowing their use as tools for the quantitative evaluation of relevant properties of nanomaterials, in particular introducing:

1) Methodologies for the probes characterization in order to quantify all the probe characteristics affecting the quantitative measurement (e.g. elastic constant, magnetic properties, etc.).
2) Measurement methodologies to be adopted to obtain accurate information about the parameters of interest, reducing artifacts and individuating all the tip-sample interactions forces affecting the measured data;
3) Methodologies for the data post-processing: study and individuation of appropriate mathematical models for the transformation of qualitative data into the values of quantitative data of interest.

In order to achieve this goal, the research activity has been organized in the following phases, which will be described in the different sections of this thesis:

- Analysis of the state of the art regarding the existing MFM based technologies and their applications to the quantitative measurement of magnetic parameters at the nanoscale, which is described in Chapter 3. This study was published in January 2016 in the chapter: **Passeri D, Angeloni L, Reggente M, Rossi M. "Magnetic Force Microscopy, in magnetic characterization techniques for nanomaterials". C. Kumar (Ed.), Springer (accepted on the 20th of January 2015).** L.A. is the second author of this chapter. L.A. performed all the reported MFM measurements ("unpublished data"), which were analysed by D.P. and L.A. D.P. and L.A. wrote the starting draft of the manuscript, which was revised by all the authors.
- The individuation of the open issues limiting the use of MFM as a nano-metrological tool and definition of the general strategies and methodologies of the project, which are described in Chapter 4.
- The experimental verification and rationalization of the open issues and limitations which emerged from the literature analysis. This phase of the project is described in Chapter 5 and has been published, in June 2015, as a conference paper: **Angeloni L, Passeri D, Reggente M, Rossi M, Mantovani D, Lazzaro L, Nepi F, De Angelis F, Barteri M. "Experimental issues in Magnetic Force Microscopy of nanoparticles". AIP Conf. Proc. 2015;1667:020010 (DOI: 10.1063/1.4922566).** L.A. is the principal author of the paper. L.A. and D.P. with the supervision of M. Rossi and D.M. designed the experiments which were carried out in the laboratories led by M. Rossi Materials, spare parts, and instrumentation were supplied by D.M. and M. Rossi. L.A. performed the experiments. The analysed samples were prepared by L.L., F.N., F.DA., under the supervision of M.B.. L.A., D.P. and M. Reggente analyzed the results, which were discussed by all the Authors. L.A. and D.P. wrote the starting draft of the manuscript, which was revised by all the authors.
- The individuation and the development of an instrumental apparatus and a methodology to overcome the individuated open issues and definition of a precise relationship between the MFM measured data and the real physical parameters of interest. This phase of the project is described in Chapter 6 of this thesis and has been published, on the 19th May 2016, in a paper: **Angeloni L, Passeri D, Reggente M, Mantovani D, Rossi M. "Removal of electrostatic artifacts in Magnetic Force Microscopy by controlled magnetization of the**

tip: application to superparamagnetic nanoparticles". Sci. Rep., 2016;6:26293 (DOI: 10.1038/srep26293). L.A. is the principal author of the article. L.A. and D.P. with the supervision of M. Rossi and D.M. designed the experiments which were carried out in the laboratories led by M. Rossi Materials, spare parts, and instrumentation were supplied by D.M. and M. Rossi. L.A. performed the experiments. L.A., D.P. and M. Reggente analyzed the results, which were discussed by all the Authors. L.A. and D.P. wrote the starting draft of the manuscript, which was revised by all the authors.

- The application of the developed technique to the quantitative measurement of parameters of interest of magnetic nanoparticles. The obtained results are described in Chapter 7 and 8, and have been reported in a first article, **Angeloni L, Passeri D, Peddis D, Mantovani D, Rossi M, Single nanoparticles magnetization curves by controlled tip magnetization magnetic force microscopy submitted to "Nanoscale" in August 2017**, and in a conference paper, **Angeloni L, Passeri D, Scaramuzzo F A, Di Iorio D, Barteri M, Mantovani D, Rossi M. "Measurement of the nonmagnetic coating thickness of core-shell magnetic nanoparticles by controlled magnetization magnetic force microscopy". AIP Conf. Proc. 2016;1749:0200060 (DOI: 10.1063/1.4954489**), published in June 2016. L.A. is the principal author of both of the papers. The first article has been submitted on Nano Letters. L.A. and D.P. with the supervision of M. Rossi and D.M. designed the experiments which were carried out in the laboratories led by M. Rossi. Materials, spare parts, and instrumentation were supplied by D.M. and M. Rossi. L.A. performed the MFM experiments. D.P. performed the SQUID experiments. L.A., D.P. and M. Reggente analyzed the MFM results, which were discussed by all the Authors. L.A. and D.P. wrote the starting draft of the manuscript, which was revised by all the authors. The second article has been published in June 2016. L.A. and D.P. with the supervision of M. Rossi and D.M. designed the experiments which were carried out in the laboratories led by M. Rossi Materials, spare parts, and instrumentation were supplied by D.M. and M. Rossi. L.A. performed the experiments. The analysed NPs were prepared by F.A.S. and D.D.I, under the supervision of M.B. L.A., D.P. and M. Reggente analyzed the results, which were discussed by all the Authors. L.A. and D.P. wrote the starting draft of the manuscript, which was revised by all the authors.

The doctoral project has been developed in collaboration between the Laboratory for Biomaterials and Bioengineering of the *Université Laval* in Québec City - Canada, and the Laboratory of Scanning Probe Microscopy of the *Sapienza - University of Rome* (Department of Fundamental and Applied Sciences for Engineering - SBAI), under the joint supervision of Prof. Diego Mantovani (*Université Laval*) and Prof. Marco Rossi (*Sapienza - University of Rome)* .

The collaboration has been based on the complemental skills and technology platforms made available by the two laboratories:

- the Laboratory of Biomaterials and Bioengineering of the *Université Laval* in Québec City works specifically on the development and fabrication of advanced materials for biomedical applications.
- the Laboratory of Scanning Probe Microscopy of the *Sapienza - University of Rome* works on the development of advanced techniques for the characterization of nanomaterials, especially through the use of Scanning Probe Microscopy tools.

1. BACKGROUND

The development of magnetic nanoparticles (MNPs) has recently attracted growing interest, due to the particular magnetic properties that occur in magnetic materials when their dimensions are reduced to the nanoscale. These properties, coupled with the nanometric size and with the possibility of opportunely coating and/or functionalizing the NPs, make these nanomaterials suitable for several biomedical applications, such as carriers for drug delivery applications, mediators for magnetic hyperthermia treatments, contrast agents for Magnetic Resonance Imaging (MRI) and markers for cell labeling.

First of all, the NPs magnetic character (multi or single-domain ferromagnetic, superparamagnetic) and the intrinsic penetrability of magnetic fields into human tissues, allows the manipulation of injected MNPs within the body by external magnetic fields and the transport of them on a specific target, allowing, as an example, the localization of therapeutic treatments (e.g. chemotherapeutic drugs or hyperthermia) which could be detrimental for healthy tissue.

The second fundamental property of nanoparticles that make them suitable for biological and biomedical applications is the size. MNPs have, in general, controllable diameters in a range of few nm to a few tens of nm. These sizes are compatible with the dimensions of the cells (10-100 μm), viruses (20-450 nm), proteins (5-50 μm) and genes (2 nm wide, 10-100 nm length) and make the NPs able to interact with and penetrate into tissues and cells.

Furthermore, MNPs can be coated with biocompatible films in order to reduce their toxicity and functionalized with organic molecules, antibodies, ligands and other chemical compounds, in order to make them able to interact and create bonds with biological entities, such as cells, providing the possibility of their use in cell labeling applications, or with drugs, providing the possibility of their use in therapeutic applications (i.e. drug delivery).

MNPs have also a resonance response to an alternated magnetic field, allowing the energy transfer from an external magnetic field to the body. MNPs can therefore be used as carriers of thermal energy on tumor sites and used for the development of localized hyperthermia treatments.

In addition, superparamagnetic nanoparticles, when are subjected to an intense magnetic field, produce intense magnetic fields oriented parallel to the applied field, which locally increase the magnetic field, significantly increasing the Larmor frequency of the

involved protons and a consequent variation of their transverse relaxation time (T_2). These characteristic make these materials particularly suitable to be used as contrast agents for Magnetic Resonance Imaging (MRI).

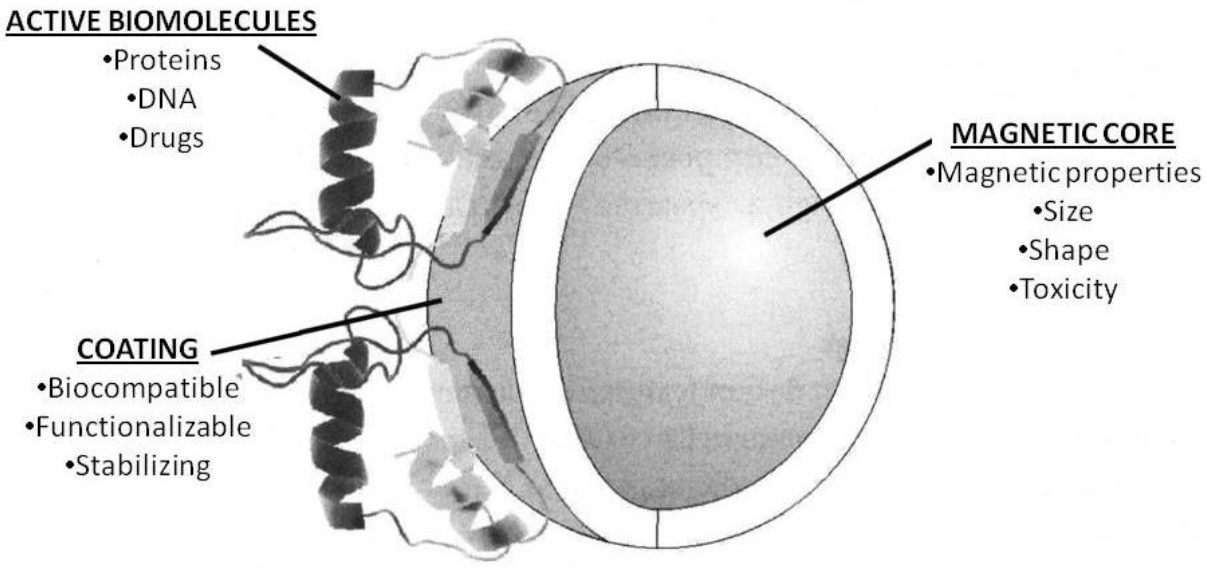

Figure 1 – Schema of a generic magnetic nanoparticle for biomedical applications [4]

In the following paragraphs a brief description of the MNPs magnetic properties and some applications is presented, in order to highlight the reason why the design of these techniques requires a detailed knowledge, so a detailed characterization, of the magnetic and structural properties of the adopted nanomaterials.

1.1 - MAGNETIC PROPERTIES

The different existing magnetic materials and their main properties are briefly summarized below in order to highlight, in the successive paragraphs, the changes which occurs when the characteristic dimensions of a material are reduced to the nanoscale.

1.1.1 - General properties of magnetic materials

Magnetic materials are, in general, classified into diamagnetic, paramagnetic and ferromagnetic. The diamagnetic materials have a negative and very small (order of 10^{-6}-10^{-5}) magnetic susceptibility χ; paramagnetic materials are characterized by a positive susceptibility of the order of 10^{-2}-10^{-4}. On the contrary a small number of substances, the ferromagnetic materials, present very high χ values, of the order of tens of thousands.

For the sake of completeness, in the following paragraphs, the main physical phenomena giving rise to the different magnetic properties of materials are briefly described.

1.1.1.1 - Diamagnetism

The diamagnetism is caused by the changes in the orbital motion of electrons when a magnetic field is applied; these changes give rise to an induced magnetic field directed antiparallel to the applied magnetic field, according to the phenomenon known as "Larmor precession".

All materials have a diamagnetic behavior, since all atoms have external electrons that shield the effect of an external magnetic field. The diamagnetic behavior is, however, detectable only in those materials in which such an effect, quantitatively very low, is not masked by other overriding possible effects; specifically, this occurs for those materials where the particles (atoms or molecules) do not possess any intrinsic magnetic moment. The magnetic susceptibility of such a type of materials (diamagnetic susceptibility) is therefore negative ($\chi < 0$), low ($\chi = 10^{-6}$-10^{-5}) and independent of temperature.

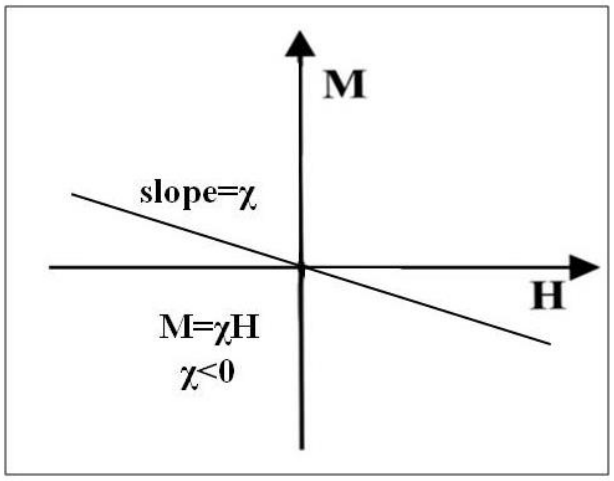

Figure 2 – M-H curve for a diamagnetic material

1.1.2 - Paramagnetism

Paramagnetism exists in materials in which the atoms, molecules or ions have a magnetic moment, due to unpaired electrons in partially filled orbitals. In the absence of any external magnetic field, the magnetic moments of the individual atoms (or molecules or ions) are randomly directed in all possible directions, due to the thermal agitation, and, consequently, the material possesses no net magnetization. When an external magnetic field is applied, the magnetic moments rotate in the direction of the

applied field. Paramagnetic materials are therefore characterized by a positive susceptibility. This phenomenon is opposed by thermal agitation which promote the restoration of the random orientation. Such behavior is summarized by the experimental Curie law:

$$\chi = \frac{C}{T} \qquad 1)$$

where T is the temperature and C is a parameter called "Curie constant" which, according to the classic theory of Langevin for a gas of molecules having magnetic moment m, in presence of low fields and at not too low temperatures, is :

$$C = \frac{\mu_0 N m^2}{3k_B} \qquad 2)$$

where N is the number of atoms for volume unit, k_B the Boltzmann constant, μ_0 the magnetic permeability of vacuum.

The Langevin theory is in agreement with the quantum theory from which we have:

$$C = \frac{\mu_0 N J(J+1) g^2 \mu_B^2}{3k_B} \qquad 3)$$

where the value of the magnetic moment associated with the total quantum number of moment J is:

$$m = -g\mu_B \sqrt{J(J+1)} \qquad 4)$$

where μ_B is the Bohr magneton and g the gyromagnetic ratio.

Therefore, the magnetization of a paramagnetic material, in correspondence of low fields and not very low temperatures, grows proportionally with the applied field. For very intense field values and for low temperatures, the magnetization tends to a constant value. Indeed, when all the elementary magnetic moments are aligned with the external field, the magnetization intensity reaches its saturation value and cannot further increase.

The magnetic susceptibility of paramagnetic media is therefore positive ($\chi > 0$), temperature dependent and can reach values of the order of 10^{-2}-10^{-4}.

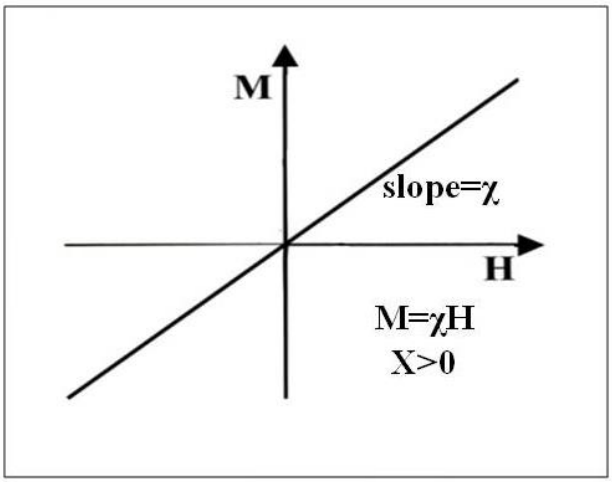

Figure 3 – M-H curve for a paramagnetic material

1.1.1.3 - Ferromagnetism

The "not magnetized" state

A macroscopic sample of a ferromagnetic material (monocrystalline or polycrystalline) is typically composed by several regions, called “magnetic domains” or “Weiss domains”, which are spontaneously magnetized in a certain direction, as schematically represented in Figure 4

Indeed, magnetic ordered materials are characterized by a magnetocrystalline anisotropy, which is due to the spin-orbit coupling, for which the alignment of the dipoles along specific crystallographic directions, defined as "preferential magnetization axes", is energetically promoted compared to other possible directions of orientation. This property is an intrinsic characteristic of the material. In a multi-domain material, in the absence of an external magnetic field, each domain is oriented along its direction of "easy magnetization".

Therefore, in a macroscopic not magnetized material, the magnetizations of the individual domains are randomly oriented in all the possible directions (which correspond to their own directions of "easy magnetization"), giving rise to an overall nul magnetization.

These domains are separated by transition regions, called Bloch walls, which are characterized by a finite thickness where a gradual variation of the spins (magnetization) orientation occurs.

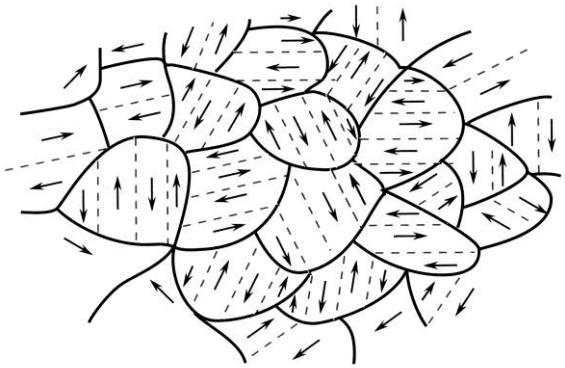

Figure 4 – Representation of magnetic domains in a ferromagnetic material

Magnetization curve and hysteresis loop

Differently from the diamagnetic and paramagnetic materials, the M-H curve of ferromagnetic materials encloses a hysteresis area. This hysteresis is due to the occurrence, during the magnetization and demagnetization process of the material, of irreversible energy dissipation phenomena.

More specifically, the magnetization curve of a ferromagnetic material can be considered as the result of two processes:

1) The Bloch walls movement, which produces an increase of the volume of the domains oriented in the direction of easy magnetization closer to the direction of the applied field;
2) The rotation of the domains magnetization in the direction of the applied field.

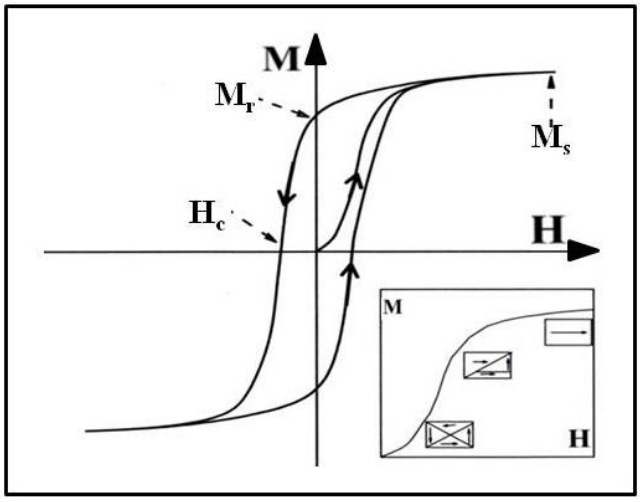

Figure 5 –M-H curve for a ferromagnetic material

In Figure 5, an example of first magnetization curve and the corresponding hysteresis loop for a ferromagnetic polycrystalline sample are shown. Each region of the curve is

characterized by a different process responsible for the increase of the magnetization intensity and the energy losses, the total contribution of which gives rise to the hysteresis.

In the first section of the curve (corresponding to low intensities of applied field) the magnetization increase is due to the movement of the Bloch walls. Such movements have irreversible character, due to the fact that the wall, moving, meets impurities of the material, such as foreign atoms, cavities, structural defects, e.g. vacancies or dislocations, or regions in which there are elastic stresses. All these "discontinuities" represent, for the Bloch walls movements, "high-energy barriers", in correspondence of which dissipation phenomena occur.

In correspondence of high values of the applied magnetic field, the energy required by the wall to overtake the high energy barriers is provided by the magnetic field also via a local orientation of the dipoles in a direction parallel to the the direction of the applied magnetic field. In this case, once the "obstacle" is overcome, the energy associated to the local rotation of the dipoles is largely dissipated, mainly because of two processes: i) the rapid variation of the magnetization causes a change of the induction field inside the crystal and, thus, produces induced leakage currents; ii) the elastic deformation effects due to the magnetization variation produce shock waves that are then absorbed.

The Bloch walls movement stops when the domain, oriented in the direction of easy magnetization closest to the applied field, coincides with the grain; over this dimension it can not grow anymore as the presence of the grain boundary prevent further displacement of the walls.

Starting from this moment, the increase of magnetization, is only due to the dipoles rotation towards the direction of the applied magnetic field. The spent energy is, in this case, the energy required to overcome the magnetocrystalline energy barrier. This process is not characterized by significant dissipation phenomena; therefore, it can be considered as a reversible phenomenon.

The maximum magnetization reached by the material is called "saturation magnetization" M_s.

With the decrease of the applied field strength a loss of magnetization occurs due to, at first, the reorientation of the dipoles within the domains along the direction of easy magnetization and, then, the Bloch walls movement.

Because of all the dissipation processes described above, in correspondence of $H = 0$ a residual magnetization is present. With the increase of H in the opposite direction, the

motion of the Bloch walls continues until the magnetization reach the zero value in correspondence of a certain intensity of applied magnetic field H_c, which is called "coercive field" (or coercivity). In correspondence of a further increase of the applied magnetic field, Bloch walls movement continues until the domains correspond to the grains. Then, rotation processes occur and saturation magnetization in the opposite direction is reached. Reversing the intensities of the applied field *H*, the described processes occur again in the opposite direction and the hysteresis loop closes.
The area enclosed by the magnetization curve (M-H curve) is, thus, proportional to the energy losses due to irreversible phenomena related to the variation of magnetization.

1.1.2 - Changes in magnetic properties with decreasing size

Hereinafter, the main phenomena occurring in a magnetic material when its characteristic size decreases under certain critical dimensions and the main magnetic properties which occur at the nanoscale are briefly described.

1.1.2.1 - The steady-state: from the multi-domain configuration to the single domain configurationIt is well known that the equilibrium state of a thermodynamic system under conditions in which the temperature (T) and the extensive variables, except the entropy, are constant, corresponds to the minimum of free energy, which can be described by:

$$A = U\text{-}TS \qquad 5)$$

where *A* is the free energy, *U* the internal energy, *T* the temperature and *S* the entropy of the system.
If the temperature of a ferromagnetic system is constant and enough lower than the Curie temperature (T_c), the system is characterized by a high level of macroscopic order. Consequently, the entropies of all the possible configurations are not significantly different. Therefore, it is possible to assume that the free energy differences between all the possible configurations of the system mainly depend on the differences in the internal energy (*U*). From a purely qualitative point of view, it is thus possible to define the steady state of a ferromagnetic structure as the state of minimum internal energy.

In order to qualitatively explain the phenomena occurring in ferromagnetic materials when their characteristic dimensions are reduced, let consider a single crystal of a ferromagnetic material, where the energy contributions affecting the state of minimum internal energy can be summarized as:

1) *The anisotropy energy*;

2) *The magnetostatic energy*;

3) *The domain walls energy*;

4) *The elastic energy*.

The *anisotropy energy* is due to the existence, in ferromagnetic crystals, of a magnetocrystalline anisotropy, which is an intrinsic characterist, due to the spin-orbit coupling. Such anisotropy energetically promotes the alignment of the magnetic dipoles along a specific direction which is defined as the "preferential magnetization axis".

This means that, from the point of view of the sole anisotropy energy, the steady state (minimum energy) of the system should be the state determined by the alignment of all magnetic dipoles along the preferential axis of magnetisation.

However, in addition to the anisotropy, other energy phenomena occur.
In particular, if we consider a single domain single crystal (as that one represented in Figure 6), it is possible to observe that, at the far ends of it, there are two opposite polarities, which produce a magnetic field extending in the surrounding space. The associated *magnetostatic energy*, which is the potential energy generated when a magnetic body is in a magnetic field**,** decreases with the decrease of the volume occupied by the field. Therefore, taking into account also the magnetostatic contribution, a multi-domain configuration which minimizes the magnetostatic effects results to be energetically favorable.

It is worth noting, however, that the presence of contiguous domains oriented in different directions, are associated to the presence of transition regions, the Bloch walls, in which a gradual variation of the orientation of the spins occurs. These regions are therefore characterized by a finite thickness, minimum energy state of which depends on the sum of two opposite energy contributions: on the one part i) the energy required to overcome the exchange interactions that promote the parallel orientation of all the dipoles, the effect of which would result in very large wall thicknesses ; on the other part ii) the effect due to the fact that the spins inside the Bloch wall are not oriented along one of the easy magnetization directions (those along which the spins inside

domains are oriented) and therefore an anisotropy energy is associated to them, the minimization of which leads to a reduction of the wall thickness.

Therefore, the domains formation is associated to an increase of the internal energy due to i) the increase of the anisotropy energy for the formation of domains that can be oriented in a different direction with respect to the axis of preferential magnetization, ii) the increase of the *elastic energy* due to magnetostriction phenomena that occur in the presence of differently magnetized domains, and, moreover, iii) the increase of the energy contribution due to the formation of Bloch walls, called "*wall energy*", which is proportional to the surface.

Considering that the magnetostatic energy increases with the volume of the space occupied by the magnetic field, and thus with the volume of the single crystal, if considered as a single domain crystal, it is easy to understand that a multi-domain configuration is energetically favored when the dimensions of the crystal are greater than a certain critical dimension. This is due to the low surface-to-volume ratio, and thus to the fact that the reduction of magnetostatic energy is predominant in respect of the increase of the wall energy. On the contrary, below a certain critical size of the crystal, the increase of the energy associated to the presence of the Bloch walls is no longer compensated by the decrease of magnetostatic energy (because of the increased surface / volume ratio) and the single domain configuration becomes the energetically favored state.

The foregoing can be explained by considering that the magnetostatic energy, for a single crystal domain, can be expressed as:

$$E_{ms} = \frac{1}{2}\mu_0 N M_s^2 V \qquad 6)$$

where M_s is the value of the spontaneous magnetization along the preferential axis of magnetisation of the crystal, N is a demagnetization factor, V is the crystal volume. If we consider, for example, a crystal in which there are two domains magnetized in opposite directions along the same axis of easy magnetization, the corresponding magnetostatic energy will be reduced by approximately 50%. Indicating with γ the sum of the terms that contribute to the increase of the internal energy due to the formation of the Bloch wall, the energy variation of the system between the single domain configuration and the configuration with two domains can be expressed as:

$$\Delta E = \gamma S - \frac{1}{4}\mu_0 N M_s^2 V \qquad 7)$$

If this difference is higher than zero, the formation of domains is energetically favored, and the steady state (lowest energy) of the system is represented by the single domain configuration. This circumstance occurs in correspondence of a surface/volume ratio:

$$\frac{S}{V} > \frac{\mu_0 N M_s^2}{4\gamma} \qquad 8)$$

Therefore, for each ferromagnetic material, there is a critical dimension ("diameter" for spherical particles), which is called single domain size D_{SD}, below which the minimum energy configuration is that of the single domain configuration.

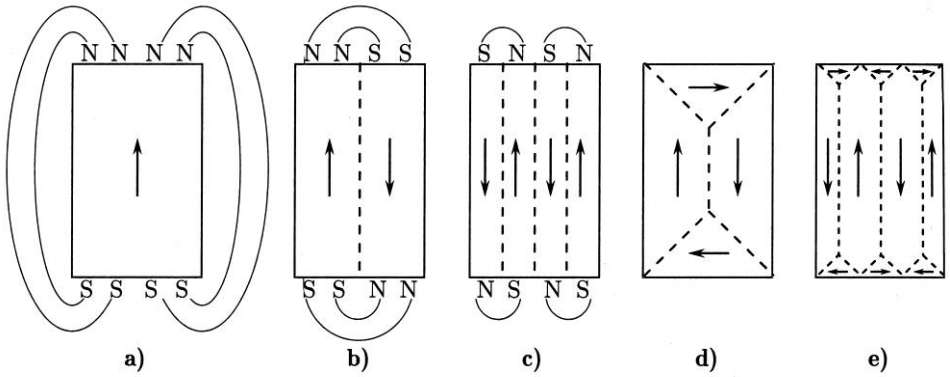

Figure 6 – Schematic representation of multi and single-domain configurations

1.1.2.1 – Superparamagnetism

Let now consider a single domain particle.

The magnetization energy of a single domain particle is generally dependent on the relative direction of the applied field with respect to to the axis of easy magnetization of the particle. The equilibrium directions are, in particular, separated by an energy barrier (ΔE_A) which depends on the volume of the particle(V_p) and the magnetocrystalline anisotropy constant (K), being, in the approximation of single axis of anisotropy:

$$\Delta E_A = K V_p \sin^2 \theta \qquad 9)$$

where θ is the angle between the magnetization direction and the preferential axis. If $\theta = 0$, i.e. if the magnetization direction coincides with the preferential axis, the potential energy of anisotropy, which represents the energy barrier to be overcome to allow changes of magnetization direction, will assume the minimum value (zero). The more θ is different from zero the greater is the energy barrier; this means that the more the

magnetic field direction is applied away from the preferential axis direction, the more the intensity of this field must be high so that the dipoles align parallel to it.

The single-domain particles, in the absence of any applied magnetic field, have, in general, the individual atomic dipoles oriented parallel to the direction of their preferential axis, which is the direction of the minimum anisotropy energy. A change in this direction of magnetization can occur only if the energy needed to overcome the energy barrier related to the new direction of orientation is provided.

The dependence of the energy barrier ΔE_A on the particle size (V_p) is the reason why, for each value of temperature (and therefore also at room temperature), there is a critical size D_{sp}, below which the energy of thermal agitation is sufficient to overcome the energy barrier of potential anisotropy, and rotate randomly the individual magnetic dipoles.

Under this condition, the behavior of the nanoparticles, from the point of view of the phenomena characterizing the magnetization process, is analogous to a paramagnetic behavior (zero coercivity H_c and zero residual magnetization M_r). This phenomenon is called superparamagnetism.

The temperature at which a nanocrystal of a given size reaches the condition of superparamagnetism is known as "blocking temperature" T_B. Below this temperature the free movement of the magnetic moments is blocked, and the material behaves as ferromagnetic; on the contrary, above it, the material has superparamagnetic behavior.

1.1.2.3 - Coercivity with decreasing grain size: Herzer diagram

Previous considerations are summarized in Figure 7, where the typical trend of coercivity as a function of the particle size is shown.

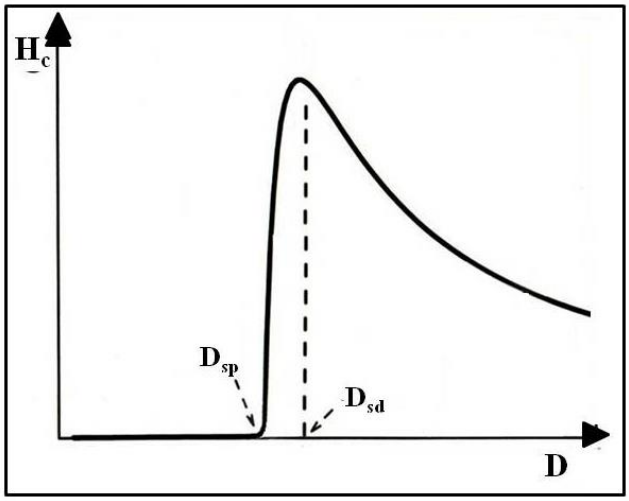

Figure 7 – Herzer diagram: coercivity as a function of the particle size

As long as the particle size is big, so that the energetically favored configuration is the multi-domain one, the movement of the Bloch walls is the dominant process in the magnetization of the material. Therefore, the coercivity, as previously described, is strongly related to dissipative phenomena which occur because of the "high-energy barriers", e.g. the impurities and the amorphous regions of material that the Bloch walls meet during their movement. With the decrease of the grain size, because of the increased surface/volume ratio and the increased percentage of amorphous regions with respect to the ordered regions, there is an increase of the coercivity of the particle. In particular, in this case, the correlation between the coercivity H_c and the average size of the grain (particle) is generally described as:

$$H_c = \frac{C}{D} \qquad 10)$$

where C is a characteristic constant of the material.

When the size of the particle becomes lower than the single domain critical size (D_{sd}), the magnetization process is due to the rotation of the domain magnetization direction away from the direction of easy magnetization. The energy dissipated during this process is therefore dependent on the magnetocrystalline anisotropy energy barrier which, being associated with the crystalline order, decreases with the decrease of the particle size, i.e. with the increase of the disordered zones. Below the critical size of single-domain a decrease of the anisotropy with the decrease of the particle size occurs. There is thus a dimensional range in correspondence of which a sharp decrease of the coercivity with the decrease of the particle size occurs.

In particular Herzer [1] found that, when the grain size (particle) is reduced below the critical size of single domain, the coercivity decreases with the decrease of the size in correlation with D^6. In particular, according to the Herzer theory, the size in correspondence of which the increase of the coercivity with the decrease of the grain size no longer occurs is given by a certain exchange length:

$$L_0 = \sqrt{\frac{A}{K}} \qquad 11)$$

where A is the so called exchange stiffness and K is the anisotropy constant.

When the grain size (particle) becomes smaller than this length, the relationship which describes the coercivity as inversely proportional to D is no longer valid, but the H_c behavior in terms of D is well described by $H_c = C' \cdot D^6$.

Below a certain critical size D_{sp}, the disorder of the material is high enough that the magnetocrystalline anisotropy energy barrier is overcome by the energy of thermal agitation; therefore the phenomenon of superparamagnetism occurs and the material, from the point of view of energy losses during the magnetization process, i.e. from the point of view of coercivity, behaves as paramagnetic (residual magnetization and coercivity nothing).

1.2 - MAGNETIC NANOPARTICLES AND BIOMEDICAL APPLICATIONS

As previously outlined, magnetic nanoparticles are finding more and more applications in several technological fields and, moreover, in the biomedical one. In the following paragraphs the main applications of MNPs in biomedical and biomedicine related fields are described.

1.2.1 - Drug delivery

The major problem associated with cancer chemotherapy concerns the non-specificity of the used drugs, which are, in most cases, introduced into the body intravenously. This administration method involves a systemic distribution of the drug which causes serious side effects due to the action of drugs, not only on carcinogenic cells, but also on the healthy ones. These side effects produce strong limitations regarding both the doses and the continuity of the therapy.

In order to overcome these limitations, great attention has been recently paid to the development of techniques and technologies able to perform localized treatments, i.e. to address drugs on specific sites.

Magnetic nanoparticles, thanks to their nanometric size can penetrate the biological tissues, and thanks to their magnetic properties, can be injected in the body (in the form of a ferroluid) and conducted on the specific target (tumor) by the application of an external magnetic field. If opportunely functionalized with chemoterapic drugs, MNPs can thus be used as carriers to release the drug on the tumor without damaging the surrounding healthy tissues. The use of magnetic drug carriers was proposed for the first time in the 70s [2], [3], and from that moment the development of novel magnetic nanoparticles continues apace.

Numerous animal studies [4]–[6] have been carried out, but the goal of clinical applications still remains unfulfilled, mainly due to some physical constraints placed upon magnetic targeting, such as the rapid decay of field strength with the target depth into the body and the difficulty of bypassing intervening vasculature and tissue structures [7], [8].

In general, the efforts are focused on the development of core-shell nanoparticles having novel functional coatings and, moreover, high-moment cores [9], [10].

Indeed, the particles magnetic properties (susceptibility and saturation magnetization), together with their volume, the magnetic field strength, and the magnetic field gradient, are essential parameters to be tuned to obtain optimal drug delivery systems, being the

magnetic force acting on a magnetic nanoparticle in the biological medium describable, using a very simplified model, as:

$$F_m = V_p(\chi_p - \chi_m)\nabla(\frac{1}{2}\vec{B}\cdot\vec{H}) = \frac{1}{2\mu_0}V_p\Delta\chi\nabla B^2 \qquad 12)$$

where V_p is the particle volume, χ_p the magnetic susceptibility of the particle, the magnetic susceptibility of the medium, B is the magnetic field strength, ΔB the magnetic field gradient.

More complete models, taking into account all the affecting parameters (hydrodynamic parameters, such as the blood flow, the concentration of the ferrofluid, the circulation time and other physiological parameters), are described elsewhere [4], [11].

1.2.2 - Hyperthermia

Hyperthermia is a cancer treatment based on the overheating of tumors to induce the apopthosis of diseased cells, while preserving the healthy ones. Indeed, tumor cells are known to die at lower temperatures than normal cells and often, depending on tumor cells, the temperature difference is higher than 1.0°C [12].

The discovery of the effectiveness of overheating treatments in cancer therapies, especially if performed in combination with other conventional treatments, such as chemotherapy and radiotherapy, has given rise to several studies aimed to the development of techniques able to localize as much as possible the overheating on malignant cells in order to preserve the surrounding healthy tissues.

The first experimental studies on the application of magnetic materials for hyperthermia date back to 1957 when Gilchrist et al [13] induced a heating on multiple tissue samples by means of γ - Fe_2O_3 particles exposed to an alternating magnetic field at a frequency of 1.2 MHz. Since then, several authors have proposed a wide variety of magnetic materials and alternating external magnetic field parameters to obtain the overheating of target tissues [14], [15]. In 1979, Gordon et al [12] introduced the concept of "intracellular hyperthermia", consisting in the use of submicrometric particles, which are able to penetrate into cell membranes, predominantly into cancer cells than normal cells. Applying a high frequency alternating magnetic field, it is thus possible to induce a more localized overheating and obtain the selective thermal destruction of tumor cells, minimizing the effect on healthy cells.

The overheating can be produced by two different phenomena: i) the Brownian relaxation phenomenon, due to the physical rotation of the particles in the fluid, and the ii) Neel relaxation, due to the rotation of the atomic magnetic moments into each particle.

In general the suitable particles for hyperthermia applications are:

1) multi or single-domain, ferri or ferro-magnetic particles;

2) superparamagnetic particles.

Ferromangnetic particles are characterized by hysteretic properties when an alternated external field is applied. The resulting energy losses give rise to magnetically induced heating. The amount of the generated heat (per volume unit) is given by the frequency of the applied field multiplied by the area enclosed in the hysteresis loop:

$$P_{FM} = \mu_0 f \oint H dM \qquad 13)$$

Other heating mechanisms, like “ferromagnetic resonance” and the heating induced by eddy currents, are negligible in this case, because of the low frequencies of the applied field (maximum 1.2 MHz for patient safety) and the limited size of the magnetic particles.

Different is the phenomenon underlying the overheating produced by superparamagnetic particles subjected to an alternated magnetic fields, which has been modeled by Rosenweig [16]. The proposed theoretical model is based on the Debye model, originally developed with the aim of describing dielectric dispersion phenomena in polar fluids. In this model, assuming negligible the inte-particles interactions, the magnetization response of the nanoparticles system when an alternated magnetic field is applied, can be described in terms of its complex magnetic susceptibility:

$$\chi = \chi' + i\chi'' \qquad 14)$$

The amount of heat generated per volume unit (P_{SPM}) is related to the χ'' phase shift according to the relation:

$$P_{SPM} = \mu_0 \pi f \chi'' H^2 \qquad 15)$$

where χ'' is described by the expression:

$$\chi'' = \chi_0 \phi (1 + \phi^2) \qquad 16)$$

where

$$\phi = f \tau_R \qquad 17)$$

and

$$\chi_0 = \mu_0 M_s^2 V/(kT) \qquad 18)$$

with M_S the saturation magnetisation and τ_R the Neel relaxation time.

This model explaines the relationship between the "heating power" and the magnetic properties (e.g. the saturation magnetization), together with the volume of the used NPs, and the consequent emerging need of specific techniques for the characterization and optimization of these properties in magnetic nanoparticles for hyperthermia systems.

Several studies have been carried out about the use of ferromagnetic and superparamagnetic nanoparticles for hyperthermia applications.

Despite the recent promising results [4], [5], some limitations still have to be overcome, which, more specifically, are:

i) The difficulty of obtaining a homogeneous distribution of MNPs in the tumor tissue, which is necessary to avoid temperature differences in the tumor. Indeed, the insufficient heating of certain parts of the tumour can cause the risk of proliferation of surviving tumour cells. In this context, several studies are carried out to improve selectivity of nanoparticles for the cancer cells by functionalization with antibodies.

ii) The difficulty of obtaining the suitable MNPs heating power, i.e the MNPs magnetic properties, in order to achieve efficient therapy temperatures, with the minimum amount of injected MNPs and respecting the limitations (medical, technical and economical) on the frequency (*f*) and the amplitude (*H*) of applied magnetic fields.

1.2.3 - Magnetic nanoparticles as contrast agents for Magnetic Resonance Imaging (MRI)

Magnetic resonance imaging (MRI), due to the extreme imaging flexibility, high patient acceptance, capability to evaluate anatomic and physiologic parameters, is consiedered to be one of the most powerful diagnostic tools in medical domain [17], [18].

MRI working principle makes use of the magnetic properties of certain atomic nuclei, and, in particular, the hydrogen nuclei (single proton) which are present in water molecules, and therefore in all body tissues.

When a nucleus interacts with a static magnetic field (B_0), the magnetic moment μ tends to align to it with a motion (precession), characterized by a certain angular frequency, which is called Larmor (or resonance) frequency, and which depends exclusively on the

type of nucleus and the intensity of the applied magnetic field B_0. MRI does not observe a single nucleus, but statistically derived from the combined effect of all the nuclei present within the analysed sample; therefore a magnetization vector $\boldsymbol{M}$ results from the the resultant sum of all the magnetic moments μ of the individual nuclei, each of which can have a parallel or anti-parallel alignment in respect to B_0.

According to the quantum mechanics laws, there is a slight excess of magnetic moments along one direction than another, and this causes the resultant vector $\boldsymbol{M}$ is never zero and therefore can be measured.

In order to detect $\boldsymbol{M}$, it is necessary to perturb the steady state of the system, for example with a radio frequency pulse (RF excitation pulse). At the end of the pulse, the equilibrium between spin and B_0 is restored, through the so called "relaxation process". More specifically, there is i) a longitudinal relaxation, characterized by the constant T_1, which concerns the energy transfer between the spins and the surrounding environment, and ii) a transverse relaxation, characterized by the constant T_2, which involves the energy transfer between the individual spins.

The equilibrium restoring of a spins system which has absorbed an RF pulse generates a MR signal, called FID (Free Induction Decay), which can be detected as an electric current from an antenna or a coil. The time trend of the generated current has the shape of a sine wave which decays with a time constant T_2*.

Once the MR signal is generated, the corresponding anatomical region is identified using the so-called magnetic field gradient coils.

Both T_1 and T_2* can be shortened by the use of a magnetic contrast agent. Currently, the most commonly used contrast agents consist in paramagnetic gadolinium ion complexes, but contrast agents based on the use of superparamagnetic nanoparticles are gaining increasing interest and finding more and more applications.

Indeed, superparamagnetic nanoparticles, when are subjected to an intense magnetic field, such as that one applied by the MRI systems, produce intense magnetic fields oriented parallel to the applied field, which locally increase the magnetic field. The sets of protons falling in these areas experience, therefore, a significant increase of the Larmor frequency and a consequent variation of their transverse relaxation time (T_2) [19], producing an increased contrast in MRI images.

Various colloidal suspension of nanoparticles of iron oxides and iron-cobalt alloys having suitable dimensions and opportunely coated, are used and studied as contrast agents in MRI imaging applications [20].

In particular, the main clinical applications include:

a) - the fast imaging of the intestine and gastrointestinal tract [21]; for these commercial products, such as Ferumoxsil [22] and Ferristirene [23], are available.

b) - imaging of the liver and spleen, where the use of superparamagnetic particles of iron oxides has allowed the characterization of various types of cancer [24];

c) - imaging of lymph nodes, where the superparamagnetic contrast media have allowed the individuation of lymph nodes with metastases [25], [26];

d) - detection of lesions in the bone marrow [27];

e) - imaging of brain tissues, for the identification of lesions produced by stroke, multiple sclerosis, lymphoma, tumor metastasis, etc. [28];

f) - the non-invasive visualization of atherosclerotic plaques in cardiovascular vessels [29].

Also in the case of the efficiency of magnetic nanoparticles as contrast agent for MRI, there is a direct relationship between the size and magnetization of the used particles and their nuclear magnetic resonance relaxation properties, which condition their efficiency [30]. The efforts in the development of these systems are therefore focused on the individuation of synthesis and characterization methods to obtain the MNPs optimal properties.

1.2.4 - Cell labeling and magnetic separation

Separation of specific biological entities from their native environment is often necessary in biomedicine in order to obtain more concentrated samples, easier to be analyzed. Magnetic nanoparticles can be used as marker for biological separation [31]–[34]. The technique consists of two consecutive phases:

1) Labelling of the biological material with magnetic nanoparticles, opportunely functionalized with specific ligand or antibodies;

2) Separation of the marked material by appropriate microfluidic devices and by the application of magnetic fields.

The phenomenon that describes the migration of a particle in a microfluidic device when a magnetic field is applied and, thus, is the base of magnetic separation process is the magnetophoresis, which can be described as:

$$F_m = N_p V_p (\chi_p - \chi_m) \nabla (\frac{1}{2} \vec{B} \cdot \vec{H}) = \frac{1}{2\mu_0} N_p V_p \Delta\chi \nabla B^2 \qquad 19)$$

where N_p is the number of magnetic nanoparticles bonded to the biological entity (for example a cell), V_p the volume of a prticle, $\Delta\chi$ the difference between the magnetic susceptibility of the particle (χ_p) and the fluid medium (χ_m). Thus, magnetic nanoparticles properties (size and magnetic characteristicss) are parameters that strictly influence the magnetophoretic mobility of a magnetically marked biological complex, together with the characteristics of the applied field and the fluid medium.

Also in the case of the development of magnetic separation systems, the capability of characterizing and optimizing these properties appears an essential requisite for the optimization of the system efficiency.

1.3 - CHARACTERIZATION TECHNIQUES

The design of all the previously described techniques and applications requires a detailed knowledge on the magnetic and structural properties of the adopted nanomaterials. As an example, the magnetic hyperthermia heating effect, the translational force exerted on drug delivery carriers, the drag force in cells magnetic separation systems, are all strongly dependent on the magnetic properties of the nanoparticles, like the magnetic susceptibility, the saturation magnetization, the shape of the magnetization curve and the eventual hysteresis area. Furthermore, it is well known that the magnetic properties of nanoparticles are strongly dependent on their size.

Therefore a characterization method able to evaluate the magnetic properties of nanoparticles to be used for biomedical applications, also in dependence of their structure and size, is needed.

In next paragraphs, the characterization techniques most commonly used to obtain information about the magnetic properties of nanoparticles are briefly described and discussed, with the aim of defining the state of the art in this field and highlighting the existing limitatations which have to be overcome as well as the needs which still have to be satisfied.

1.3.1 - Conventional techniques: Statistical magnetic characterization

The common approach to obtain information about the magnetic behavior of nanoparticles is the macroscopic measurement on an array or a dispersion (ferrofluid) of several thousands of similar particles, which furnish information about the global magnetic behavior of numerous nanoparticles populations. To do that, some standard techniques, like Superconducting Quantum Interference Devices (SQUID) [35] or Vibrating Sample Magnetometer (VSM) [36] and Alternative Gradient Field Magnetometer (AGFM) [37], are widely used.

Superconductive Quantum Interference Divices (SQUID) are superconducting instruments capable of measuring extremely weak magnetic fields and currents, which have been widely used for magnetometry in different fields of medicine, metrology and science [38], [39]. The SQUID consists of one or (more often) two Josephson junctions, generally having an area of at least 0.5 μm^2, connected to each other to form a closed superconducting ring. The combined properties of the Josephson effect and the quantization of the magnetic flux in a superconducting ring make these devices able to

transform a small magnetic flux variation in an easily measureable (by simple lock-in techniques) electrical signal. Indeed, the sample flux is transferred to the input coil of the SQUID via a superconducting pick up coil, allowing the study of the magnetization behaviour in response to an applied magnetic field. The main limitation of SQUIDs is the necessity of using superconducting materials, which implies the use of very low temperatures and, consequently, complex and expensive refrigeration systems.

Vibrating sample magnetometer (VSM) working principle is based on the Faraday's law of induction, according to which an alternating magnetic field produces an electric field. In this technique, the sample is placed in a constant magnetic field and then put in mechanical oscillation through the use of a piezoactuator. The constant magnetic field magnetizes the oscillating sample, the magnetic dipole moment of which creates an alternating magnetic field. This AC field produces an electric field in the pick-up coils. The measured current (or voltage) is thus proportional to the sample magnetic moment and furnish information about the magnetization state of the sample.

The **Alternative Gradient Field Magnetometer (AGFM),** in stead of using a vibrator to put the sample in oscillation and measuring the voltage induced in a set of sensor coils, uses a set of gradient coils to produce an AC field. The AC field creates a force on the sample which causes the sample to start vibrating with amplitude proportional to the moment of the sample. The actual sensor in the system is a displacement sensor or a force sensor, usually a piezo electric device.

These conventional techniques are, currently, well established methods for the characterization of magnetic nanoparticles. Nevertheless, they are characterized by an intrinsic limit: the statistical character do not allow the detection of magnetic properties of single particles, which could furnish important information to deeply understand the phenoma regulating the magnetism at the nanoscale, and the evaluation of these properties in dependence of the particles size is not explicit.
This is the reason why several efforts are focusing on the research and development of new techniques with more and more high resolution, able to study the magnetic behaviour of single, smaller and smaller, isolated nano-objects, such as a single nanoparticle.

1.3.2 - «Single nanoparticle» characterization techniques

The dream of measuring the magnetization reversal of single magnetic particles goes back to the 50s, with the pioneering works of Néel [40] and Morrish and Yu [41], who used a quartz-fiber torsion balance to carry out magnetic measurements on individual micrometric γ- Fe_2O_3 particles with the aim of demonstrating the existence of the single-domain status.

Today, the study of the magnetization evolution mechanisms of single magnetic nanomaterials under external magnetic fields is still a hot topic in magnetism: several techniques have been "explored" but all of them present some limitations and a standard method to quantitatively measure the main magnetic parameters of isolated nanomaterials has not been individuated yet.

The magnetization reversal of single micro and nanostructures can be, for example, characterized by different techniques such as magnetoresistance techniques [42], Spatially resolved Kerr effect (MOKE) [43] or magneto-optical scanning near field optical microscopy [44], but greater attention is paid to techniques having higher resolution and the capability of a more detailed study of the magnetization reversal of nanometer-sized nanoparticles, like micro and nano-SQUID, Transmission Electron Microscopy (TEM) based techniques , such as differential phase contrast mode (DPC) or off-axis electron holography, X-ray microscopies, such as X-Ray Photoemission Electron Microscopy (XPEEM), and ballistic Hall micro-magnetometry systems, which are briefly discussed below.

1.3.2.1 – Micro and Nano-SQUID

Conventional SQUIDs instrumentation is not well suited for measuring the magnetization of single sub-micron objects because the separation of SQUID and pick up coils leads to a too small coupling factor. Nevertheless, a higher coupling factor can be achieved by coupling the sample directly with the SQUID loop. But in this case, the magnetic field applied to the sample is also applied to the SQUID, reducing the SQUID sensitivity. In order to improve the sensitivity to a high field applied in the SQUID plane, thanks to the development of electron beam lithography fabrication techniques, nanobridge-DC-SQUID technique has been developed [45]. This technique uses the Josephson effect in nanobridge junctions, instead of the commonly used tunnel junctions, allowing the application of several tesla in the plane of the SQUID without dramatically reducing the SQUID's sensitivity.

After the development of the micro-SQUID technique in the early 1990s [46], the study of magnetization reversal in magnetic nanostructures began in 1993 [27]. The first studied systems were micrometer-sized particles containing about 10^{10} magnetic moments. During the following years, the micro-SQUID technique has been improved to study smaller and smaller systems. In 2000, clusters containing about 10^3 magnetic moments could be studied. This achievement raises the question whether further improvements might be possible. The fundamental limit of a SQUID is the quantum limit, which corresponds to a sensitivity of about one magnetic moment for a SQUID with $1\mu m^2$. One might come close to this limit by using shunted SQUIDs [47]. Another possibility could be a reduction of the section of the nanobridges [48]. The development of nanofabrication techniques have led to nano-SQUIDs. There are two types of nano-SQUID: either the cross section of the Josephson junctions is reduced to about 1 nm by using carbon nanotube junctions [37] or the loop size is reduced to a few 100 nm [49]–[53]. Both types of nano-SQUIDs lead to a significant improvement concerning the detection of magnetization switching of individual magnetic particles or molecules. Nano-SQUIDs are therefore very promising for quantum information processing based on spin systems [54], [55], but some disadvantages, such as the complicated sample prepration and the limited range of applicable temperatures and magnetic fields, still limit the wide application of this technique to the magnetic characterization of single nanomaterials.

1.3.2.2. - Ballistic Hall micro-magnetometer

Ballistic Hall micro-magnetometer presents some advantages in respect to SQUID, since it can be used with a comparable sensitivity (which could be further improved by reducing, for example, the detection area) in a much broader temperature range ($T<80K$) and in magnetic fields of several Tesla applied in any direction [56]. The standard Hall magnetometer working principle is based on the fact that the linear Hall resistance of a two-dimensional electron gas (2DEG) arising from a magnetic field is proportional to the magnetic flux density B by a factor depending on the electron sheet density and the electronic charge. Therefore, by measuring the Hall resistance (R_{Hall}), an unknown magnetic flux can be studied. In the nanotechnology field, the classical Hall effect, based on the diffusive transport regime, has been applied only to the magnetic characterization of lithographically produced nanostructures [57]–[59]. More recently, Hall micro-magnetometers, based on the ballistic electron transport, have been

developed and applied to study the flux penetration and the magnetisation of single lithographically produced disks (having diameters in the range 100nm-1μm) [60], [61]. The main limit of this technique is represented by the necessity of positioning the analysed nanostructures in the sensitive region of the Hall micro-magnetometer. This can be achieved, for example, by directly grow the nanostructures on the desired region of the magnetometer [62], but the analyzable samples are inevitably limited. Otherwise, particular instrumentation, such as opportune manipulators or an AFM apparatus, can be used to select a single nano-object and place it in the desired region of the magnetometer, making the instrumentation required to perform this kind of measurements more complex and expensive.

As an example of successful application of this technique, using an AFM apparatus to visualize and position the single nanoparticle, Kuhun et al [56], measured the hysteresis loop of a 20 nm Fe nanoparticle. Nevertheless, the complicated sample preparation and the necessity of additional instrumentation (manipulators, AFM, microscopy systems, etc) to directly grow or place the sample in the magnetometer sensitive area, strongly limit the use of this technique in the magnetic characterization of single nano-objects.

1.3.2.3 – Transmission Electron Microscopy (TEM) techniques

Other methods suitable to probe magnetic field at the nanoscale and proposed for the magnetic characterization of single nano-objects are Transmission Electron Microscopy (TEM) based techniques , such as differential phase contrast mode (DPC) or off-axis electron holography.

Differential phase microscopy is an in-focus imaging technique performed using the scanning mode in TEM (STEM). A quadrant-split detector is placed in the diffraction plane of the microscope. The difference in the signal in the different parts of the detector, which are proportional to the magnetic deflection of the beam, reveal the magnetic components of the sample. If a system able to remotely control the microscope functions is available, the hysteresis loop of a sample can be generated, by recording a huge amount of DPC images of the sample in different conditions of applied magnetic field, which can be obtained by simply tilting the sample holder. Indeed, in TEM, the vertical magnetic fields caused by the lenses can be used to produce in-plane magnetic fields with different magnitudes: if the sample holder is tilted in the vertical field, the sample experiences an in-plane component, whose magnitude varies with the sine of the tilting angle. This method has been used by Uhlig et al [63] to measure the

magnetic hysteresis loop of 1.5 μm rings and elliptic particles having dimensions of 20nm (thickness) x500nm x 1 μm, which represent the smaller samples ever magnetically characterized by this technique. This technique, being basically an imaging technique, provides the advantage of visualizing the magnetic domains structure at any point of the loop. Nevertheless, the long duration of the measurement procedure is one of the main disadvantages which, together with the complicated sample preparation, typical of transmission techniques, limits its use for the quantitative magnetic characterization of single nanoparticles.

Electron holography allows one to map the local magnetization with a spatial resolution down to few nanometers and sensitivity of about the order f $\pi/100$ radians [64]. It provides the possibility of obtaining information on the magnetostatic potential throughout the sample and the fringing field in the regions above and below the sample. In off axis electron holography, an electron hologram is recorded with a coherent electron beam and an electron biprism; the magnetic information is extracted by an optical (laser) or an electronic (digital) image reconstruction process, allowing the visualization of the magnetic domains structure of a sample with a very high resolution. The technique is widely used in nanoscale magnetic characterization and the domain structure of several single magnetic nano-object with size lower than 50 nm, have been analyzed [65], [66]. Nevertheless, some disadvantages, such as the limited area of view (<0,5 um in width), and the necessity of special hardware including a field emission source and a bi-prism, together with the complex sample preparation typical of transmission techniques, still limit its use.

1.3.2.4 – X-ray based techniques

All the described techniques require highly specialized or complicated sample preparation, and only very few nanoparticles from a microscopic batch can be analyzed in a reasonable time, resulting in a limited statistic.

This limit is not present in X-Ray based techniques, such as soft X-ray spectroscopies [67] like X-ray holography [68] and transmission X-ray microscopy [69]–[71] which, with the recent developments, allow one to obtain the magnetic imaging of a nanomaterial with a claimed lateral resolution of about 25 nm. Nevertheless, these techniques, being magnetic imaging techniques, do not allow the quantitative measurement of magnetic parameters, such as the magnetic moment, and can be applied only to samples transparent to X-rays.

By contrast, a simultaneous quantitative evaluation of the chemical state, the coercive field, and the magnetic moment, without requiring samples transparent to X-rays, can be obtained by X-Ray Photoemission Electron Microscopy (XPEEM), which is a particular photoelectron microscopy technique performed in combination with synchrotron light. This technique is conventionally employed as a high resolution (30-100 nm) imaging technique and for the quantitative micro-spectroscopy [72]. If the polarization of X-rays is variable, it is also possible to employ the magnetic circular dichroism (XMCD) and the magnetic linear dichroism (XMLD) to obtain the magnetic imaging [73], [74] and then the quantification of spin and orbital moment [75] of a given sample. The research efforts, in this field, are mainly focused on improving of the lateral resolution. For example, the combination of XPEEM with other high resolution microscopy techniques, such Scanning Electron Microscopy (SEM) or Atomic Force Microscopy (AFM), has been proposed [76], [77]. Furthermore, latest advancements concern the development of instruments with aberration correctors, with which a spatial resolution below 10 nm could be achieved [78], [79], and the use of dielectric multilayer mirrors as sample holders to perform depth resolved XPEEM via standing wave excitation [80], [81] and obtain, for example, a "map" of the bulk and surface magnetization of a three-dimensional nanostructure [82].

Nevertheless , the difficulty of applying magnetic fields during the measurement, still represents the major drawbacks in the use of XPEEM for the magnetic characterization of nanomaterials. Only Sandig et al [83] and Kronast et al [77] succeeded in performing measurements of the magnetization curves of single Fe nanocubes (18 nm) through XPEEM technique, coupled with Scanning Electron Microscopy (SEM), by using particular custom made magnetic sample holders, the special geometry of which allows the application of laterally confined magnetic fields (of several tens of mT) with minimum deflection of photoelectrons and without affecting the spatial resolution.

Despite the promising results obtained with this system, the use of XPEEM for the study of the magnetic behavior of single nano-objects is still limited, probably due to the complex instrumentation, based on the use of the synchrotron light, which is expensive and not easily accessible.

1.3.3 - Limits of "existing" characterization techniques

All the previously described technique present some limitations, which have limited, until know, their wide use in the quantitative magnetic characterization of single nano-objects, such as nanoparticles. These limitations are summarized in Table 1.

Table 1 – Recapitulatory table about the characteristics of existing magnetic characterization techniques

Technique	Size of smaller measured object	Limitations
SQUID	-	- statistical measurement - limited range of working temperature (low T)
VSM	-	- statistical measurement
AGFM	-	- statistical measurement
Nano-SQUID	8 nm [84]	- complicated sample preparation - limited range of working temperature (low T) - limited range of applicable magnetic fields
Ballistic Hall micro-magnetometer	20 nm [56]	-Complicated procedure and sample preparation
TEM: Differential phase microscopy	20nm x 500nm x1µm elliptic particle [63]	-Complicated sample preparation -long duration of the measurement procedure
Electron holography	< 50 nm [65], [66]	- Complicated sample preparation -limited area of view (<0,5 um in width) -necessity of particular instrumentation: special hardware including a field emission source and a bi-prism
XPEEM	18 nm Fe nanocubes [77]	- Requires syncrotron light (not easily accessible and expensive) -Difficulty of applying magnetic fields during imaging (requires particular sample holders) -Need to be coupled with a high resolution microscopy system (SEM or AFM)

Because of the drawbacks present in each of the existing techniques, none of them has been employed and recognized as a standard technique for the characterization of nanoparticles.

1.3.4 - Magnetic Force Microscopy: A possible solution?

Magnetic Force Microscopy is an Atomic Force Microscopy based technique which, in respect to all these techniques, appears as a potential suitable technique for the study of single nanostructures, thanks to its nanometric lateral resolution (10-20nm) comparable to transmission techniques, its applicability to all kinds of nanomaterials without particular sample preparation, and its capability to map the magnetic evolution with respect to an applied field.

Nevertheless, the potentialities of MFM in the measurement of quantitative magnetic parameters (such as the hysteresis loop) of single objects at nanometric scale is still not completely exploited and only few results are available. This is mainly due to some limitations of the techniques, which still limit the capability of the technique of

performing quantitative measurement of the magnetic parameters, such as the magnetic moment.

In the next chapter the physical phenomena and the working principle of MFM, as well as the state of the art regarding the applicability of the technique to qualitative and quantitative characterization of magnetic nanomaterials are described in detail, highlighting the potentialities of the technique and the limitations which still have to be overcome in order to obtain the quantitative magnetic characterization of individual magnetic nanoparticles.

2. STRUCTURE OF THE THESIS

As described in Chapter 1, magnetic nanoparticles are gaining increasing interest in several technological fields, and especially in the biomedical one, thanks to their nanometric size and their particular magnetic properties. The most promising and studied applications concern both diagnostic and therapeutic treatments, such as contrast agents for MRI, drug delivery and hyperthermia treatments. The design and the optimization of these techniques require a detailed knowledge on the magnetic and structural properties of the adopted nanomaterials. The use of proper characterization methods to quantitatively measure the magnetic properties of nanoparticles, also in dependence of their chemical composition, structure, size and shape is very important from both a purely scientific and a practical point of view. Conventional methods allow the statistical measurement of the magnetic characteristics of numerous populations of nanoparticles, but do not allow the quantitative characterization of single nano-entities, which is still a big challenge in the scientific community. Several techniques have been proposed, studied and developed with the aim of selecting single nano-objects and quantitatively characterize their magnetic properties, but some limitations still characterize these techniques, such as the complexity of the sample preparation or the necessity of using advanced, expensive and not easily accessible instrumentation.

In this context, Magnetic Force Microscopy (MFM), the working principle and instrumental apparatus of which is described in detail in next Chapter 3, potentially appears as a possible solution to achieve the goal of the quantitative magnetic characterization of single nanoparticles. This hope is mainly due to its resolution and sensitivity comparable to those of electron techniques and to the fact that MFM does not need any particular sample preparation and its instrumental apparatus is very simple and accessible to most of scientific laboratories**.**

Nevertheless, the use of MFM technique as a magnetic nanometrology tool, especially for the quantitative measurement of magnetic properties of single NPs, is still a challenge, demonstrating the need of a further improvement of the technique.

In this context, the main objective of the project is the development of an instrumental apparatus and an experimental procedure to obtain quantitative measurements of nanoparticles magnetic properties by Magnetic Force Microscopy (MFM), overcoming the limitations which still affect the technique and impede its use as a magnetic nanometrology tool.

In Figure 8 a schema representing the logical structure of the thesis is represented.
First of all, a detailed analysis of the state of the art regarding the working principle and the applications of MFM has been performed; this analysis is reported in next Chapter 3. Some of the factors affecting MFM measurements, representing some of the possible reasons of the lack of quantitative MFM data, have been individuated and described in paragraph 3.4. On the basis of the limitations of the technique emerged from the literature analysis, the precise objectives and the different phase of the project have been defined; these objectives are enunciated and described in details in Chapter 4. In Chapter 5, Chapter 6, Chapter 7 and Chapter 8 the developed strategies and the obtained results related to each phase of the project are reported.

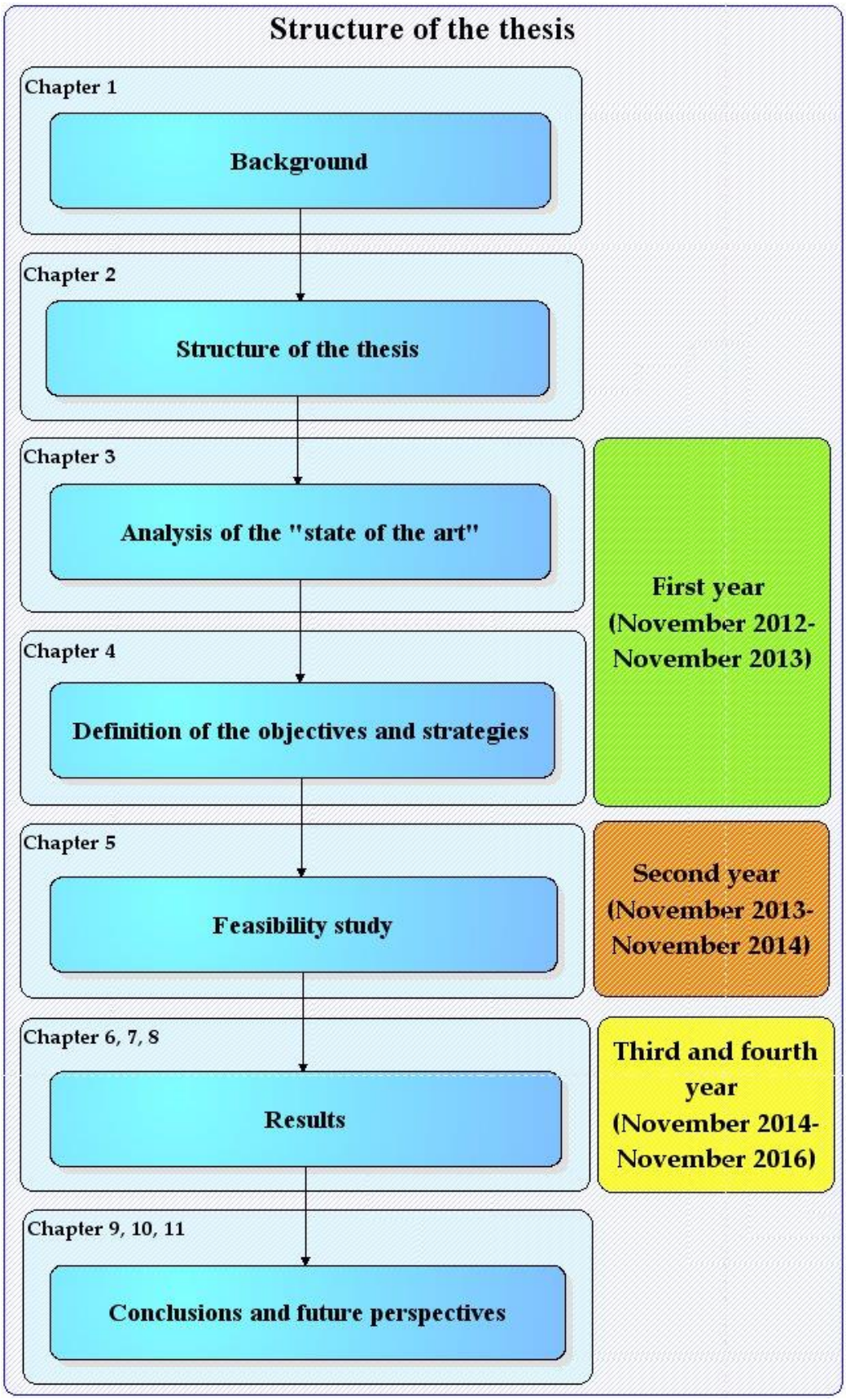

Figure 8 – Schema representing the structure of the thesis

3. MAGNETIC FORCE MICROSCOPY

OVERVIEW

Magnetic force microscopy (MFM) refers to a family of scanning probe techniques based on atomic force microscopy (AFM), which allow one to image the magnetic properties of the sample surface at the nanoscale, simultaneously to its topography. Here, we review the most widespread MFM techniques, mainly dynamic MFM although static MFM is also briefly described for the sake of completeness. We illustrate the working principles, the experimental setups, and the analytical models describing the MFM response, which are fundamental for understanding and quantitatively interpreting the contrast in MFM images. An overview is given of the application fields of MFM, which cover almost all the magnetic materials, from recording media to ferromagnetic materials, nanomaterials and nanoparticles, alone and in organic or biological systems. Finally, some advances, hot topics, new applications, and open issues are presented, including the effect of external magnetic fields, nonmagnetic interactions, MFM tips calibration and advanced probes, and magnetic imaging with variable temperature.

3.1 - INTRODUCTION

Magnetic nanomaterials and nanosystems have been experiencing constantly growing interest for a wide number of applications, e.g., environmental, catalysis and biomedical nanotechnology [85]–[88]. Among these, in the biomedical sector exciting new applications of magnetic nanomaterials have been proposed, e.g., cell labelling, drug delivery, contrast agents for magnetic resonance imaging (MRI) [85], [89], [90]. These applications are triggered by the unique magnetic properties of nanoscale materials, which may be dramatically different from those exhibited by their bulk counterparts as a result of the superimposition of surface and quantum effects. The former are produced by the higher surface-to-volume ratio, as a consequence of which the properties of nanomaterials are dominated by those of surface instead of bulk atoms, while the latter are produced by the reduced dimensions of the single nanomaterial which are comparable with those typical of the delocalization of the electron states [1,8]. In particular, the size reduction in nanomaterials produces properties not observed in their macroscopic counterparts, such as the transition from ferromagnetism to superparamagnetism and the consequent disappearance of the hysteresis in the magnetization curves, the dependence of the magnetic coercivity and the saturation

magnetization on the dimensions, as well as the appearance of magnetic moments in small nanoparticles of nonmagnetic materials [85], [91]. In order to design new magnetic nanomaterials and nanosystems for specific applications, techniques capable of characterizing their magnetic properties at the nanoscale are required. Instead of global measurements which report the average magnetic response of a wide number of units of a given nanomaterial, the ultimate goal of these novel techniques is the possibility of probing the magnetic response of a single specific unit.

Since their invention in the 1980s, scanning probe microscopy (SPM) techniques have spread through the community of researchers in the field of nanotechnology due to their capability of imaging the sample surface with unpreceded nanometer or sub-nanometer resolution. Indeed, in SPM the sample surface is not imaged by collecting diffracted electromagnetic waves, but by 'touching' the surface with a sharp tip which is maintained in proximity of the surface by monitoring a tip-sample distance dependent physical parameter. In scanning tunneling microscopy (STM), such a parameter is the tunneling current flowing between the (conductive) tip and a (conductive) sample when a dc bias voltage is applied between them [92], [93]. In atomic force microscopy (AFM), such a parameter is the deflection of a micro-fabricated cantilever at the very end of which the tip is located [94]. Therefore, AFM can be used on a wider variety of samples, either conductive or insulating, from stiff to soft polymeric and biological materials, either in air, in vacuum or in liquid environment. By controlling the tip-sample distance, different interaction forces can be probed, from short-range repulsive forces between electronic orbitals, van der Waals forces, to electric and magnetic long-range interactions [95], [96]. Thus, many different AFM-based techniques have been developed which allow one to measure mechanical, thermal, chemical, electric or magnetic properties at selected locations on the sample surface, as well as to qualitatively or quantitatively map them simultaneously to the topographical reconstruction [97]–[105]. Among these, magnetic force microscopy (MFM) refers to a family of techniques, constantly improved since the first reporting in 1987 [106], [107], which allow one to map the tip-sample magnetic interactions through the use of tips coated with magnetic layers. MFM has been demonstrated to be a versatile technique, having extended its range of applications from the original magnetic storage media, to magnetic thin films and nanomaterials. To this aim, experimental setup and theoretical models have been continuously refined in order to address new challenging samples.

In this chapter, after a brief introduction to AFM, the most widespread MFM methods are reviewed in details describing the experimental setup, the operation principles, the mechanisms of contrast formation, and the theoretical models which are at the basis of the interpretation of magnetic images. The application fields of MFM are then briefly reviewed, in order to give an idea of the broad range of materials on which MFM can be effectively used, from magnetic storage media, biogenic or synthetic magnetic nanomaterials alone, in nanocomposites, or in biological systems. Finally, some advances and open issues in MFM are reviewed, including the development of more comprehensive models for the tip-sample magnetic interaction, the application of additional external magnetic fields, the effect of nonmagnetic tip-sample interactions, magnetic measurements with variable temperature, and the realization of advanced tips.

3.2 - EXPERIMENTAL AND INSTRUMENTAL METHODOLOGY

3.2.1 - Atomic Force Microscopy

Differently from other microscopy techniques where the images of the samples are obtained by collecting electromagnetic waves diffracted by the object, in AFM the morphology of the sample is reconstructed by scanning its surface using a sharp tip placed at the end of a microfabricated cantilever, which is generally a few hundreds of microns long, a few tens of microns wide, and a few microns thick. As an example, scanning electron microscopy (SEM) images at different magnification of a cantilever, coated with a magnetic Fe layer a few tens of nanometers thick, used in AFM/MFM analysis are shown in Fig. 9. The two most common AFM operation modalities are the contact and the tapping mode, which are briefly described in the following.

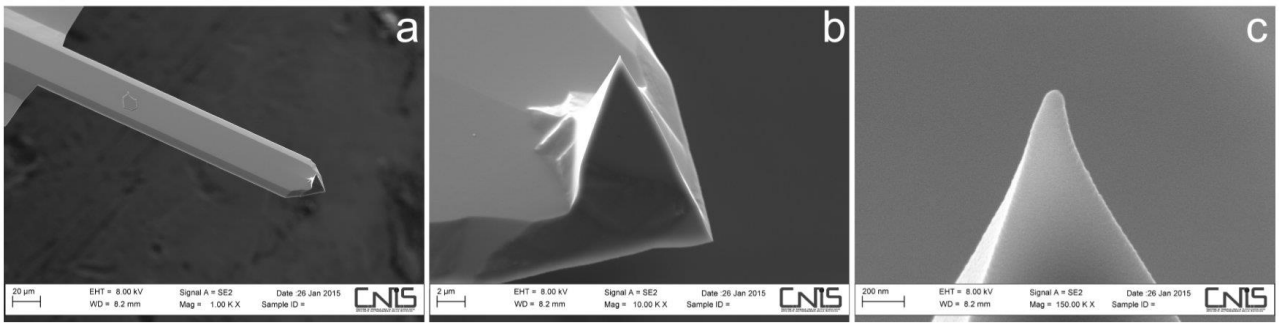

Figure 9 - Example of scanning electron micrographs of an AFM/MFM cantilever (a) with details of the tip at different magnification (b and c, respectively). The cantilever (MESP-LC, Bruker Inc.) is coated with a magnetic Fe layer a few tens of nanometers thick. Images courtesy of Francesco Mura (CNIS - Research Center for Nanotechnology applied to Engineering of SAPIENZA University of Rome).

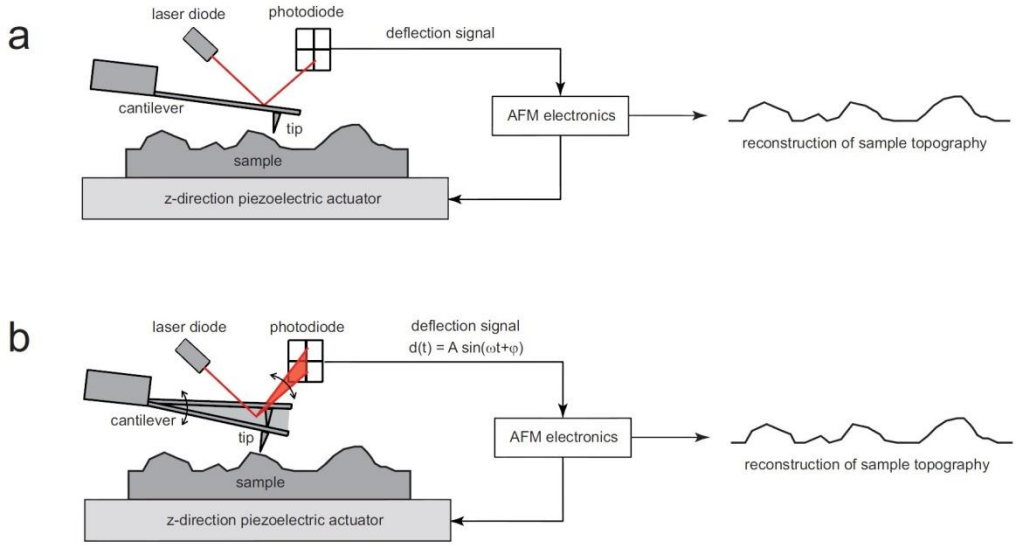

Figure 10 - Sketch of contact (a) and semi-contact (b) AFM operation modes.

3.2.1.1 - Contact mode

In AFM contact mode, which is sketched in Fig. 10a, the tip is constantly kept in close proximity of the surface during the whole image acquisition. Tip-sample interaction is dominated by the Repulsive forces between the electronic orbitals of the surface atoms of the tip and the sample. As a result, the cantilever is deflected and the actual deflection is monitored by an optical lever system. A beam from a laser diode impinges on the back of the end of the cantilever, in correspondence of the tip, is reflected and then collected by a four sectors photodiode. The cantilever deflection is measured as the difference between the signal detected by the upper and lower two sectors. As the tip scans the surface, the actual value of the cantilever deflection changes due to the variations in the local value of the height of surface features. In principle, the deflection signal could be sampled at each of the points of the discrete array in which the surface is divided to reconstruct an image of the surface. Although this method, generally referred to as constant height mode, may offer some advantages in terms of sensitivity and maximum scan rate allowed, it is actually hardly ever used due to the diffculty in converting variations in the deflection signal into the corresponding height values of the scanned features as well as to the risk of damaging the tip. In fact, the deflection signal is used by the AFM electronics as the input signal of a feedback loop to control a piezoelectric actuator along the vertical *z* direction.

The actuator modifies the cantilever-sample distance acting either on the sample (as sketched in Fig. 10a) or on the cantilever in order to maintain the cantilever deflection at a constant value (set point). The variations in the extension of the piezoelectric actuator

are equal to the variations in the height of the reliefs on the sample surface and thus are recorded at each point of the scanned area. The obtained matrix is the reconstruction of the topography of the sample. The image is acquired by applying a constant force between the tip and the sample, i.e., a static load F_L given by $F_L = k_c d_{sp}$ where k_c is the spring constant of the cantilever and d_{sp} is the set point deflection, so that this modality is usually referred to as constant force mode.

The continuous contact increases the risk of damaging soft samples, like polymer or biological materials, as well as of damaging or contaminating the tip. Therefore, contact mode imaging is generally performed using soft cantilevers with k_c usually lower than 1 N/m, unless higher values are required for particular advanced AFM contact mode based techniques, e.g., for themapping of the mechanical properties of the sample surface [108]–[111].

3.2.1.2 - Intermittent contact mode

A less invasive operation modality is represented by the AFM intermittent contact mode, also referred to as semi-contact or tapping mode, which is sketched in Fig. 10b. The cantilever is set into sinusoidal oscillation at (or near) one of its free flexural resonance frequencies, generally the first one (namely, f_0). The cantilever deflection signal thus contains an ac component at the excitation angular frequency ω, where $\omega = 2\pi f_0$ if the cantilever is excited at its free flexural resonance. The oscillation amplitude A and the phase shift φ referred to the driving signal are detected by analyzing the cantilever deflection signal using a lock-in amplifier. As the cantilever approaches the surface, the tip periodically touches the surface in correspondence of the lower part of its motion. This results in a decrease in the value of A from its initial value A_0, corresponding to the tip not interacting with the surface. The actual value of A is used by the AFM electronics as the input signal of a feedback loop to control a piezoelectric actuator along the vertical z direction. Analogously to what happens in the contact mode, the cantilever-sample distance is modified to maintain the cantilever oscillation amplitude at a constant set point value A_{sp}. The variations in the extension of the piezoelectric actuator, equal to the variations in the height of the features on the sample surface, are recorded at each point of the scanned area and used to reconstruct the sample topography. In tapping mode, the contact between the tip and sample is limited to a fraction of the oscillation period, which is related to the set point ratio $r_{sp} = A_{sp}=A_0$: the lower r_{sp}, the longer the interaction time. On the basis of r_{sp}, different tappin mode

regimes can be identified (light, moderate, or hard) which correspond to different severity of the tip-sample interaction (from less to more severe, respectively) [112]–[114]. Differently from contact mode, in AFM intermittent contact mode stiffer cantilevers are employed as they generally show more clear resonances. Overall, the possibility of modulating the interaction time renders the tapping a most versatile operation mode. Indeed, it can be effectively used on a wide variety of samples, from stiff materials to soft polymers or biological systems, as it reduces the risk of damaging the sample or the tip. For these reasons, tapping mode is often the default operation modality of many AFM setups.

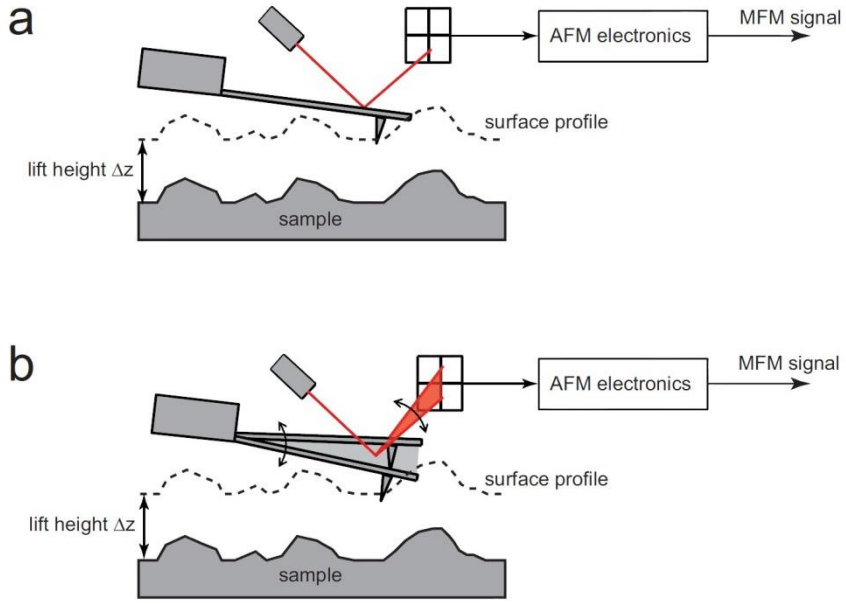

Figure 11 - Sketch of working principle of the second pass of static (a) and dynamic (b) MFM. In both the modes, during the second pass the line is scanned by maintaining the cantilever at a constant distance from the surface, i.e., the lift height Δ*z*. The magnetic signal is represented by the cantilever deflection in static MFM (a) or some oscillation parameters of the vibrating cantilever in dynamic MFM (b).

3.2.2 - Magnetic force microscopy

MFM refers to a family of techniques developed since the last years of the 1980s [106], [115]. Some of these techniques have fallen into desuetude due to their intrinsic limitations, while others have been lately developed to explore exciting innovative applications for the study of magnetic properties of materials at the nanoscale. In this section, we focus on the working principles of the most widespread MFM techniques, illustrating some of the recently developed MFM techniques in the last part of the chapter.

All MFM methods have in common the use of tips sensitive to external magnetic fields. Apart from recently developed innovative tips, commercial probes are commonly available where standard cantilevers are coated with magnetic layers, e.g., containing cobalt or iron. An example of commercial tip coated with an iron based magnetic layer is shown in Fig. 9. Different coatings are responsible for different properties of the tip, both geometrical (e.g., the increase of the tip radius) and magnetic (e.g., magnetic moment and coercivity). In order to detect the magnetic field produced by the sample, MFM probes have to be magnetized. The magnetization of the tip can be
carried out ex situ, i.e., before the tip is mounted on the setup, or in situ, i.e., directly with the tip mounted on the AFM head, using a permanent magnet or an electromagnet. Finally, a permanent magnet or an electromagnet can be featured by the experimental apparatus in order to apply an additional magnetic field during the measurements. The most diffused MFM techniques are "two-pass" methods, which means that images are obtained by scanning each line twice before moving to the subsequent one. In the first pass, the height profile of the line is recorded either in contact or in tapping mode and is used to reconstruct the surface topographic image. In the second pass, the same line is scanned with the cantilever lifted from the sample surface, as sketched in Fig. 11. The height profile of the line recorded in the first pass is used to maintain the cantilever at a constant distance from the sample surface, namely, the lift height Δz, which is selected high enough so that the tip does not experience the short-range forces, e.g., van der Waals interactions, but only the long-range magnetic (and electric) ones. Thus, in the second pass, the cantilever deflection signal is analyzed to obtain a signal which is the expression of the tip-sample magnetic interaction. This signal is recorded along the scanned line and used to reconstruct an image in which the contrast is related to the magnetic characteristics of the tip and the sample. The actual signal recorded during the second pass depends on the specific MFM technique.
Indeed, it can be the static deflection of the cantilever in the so-called static MFM, which is sketched in Fig. 11a. Alternatively, in the so-called dynamic MFM, sketched in Fig. 11b, it can be represented by some oscillation parameters, e.g., amplitude, resonance frequency, phase shift, of the cantilever set into vibration. Dynamic MFM is the most widespread MFM methodology.
In the following, both static and dynamic operation principles are described in details.

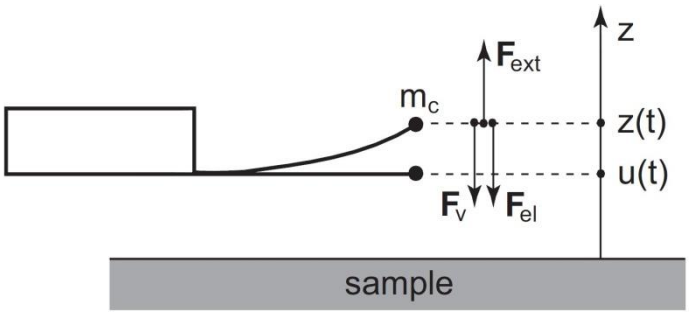

Figure 12 - Sketch representing the forces acting on the cantilever. The position along the vertical axis of the undeflected and deflected cantilever are indicated with $u(t)$ and $z(t)$. The cantilever is subjected to the external force F_{ext} (a generic external force which in MFM is ideally given by the sole tip-sample magnetic interaction force although actually also electrostatic interaction forces are generally present), the elastic force F_{el}, and the viscous force F_v, which are supposed to be applied to a punctiform mass m_c, namely, the equivalent mass of the cantilever.

3.2.2.1 - Static magnetic force microscopy

In static MFM, the tip-sample magnetic interaction is monitored by recording the deflection of the cantilever during the second pass, which is proportional to the actual magnetic force sensed by the tip. Indeed, let us assume that the sample surface is in the O_{xy} plane and the vertical z axis is oriented as in the scheme reported in Fig. 12. In the absence of external forces, the cantilever is not deflected. We indicate with $u(t)$ the position of the undeflected cantilever end, which may vary only due to rigid displacements of the whole tip-cantilever-chip system. At equilibrium $u(t)$ is given by its static value u_0. In presence of external forces the cantilever is deflected and the position of its end is $z(t)$. $z(t)$ may vary due to rigid movements of the tip-cantilever-chip system as well as to displacements affecting the cantilever alone, e.g., in case the cantilever is deflected or set into oscillations. At equilibrium the position of the deflected cantilever is given by its static value z_0. The time-varying cantilever deflection is thus expressed by $d(t) = z(t)-u(t)$ and its static value is given by $d_0 = z_0-u_0$ [116].

When the second pass is performed with the tip lifted from the surface, the tip itself experiences the external magnetic force $F_{ext} = F_{ext}\mathbf{z}$, repulsive in the example in Fig. 12. Considering only the z component of F_{ext} does not represent a reduction of the generality of the following discussion. Indeed, the deflection of the cantilever depends only on the vertical components of forces, while the horizontal components are responsible for the torsion of the cantilever which we are not presently interested in. Note also that F_{ext} is the generic external force the cantilever is subjected to. In MFM, it is ideally given by the sole tip-sample magnetic interaction force although actually also

electrostatic interaction forces are generally present. The deflection of the cantilever produces an elastic force $F_e = k_c d\mathbf{z}$. These forces are supposed to be applied to a punctiform mass m_c, namely, the equivalent mass of the cantilever [116]. The modulus of the viscous force F_v is proportional to the velocity and, thus, $F_v = 0$ when the static response of the cantilever is concerned. In these conditions, at equilibrium $F_{ext} = F_e = k_c d_0$ and thus

$$d_0 = \frac{F_{ext}}{k_c} \qquad 20)$$

Therefore, the images of the cantilever deflection collected during the second pass constitute maps of the modulus and the direction of the magnetic force between the tip and the sample: positive (negative) values of the deflection indicate a repulsive (attractive) interaction, while its absolute value is proportional to the modulus of the magnetic force.

The main limitation of static MFM is represented by its sensitivity, which can be evaluated as $S = \partial d_0/\partial F_{ext} = 1/k_c$. Therefore, soft cantilevers with low k_c are needed to achieve the sensitivity required for the imaging of the magnetic fields produced by the investigated samples, while in the same conditions stiffer cantilevers would hardly be deflected. Nevertheless, the use of soft cantilevers, which generally do not show clear resonances, forces one to perform the first pass in contact mode. This may increase the risk of damaging the magnetic coating of the tip and represents a major limitation to the use of static MFM.

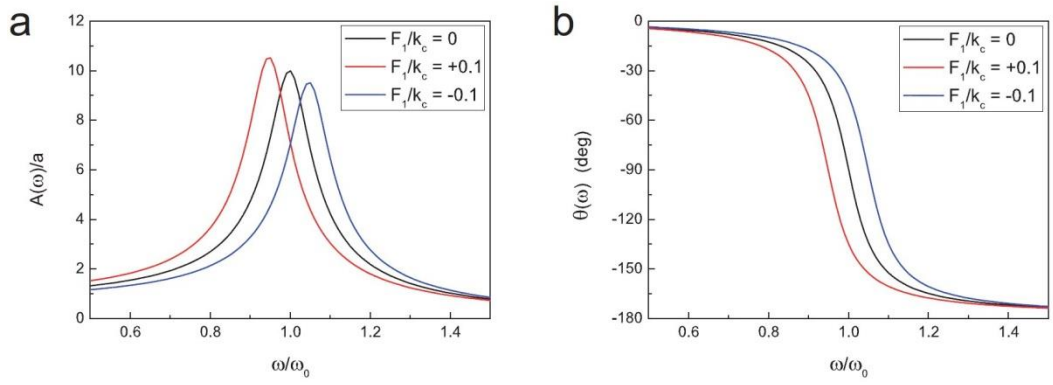

Figure 13 - Amplitude and phase of the cantilever oscillation as a function of the angular frequency ω of the bimorph excitation in the case of uniform external force (black solid line), i.e., zero gradient of the force F_1, and in the two exemplifying cases of gradient of the force F_1 equal to +10% and -10% of the cantilever spring constant kc (red and blue solid line, respectively).

3.2.2.2 - Dynamic magnetic force microscopy

Currently, the most widespread MFM modality is represented by dynamic MFM, the working principle of which is schematically illustrated in Fig. 11b. In the first pass the height profile is acquired in tapping mode. The second pass is performed maintaining the tip at constant distance from the surface, i.e., the lift height Δz, with the cantilever oscillating at (or near) its free resonance frequency in air. The selected oscillation amplitude is generally a fraction of that used in the first pass.

Fig. 12 reports a schematic representation of the forces acting on the cantilever [116]. The cantilever is subjected to the external force $\boldsymbol{F}_{ext} = F_{ext}\boldsymbol{z}$, the elastic force $\boldsymbol{F}_{el} = -k_c d\boldsymbol{z}$, where k_c and d are the spring constant and the deflection of the cantilever, and the viscous force $\boldsymbol{F}_v = -v\boldsymbol{z}$, where v is the velocity of the cantilever and is a damping coeffcient. These forces are supposed to be applied to a punctiform mass m_c, namely, the equivalent mass of the cantilever. As a result of these forces, the cantilever is deflected. The position along the vertical axis of the end of the undeflected and deflected cantilever are indicated with $u(t)$ and $z(t)$, respectively. Thus, the cantilever deflection is $d = z - u$. Under such assumptions, the equation of motion of the system along the z axis can be written as:

$$m_c \ddot{z} + \gamma \dot{z} + k_c (z - u) = F_{ext} \qquad 21)$$

The chip of the cantilever is coupled with a bimorph, which is used to set the system into oscillation at a generic frequency ω. Thus, the position of the undeflected cantilever

can be expressed as $u(t) = u_0 + a\ e^{i\omega t}$, where u_0 is its equilibrium value and a is the oscillation amplitude of the bimorph.

As a result, the actual position of the cantilever end can be expressed as $z(t) = z_0 + \zeta(t)$, where $\zeta(t)$ is a time-varying function describing the variation of the position of the deflected cantilever end from its equilibrium value z_0.

With these assumptions, Eq. (21) can be rewritten as:

$$m_c \ddot{z} + \gamma \dot{z} + k_c\left(z_0 + \xi(t) - u_0 - a \cdot e^{i\omega t}\right) = F_{ext} \qquad 22)$$

Uniform external force. First, let us consider the case of external force uniform along the z axis, i.e., $F_{ext}(z) = F_0$ [116]. In this case, since at equilibrium

$$F_0 = k_c(z_0 - u_o) \qquad 23)$$

Eq. (22) can be simplified as

$$m_c \ddot{z} + \gamma \dot{z} + k_c\left(\xi(t) - a \cdot e^{i\omega t}\right) = 0 \qquad 24)$$

which is the well-known equation of harmonic motion. The solution of Eq.(24) can be found in the form $\zeta(t) = \tilde{A}\ e^{i\omega t}$ where $\tilde{A} = A(\omega)\ e^{i\theta(\omega)}$ is a complex function of ω with modulus $A(\omega)$ and phase $\theta(\omega)$. After calculating the derivatives and substituting them in Eq. (24), we obtain

$$-m_c\omega^2\tilde{A} + i\omega\gamma\tilde{A} + k_c\left(\tilde{A} - a\right) = 0 \qquad 25)$$

from which

$$\tilde{A} = \frac{ak_c}{(k_c - m_c\omega^2) + i\omega\gamma} \qquad 26)$$

is retrieved. The modulus and the phase of $\tilde{A}$ can be calculated as

$$A = \frac{ak_c}{\left[(k_c - m_c\omega^2) + \omega^2\gamma^2\right]^{1/2}} \qquad 27)$$

and

$$\theta = \arctan\left(-\frac{\omega\gamma}{k_c - m_c\omega^2}\right) \qquad 28)$$

respectively. We can define the resonance frequency ω_0 and the quality factor Q as

$$\omega_0 = \sqrt{\frac{k_c}{m_c}} \qquad 29)$$

$$Q = \frac{m_c \omega_0}{\gamma} \qquad 30)$$

respectively. Thus, Eqs. (27) and (28) can be rewritten as

$$A(\omega) = \frac{aQ}{\left[Q^2 \left(1 - \frac{\omega^2}{\omega_0^2} \right)^2 + \frac{\omega^2}{\omega_0^2} \right]^{1/2}} \qquad 31)$$

and

$$\theta(\omega) = \arctan\left(- \frac{\omega}{Q\omega_0 \left(1 - \frac{\omega^2}{\omega_0^2} \right)} \right) \qquad 32)$$

respectively. The dependence of A and θ on ω is represented by the black solid line in Fig. 13a and b, respectively. The curves are obtained assuming ω_0 = 10 rad/s and Q = 10. Such values are not representative of those of real cantilevers, as in the latter ω_0 (Q) is generally three or four (one or two) orders of magnitude higher.

As a result, the presence of an external force uniform along the vertical axis modifies the static deflection of the cantilever according to Eq. (23), but does not affect the oscillation parameters of the cantilever. In particular ω_0 is unvaried with respect to the case of no external forces, in both cases being given by Eq. (29). Moreover, as in the case of absence of external forces, if the cantilever is driven at its resonance frequency the measured phase shift is $\theta_0 = -\pi/2$, independently from the value of F_0.

Not uniform external force. Now, let us consider the more realistic case of external force not uniform along the *z* axis [116]. If the oscillation amplitude of the cantilever can be considered small compared to the typical variation distances of the force field, *Fext* (*z*) can be approximated as

$$F_{ext}(z) = F_0 + F_1(z - z_0) = F_0 - F_1 \zeta(t) \qquad 33)$$

where

$$F_1 = \left. \frac{\partial F(z)}{\partial z} \right|_{z=z_0} \qquad 34)$$

is the gradient of the external force (in general F_1 will be function of z, so that $F_1 = F_1(z)$). Substituting into Eq. (22) and being still valid Eq. (23), the equation

$$m_c \ddot{z} + \gamma \dot{z} + k_c\left(\xi(t) - a \cdot e^{i\omega t}\right) = F_1 \zeta(t) \qquad 35)$$

is obtained, which can be rearranged as

$$m_c \ddot{z} + \gamma \dot{z} + (k_c - F_1)\zeta(t) = a e^{i\omega t} \qquad 36)$$

Analogously to the case of uniform external force discussed above, the solution of Eq. (36) can be searched for in the form $\zeta(t) = \tilde{A}\exp(i\omega t)$. Following the same procedure used in the case of uniform external force to retrieve Eq. (26), the solution for $\tilde{A}$ as a function of ω is

$$\tilde{A} = \frac{a k_c}{\left[(k_c - F_1) - m_c \omega^2\right] + i\omega\gamma} \qquad 37)$$

the modulus and phase of which can be obtained as

$$A = \frac{a k_c}{\left[(k' - m_c\omega^2)^2 + \omega^2\gamma^2\right]^{1/2}} \qquad 38)$$

and

$$\theta = \arctan\left(-\frac{\omega\gamma}{k' - m_c\omega^2}\right) \qquad 39)$$

respectively, where $k' = k_c\left(1 - \frac{F_1}{k_c}\right)$. Defining

$$\omega'_0 = \sqrt{\frac{k'}{m_c}} = \omega_0\sqrt{1 - \frac{F_1}{k_c}} \qquad 40)$$

Eqs. (38) and (39) can be rewritten as

$$A(\omega) = \frac{aQ\dfrac{\omega_0^2}{\omega'^2_0}}{\left[Q^2\left(1 - \dfrac{\omega^2}{\omega'^2_0}\right)^2 + \dfrac{\omega^2\omega_0^2}{\omega'^4_0}\right]^{1/2}} \qquad 41)$$

and

$$\theta(\omega) = \arctan\left(-\frac{\omega\omega_0}{Q(\omega'^2_0 - \omega^2)} \right) \qquad 42)$$

respectively. As examples, the dependence of A and θ on ω in the case of $\mathbf{F}_{ext}$ not uniform is represented in Fig. 11a and b, respectively, assuming ω_0 = 10rad/s, Q = 10 and ratio $F_1=k_c$ = ±0:1 (red and blue solid lines).

The above reported equations indicate that in dynamic MFM the actual value of the force experienced by the tip affects the static deflection of the cantilever but not its oscillation parameters. The static deflection is generally not monitored in dynamic MFM, also due to the fact that relatively stiff cantilevers are commonly used, which do not ensure suffcient sensitivity of the cantilever deflection to force variations. Conversely, the oscillation parameters are influenced only by the gradient along z of the component along the z axis of the external force. These oscillation parameters (amplitude, phase, and resonance frequency) are those commonly monitored in dynamic MFM to perform the magnetic imaging of the sample.

Contrast formation MFM images are generally obtained by recording, during the second pass, the phase shift of the cantilever driven at fixed frequency.

Alternatively, the actual resonance frequency of the cantilever is acquired.

Examples of MFM characterization of different samples are reported in Fig. 14, which shows the topography (left column) and the corresponding MFM phase image (right column) acquired on a floppy disk (Fig. 14a and b), a recording tape (Fig. 14c and d), CoCr (Fig. 14e and f) and Fe (Fig. 14g and h) based thin films a few tens of nanometers thick deposited on Si substrates, the latter two examples being the magnetic coating of two different MFM commercial cantilevers. In all the examples in Fig. 14, MFM phase images reveal magnetic features not observable in the topography. Although some MFM setups may allow one to acquire also the actual amplitude of the cantilever driven at fixed frequency in the second pass, such images are less commonly reported and discussed in literature. Therefore, we now focus on understanding the formation of the contrast only in MFM resonance frequency and phase images in presence of a magnetic external force.

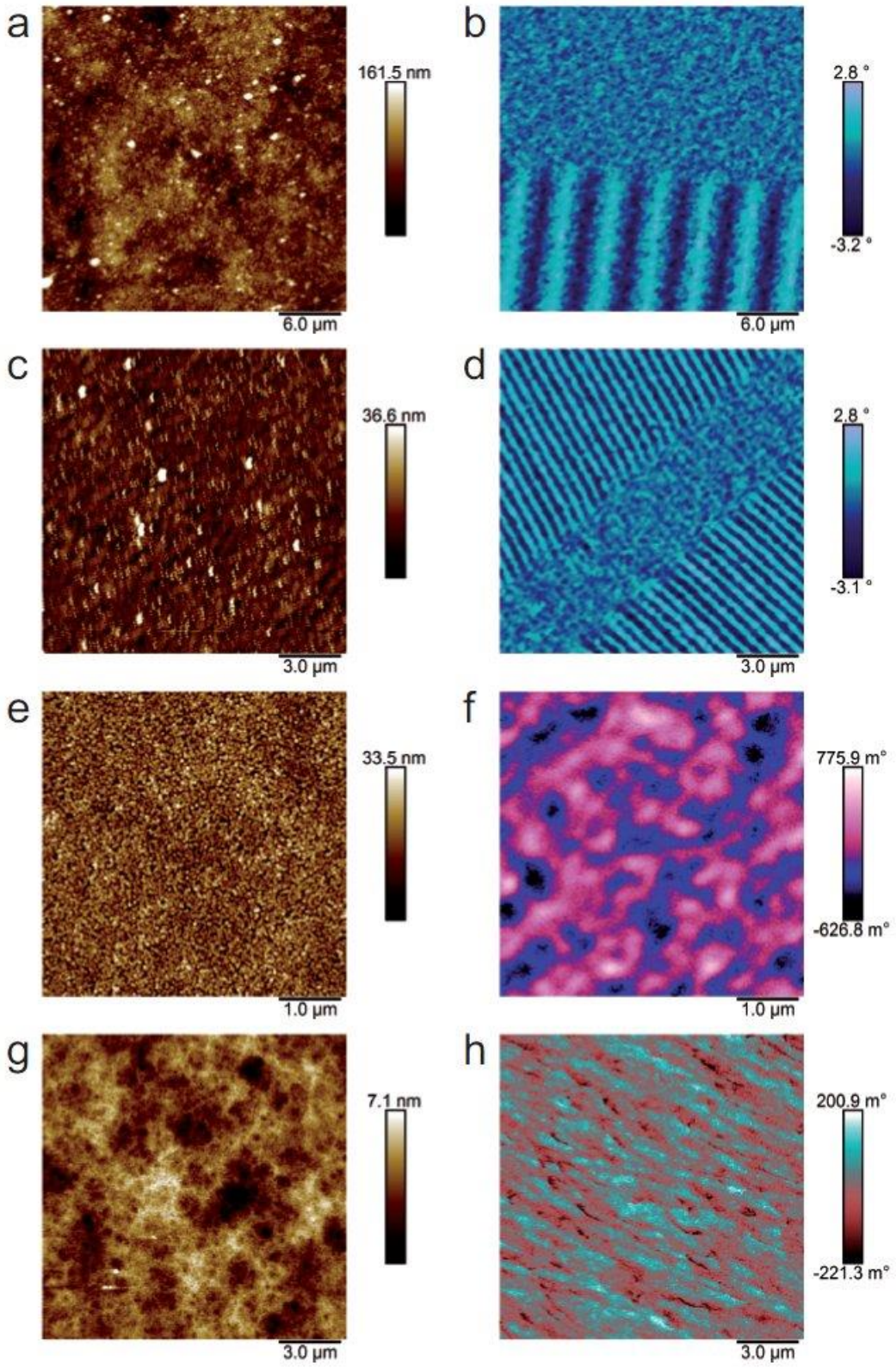

Figure 14 - Examples of topography (left column) and MFM phase image (right column) acquired on different sample: floppy disk (a and b); recording tape (c and d); Co (e and f) and Fe (g and h) based thin films. Authors' unpublished data.

In the absence of $\boldsymbol{F_{ext}}$, the cantilever amplitude and phase response to a sinusoidal excitation is represented by the black solid lines in Fig. 11a and b, respectively. If the MFM image is obtained acquiring the resonance frequency, the constant value ω_0 is recorded. If the MFM image is obtained acquiring the phase at fixed excitation frequency ω, the constant value $\theta(\omega)$ is obtained, e.g., if the bimorph is driven at the resonance frequency ω_0 the phase value $\theta = -\pi/2$ is measured. In presence of an external force acting on the tip, a positive (negative) force gradient F_1 decreases (increases) the resonance frequency. Analogously, if the cantilever is driven at fixed frequency a positive (negative) force gradient F_1 decreases (increases) the phase. These shifts in the resonance frequency ($\Delta\omega_0$) and phase ($\Delta\theta$) can be easily related to the force gradient (more specifically to the ratio $F_1=k_c$) in case of small force gradients. Indeed, when $F_1=k_c \ll 1$, the first order expansions of ω_0' and θ from Eqs. (40) and (39) lead to the approximated expressions

$$\Delta\omega_0 = \omega'_0 - \omega_0 = -\frac{1}{2}\omega_0 \frac{F_1}{k_c} \qquad 43)$$

and

$$\Delta\theta = -Q\frac{F_1}{k_c} \qquad 44)$$

for the resonance frequency and phase shift, respectively [116]. For the sake of completeness, we also report that analogous approximations exist for the variation of the cantilever oscillation amplitude ΔA. Indeed, if the cantilever is excited at the free resonance ω_0 and thus the free oscillation amplitude is given by $A_0 = A(\omega_0) = aQ$, the corresponding variation in the oscillation amplitude ΔA_0 is given by

$$\Delta A_0 = \frac{1}{2} A_0 Q^2 \frac{F_1^2}{k_c^2} \qquad 45)$$

which represent a second-order perturbation being proportional to $(F_1/k_c)^2$ and, thus, is negligible with respect to $\Delta\omega_0$ and $\Delta\theta$ [116]. Moreover, ΔA_0 is insensitive to the sign of the force gradient. To complete the discussion, we observe MFM can be performed not only at the resonance ω_0, but also slightly off resonance at an angular frequency ω automatically set by the instrument and/or manually selected by the user.

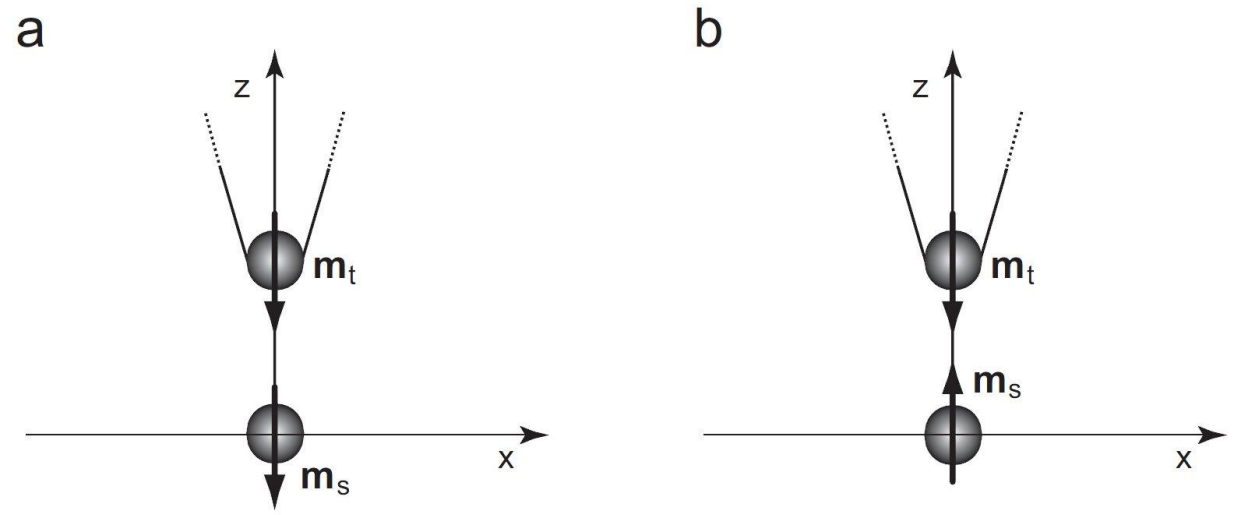

Figure 15 - Sketch illustrating the simplest model for describing the the tip-sample interaction. The tip and the sample are modeled as two punctiform magnetic dipoles on the *z* axis. The dipoles have moments m_t and m_s, respectively, with components only along the *z* and are assumed either parallel (a) or antiparallel (b).

If one is strictly interested in cantilever oscillation amplitude images when performing MFM, an optimum frequency ω_m exists that maximizes the derivative of $A(\omega)$ curve and thus the sensitivity of ΔA to $F_1=k_c$. In correspondence of such a frequency, given by $\omega_m = \omega_0(1\pm 1/\sqrt{8Q}$, the amplitude in the absence of external force gradient is $A_m = A(\omega_m) \approx 0.82 A_0$ [116], [117] and the first-order perturbation of the amplitude variation on the force gradient is

$$\Delta A_m = \frac{2}{3\sqrt{3}} Q A_0 \frac{F_1}{k_c} \qquad 46)$$

Nevertheless, to the best of our knowledge, amplitude MFM images have been used in early works, but have been hardly ever reported and quantitatively analyzed in recent literature [117]. Conversely, resonance frequency and phase shifts are undoubtedly the quantities most commonly acquired to perform MFM imaging and, thus, in the following only these two parameters are considered as the possible MFM signals.

3.2.2.3 - Examples of MFM response

Magnetic dipoles. We now discuss the illustrative example of the magnetic interaction between the tip and the sample, both modeled with punctiform magnetic dipoles with moment $\boldsymbol{m}_t$ and $\boldsymbol{m}_s$, respectively. Despite being an admittedly extremely simplified example, it is nonetheless useful to go into the mechanism of contrast formation in

MFM thoroughly. In addition, although it cannot be immediately invoked in the case complex magnetic domains, as those in recording media, such a model may serve as an effective basis to rationalize the MFM response of magnetic nanoparticles.

Here, we suppose the two dipoles having only the vertical component. First, let us suppose $\boldsymbol{m}_s$ placed in the origin of a *Oxyz* cartesian coordinate system and $\boldsymbol{m}_t$ placed in the point with coordinates *(0,0,z).* In the case sketched in Fig. 15a, $\boldsymbol{m}_t = -m_t\boldsymbol{z}$ and $\boldsymbol{m}_s = m_s\boldsymbol{z}$. In these conditions, the force acting on the dipole $\boldsymbol{m}_t$ is given by

$$F_z = -\frac{3\mu_0 m_t m_s}{2\pi z^4} \qquad 47)$$

which is attractive, and the gradient by

$$F_z' = \frac{\partial F_z}{\partial z} = \frac{6\mu_0 m_t m_s}{\pi z^5} \qquad 48)$$

which is positive and thus produces negative $\Delta\omega_0$ and $\Delta\theta$ shifts. Conversely, if the magnetic dipoles are oriented as in Fig. 15b ($\boldsymbol{m}_t = -m_t\boldsymbol{z}$ and $\boldsymbol{m}_s = -m_s\boldsymbol{z}$), the interaction force and its gradient are given by Eqs. (28) and (29) with opposite signs. Thus, the force is positive (i.e., repulsive) and the gradient negative (i.e., producing positive $\Delta\omega_0$ and $\Delta\theta$ shifts). We emphasize here that the sign of $\Delta\omega_0$ and $\Delta\theta$ is not directly related to the sign of the force, i.e., to the attractive or repulsive nature of the tip-sample interaction, but to that of force gradient. Nevertheless, in the case of magnetic field produced by dipoles on the sample, the modulus of the force decreases a *z* increases independently from the sign of the force. Thus, the sign of the gradient is always opposite to that of the force and thus, from a practical point of view, the sign of $\Delta\omega_0$ and $\Delta\theta$ can be directly related to the attractive or repulsive nature of the tip-sample interaction. This justifies the analysis of the contrast in MFM images also in terms of attraction or repulsion of the tip, which is occasionally found in literature. Nonetheless, if in a (confined) region of the space the tip experienced a force increasing in modulus with *z*, the sign of the shifts $\Delta\omega_0$ and $\Delta\theta$ would be always opposite to that of F'_z, but a positive (negative) shift would now indicate an attractive (repulsive) tip-sample interaction.

As a second example, we discuss the 2D MFM imaging of a magnetic dipole. First, we suppose the tip and the sample as two magnetic dipoles with moments $\boldsymbol{m}_t = -m_t\boldsymbol{z}$ and $\boldsymbol{m}_s = -m_s\boldsymbol{z}$, respectively. We assume $\boldsymbol{m}_s$ placed in the *Oxyz* origin of a Cartesian coordinate

system and $\boldsymbol{m}_t$ in the point (x,0,z) as illustrated in Fig. 16a. The vertical component of the force acting on $\boldsymbol{m}_t$ is given by

$$F_z = \frac{3\mu_0 m_t m_s}{4\pi} \frac{z}{(x^2+z^2)^{5/2}} \left(3 - \frac{5z^2}{x^2+z^2} \right) \qquad 49)$$

The dependence of F_z on x is plotted in Fig. 16b (black solid line) for z = 100 nm, which represents also the profile of the magnetic image of the sample dipole recorded with static MFM. In order to simulate the profile of the magnetic image recorded with dynamic MFM, $F'_z = \partial F_z/\partial z$ has to be calculated from Eq. (30). $-F'_z$ is plotted in Fig. 16b (red solid line) for z = 100 nm, where the sign is changed so that the curve is proportional to the profile of the $\Delta\omega_0$ and $\Delta\theta$ magnetic images obtained in dynamic MFM. Thus, in this case the MFM image of $\boldsymbol{m}_s$ is given by a dark circle surrounded by less intense bright halo. This kind of features can be found, for example, in the MFM images of magnetic nanoparticles. It is well known that the features in AFM topographical images represent the convolution between the actual sample morphology with and the tip shape, which is one of the sources of AFM lateral resolution limit. In addition to tip-shape induced geometrical artifacts, Fig. 16b shows that in MFM even a punctiform tip produces a broadened image of a punctiform magnetic dipole, which limits the resolution of two neighboring magnetic dipoles [118]. Such broadening is strictly related to the lift height. Indeed, simple calculations show that the maximum in the $-F'_z$ profile (corresponding to the bright halo in dynamic MFM images) is located at x_{max} = 0.84z. Moreover, the finite size of the magnetic tip produced an additional broadening of the sample dipole, which further reduces the MFM lateral resolution [118].

A second possible configuration of the dipoles representing the tip and the sample is depicted in Fig. 16c, in which the tip magnetization is vertical ($\boldsymbol{m}_t = -m_t\boldsymbol{z}$) while that of the sample is horizontal ($\boldsymbol{m}_s = m_s\boldsymbol{x}$). In this case, the vertical component of the force acting on mt is given by

$$F_z = \frac{3\mu_0 m_t m_s}{4\pi} \frac{x}{(x^2+z^2)^{5/2}} \left(-1 + \frac{5z^2}{x^2+z^2} \right) \qquad 50)$$

which is plotted in Fig. 16d (black solid line) together with the additive inverse of its gradient $-F'_z$ (red solid line) that simulates the recorded MFM profile.

Although the vertical direction is somehow the most natural choice for the tip magnetization due to geometrical considerations, MFM tips can be magnetized in other directions. In particular, horizontal magnetization of the tip is common as well, e.g., when studying in-plane magnetic domains.

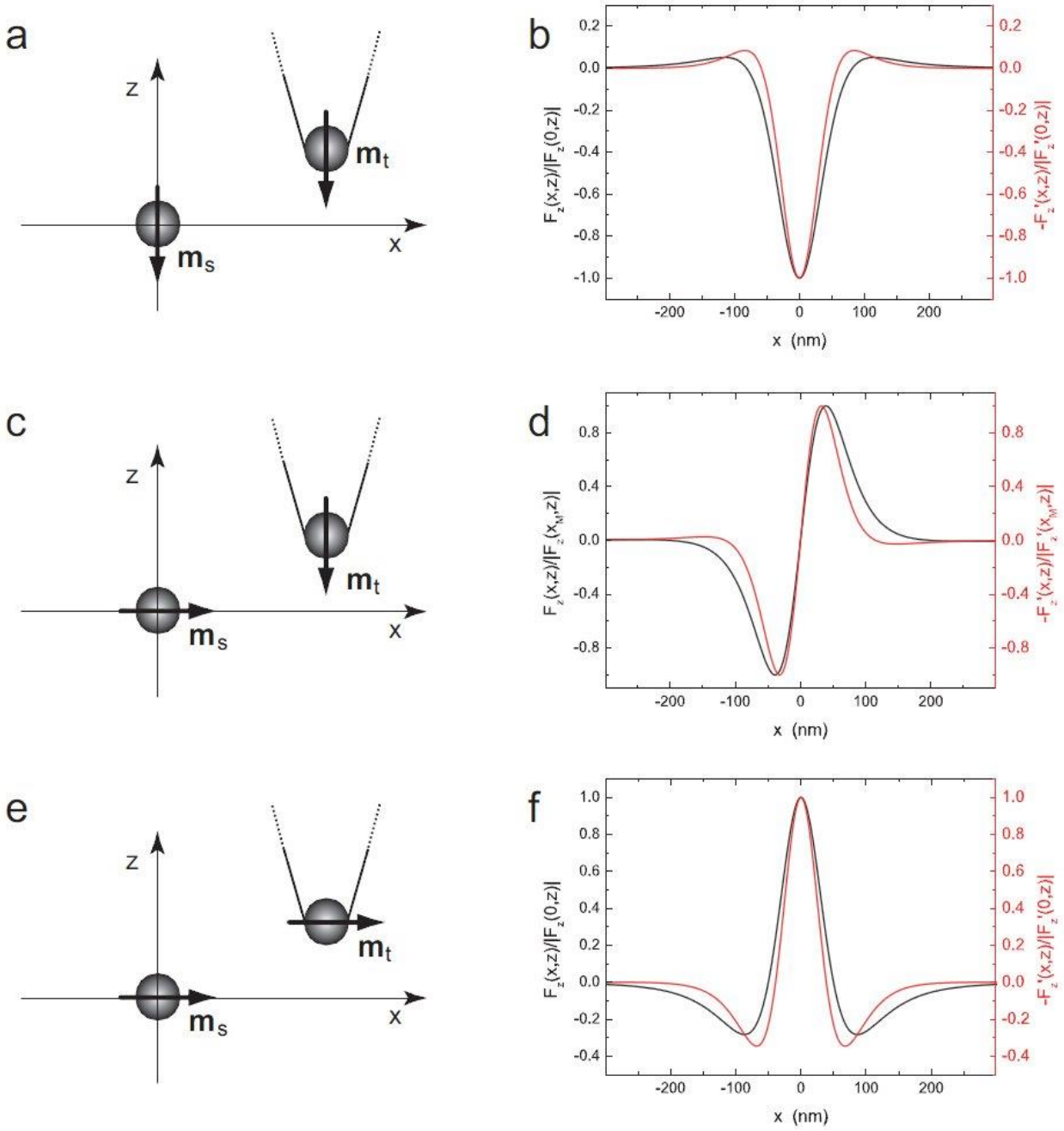

Figure 16 - Sketches of different configurations of tip and sample magnetic moments, i.e, both vertical (a), tip vertical and sample horizontal (c), and both horizontal (e), with the corresponding simulated force along *z* axis F_z (black curves) and gradient $\Delta F'_z$ (red curves). The sign of F'_z is changed so that the curve is proportional to the profile of the magnetic images obtained in dynamic MFM. Curves have been normalized for the sake of readability.

This situation is sketched in Fig. 16e, in which $\boldsymbol{m}_t = m_t\boldsymbol{x}$ and $\boldsymbol{m}_s = -m_s\boldsymbol{x}$ are assumed. Now the vertical component of the force acting on $\boldsymbol{m}_t$ is given by

$$F_z = \frac{3\mu_0 m_t m_s}{4\pi} \frac{z}{(x^2+z^2)^{5/2}} \left(1 - \frac{5x^2}{x^2+z^2}\right) \qquad 51)$$

which is plotted in Fig. 16d (black solid line) together with the additive inverse of its gradient $-F'_z$ (red solid line) which simulates the MFM recorded profile.

Finally, we explicitly observe that in the above illustrated examples the magnetization of both the tip and the sample is considered constant during the imaging. Unless the sample produces a significant magnetic field, this assumption is generally verified for the tips. Conversely, if the sample is constituted by a superparamagnetic nanoparticle and in the absence of an external magnetic field applied to maintain the orientation of $\boldsymbol{m}_s$, the latter is oriented by the magnetic field generated by the tip and thus rotates during the scanning. This further broadens the dark circle corresponding to dipole in MFM images [119].

Periodic magnetic domains. As a further illustrative example, we discuss the MFM response on samples constituted by a pattern of period magnetic domains. This is the typical case of magnetic recording media, in which periodic magnetic domains exhibit magnetization along the same axis with alternated directions. Being periodic magnetic recording media among the first typologies of magnetic materials studied by MFM, several efforts have been made to derive comprehensive analytical models of the MFM response on such kind of samples. These included the presence of alternated vertical and/or horizontal magnetic domains, in-plane alternated domains separated by abrupt domain walls or transition zones where the magnetization is described by an arctan function to model Bloch walls [116], [118], [120], [121].

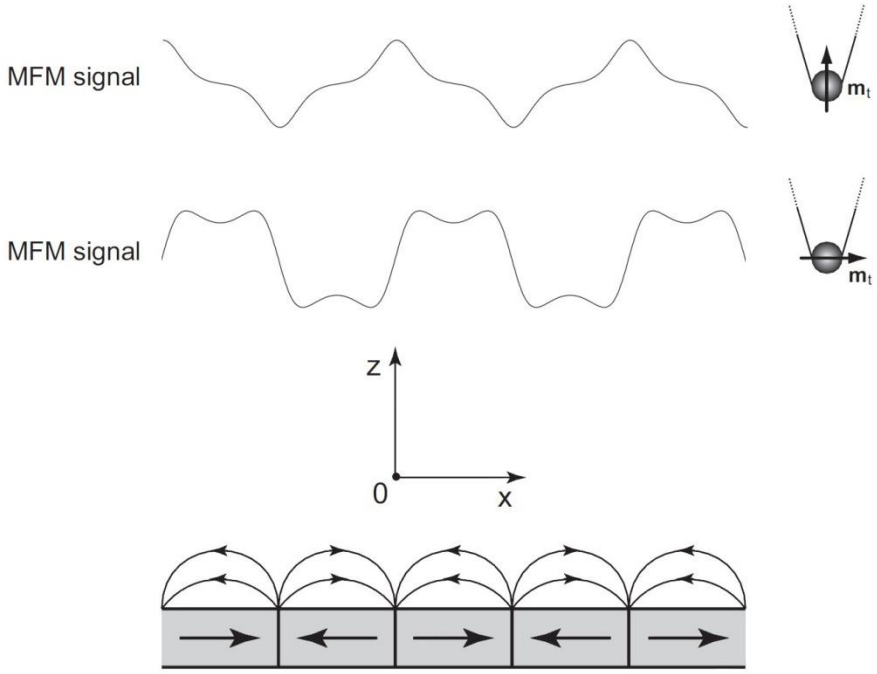

Figure 17 - Sketch of the orientations of the magnetic domains in period recording media (e.g., standard floppy disks) with the indication of the lines of the magnetic field. Correspondingly, the profile of the dynamic MFM signal is simulated for the cases of vertically and horizontally magnetized tip as illustrated on the right of each profile.

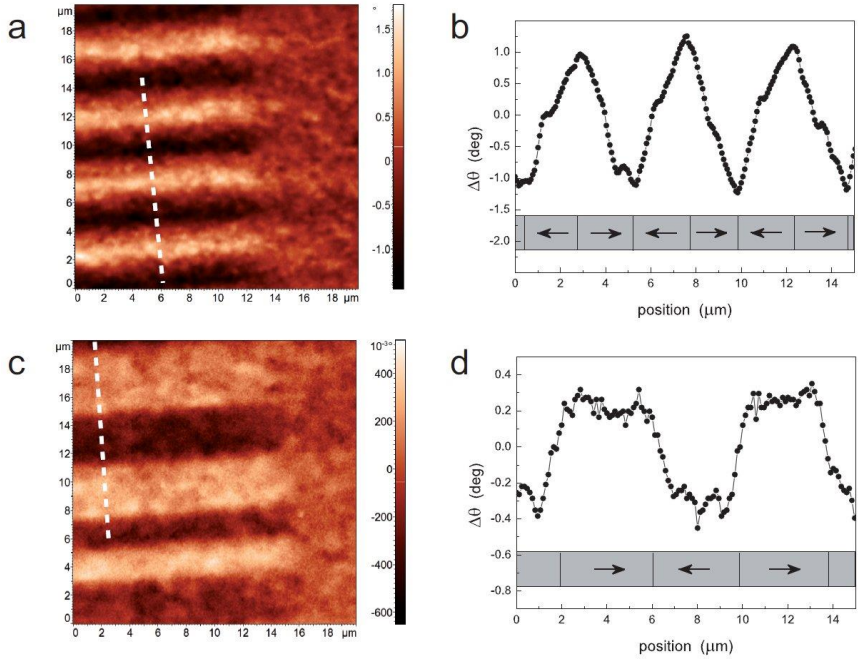

Figure 18 - Typical experimental MFM phase images acquired on a standard floppy disk using a vertically (a) and horizontally (c) magnetized tip, together with two profiles extracted from the MFM maps - (b) and (d), respectively. The pattern of the magnetic domains as deduced from the curves is reported assuming the tip magnetized as in Fig. 16. Unpublished data.

Here we describe a versatile approach which models periodic magnetic recording media with in-plane magnetized domains with arbitrary profiles of the periodic magnetization. Let us assume that the domains are magnetized along the *x* direction, as sketched in Fig. 17. The magnetization is periodic along the *x* axis with spatial period λ and uniform along the *y* axis. Being periodic, the magnetization can be expanded in Fourier series, where the generic *n*-th harmonic component has amplitude M_n and phase φ_n. The magnetic flux density **B** (the lines of which are represented in Fig. 17) has two components along the *x* and *z* axes, namely, B_x and B_z, which are given by

$$\begin{pmatrix} B_x \\ B_z \end{pmatrix} = \mp \sum_n \frac{\mu_0}{2}(1-e^{-nkb}) M_n e^{-nkx} \begin{pmatrix} \cos(nkx+\varphi_n) \\ \sin(nkx+\varphi_n) \end{pmatrix} \qquad 52)$$

where $k = 2\pi/\lambda$ and *b* is the thickness of the magnetic layer [122]. B_x is maximum in correspondence of the center of the domains and is zero in correspondence of the domain transitions. Conversely, B_z is maximum in correspondence of the transitions while it is zero in the center of the domains.

Since the tip experiences a force given by $F = -\nabla(\boldsymbol{m}_t \cdot \boldsymbol{B}_s)$, a vertically magnetized tip ($\boldsymbol{m}_t = m_t\boldsymbol{z}$) is sensitive to B_z ($F'_z = -\partial^2(m_t B_z)/\partial z^2$), while a horizontally magnetized tip ($\boldsymbol{m}_t = m_t\boldsymbol{x}$) to B_x ($F'_z = -\partial^2(m_t B_x)/\partial z^2$). As the magnetic response in dynamic MFM, e.g., $\Delta\theta$ is proportional to $-F'_z$, it can be easily calculated as

$$\begin{pmatrix} \Delta\theta_h \\ \Delta\theta_v \end{pmatrix} = \pm C \sum_n (nk)^2 (1-e^{-nkb}) M_n e^{-nkx} \begin{pmatrix} \cos(nkx+\varphi_n) \\ \sin(nkx+\varphi_n) \end{pmatrix} \qquad 53)$$

where *C* is the product of all the coeffcient independent from *n* and the subscripts *h* and *v* indicate the MFM response with the tip magnetized along *x* and *z*, respectively. As an example, the simulated profiles of the dynamic MFM response with horizontally and vertically magnetized tip are reported in Fig. 17 for the case of uniformly magnetized domains, i.e., with the magnetization represented by a square wave. Simulations have been performed assuming λ = 3 μm, *b* = 2μm, *z*=500 nm. The profiles are obtained taking into account the first 30 harmonic components (only odd values of *n* are present in the Fourier expansion of the square wave). The magnetization of the tip is sketched in correspondence of each of the two profiles. As examples of experimentally measured MFM responses, Fig. 18a shows a typical dynamic MFM phase image collected on a standard floppy disk with a vertically magnetized tip at a lift height of 50 nm. Fig. 18b shows a $\Delta\theta$ profile extracted in correspondence of the dashed line in Fig. 18a. Fig. 18c reports a typical dynamic MFM phase image collected with an horizontally magnetized

tip at lift height of 50 nm. Fig. 18d shows a $\Delta\theta$ profile extracted in correspondence of the dashed line in Fig. 18c. The contribution of each harmonic component decreases exponentially as z increases with a decay length proportional to $1=n$. As z increases, only the fundamental terms of Eq. (34) contribute to the MFM response, which is thus given by a pure cosine or sine wave, i.e., $cos(kx + \varphi_1)$ or $sin(kx + \varphi_1)$ in case of horizontal or vertical magnetization of the tip [122], [123].

3.3 - "STATE OF THE ART"

3.3.1 - Overview of applications

Taking advantage of the unique combination of high resolution imaging capability at the nanoscale and high sensitivity to localized magnetic fields with nanometer spatial resolution, MFM has been successfully used to study the magnetic properties of a wide range of materials. In the following, we give an overview of different typologies of materials characterized by MFM. In the last part of the chapter, we describe some applications which we consider advanced, recent, niche, or which in our view may represent possible starting point of new research fields to which MFM may give a significant contribution.

Magnetic recording media. Periodic magnetic recording media were among the first typologies of materials investigated by MFM [118], [121], [124]–[127]. Really, on the basis of our experience, such kind of materials are particularly suitable for MFM characterization. Indeed: (i) their periodic high-moment domains produce amazing contrast patterns in MFM images; (ii) the domains are micrometric and thus do not represent a challenge for MFM lateral resolution; (iii) their surface is almost uniform and thus there is almost no crosstalk between topographical and magnetic images; (iv) imaging can be easily performed in air, at room temperature and ambient conditions. Indeed, as they are pretty well characterized, recording media can be used as reference samples in MFM. Finally, we recently reported that recording media may represent standard substrates on which depositing soft thin films in order to measure the thickness of the latter [123].

Superconductors A few years after its invention, MFM has been proposed for the nanoscale investigation of both conventional and high-Tc superconductors [128], [129]. Currently, together with other techniques like scanning superconducting quantum

interference device (SQUID) microscopy (SSM) and scanning Hall bar microscopy (SHM), MFM is recognized as one of the most powerful scanning magnetic imaging tools for applications to the study of superconductors [130]. Indeed, MFM has the highest spatial resolution, although it depends on the tip-sample lift height as shown before and a relatively high sensitivity to magnetic fields which nevertheless depends on the magnetic moment of the tip [130]. MFM has been demonstrated to allow one to evidence phase transitions distinguishing Meissner and Shubnikov phase of a high temperature superconductor [131]. The spatial resolution and sensitivity allow one to directly image the high-localized superconducting vortices [132]–[135], vortex-antivortex structures [136], flux distributions [137]. Finally, the magnetic field generated by the MFM tip has been taken advantage of for vortices manipulations [130], [138]. As a final consideration, the application of MFM to superconductors requires cryogenic instrumentation which may be not featured on common MFM setups.

Magnetoresistive materials. In ferromagnetic structures, changes in the magnetization state of may be reflected in changes in the electric resistance of the sample. This is the result of both the anisotropy of the material (i.e., the relative directions of electric current and magnetization) and the appearance of domain walls. This effect is referred to as magnetoresistance. MFM has been used in combination with in situ magnetoresistance measurements to study the relation between magnetic domain structure and the magnetoresistance in ferromagnetic thin film structures [139]. Moreover, low temperature MFM has been used to observe the structure of magnetic domains in the so-called "colossal magnetoresistive materials", i.e., compounds showing large changes in resistance when magnetic field is applied [140].

Ferromagnetic materials. A wide variety of structures (bulk single crystals, thin films, nanostripes, nanodisks, dots) of ferromagnetic materials containing, e.g., iron, nickel, and cobalt, have been studied by MFM, which easily evidenced the patterns of magnetic domains and their dependence on different process parameters [141]–[146].Subsurface magnetic imaging by MFM was demonstrated by detecting ferromagnetic nanoparticles formed by ion implantation under the surface of Al_2O_3 and SiO_2 [147]. MFM characterization of ellipsoidal nanomagnets isolated or arranged in arrays where single elements were coupled along the major or minor axes evidenced the dependence of the

magnetic states at remanence on the particular arrangement [148]. Jaafar et al [149] demonstrated that the domain configuration (from single- to multi-domains) in Co nanowires with the same length and different thickness and width strongly depended on the aspect ratio of the nanostructure. From statistics on the MFM images collected at different applied magnetic fields, Tabasum et al [150] retrieved the magnetization hysteresis curves of arrays of Ni nanowires and nanotubes, which were found in fairly good agreement with macroscopic data obtained by alternating gradient force magnetometry (AGFM). Also, MFM has been recently employed to study the magnetic properties of Co grown on graphene layers [151]. Bliznyuk et al [152] used MFM to analyze the behavior of networks of self-assembled 1D nanochains of Ni nanoparticles under the influence of an external magnetic field, observing an antiferromagnetic intra-chain order. Finally, differently from Co, Fe, and Ni which exhibit Curie temperature well above ambient temperature, MnAs exhibits the ferromagnetic to paramagnetic phase transition at 45°C, and thus the coexistence of magnetic and nonmagnetic phases at room temperature.

MFM characterization of MnAs epitaxial films evidenced temperature hysteresis and the spin configurations of vertical Bloch line structures [153], [154].

Magnetic nanoparticles. Among other nanostructures, magnetic nanoparticles (NPs) have undoubtedly a lead role in scientific and technological applications, in particular in the constantly expanding field of nano-bio-medical technologies [85]. Thus, it is not surprising that the qualitative and quantitative study of magnetic NPs has become one of the most crucial fields of application of MFM. Although the imaging of magnetic NPs using MFM is quite straightforward from a qualitative point of view, quantitative analysis of MFM images of magnetic NPs still presents some challenges. A plenty of works have been devoted to analyze thoroughly the capabilities of MFM in the investigation of magnetic NPs, addressing both from theoretical and experimental point of view several issues, challenges and still open problems. Among the others, the modeling of tip-sample interaction, the importance of external magnetic fields, the response on superparamagnetic and ferromagnetic NPs, the discrimination between magnetic and nonmagnetic NPs, and artifacts[119], [155]–[160]. Due to their more general importance in MFM, some of these issues are discussed in details in the last part of this chapter.

Biomedical applications. In recent years, MFM has been finding constantly increasing applications in the study of purely organic or hybrid organic/inorganic materials with magnetic properties, including isolated molecules, films, nanohydrogels or vesicles loaded with magnetic NPs [161]–[167] as well as in nano-bio-systems. Among these, MFM has been employed in the study of nanowires obtained by the assembly of Fe_3O_4 NPs using DNA molecules as molecular scaffolds [168] as well as of Co based NPs synthesized using virus capsids as nanoreactors [169]. In different studies, MFM was employed to investigate ferritin molecules [170], to confirm the magnetic properties of iron oxide core after O_2 plasma etching [171], to distinguish apoferritin from ferritin [172], [173], and to study magnetoferritin synthesized using ferritin molecules as nanoreactors [161]. MFM has been used to investigate magnetosomes from magnetotactic bacteria [174]–[179] and microscopic clusters of magnetic nanomaterials human hippocampus [180], [181]. By conjugating magnetic nanomaterials to antigens, magnetic biomarkers can be realized which allow the detection of specific molecules and receptors using MFM [182], [183]. Finally, in our view, one of the most promising but still challenging applications of MFM is the study of cellular uptake of magnetic NPs [123], [184], [185].

3.3.2 - MFM measurements with external magnetic fields

Commercial AFM instrumentation can be equipped with systems able to produce adjustable magnetic field both perpendicular (out-of-plane) and parallel (in-plane) to the sample surface, through the use of electromagnets placed under or around the sample. This instrumental equipment can be used to study the evolution of the magnetic state of a sample in response to the application of an external magnetic field. Specifically, two different kinds of measurements can be conducted, i.e., remanent and in-field magnetization.

Remanent MFM measurements. MFM images can be recorded after the application and the switching off of an external magnetic field. This procedure allows one to study the remanent magnetization state of the analyzed sample and its evolution as a function of the previously applied magnetic field. These MFM measurements are particularly interesting for applications which take advantage of the magnetization state of the materials in the absence of a magnetic field. For example, the switching behavior and

the remanent saturation magnetic state of magnetic nanopatterns [186] and magnetic logic devices [187] are widely studied for recording media applications.

In field MFM measurements. In-field MFM images can be recorded during the application of an external magnetic field to the sample. The resulting magnetic maps represent, in this case, the magnetization state of the sample when it is subject to a magnetic field. This kind of measurements are applied to study materials for applications which exploit the presence of an external magnetic field. For example, in-field MFM measurements are used to study the magnetization reversal processes of nanomaterials, such as single nanowires [188], [189], magnetic nanoparticles [178], magnetic tunnel junction rings [190], and nanocomposite structures for the fabrication of discrete track media and bit-patterned media [191], or to analyze the evolution of magnetic domains and domains wall structures, in response to both perpendicular (out-of-plane) and parallel (in-plane) external fields, of magnetic multilayer films [192].

3.3.3 - Statistical quantitative MFM measurements

Magnetic patterned arrays, such as arrays of lithographically defined magnetic dots and islands, nanowires, and nanotubes, are widely investigated to obtain high density recording media. These magnetic structures act as single-grain single-domain bits providing a higher thermal stability with respect to granular media. However, because of the magnetostatic interactions between the nanometer magnetic entities, dense magnetic patterns properties are subjected to a certain element-to-element variations. These variations produce the widening of the switching field distribution and cause the increase of write-in-errors. A narrow switching field distribution is required to record into each individual bit without disturbing the magnetic behavior of the surrounding neighbors, but it is still difficult to obtain also because a proper understanding of all the physical phenomena which regulate the switching processes has not been obtained yet.

A proper characterization of the switching field distribution is then required, in order to deeply understand the switching mechanisms and to properly optimize the performances of dense magnetic patterns. Thanks to its capability of visualizing the magnetic switch (bright/dark contrast) of nanometer domains in response to external magnetic fields with nanometer lateral resolution, MFM is a powerful tool to investigate the local switching behavior of bit patterned media and to measure the switching field distribution.

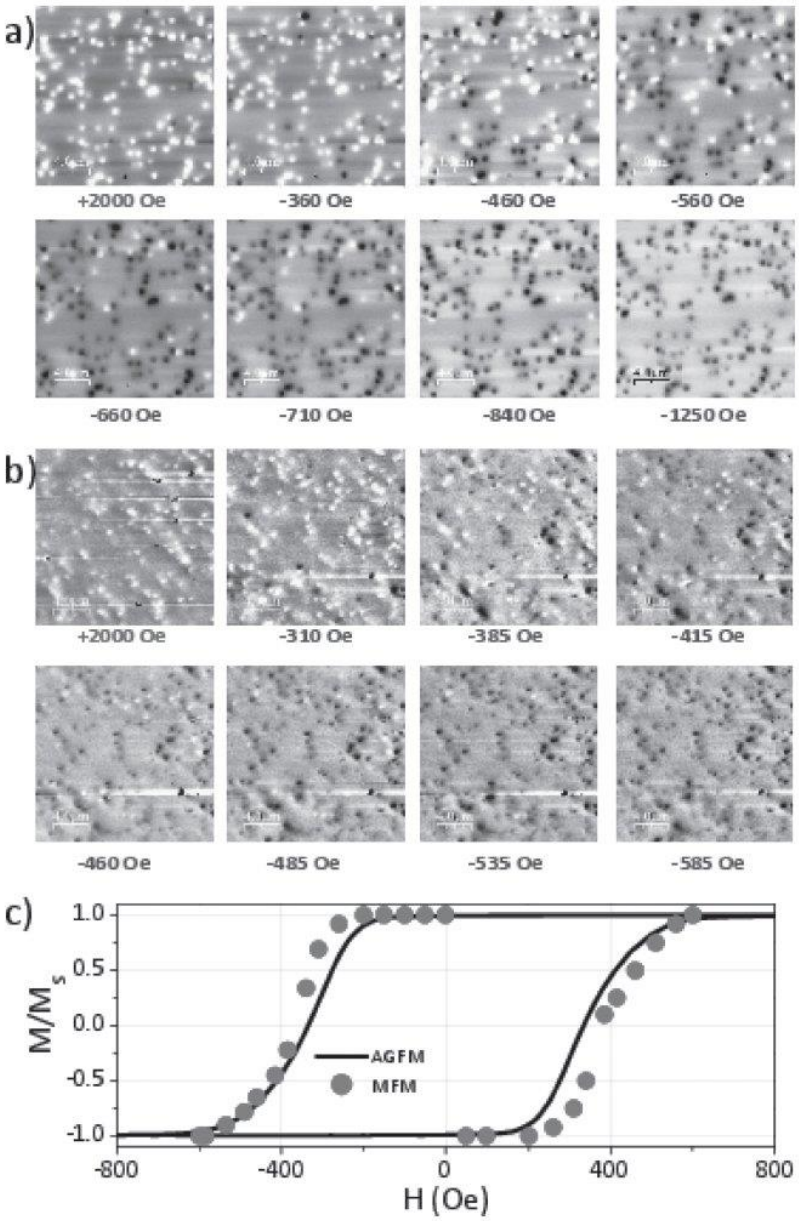

Figure 19 - MFM images of (a) Co55Fe45 and (b) Ni80Fe20 nanowire arrays (both the types of nanowires with diameter of 70 nm) at zero field after saturation in a positive 2 kOe field and then in a variety of unsaturated remanent states obtained by changing each time the magnetic state of the nanowirearray from saturation to a given negative field and then to remanence by reducing the field to zero. (c) Hysteresis loop of the Ni80Fe20 nanowire array measured by AGFM (solid line) and MFM (symbols) with the applied field parallel to the wire axis. Reprinted with permission from [193].

The remanent hysteresis curves and the switching field distribution of magnetic arrays can be measured by MFM applying to the sample out-of-plane magnetic fields and counting the number of magnetically reversed entities [194]. The sample is previously saturated along one direction; reversal fields with different intensities are then applied and removed. After the application of each field, intensity MFM images are recorded, allowing one to visualize and count the switched magnetic elements [195]–[197]. This

procedure is particularly easy when the magnetic elements of the analyzed arrays are characterized by a large shape anisotropy, such as the case of magnetic nanowires shown in Fig. 19 [193]. In this case, if the external magnetic field is applied along their easy axis, only two contrasts in MFM images are possible, which correspond to the 'up' and 'down' states. Thus, the local hysteresis loop can be calculated by counting the number of dark and white structures and the normalized magnetization can be obtained by

$$\frac{M^{MFM}(H)}{M_s^{MFM}} = \frac{n_{up} - n_{down}}{n_{up} + n_{down}} \qquad 54)$$

where n_{up} and n_{down} are the number of the magnetic elements with up and down states, M_s^{MFM} is the remanent saturation magnetization (which correspond to the total number of magnetic elements) and $M^{MFM}(H)$ is the remanent magnetization after the application of an external magnetic field.

As shown in Fig. 19c, the hysteresis curve retrieved with MFM presented a pretty good agreement with those obtained by standard methods, such as alternating gradient field magnetometer (AGFM) [193]. To achieve further information about the magnetic behavior of dense magnetic patterns, it is also possible to measure the in-field local magnetic hysteresis curve by in-field MFM measurements, during which the applied magnetic field is not switched off. In this case the normalized hysteresis loop represent the evolution of the effective magnetization in presence of an applied magnetic field [150]. For this kind of materials the complete coincidence of the in-field magnetic hysteresis curve with the remnant hysteresis curve is desirable and generally achieved.

Nevertheless, in-field MFM measurements can be used to verify the equivalence of the curves.

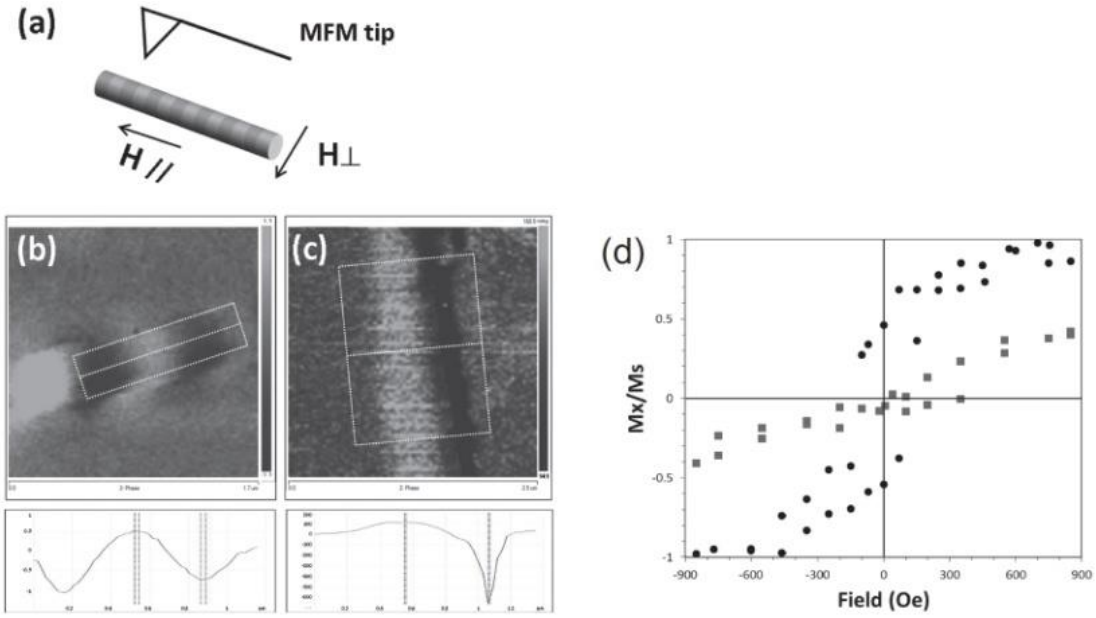

Figure 20 - (a) Schematic drawing of MFM measurement on a multilayered nanowire with parallel (460 Oe)/perpendicular fields (550 Oe). (b) and (c) MFM phase image of a multilayered nanowire under parallel/perpendicular fields and corresponding step analysis. (d) Hysteresis loops of a multilayered Fe-Ga/Cu nanowire measured by MFM under parallel (circles) and perpendicular fields (squares). Reprinted with permission from [198].

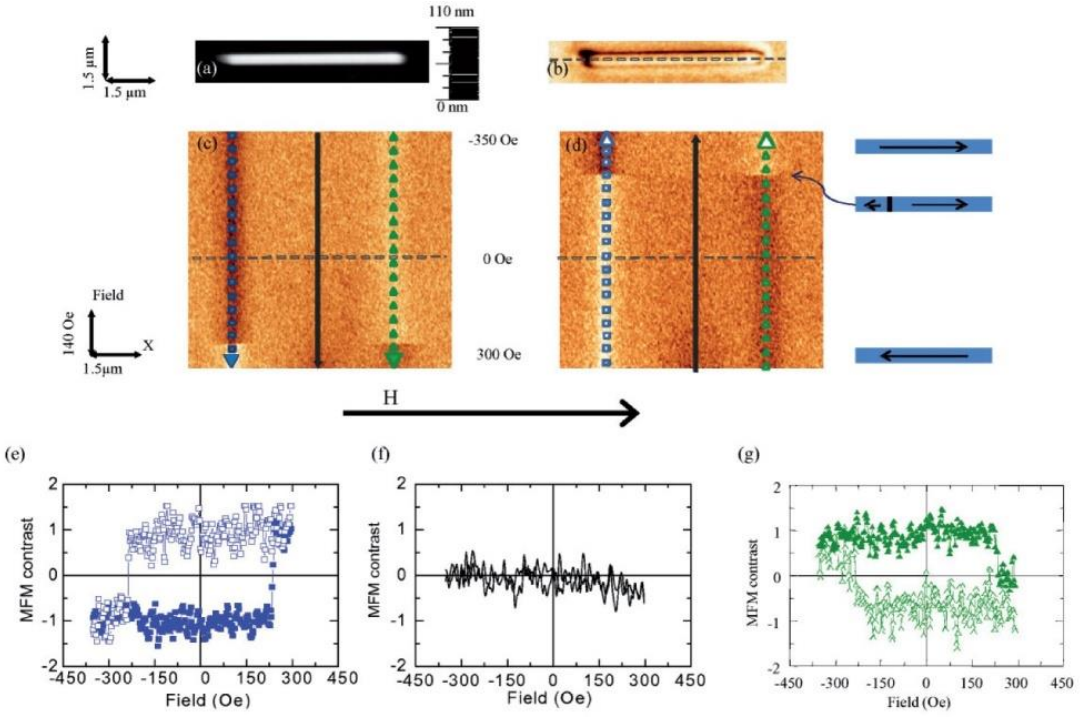

Figure 21 - Topography and in-remanence magnetic image of a single-domain Co nanowire. (a) Topography and (b) MFM image in remanence of nanowire; (c)-(d) MFM-based mode images and (e)-(g) profiles corresponding to hysteresis loops. The frequency shift contrast for all the MFM images is 8:5 Hz. Reprinted from [149].

3.3.4 - Quantitative MFM measurements on single nanomaterials

The study of magnetization evolution mechanisms of magnetic nanomaterials under external magnetic fields is a hot topic in magnetism. The magnetization reversal of nanostructures can be characterized by different techniques such as magnetoresistance techniques [199], spatially resolved Kerr effect (MOKE) [200], magneto-optical scanning near field optical microscopy [201], Hall micromagnetometry [202], Lorentz transmission electron microscopy and scanning transmission x-ray microscopy, micro and nano-SQUID [54], [55], Transmission Electron Microscopy (TEM) based techniques , such as differential phase contrast mode (DPC) [63], or off-axis electron holography [65], [66], X-ray microscopies, such as X-Ray Photoemission Electron Microscopy (XPEEM) [77], and ballistic Hall micro-magnetometry [56].

MFM, in respect to all these techniques, appears as the potentially most suitable technique for the study of single nanostructures, thanks to its nanometer lateral resolution (10-20 nm) comparable to transmission techniques, its applicability to all kinds of nanomaterials without particular sample preparation, and its capability to map the magnetic evolution with respect to an applied field. Nevertheless, the potentialities of MFM in the measurement of quantitative magnetic parameters (such as the hysteresis loop) of single objects at nanometric scale are still not completely exploited and only a few results are available.

Magnetic nanowires. Because of their easily interpretable magnetic structure, bistable magnetic nanomaterials (such as nanowires) are the most studied materials through MFM techniques. In this case, the magnetization state of the sample can be visualized as an alternation of bright and dark contrast (phase, amplitude or frequency shift) in correspondence of the analyzed magnetic structure, as shown in Fig. 20 [198]. The evolution of the magnetization state of the sample can be evaluated acquiring different images with different external magnetic fields and measuring the dark/bright contrast in a selected line or region. The dark/bright contrast as a function of the applied magnetic field represents the hysteresis loop of the analyzed structure, allowing the definition of the coercivity H_c and the saturation magnetic field H_s. This method has been used to characterize the hysteresis loop of individual nanowires both under parallel and perpendicular magnetic fields [198]. The MFM hysteresis loops of single nanowires obtained by MFM can also be compared with hysteresis data obtained by other standard

techniques, such as VSM, on bulk nanowires arrays, in order to study the role of inter-wire dipolar interactions in nanowire arrays systems [203].

A faster method to study and visualize the evolution of the magnetization state of single nanowires consists in recording only one MFM image varying continuously the applied magnetic field during the scan, as proposed by Jaafar et al [149]. An example of this kind of analysis is represented in Fig. 21. The in-plane magnetic field is applied along the *x* direction and it is changed along the *y* direction. Thus, the *y* scale corresponds to the external magnetic field intensity. Hysteresis loops have been obtained by measuring the MFM profiles along the *y* direction (which correspond to the applied magnetic field), as shown in Fig. 21, in different lines of the scanned area.

This method allows one to continuously visualize the magnetization evolution of the sample and to measure the hysteresis loops faster than acquiring different images with different intensities of external field. Nevertheless, its application is limited to structures with simple magnetic configurations and geometry.

Magnetic micro and nano-dots. The study of the hysteresis loop of magnetic element having more complex domains structure (i.e., magnetic vortex) requires a more detailed data analysis. A method based on the measurement of the integral value of the cantilever phase (of frequency/amplitude) shift (e.g., the integral value of the MFM contrast/colour) has been proposed by Rastei et al [204] to measure the magnetization evolution of single micro-dots. The magnetization state of the element is derived by integrating the magnetic signal over the whole element surface, allowing one to extract the hysteresis curve of single magnetic element. More complex data analysis can also be applied to obtain a better resolution and more local information about micro-dots magnetic behavior, as proposed by Coïsson et al [203], who succeded to quantitatively measure the local hysteresis loops and determine the magnetic vortex chirality of dots having minimal lateral size of around 800 nm [205], [206].

Magnetic nanoparticles. The quantitative measurement of the magnetic properties of single nanoparticles with diameter lower than 100 nm is still a big challenge.

Only qualitative studies about the magnetization reversal of magnetic nanoparticles having size lower than 100 nm have been performed, by detecting the changes in the contrast resulting from the reorientation of the NP magnetization direction with respect to the tip magnetization.

For example, Moya et al [207] studied the magnetization reversal at remanence of single $Fe_{3-x}O_4$ cubic NPs with size of 25-30 nm, by applying an in-plane magnetic field and analysing the correspondent contrast variation. This study allowed the authors to directly observe the orientation of the easy axes in individual ferrimagnetic NPs and to individuate the polarity and the orientation of the particle domains, which furnish information about the rotation process (coherent in that case) dominating the reversal process.

Pinilla-Cienfuegos et al [208] used Low-Temperature – MFM (LT-MFM) to visualize and qualitatively study the magnetization reversal behaviour of KNiCr single nanoparticles or agglomerates of nanoparticles having diameter around 20 nm, also in dependence of the temperature.
Nevertheless, currently, no quantitative evaluation about the magnetic properties of neither single NPs neither agglomerates, such as the quantitative curve of the sample magnetization as a function of the applied magnetic field or the coercive field, has been obtained.

And yet, the extraction of quantitative information about the properties of magnetic NPs from MFM data is, in principle, possible. Indeed, when the MFM tip is on the vertical of the NP, assuming that the NP is small enough so that its magnetization is saturated and that its moment is parallel to that of the tip as in the sketch in Fig. 15a, the moment of the NP is given by $m_s = 4/3\pi M_s d^3/8$, being M_s the saturation magnetization of the NP and d its diameter. The MFM response is proportional to $F'z$ given by Eq. (48), which now can be more conveniently rewritten as:

$$F'_z = \mu_0 m_t M_s \frac{d^3}{(\Delta z + d/2 + \delta_t)^5} \qquad 55)$$

where the effective distance between the two moments is given by the sum of the lift height Δz, the NP radius $d/2$, and the position δ_t of the equivalent magnetic moment of the tip measured from the tip apex [155]. Eq. (55) predicts the contrast in MFM images and could be used to extract quantitative information about the magnetic properties of the sample from experimental MFM signal versus d or Δz curves. Nevertheless, the simple model in Eq. (55) was successfully used only by Schreiber et al [155] and

Sievers et al [156] to calibrate the magnetic probe used and analyze their MFM data collected on magnetic NPs, obtaining reasonable values of single NPs magnetic moment. Conversely, almost linear $\Delta\theta$ versus d curves have been recently reported by Cordova et al [209]. Recently, we observed a pretty good agreement with Eq. (55) in the case of small NPs in the core of magnetoferritin molecules, while an almost linear dependence between $\Delta\theta$ and d in case of bigger NPs without the application of an external field but under the effect of the sole magnetic field generated by the MFM tip [161]. At the same time, our $\Delta\theta$ versus Δz curves could not be rationalized by Eq. (55), which we attributed to the not uniform magnetization of big NPs by the rapidly decaying field of the tip [161]. So, we proposed more complex empirical models based on the experimental data, which nevertheless found only partial confirmation by other independent characterizations such as electron microscopy [161]. Finally, a more realistic and accurate model of the MFM tip was proposed by Häberle et al [158], who derived relatively simple analytical equations introducing the concept of 'pseudo-pole', obtaining an amazingly good agreement with experimental data.

Therefore, a certain incongruence between experimental data and existing theoretical models of the tip-sample magnetic interactions exists and the quantitative evaluation of the magnetic properties of single nanoparticles, having size lower than 100 nm, by MFM, especially in dependence of an applied magnetic field, is still not trivial to be obtained. This is probably due to some limitations of the MFM techniques which have still not been overcome and which are described in details in the following paragraphs.

3.4 - FACTORS AFFECTING MFM MEASUREMENTS

3.4.1 - Nonmagnetic tip-sample interactions

The lift height mode allows one to separate short-range tip-sample interactions (i.e., Van der Waals forces) from the long-range interactions (e.g., magnetic interactions), leading to the separation of the "topography" (which is due to atomic/short-range forces) from the magnetic signal. Nevertheless, not only magnetic interactions occur at large tip-sample distances, but also electrostatic forces can produce a contrast in MFM images. Indeed, a capacitive coupling is generally observed between the tip and the sample. The tip-sample capacitance C_{ts} can be defined, which is generally dependent on the shape of the tip (including the apex, the cone, the cantilever, and the chip) and is a function of the tip-sample distance z [210], [211]. In the absence of localized

electrostatic charges on the sample surface, the tip-sample electrostatic interaction force is given by

$$F_z = \frac{1}{2} V_{dc}^2 \frac{\partial C_{ts}}{\partial z} \qquad 56)$$

and its gradient by

$$F'_z = \frac{1}{2} V_{dc}^2 \frac{\partial^2 C_{ts}}{\partial z^2} \qquad 57)$$

where V_{dc} is the tip-sample bias which is supposed constant [116].

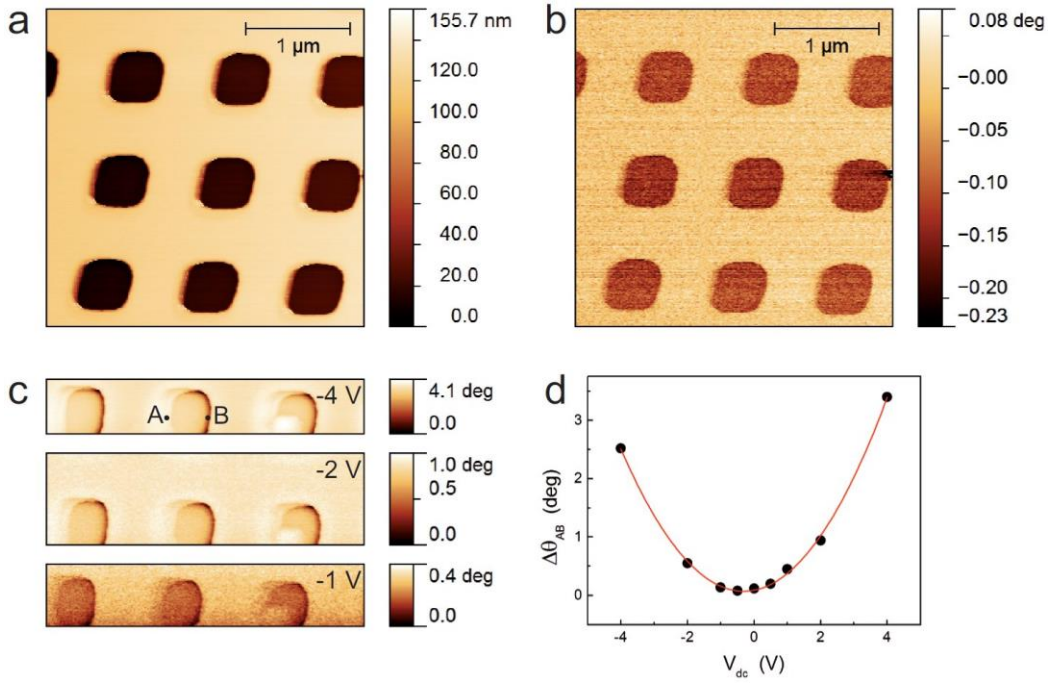

Figure 22 - MFM characterization of a nonmagnetic calibration reference sample: (a) topography and (b) MFM phase image obtained with V_{dc} = 0V; (c) details of MFM phase images obtained with V_{dc} = -1 V, -2 V, and -4 V; (d) plot of the experimental contrast $\Delta\theta_{AB}$ measured between the points A and B indicated in (c) as a function of V_{dc} (symbols) together with the corresponding parabolic fit according to Eq. (38) (solid line). Authors' unpublished data.

For example, although more accurate models for the tip-sample capacitance have been retrieved, we can assume C_{ts} as that of a plain capacitor, i.e., $C_{ts} = \varepsilon_0 S_{eff}/z$, where S_{eff} is the effective area of the plates. In this case, the electrostatic interaction force and its gradient are given by $F_z = -\varepsilon_0 S_{eff} V_{dc}^2/2z^2$ and $F'_z = \varepsilon_0 S_{eff} V_{dc}^2/z^3$, respectively. As an example, Fig. 22 shows the effect of nonmagnetic tip-sample interactions in the MFM characterization of a nonmagnetic sample, i.e., an AFM calibration reference sample. Fig. 22a shows the topography of the sample characterized by an array of holes about

100 nm deep. Fig. 22b shows the corresponding MFM phase image in the absence of an applied tip-sample bias voltage V_{dc}, clearly showing topography-induced artifacts. The application of different values of V_{dc} affects the MFM phase images, as shown in the details reported Fig. 22c obtained for V_{dc}=*-1V*, *-2V*, and *-4 V*. Fig. 22d shows the contrast $\Delta\theta_{AB}$ experimentally measured between a downward and an upward step of the sample (i.e., the points indicated with A and B in Fig. 22c), which corresponds to the most marked contrast in the MFM phase image produced by the abrupt change in the sample height, as a function of V_{dc}. The contrast is reported instead of the bare MFM phase shift as it is less affected by occasional variations in the phase among two subsequent images and by artifacts introduced during the post-experiment data manipulation [123]. The fit of the experimental data confirms the dependence of the gradient on $V_{dc}^{\,2}$, as expected from Eq. (38).

The presence of non-magnetic interactions in MFM measurement can be also interpreted considering that the probe and the sample are characterized by different work functions, which give rise to a contact potential difference (CPD), producing a nonmagnetic interaction between the tip and the sample.

Therefore, especially in the case of nonhomogeneous samples, such as nanomaterials deposited on flat substrates, the electrostatic tip-sample interaction produces an additional contrast in MFM images, which can be easily confused with the magnetic one [212]. Electrostatic forces are often neglected in the analysis of MFM images, but their contribution has been demonstrated to be significant in respect to the magnetic one, especially in the case of samples with low stray fields, such as magnetic nanomaterials. Thus, the correct interpretation of MFM data cannot be obtained neglecting the presence of an adding contrast in the images, which is due to nonmagnetic tip-sample forces. Despite its crucial importance, limited studies have been carried out with the aim of distinguishing or eliminating the electrostatic signal in MFM images.

External magnetic field. The first method to verify the magnetic nature of the detected contrast consists in the application of an external magnetic field [213], [214]. The changes of the contrast in response to the external magnetic field represent the evidence of the presence of a magnetic tip-sample interaction. Nevertheless, if a quantitative analysis of the magnetic characteristics of the sample is needed, a method to eliminate the electrostatic contribution from MFM images is needed.

Variable electric bias voltage. The electrostatic contribution is present in MFM images because of the tip-sample contact potential difference (CPD). Consequently, this contribution can be eliminated compensating the contact potential difference by the application of an appropriate bias voltage (V_{bias}) between the tip and the sample, which has to be $V_{bias} = -V_{CPD}$. In order to determine the contact potential difference, the detected MFM signal (phase or frequency shift) as a function of the applied bias voltage has to be recorded. In this way, a parabolic curve is measured and the value $V_{bias} = V_{CPD}$ can be individuated at its vertex. This method has been demonstrated to be able to successfully remove the electrostatic contributions from images acquired even at small lift height, when homogeneous samples are analyzed [215] and to distinguish magnetic from nonmagnetic nanostructures [157]. Nevertheless, if the analyzed sample is composed by more than one material, as in the case of magnetic nanomaterials deposited on substrates, each material has a different work function. Thus, in this case, the electrostatic contribution is dependent on the point of the scanned area (i.e., the material in each point of the scanned area) and cannot be completely removed in each position by the application of a single, fixed, compensation bias voltage value.

Kelvin probe force microscopy. A possibility to evaluate and eliminate the electrostatic contribution in MFM images of non-homogenous samples is the use of Kelvin probe force microscopy (KPFM). Through the use of a lock-in system, KPFM allows the measurement of the contact potential difference in each point of the scanned area and the compensation of local contact potential difference variations by opportunely adjusting the applied V_{bias} during the scanning. Jaafar et al [216] developed a KPFM-MFM combined technique to evaluate and eliminate the electrostatic contribution in MFM images, the effectiveness of which were demonstrated obtaining pure magnetic images of Co nanowires deposited on Si substrates, as shown in Fig. 23.

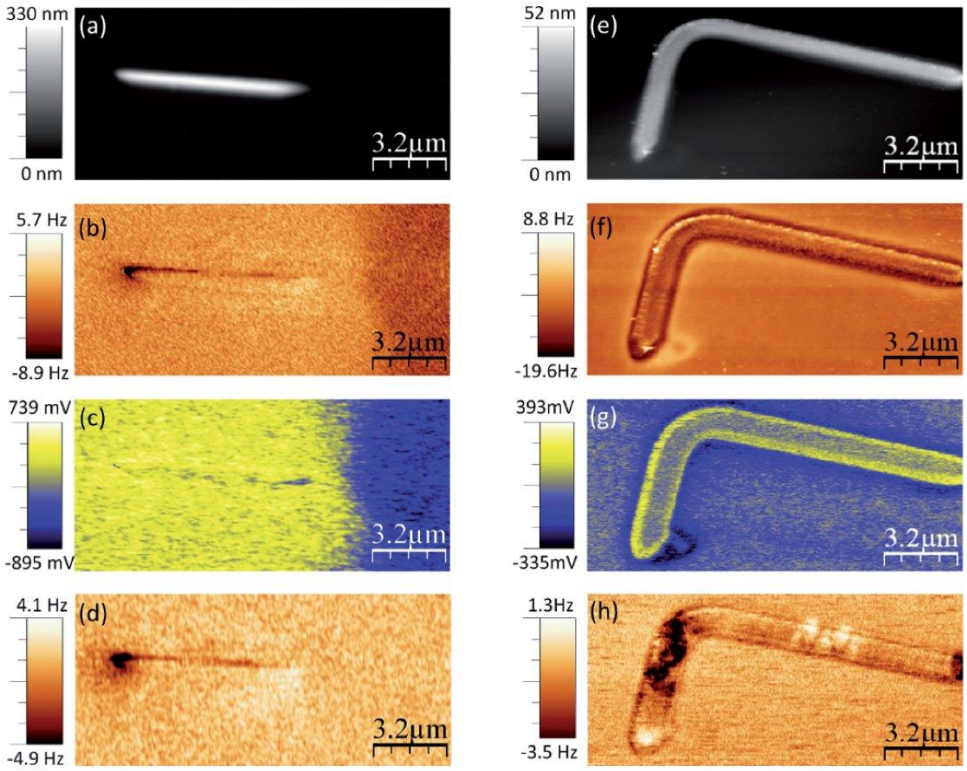

Figure 23 - Topography of (a) Co nanowires and (e) L-shaped Co nanostructure. (b) and (f) frequency shift images measured without KPFM acquired at a retrace distance of 30 nm and 25 nm respectively. (c) and (g) surface potential images obtained by the KPFM technique. (d) and (h) MFM images (frequency shift) of the Co nanostructures measured when the KPFM bias correction was switched on. Reprinted from [216].

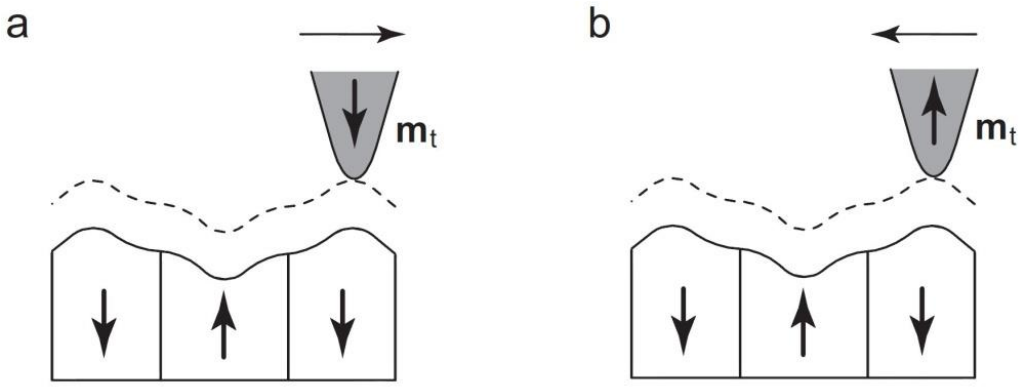

Figure 24 - Sketch of the principle of SM-MFM. Both the scans are performed in tapping mode, but the magnetic moment of the tip m*t* is reversed between them, as schematized in (a) and (b). The sum of the signals gives the atomic and the electric forces, while the difference of the signals gives the sole magnetic forces [217].

Switching magnetization magnetic force microscopy. Lateral resolution and sensitivity of MFM technique can be improved keeping the tip-sample distance as small as possible. However, at short tip-sample distance, both long-range (e.g., magnetic and electrostatic) and short-range (van der Waals) tip-sample interactions occur and are of the same order of magnitude. In order to improve the spatial resolution of the MFM imaging technique, taking into account the effects nonmagnetic tip-sample interactions (i.e., van der Waals and electrostatic forces) in MFM images, Cambel et al [217], [218] proposed an alternative method to the conventional lift-mode MFM, which is called switching-magnetization magnetic force microscopy (SM-MFM). The technique consists in a 'two-pass' method: each line of the analyzed surface is scanned twice in conventional tapping mode, with opposite tip magnetization orientation, as shown in Fig. 24. If the sample is not affected by the tip stray field, when the probe magnetization is reversed, a magnetic contrast with opposite sign is detected, while the atomic (van der Waals) and electrostatic contributions remain unchanged. Thus, adding the traces obtained with opposite tip moments, the magnetic signal is nullified and only the contrast due to the atomic and electrostatic tip-sample interactions is visible.

This image results in the "topography" map. On the contrary, subtracting the traces obtained with opposite magnetic moments, the topography (atomic) and electrostatic signal is nullified and only the magnetic tip-sample interactions give rise to the contrast which is visible on the image. To perform this technique magnetic probes with particular characteristics are needed: (i) SM-MFM tips must have low magnetic moment, must be noninvasive within the tapping mode, i.e., the stray field of the tip must not produce significant changes of the magnetization state of the sample during the scanning; (ii) SM-MFM tips must exhibit low coercivity, in order to enable easily the switching of the tip magnetization, i.e., the tip magnetic moment orientation must be inverted applying relatively low external magnetic fields in order to not significantly vary the magnetic configuration of the analyzed sample; (iii) SM-MFM tips must exhibit single-domain state at remanence in order to maintain the magnitude of the tip magnetization constant during the tapping mode scanning and not affected by the stray field of the sample.

3.4.2 - Tip-sample mutual magnetization

In order to interpret the MFM results, it is necessary to make some simplifying hypothesis about the magnetic characteristics of the tip and the sample. The hypothesis

of weak tip-sample interactions corresponds to the assumption that the magnetization states of the MFM tip and the analyzed sample do not change due to the tip-sample mutual interactions. Thus, their magnetization is considered rigid during MFM measurements. However, not always this assumption can be considered valid. The analysis and the interpretation of MFM images cannot be made disregarding the different situations which are possible during MFM measurements.

In some cases, the hypothesis of weak tip-sample interactions is valid and the MFM contrast can be considered dependent only on the magnetization of the tip and the sample (direction and intensity). This kind of contrast is called "charge contrast" [219] and it is representative of the unaffected magnetization state of the sample. In this case, reversing the probe magnetization (or the sample magnetization), a magnetic contrast with opposite sign must be detected. This phenomenon can be observed with ferromagnetic samples with high coercivity (higher than the stray field of the tip) and stray fields significantly smaller than the coercive field of the MFM tip.

However, in several cases, the sample magnetization and/or the tip magnetization cannot be considered perfectly rigid during MFM measurements. The mutual magnetic interaction between the tip and the sample can produce reversible or irreversible changes of the magnetization of the sample and/or the tip. An additional attractive tip-sample force is experienced by the tip because of the polarization of one element in the same direction of the other one [219]. For example, when soft magnetic materials having low coercivity (lower than the tip magnetic stray field) are analyzed, the magnetic field induced by the probe can be suffciently high to produce a magnetization of the sample in the same direction of the magnetization of the probe. Indeed, in this case, reversing the direction of the tip magnetization, the phase contrast does not change its sign, indicating that the analyzed sample is magnetized by the tip magnetic stray field. On the contrary, hard magnetic samples, such as magnetic recording films, with high magnetic stray fields, can induces changes in the magnetization state of the tip. For example it has been demonstrated that the horizontal magnetization component of the tip can be subjected to significant variations while scanning hard disk magnetic patterns [220].

Furthermore, recent applications of MFM technique involve the use of external magnetic fields in order to study the evolution of the sample magnetization as a function of the applied magnetic field. In this case, the intensity of the applied magnetic field should be high enough to induce variations in the sample magnetization but low enough

to not produce significant variations in the magnetization state of the tip. If these conditions are not verified, also the changes in the tip magnetization have to be taken into account to correctly analyze the measured data.

Consequently, in order to accurately interpret the MFM data and to obtain quantitative information about the magnetic characteristics of the analyzed samples, it is necessary to take into account all the experimental conditions and to appropriately choose the measurement parameters, such as the magnetic characteristics of the probe and the intensity of applied external magnetic fields. To do that, the precise knowledge of the tip magnetic characteristics is needed.

3.5 - MFM PROBES

3.5.1 Probe calibration

The accurate characterization of MFM probes is necessary to improve the MFM data interpretation, to prevent, reduce or quantify the effect of the tip stray field on the sample magnetization, to eliminate or reduce the effect of an external magnetic field on the tip magnetization and, also, to choose accurate tips and accurate measurement parameters for each particular experiment.

A complete magnetic characterization of the tip is obtained when the following magnetic parameters are defined: saturation magnetic field H_s (in-plane and out-of-plane), coercive magnetic field H_c (in-plane and out-of-plane), tip magnetic stray field H_t, and tip magnetic charge q. Different methods have been proposed to magnetically characterize MFM probes.

The first method which has been developed to determine the hysteresis loop of MFM tip is based on the use of a straight current wire [221], but the magnetic moment in the tip axis (m_z) is not easy to be determined. When using a current carrying wire, the MFM contrast has to be analyzed above an edge of the wire in order to sense the z component of the stray field. This can produce an additional topographical effect and electrostatic contributions due to contact potentials between the tip and the current-carrying wire. To avoid this problem, the wires can be covered with an insulating film, or with a conducting film connected to the tip in order to electrostatically shield the tip. Because of the complicated procedure, different approaches have been proposed.

For example, in order to easily calculate the magnetic properties of the tip, a method based on the use of current-carrying micro-rings has been developed. The metal rings are fabricated using electron-beam lithography and a lift-off technique [222].

Controllable current is made to go through the metal rings and a vertical magnetic field at the center of the ring is produced, with intensity

$$H_z = \frac{R^2}{2(z^2+R^2)^{3/2}} I \qquad 58)$$

where R is the ring radius and I the ring current. The MFM phase shift is calculated as

$$\Delta\theta = -\frac{3R^2QI}{2k_c}\left[\frac{qz}{(z^2+R^2)^{5/2}} + \frac{m_z(R^2-4z^2)}{(z^2+R^2)^{7/2}}\right] \qquad 59)$$

where q is the effective magnetic charge and m_z the effective magnetic moment of the tip. Measuring the quality factor Q and the elastic constant k_c of the cantilever, Eq. (59) can be used to determine q and m_z of the tip.

Fixing a value of the current I, the cantilever phase shift at different tip-ring separation distances is acquired, recording images at different lift-heights. The curve of the phase shift as a function of the tip-ring separation can be fitted with Eq. (40) and the parameters q and m_z can be determined [223].

A further development of the theoretical model has been introduced by Lohau et al [224], through the use of an additional fitting parameter δ_t, which represents the distance of the imaginary point-probe from the tip apex. The introduction of this parameter allows one to take into account that the actual distance between the imaginary point-probe and the substrate is not necessarily equal to the lift height.

Furthermore, by applying external magnetic fields, it is possible to measure the hysteresis loop of a MFM tip, plotting the MFM contrast at the center of the current-carrying ring (with an appropriate fixed current) as a function of the intensity of the external magnetic field [225]. Further information about MFM tip magnetic characteristics can be achieved with this method, such as the saturation field H_s, the coercive field H_c and the shape of the hysteresis loop.

The fabrication of the microscale rings requires the use of electron-beam lithography, which is expensive and not practical for most MFM users. For this reason, a similar calibration method has also been proposed, which uses a circuit with two long parallel straight wires on micro- or nano-scale fabricated by photolithography techniques. Also in this case, describing the MFM tip as a point dipole and combining it with the equation of the z component of the field produced by the two parallel wires, it is possible to fit the curve of the MFM contrast measured at the center of the two wires as

a function of the tip-substrate separation. In this way the effective magnetic moment m_z and the effective magnetic charge q can be determined [226], [227].

The limit of these techniques is that when MFM tip is close enough to the current rings or wires, the magnetic stray field produced by the tip can possibly affect the current distribution in the ring or the wires and (more important) the magnetic field produced by the current can alter the magnetic moment of the tip. To obtain an accurate tip calibration, it is necessary to minimize these effects, choosing an optimized separation between the tip and the current source.

Other MFM probes calibration procedures consist in the use of reference samples, with known magnetic structures, such as hard disks or other magnetic patterned structures. In these cases, the magnetic behavior of the tip is studied through the application of external magnetic fields during the sample scan and through the analysis of the evolution of the MFM contrast as a function of the applied field. In order to study only the evolution of the tip magnetization in response to the external magnetic field, samples with high coercivity (significantly higher than MFM probes coercivity), such as commercial hard disks, have to be used [220]. The MFM contrast versus the applied magnetic field curve represents the hysteresis loop of the MFM tip. Thus, from these curves it is possible to determine the tip saturation magnetic field H_s, and the coercive magnetic field H_c. The axial (out-of-plane) and in-plane magnetic hysteresis curves of several commercial tips have been characterized using this method [228]. Furthermore, the magnetic stray field of the tip can be calculated imaging sample with a very well known magnetic moment distribution, previously characterized by the use of other magnetic standard characterization techniques (such as VSM or SQUID). Saturating the sample in the opposite direction in respect to the tip magnetization and recording MFM images under zero applied magnetic fields, the changes of the magnetization state of the sample in respect to the remanent state are due only to the effect of the magnetic stray field of the MFM probe. Thus, comparing the $M=M_s$ values obtained with MFM images with $M_r=Ms$ values obtained by VSM it is possible to calculate the magnetic stray field of the tip. Samples consisting in arrays of nanowires are particularly appropriate for this kind of analysis, because nanowires, thanks to their high shape anisotropy, present axial easy axis. If only axial magnetic field are applied (such as the magnetic field of the tip, when it is magnetized along the vertical direction) the nanowires present only two possible magnetic states with the magnetization oriented either up or down. This results in a positive or negative contrast in MFM images, depending on the direction of the tip

magnetization. In this way it is possible to count the number of nanowires which switch under the effect of the tip magnetic stray field and easily calculate the $M=M_s$ value [228].

3.5.2 - Advanced probes

The lateral resolution, the sensitivity, the stability and the accuracy of MFM measurements are strongly dependent on the characteristics of the MFM probes, which have to meet the following requirements:

1) High lateral resolution;
2) High sensitivity;
3) High magnetic stability (in response to the sample stray field and to an eventual external magnetic field during in-field measurements);
4) Mechanical and chemical stability;
5) Possibility to be easily calibrated in order to obtain quantitative data analysis.

The simplest and most common way to obtain magnetic MFM probes is to coat a nonmagnetic AFM tip with a magnetic material. Most commercially available MFM probes consist in microfabricated silicon conical tips coated with for example Fe, CoCr or CoCrPt films. Recently, different technological strategies have been proposed to improve MFM probes properties. The lateral resolution can be improved decreasing the thickness of the coating (i.e., reducing the physical size of the probe and, thus, the tip-sample interaction volume), but most of the magnetic films industrially used exhibit lower remanent magnetic moment (i.e., lower magnetic sensitivity), when the thickness is reduced. Nevertheless, it has been demonstrated that it is possible to improve the magnetic lateral resolution (e.g., to reduce the size of the probes) using magnetic coatings with appropriate characteristics, such as antiferromagnetically coupled layer structures [229]–[231], which act as point dipoles, and magnetic layers with perpendicular magnetic anisotropy [232], [233], which exhibit large remanent magnetic moment also when the thickness of the coating is small. These strategies present the advantage of the simple fabrication process, such as magnetron sputtering, which is a suitable technology for industrial production. Nevertheless, the conical shape complicates the quantitative characterization of the probes limiting it to samples with magnetic characteristics similar to the reference sample used for calibration. The calibration can be simplified using cylindrical probe magnetized along the cylinder axis, which has been proposed as the ideal sensor shape by Porthun et al [234]. This probe

can be modeled as an extended dipole and, if the height of the probe (i.e., the distance between the two dipole's monopoles) is larger than the decay length of the sample magnetic stray field, only the monopole close to the sample surface can be considered involved in the tip-sample interaction. Coherently with the force transfer function approach proposed by Hug et al [235], a cylindrical probe with high aspect ratio (i.e., with diameter smaller and length larger than the size of the analyzed magnetic sample) can be considered to act as a point charge and the tip sample interaction force is then proportional to the sample stray field. Thus, in this case, a universally applicable calibration can be obtained through the definition of the value of the lower monopole and its position. On the basis of this concept, several efforts have been done to fabricate a cylindrical MFM probe with high aspect ratio and different technological strategies have been proposed. For example, a bar shaped magnetic sensor has been produced depositing a Co film on a side of a freestanding SiN plane [236]. A promising technological solution is represented by carbon nanotubes coated with magnetic films, attached to microfabricated silicon tips [237]–[239]. The small diameter of these probes provide a very good lateral resolution and their high aspect ratio leads to a simple calibration procedure.

Further improvements of MFM probes performances have been obtained by using iron filled carbon nanotubes (FeCNTs) consisting in a cylindrical single domain single crystalline nanowire enclosed in a carbon nanotube, attached to standard silicon tips [240]. Within the high lateral resolution and the high aspect ratio, this technology provides a higher sensitivity thanks to the high saturation magnetization of iron (filling material) and higher chemical and mechanical stability, thanks to the protecting carbon shell, which prevents oxidation and abrasion phenomena. Furthermore, the large magnetic shape anisotropy of FeCNTs probes implies that the axis of easy magnetization is coincident with the longitudinal axis of the nanowire, producing a stable magnetization along this direction even in moderate perpendicular magnetic field. This makes this kind of probe particularly suitable for inplane in field MFM measurements [241], [242]. Finally, multi-functional MFM probes were obtained by functionalizing AFM tips attaching on their apex a single ferritin molecule thus realizing probes sensitive to magnetic forces as well as to biomolecular interactions with DNA on surfaces [243].

3.6 - CONCLUSION AND FUTURE PERSPECTIVE

The most widespread techniques of the MFM family have been reviewed. Mainly dynamic MFM, but also static MFM for the sake of completeness, has been illustrated describing the working principles, the experimental setups, and the analytical models describing the MFM response, that are fundamental for understanding and quantitatively interpreting the contrast in MFM images. For the convenience of the reader, all the possible materials in the study of which MFM finds applications have been described. Finally, we presented some advances, hot topics, new applications, and still open issues. Overall, despite having been used for more than 20 years, there is still "a plenty of room" for advances in MFM techniques. These should be aimed at increasing the accuracy of quantitative measurements, by developing techniques to decouple nonmagnetic effects that do not require too much time consuming measurement sessions or too complicated and diffcult to standardize experimental setups. Also, the range of investigable samples should be expanded, in particular toward those generating ultrasmall magnetic stray field such as magnetic nanomaterials embedded in biological matrices.

4. OBJECTIVES AND STRATEGIES OF THE THESIS

4.1 - MAGNETIC NANOPARTICLES AND MAGNETIC FORCE MICROSCOPY: OPEN ISSUES AND GENERAL OBJECTIVES OF THE PROJECT

With reference to the analysis of the literature regarding the development and application of MFM to the study of single magnetic nanoparticles, previously described in Chapter 3, some considerations can be extrapolated and summarized as follows:

1) MFM is an established technique for the magnetic imaging and verification of the magnetic nature of single NPs, but the quantitative evaluation of the magnetic properties of single entities is still an unsolved challenge.
2) Some limitations still affect the MFM technique and limit its use for the quantitative characterization of single nano-objects, such as nanoparticles. Specifically, these limitations are:
   - The presence of non-magnetic tip-sample interactions, which produce an additional contrast in MFM images, "hiding" the real magnetic signal and making extremely difficult the quantitative interpretation of MFM data.
   - The presence of the magnetic stray field produced by the probe during the scanning, which represents an additional field in respect to the externally applied magnetic field, which is not easy to be quantified and taken into account.
   - The lack of a theoretical model describing the tip-NP magnetic interactions consistently with the measured experimental data and the consequent difficulty in retrieving, from the measured data (amplitude, frequency or phase shift), quantitative information about physical magnetic parameters (e.g. the magnetization).
3) These limitations quantitatively affect the MFM data and make MFM users unable to obtain information directly related to the magnetic physical properties of single nano-objects; therefore, they need to be overcome in order to be able to use MFM technique as a quantitative tool for the accurate characterization of single magnetic nano-objects, such as nanoparticles.

In this context, the main objective of the project is the development of an experimental procedure and an instrumental apparatus to obtain quantitative measurements of

nanoparticles magnetic properties by using Magnetic Force Microscopy (MFM), overcoming the limitations which still affect the technique.

In Figure 25, a schema representing the different phases and the main strategies of the project is reported. Specifically, the project is composed by five different phases: i) the experimental verification and rationalization of the open issues and the problems limiting the applicability of MFM to the quantitative magnetic characterization of single NPs; ii) the development of an instrumental apparatus and a measurement procedure to evaluate and eliminate the electrostatic artifacts quantitatively affecting the MFM data; iii) the individuation of a theoretical model describing the magnetic tip-NP magnetic interaction, coherent with the experimental data; iv) the development of a procedure to quantitatively measure the magnetic properties of single nanoparticles by MFM; v) the development of a procedure to quantitatively measure the thickness of the non-magnetic coating of core-shell NPs by MFM.

Each of these phases is described in detail in the following paragraphs.

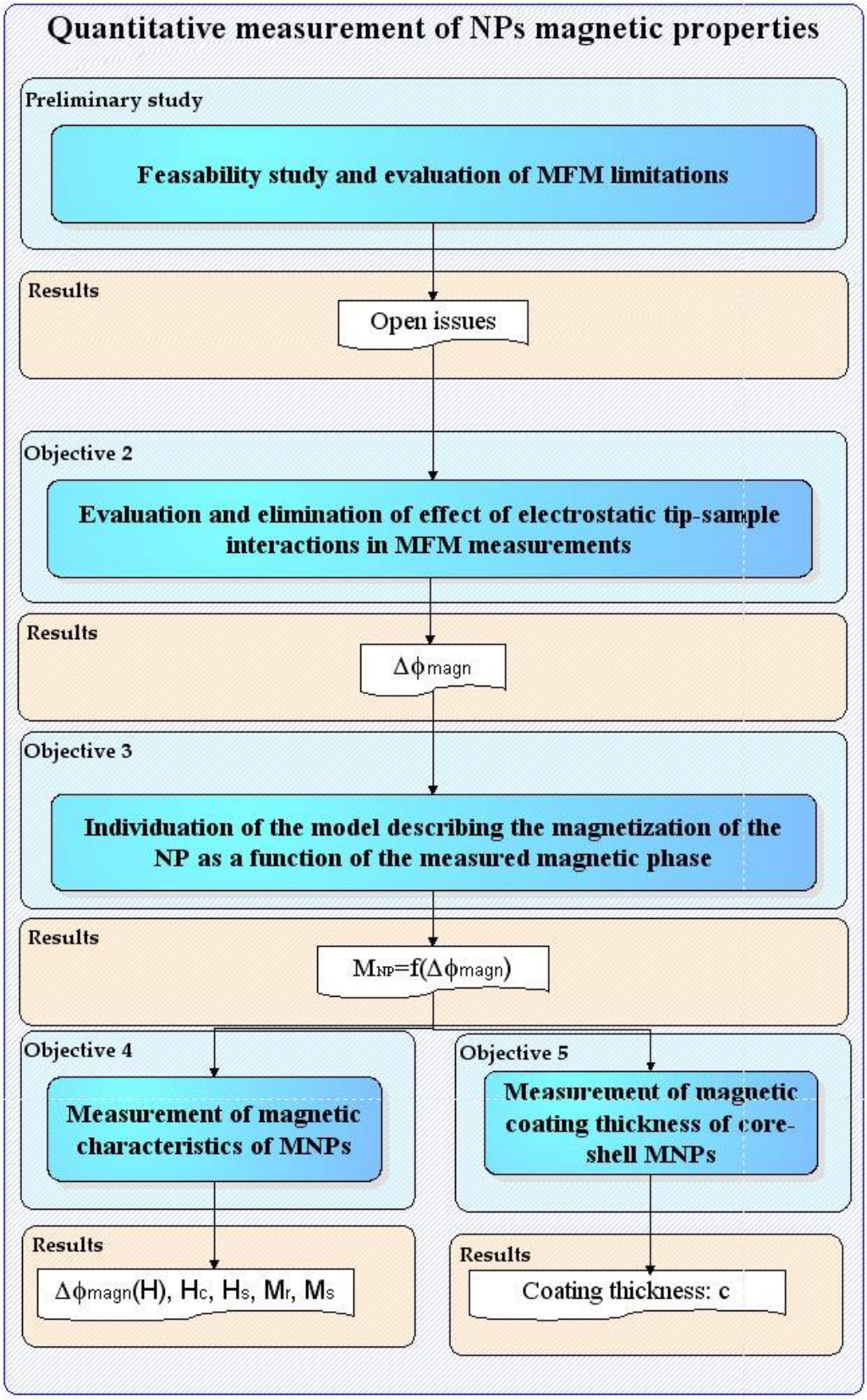

Figure 25 – General schema of the methodology for the magnetic characterization of MNPs by MFM

4.2 - OBJECTIVE 1: VERIFICATION AND RATIONALIZATION OF THE OPEN ISSUES

The first objective of the project was the individuation of the possible phenomena affecting MFM measurements and, more specifically, the experimental verification and rationalization of the open issues already individuated by the analysis of the literature.

The strategy which has been followed consists in acquiring MFM data on different magnetic nanoparticles and in different experimental conditions in order to:

- Verify and evaluate the presence of non-magnetic tip-sample interactions;
- Verify and analyse the effect of the probe magnetic stray field and an external magnetic stray field on the magnetization state of nanoparticles;
- Verify and analyse the eventual inconsistency of quantitative experimental data with the theoretical model and individuate the cause on the basis of the experimental observations.

To do that, two different experiments have been performed:

1) Two different kinds of nanoparticles (the first consisting in the sole magnetic cores, the second consisting in the magnetic cores covered with an external coating of a different material, i.e. having different "electric properties" and no magnetic behavior) have been analysed in the same experimental conditions (i.e. with a standard magnetized probe, without applying any external magnetic field) in order to:
   - analyse the MFM contrast obtained on a simple model (only magnetic cores) of magnetic nanoparticles and experimentally verify the eventual inconsistency of the experimental MFM data with the theoretical models describing the tip-NP interaction as a pure magnetic interaction.
   - analyse the effect on MFM data of the presence of a non-magnetic and electrically" different coating on the MFM data.
2) The same sample of nanoparticles (Fe_3O_4) has been analysed in different experimental conditions, i.e. i) with a not-magnetized probe in the absence of any external magnetic field, ii) with a standard magnetized probe in the absence of any external magnetic field, iii) with a standard magnetized probe in presence of an intense external magnetic field, in order to:
   - explicitly visualize and quantitatively extrapolate the effect of non-magnetic tip-NP interactions;

- explicitly visualize the effect of the magnetic tip-NP interactions, due to the magnetization of the NP induced by the sole magnetic stray field of the probe, quantitatively compare the obtained contrast with the non-magnetic one and verify the presence of the effect of the probe magnetic stray field on the magnetization state of single nanoparticles;
- analyse the effect of an external magnetic field on the detected MFM contrast, comparing the results obtained with and without the application of an external magnetic field;
- verify the consistency/inconsistency of the standard MFM data (acquired with a magnetic probe, in the absence or presence of an external magnetic field) with the theoretical model describing the tip-NP interactions as the interactions between two punctiform magnetic dipoles.

In the schema reported in Figure 26, the objectives, the strategies, the experimental measurements and the data processing used to achieve this first objective are summarized. The obtained results are described in Chapter 5 (Article 1) of this thesis.

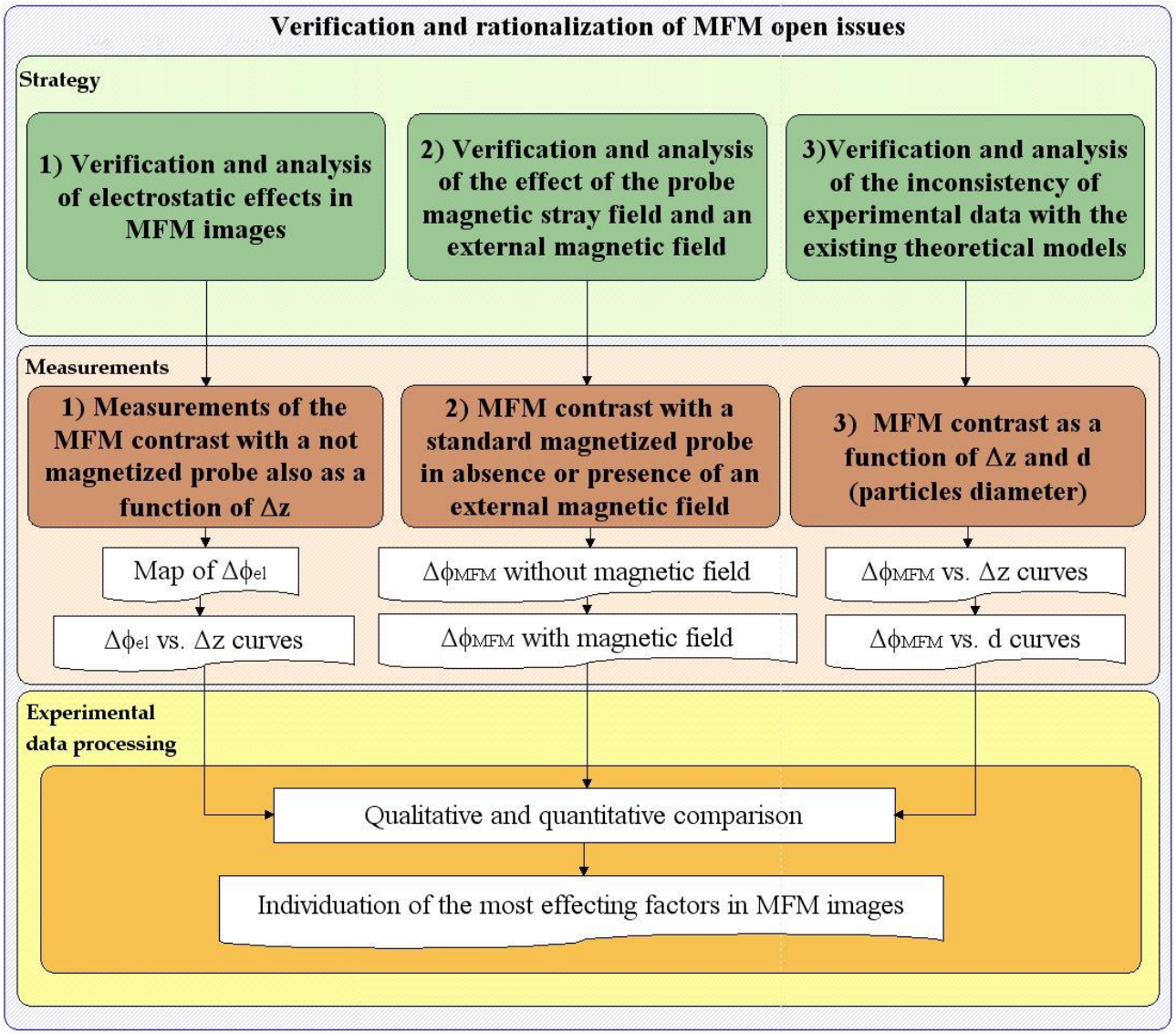

Figure 26 – Schema of the strategies, the experimental measurements and the data processing used in the first phase of the project

4.3. - OBJECTIVE 2: REMOVAL OF ELECTROSTATIC CONTRIBUTION

As deduced by the analysis of the literature and verified by the preliminary analysis (objective 1, see results reported in Chapter 5), MFM measurements are affected by the presence of electrostatic interactions between the tip and the sample giving rise to a significant additional signal, which can be easily confused with the magnetic one. Thus, the quantitative measurement of the magnetic properties of NPs (or another kind of magnetic sample) by MFM, which is the main objective of the thesis, requires the preliminary evaluation of the electrostatic tip-sample interactions and the development of a methodology to eliminate this effect from the quantitative data.

Some strategies have been already proposed in the literature (which are described in Chapter 3 of this thesis), but the limited applicability or the complex required instrumentation make these techniques difficult to be applied in all laboratories practice.
Therefore, the project plan include a "preliminary" but essential phase in which a strategy, a specific instrumental apparatus and a measurement procedure are developed and optimized in order to achieve the objective of depurating the MFM data from the signal due to non-magnetic phenomena.
In the following Figure 27 the elaborated strategy and the main activities (experimental measurements and data processing) which has been carried out in order to evaluate and eliminate the electrostatic effects on MFM measurements are summarized.
The strategy basically consists in the development of a system able to obtain the magnetization and the demagnetization of the tip *in situ,* i.e. without moving the probe from the scanned area.
In principle, the demagnetization of the probe can be obtained i) through the application of a decreasing alternate magnetic field with an appropriate frequency and initial amplitude or ii) by applying a continuous magnetic field having intensity equal to the coercive field of the probe and opposite direction in respect of the probe magnetization.
We firstly implement the second methodology: we developed an instrumental apparatus and an experimental procedure able to individuate the value of the coercive field of the used probe and apply it to the tip-sample system in order to demagnetize the probe without moving it from the scan area. The developed apparatus and procedure are described in detail in the Chapter 6 (article 2) of this thesis. Further advancement of the apparatus could allow us to apply also the methodology of the alternate magnetic field, but the optimization of the equipment and the evaluation of the effective improvement of the demagnetization process are still ongoing and not reported in this thesis.
With the demagnetized tip an image concerning only the electrostatic signal ($\Delta\varphi_{el}$) can be obtained, while, scanning the same area with the magnetized tip a standard MFM image, i.e. concerning the magnetic and electrostatic tip-sample interactions ($\Delta\varphi_{mag}+\Delta\varphi_{el}$), can be obtained. By subtracting the fist image to the second one, a "real" magnetic image ($\Delta\varphi_{mag}$) could be obtained.
The strategy, the experimental apparatus and the results obtained applying this method are reported and described in details in Chapter 6.

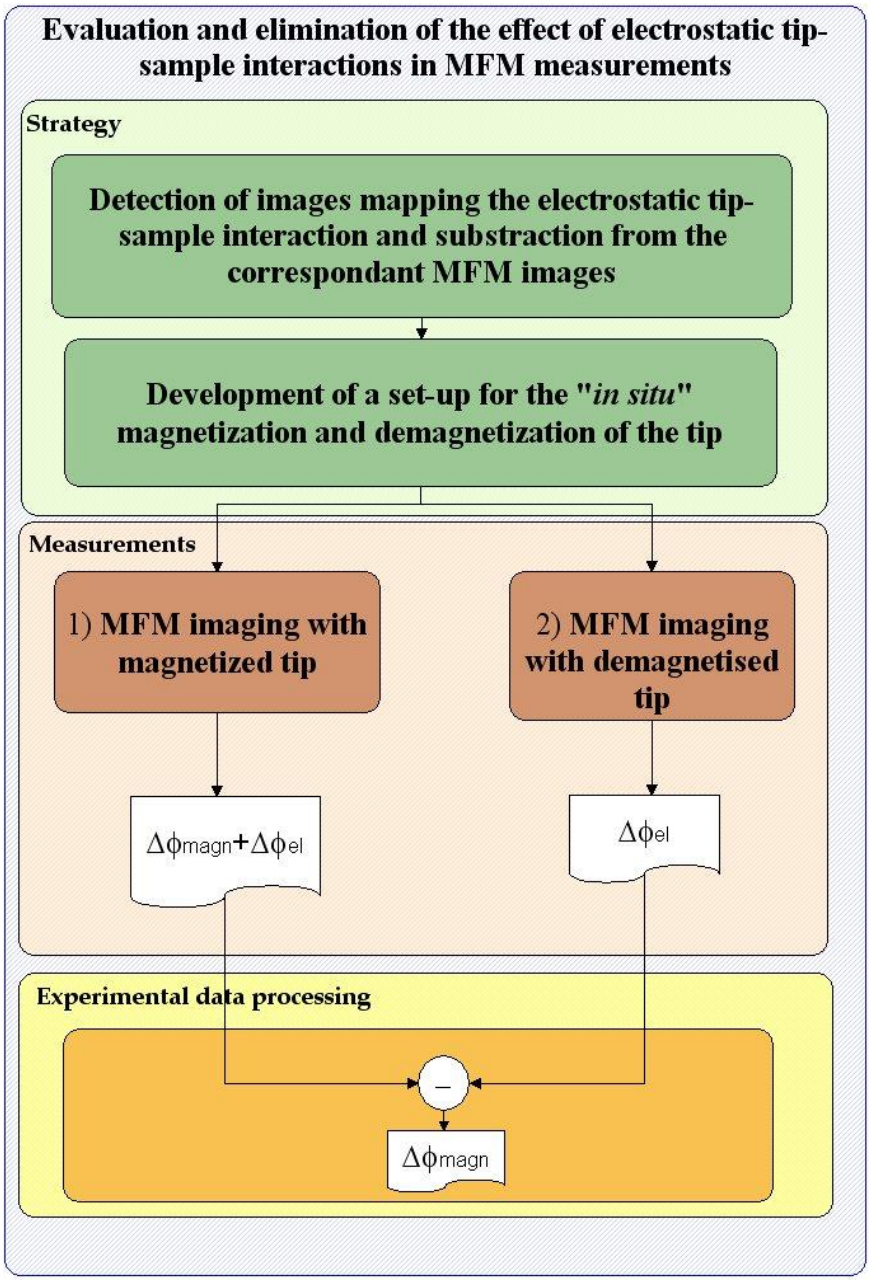

Figure 27 - Schema of strategies and activities for the evaluation and elimination of the electrostatic effects in MFM images

4.4 - OBJECTIVE 3: INDIVIDUATION OF THE MODEL

The third objective of the project is based on the assumption that the presence of the additional signal due to the non-magnetic tip-sample interactions is the cause of the discrepancy between the experimental MFM data and the theoretical models describing the interaction between the probe and the NPs as a pure magnetic interaction, observed in the literature and in thepreliminary results (Chapter 5 – Article 1).

On the basis of this hypothesis, once the electrostatic effects are removed from MFM images and the "pure" magnetic signal is obtained, it could be possible to more easily

individuate the model which better describe the magnetic interaction occurring between the probe and the NP in MFM measurements, accordingly with experimental data. The individuation of a proper theoretical model is necessary to define the relationship between the measured MFM signal (the MFM phase in our case) and the magnetization of an analysed NP.

In Figure 28 the strategy, the necessary experimental measurement and the data processing of this phase of the project are summarized. By acquiring several "pure magnetic" images with different lift height (or images of NPs having different sizes, using the same lift height), a curve of the pure magnetic signal as a function of the tip-NP distance (or as a function of the nanoparticles diameter) can be obtained. By fitting this experimental curve with the models describing the magnetic interaction between a MFM probe and a NP it could be possible to find the best model describing the magnetic phenomena occurring during MFM images.

The obtained results are described in Chapter 6 (Article 2) of this thesis.

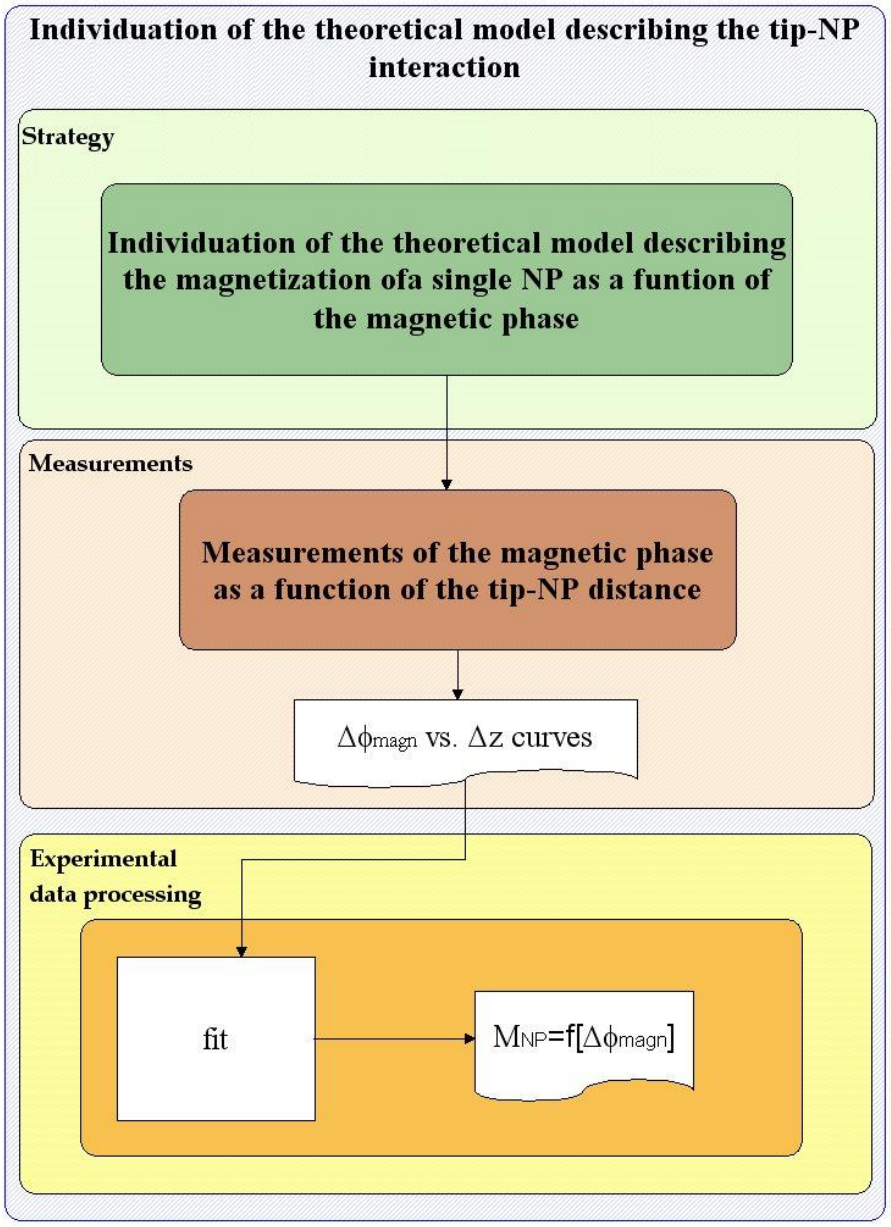

Figure 28 - Schema of strategies and activities for the individuation of the theoretical model describing the tip-NP interaction

4.5. - OBJECTIVE 4: MEASUREMENT OF MAGNETIZATION CURVES OF SINGLE NANOPARTICLES

After establishing the procedure to estimate and eliminate the electrostatic effects and after individuating the theoretical model describing the magnetic tip-NP interaction, the main magnetic parameters (magnetization curve) of single NPs could be, in principle, evaluated by following the strategy schematized in Figure 29.

Through the application of continuous magnetic field with different intensities (H) and through the evaluation of the correspondent phase contrasts ($\Delta\varphi(H)$), the values of the coercive magnetic field H_c and the saturation magnetic field H_s of the analysed NP can

be determined. H_c will be determined as the value of the magnetic field, in correspondence of which the magnetic phase contrast of the nanoparticle is zero. H_s will be determined as the value of the magnetic field in correspondence of which a further increasing of the field intensity does not produce an increasing in the phase contrast of the nanoparticle. Furthermore the values of the phase shift as a function of the applied magnetic field H $(\Delta\varphi(H))$ will be collected. Using an adequate theoretical model, the values of the phase shift can be converted in values of the nanoparticle's magnetization M_{NP}. In this way the magnetic hysteresis curve $(M(H)=f[\Delta\varphi(H)])$ of a single nanoparticle could be determined.

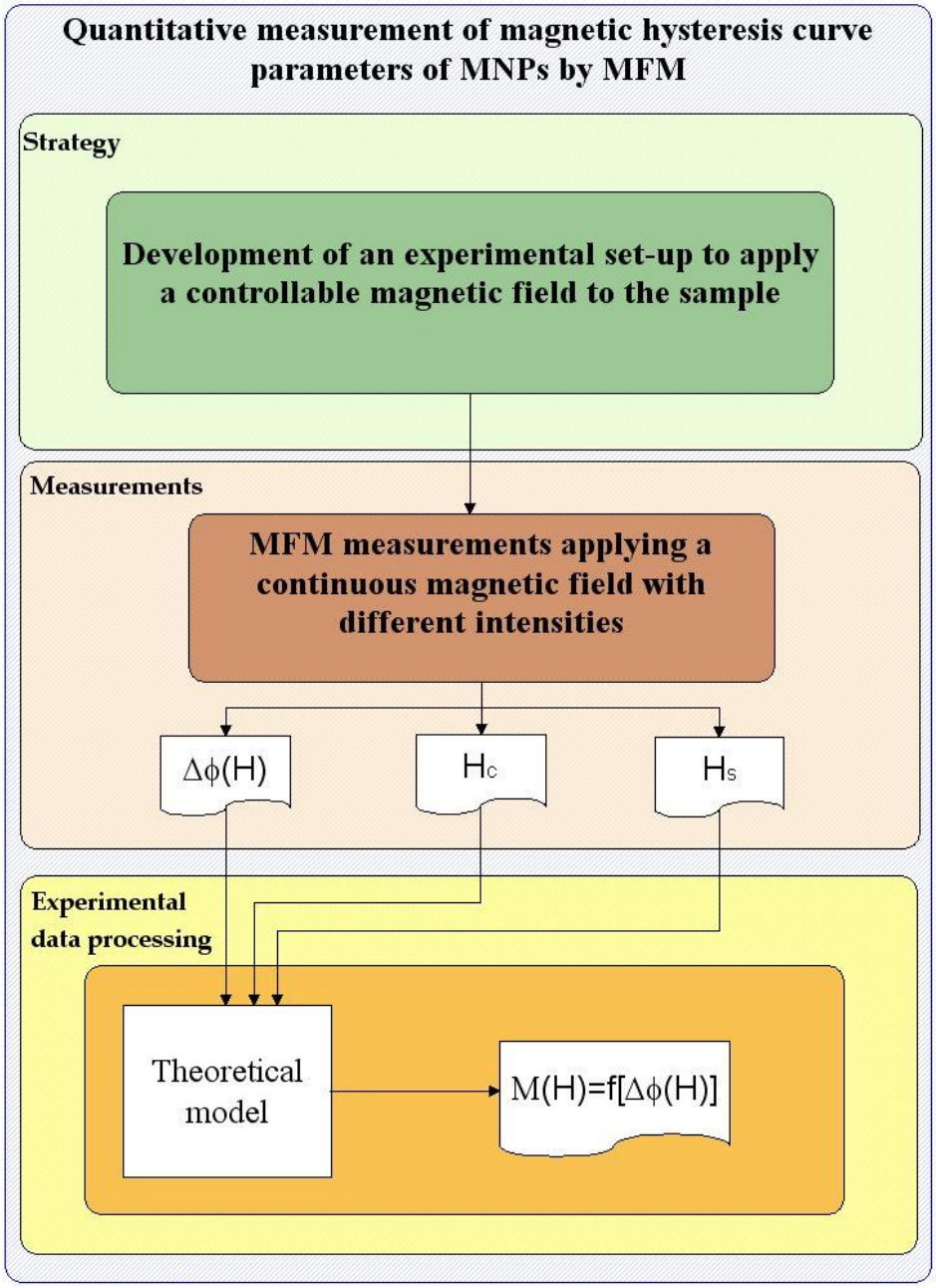

Figure 29 - Schema of strategies and activities for the quantitative measurement of magnetic parameters of MNPs by MFM

4.6 - OBJECTIVE 5: MEASUREMENT OF THE NONMAGNETIC COATING THICKNESS OF CORE-SHELL MAGNETIC NANOPARTICLES BY CONTROLLED MAGNETIZATION MAGNETIC FORCE MICROSCOPY

MNPs, in order to be used for biomedical applications, often need to be coated with non-magnetic coatings, with the aim of improving the dispersion stability, the biocompatibility and bio-functionality [244]. Therefore, the optimization of these systems requires the deep characterization not only of the magnetic core, but also of the coating features. Beside the chemical and physical properties of the coating, its

thickness is another important property which can influence the size, the shape and the overall magnetic behavior of the NPs system [245-248].

Also in this context, MFM can be considered as a useful tool for the measurement of the thickness of NPs non magnetic coatings. Indeed, the possibility of using MFM for the measurement of the thickness of non-magnetic coatings deposited on magnetic substrates has already been demonstrated [123].

Since the magnetic signal is dependent on the distance between the tip and the magnetic NP, more in particular by the distance between the two equivalent magnetic dipoles, through the comparative measurement of NPs with and without coating under the same experimental conditions, it may be possible to deduce the thickness of the non-magnetic coating.

Nevertheless, because of all the limitations characterizing the applicability of MFM techniques to the characterization of magnetic nanoparticles and because of the lack of a univocal model describing the tip-NP magnetic interaction, this method has never found application to the measurement of the coating of MNPs.

Once individuated the best theoretical model describing the tip-NP interaction as a function of the tip-MNP distance, it should be possible to apply this method to the measurement of the thickness of the coating on MNPs.

In Figure 30, the schema of the adopted strategy is reported. The preliminary results obtained in this field are reported in Chapter 8.

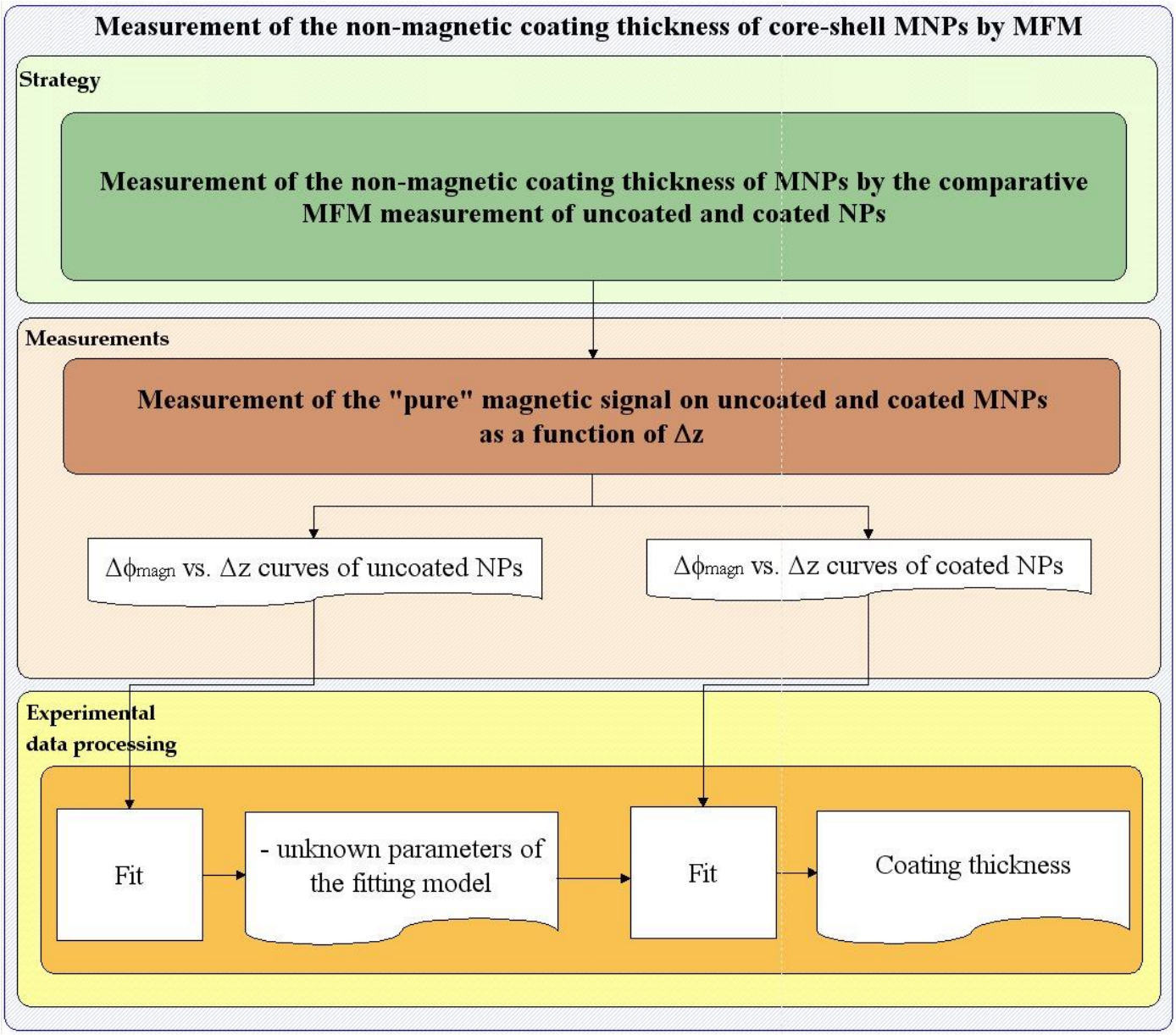

Figure 30 - Schema of strategies and activities for the quantitative measurement of the thickness of the non-magnetic coating of core-shell NPs

5. EXPERIMENTAL ISSUES IN MAGNETIC FORCE MICROSCOPY OF NANOPARTICLES

L. Angeloni [1, 2 a)] , D. Passeri[1], M. Reggente[1], M. Rossi[1,3], D. Mantovani[2], L. Lazzaro[4], F. Nepi[4], F. De Angelis[5, 6],¶ and M. Barteri[4]

[1] *Department of Basic and Applied Sciences for Engineering, SAPIENZA University of Rome, Via A. Scarpa 16, 00161, Rome, Italy*

[2] *Department Min-Met-Materials Eng. & University Hospital Research Center, Laval University, Quebec City, Canada*

[3] *Research Center for Nanotechnology applied to Engineering of SAPIENZA University of Rome (CNIS), Piazzale A. Moro 5, 00185, Rome, Italy*

[4] *Department of Chemistry, SAPIENZA University of Rome, Piazzale A. Moro 5, 00185, Rome, Italy*

[5] *Department of Anatomy, Histology, Forensic Medicine and Orthopaedics, SAPIENZA University of Rome, Rome, Italy*

[6] *Center for Life Nano Science@Sapienza, Istituto Italiano di Tecnologia, Rome, Italy*

a) Corresponding author: livia.angeloni@uniroma1.it

Published in:
AIP Conference Proceedings
1667 - NANOFORUM 2014, 22–25 September 2014
Location: Rome, Italy
Published: June 2015
DOI: 10.1063/1.4922566

http://aip.scitation.org/doi/abs/10.1063/1.4922566

Resumé

Le développement de nanoparticules magnétiques pour des applications biomédicales à besoin d'une caractérisation détaillée de leurs propriétés magnétiques, en relation non seulement avec leur structure chimique, mais aussi leur morphologie et leur taille. La microscopie à force magnétique (MFM), grâce à sa résolution latérale nanométrique et sa capacité à détecter des champs magnétiques faibles, apparaît comme un outil puissant pour la caractérisation des propriétés magnétiques de nanoparticules simples, ainsi que leurs caractéristiques morphologiques. Néanmoins, l'application de MFM aux mesures quantitatives des propriétés magnétiques à l'échelle nanométrique est encore une question ouverte en raison d'une certaine incongruité entre les données expérimentales et les modèles théoriques existants qui decrivent les interactions magnétiques d'échantillon de pointe. Dans ce travail, on analyse des données MFM acquises sur différentes nanoparticules magnétiques dans différentes conditions expérimentales (sondes magnétisées et non magnétisées, mesures en presence ou en absence d'un magnetique), afin d'individualiser les phénomènes possibles affectant les mesures MFM. Ceux-ci incluent des artefacts induits par la topographie résultant du couplage capacitif entre l'échantillon et la pointe, que nous proposons ici pour la première fois. Dans le cas des mesures effectuées en présence d'un champ magnétique externe, des signaux MFM beaucoup plus intenses ont été détectés car ils produisent la saturation de l'aimantation des nanoparticules, qui n'est pas entièrement obtenue par le seul champ produit par la pointe pendant le balayage. Néanmoins, même dans les mesures effectues en presence d'un champ magnetique, les résultats ont mis en évidence la présence d'effets électrostatiques significatifs dans les images MFM, qui apparaissent donc comme un facteur important à prendre en compte pour l'interprétation quantitative des données MFM.

Abstract

The development of magnetic nanoparticles for biomedical applications requires a detailed characterization of their magnetic properties, with relation not only to their chemical structure, but also their morphology and size. Magnetic force microscopy (MFM), thanks to its nanometric lateral resolution and its capability to detect weak magnetic fields, appears as a powerful tool for the characterization of the magnetic properties of single nanoparticles, together with their morphological characteristics. Nevertheless, the application of MFM to the quantitative measurements of magnetic properties at the nanoscale is still an open issue because of a certain incongruence between experimental data and existing theoretical models of the tip-sample magnetic interactions. In this work, MFM data acquired on different magnetic nanoparticles in different experimental conditions (magnetized and not magnetized probes, out-of-field and in-field measurements) are analyzed, with the aim of individuating the possible phenomena affecting MFM measurements. These include topography-induced artifacts resulting from the tip-sample capacitive coupling, which we propose here for the first time. In case of measurements performed in presence of an external magnetic field, much more intense MFM signals were detected as it produces the saturation of the magnetization of the nanoparticles, which is not completely obtained by the sole stray field produced by the tip. Nevertheless, even in in-field measurements, the results evidenced the presence of significant electrostatic effects in MFM images, which, therefore, appear as an important factor to be taken into account for the quantitative interpretation of MFM data.

5.1 - INTRODUCTION

Magnetic nanoparticles (NPs), thanks to their special magnetic properties, are finding growing interest in several technological fields, such as data storage technology, environmental, and biomedical applications [244]–[246]. Especially in the biomedical field, magnetic NPs are considered a promising technology due to their particular magnetic properties, sizes, and the possibility to be functionalized with specific molecules or drugs. These characteristics make them particularly suitable as carriers for drug delivery systems, mediators for magnetic hyperthermia treatments, contrast agents for magnetic resonance imaging (MRI) and markers for cell labelling [247]–[250]. The design and the optimization of these systems require a detailed knowledge of the magnetic and structural properties of the adopted nanomaterials. For example, the magnetic hyperthermia heating effect, the translational force exerted on drug delivery carriers, the drag force in cells magnetic separation systems are strongly dependent on the size and the magnetic properties of the nanoparticles, like the magnetic susceptibility and the saturation magnetization, which are, in turn, dependent on their size and morphology [85], [244]. Therefore, characterization methods able to measure the magnetic properties of single NPs, also in dependence of their structure and size, are required for the fundamental study of the magnetic behavior of novel nanomaterials, as well as for the quality control of the synthesis processes aimed at specific applications.

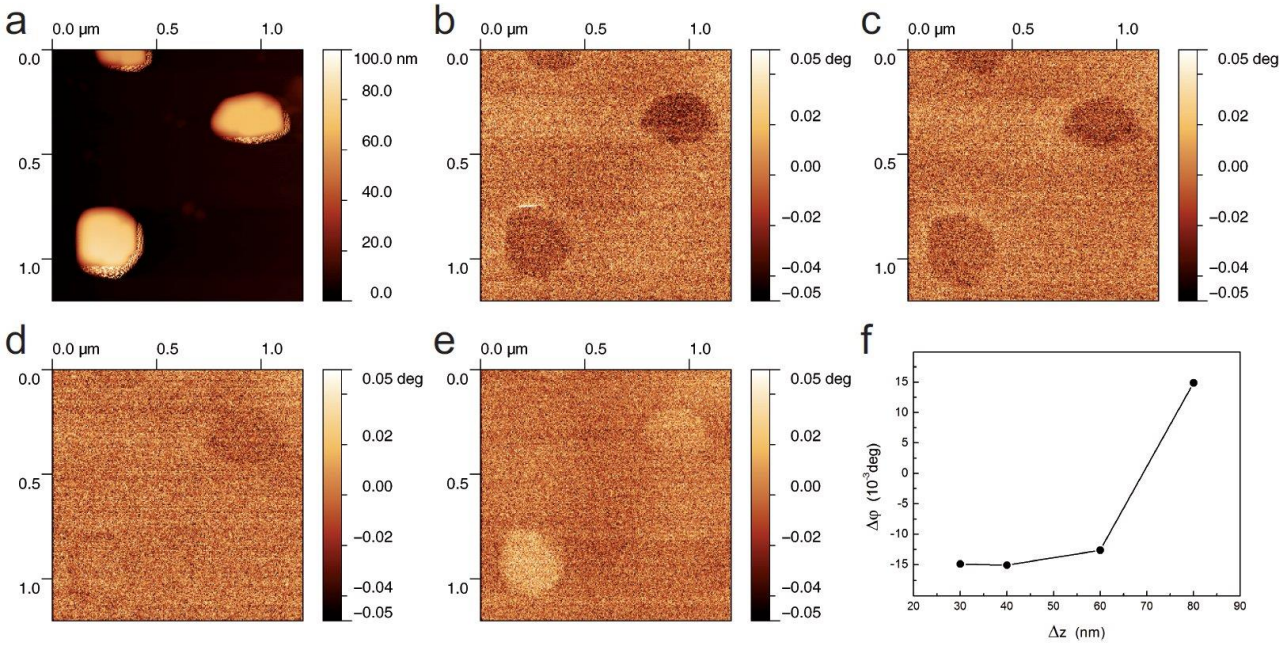

Figure 31 - Topography (a) and phase MFM images of Fe NPs detected at lift height Δ*z* of 30 nm (b), 40 nm (c), 60 nm (d), 80 nm (e); phase contrast Δφ as a function of Δ*z* (f).

Standard techniques, like superconducting quantum interference devices (SQUIDs)[251] [252] or vibrating sample magnetometer (VSM) [253], allow the detection of global magnetic properties of NPs populations, but the detection of magnetic properties of single particles is not possible and the evaluation of their dependence with their size and shape is not explicit.

Thanks to its capability of simultaneously mapping the topography and the magnetic domains distribution of a sample with nanometric lateral resolution and high sensitivity, magnetic force microscopy (MFM) is a powerful tool for the morphological and magnetic characterization of single NPs [155], [156], [161], [209]. Nevertheless, some experimental and theoretical still open issues limit the accuracy of quantitative MFM. Among them, a certain incongruence between experimental data and existing theoretical models of the tip-sample magnetic interactions which is attributable to both the use of not enough accurate models and to the effect of electrostatic tip-sample interactions on MFM measurements.

In this work, we present a MFM study on different magnetic NPs in different experimental conditions, with the aim of individuating the possible phenomena which affect MFM measurements. Fe and Fe-Cu NPs have been analyzed in order to highlight how the electric properties of nonmagnetic coatings alter the MFM response, which therefore is not interpretable using simple analytical models. Moreover, MFM has been carried out on the same Fe_3O_4 NPs

in different experimental conditions, i.e., using a not magnetized tip, with a magnetized tip in the absence of external magnetic fields, and with a magnetized tip in presence of an external magnetic fields. The obtained data are compared and analyzed in order to: (i) highlight the importance of evaluating and removing the effects of the electrostatic tip-sample interactions in MFM measurements in order to quantitatively analyze the magnetic signal; (ii) illustrate for the first time a mechanism of topography-induced artifacts in MFM images produced by the tip-sample capacitive coupling; (iii) evidence the usefulness of inducing a stable magnetization of the NPs independent on the tip-sample distance. Indeed, the NPs magnetization cannot always be obtained by the sole magnetic field produced by the probe and the application of an external magnetic field is required.

5.2 - THEORY OF MAGNETIC FORCE MICROSCOPY

MFM is usually performed using a standard atomic force microscopy (AFM) apparatus equipped with a magnetic probe, generally consisting in a Si cantilever with a tip placed at its free end, coated with a nanometric film of ferromagnetic material (generally Fe or CoCr alloys). The cantilever is set into oscillation at a frequency f_0 close to its free resonance frequency. The magnetized tip, interacting with a magnetic sample, experiences a magnetostatic force which produces a variation in the dynamic behavior of the cantilever, describable as a shift in the resonance frequency Δf , in the phase $\Delta\varphi$, and in the oscillation amplitude ΔA.

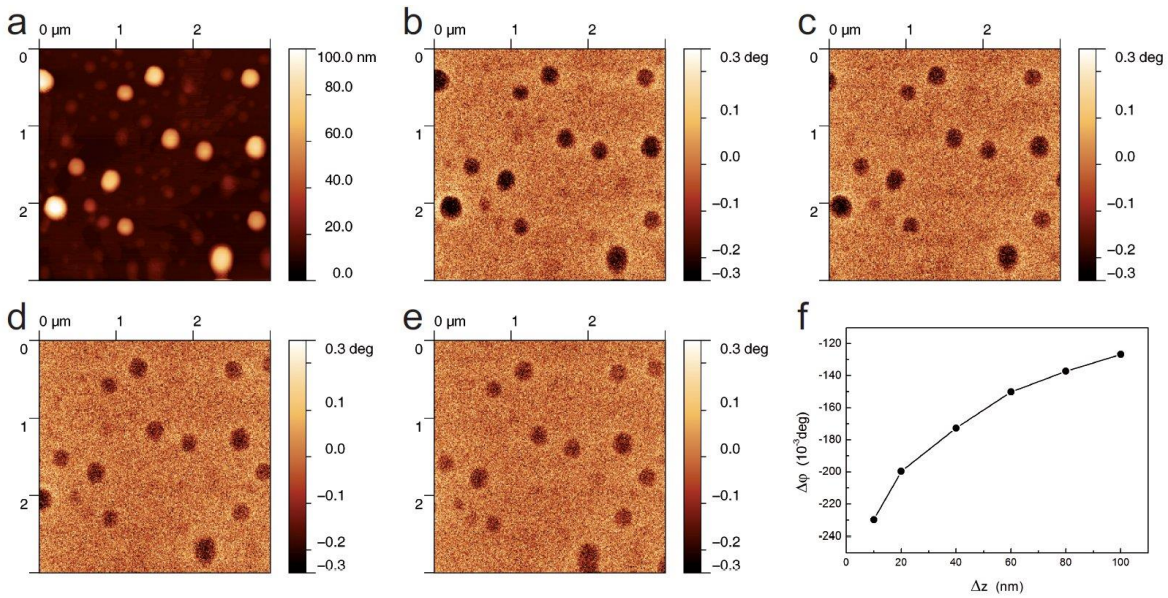

Figure 32 - Topography (a) and phase MFM images of Fe-Cu NPs detected at lift height Δ*z* of 20 nm (b), 40 nm (c), 80 nm (d), 100 nm (e); phase contrast Δφ as a function of Δ*z* (f).

The measurement of one of these parameters (e.g., $\Delta\varphi$) in each point of the scanned area allows the reconstruction of a map (MFM image) related to the local orientation and intensity of the sample magnetization. In order to detect long-range magnetic forces without any effect of short-range tip-sample interactions such as atomic (van der Waals) and chemical forces, MFM is performed using the so called lift mode, in which the surface is first scanned in tapping mode to acquire the topography and then a second scan is performed in dynamic non-contact mode to acquire the map of the magnetic domains (MFM image). In the second pass, the probe is brought at distance Δz from the sample surface (namely, the lift height) at which short-range forces are vanished and is forced to follow a trajectory coincident with the previously recorded sample profile, which prevents the effects of variations of the tip-sample distance due to the surface features. In MFM measurements of superparamagnetic NPs carried out with a vertically magnetized tip without applying any external magnetic field, the NPs magnetization is induced by the magnetic stray field of the probe during the scan and, then, is oriented along the same direction of the tip magnetization. Describing the tip and the NP as two magnetic dipoles with moments m_{tip} and m_s, respectively, when the tip is placed in correspondence of the center of the NP at a vertical distance distance z, the phase shift $\Delta\varphi$ is given by

$$\Delta\varphi = \frac{Q_c}{k_c}\frac{\partial F_z}{\partial z} = \mu_0 m_{tip} M_s \frac{Q_c}{k_c}\frac{d^3}{\left(\Delta z + c_s + \frac{d}{2} + \delta_{tip}\right)^5} \qquad 60)$$

where: Q_c and k_c are the cantilever quality factor and spring constant, respectively; $\partial F_z/\partial z$ is the gradient along the vertical axis z of the vertical component of the magnetostatic tip-sample interaction force F_z; μ_0 is the permeability of free space; M_s is the magnetization of the sample, d is the radius of the NP, c_s is the thickness of the nonmagnetic coating of the NP, and δ_{tip} is the position of the equivalent moment m_{tip} from the tip apex [224]. The presence of a nonmagnetic coating - either diamagnetic or paramagnetic - does not directly affect the intensity of the magnetic signal, as the contribution to magnetic field due to its magnetization is negligible with respect to that of the magnetic core. Nevertheless, the presence of the nonmagnetic coating reduces the magnetic signal detected by the MFM probe because: (i) for the same diameter of the magnetic core and the same value of Δz, it increases the actual distance between the tip and magnetic core, which corresponds to a less intense local magnetic field; (ii) for the same diameter of the whole NP, the presence of the coating reduces the amount of magnetic material of the NP. Ideally, after the calibration of the mechanical (Q_c and k_c) and magnetic (m_{tip} and δ_{tip}) characteristics of the probe, the MFM signal can be used to retrieve quantitative information about the magnetization state of each imaged NP [155], [156], [161].

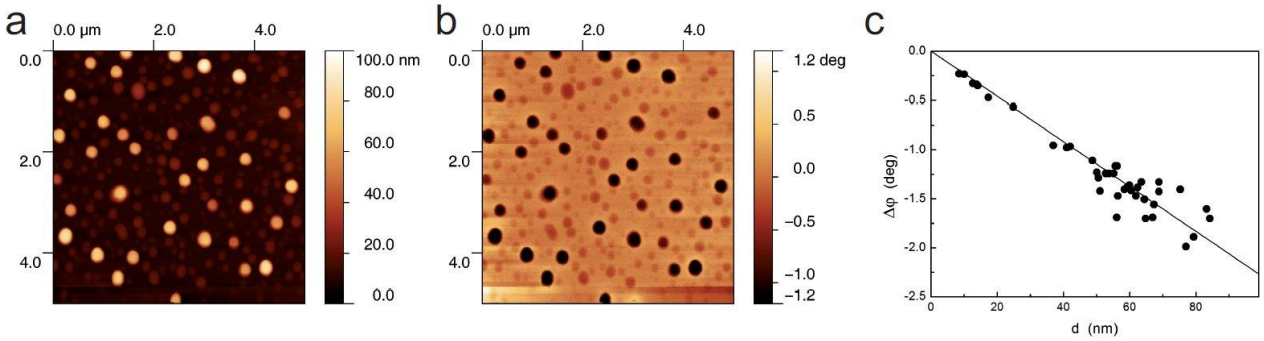

Figure 33 - Topography (a) and MFM phase image (b) of Cu-coated Fe NPs; phase contrast Δφ as a function of the nanoparticles diameter *d* (c).

However, not always experimental data seem consistent with this model, which complicates their quantitative interpretation [161], [209]. In particular, the presence of electrostatic interactions between the tip and the sample during MFM measurements produces additional signals not independent from magnetic interactions [157], [212], [216]. Furthermore, in some cases, it has been shown that a uniform magnetization of

superparamagnetic nanoparticles cannot be obtained by the sole effect of the probe magnetic stray field, but an external magnetic field should be applied to obtain a stable magnetic moment [155].

5.3 - EXPERIMENTAL

Materials. The material used to prepare magnetic nanoparticles is the metallic iron which has a ferromagnetic behavior with a Curie temperature T_c = 770°C, but, it is superparamagnetic at the nanometer scale. Metallic iron (Fe(0)) to the nanometric size is a pyrophoric compound as it has a high reactivity toward oxygen. For this reason, it is essential that all stages of the synthesis and the coating of Fe(0) NPs are carried out under an Ar atmosphere using previously degassed solvents. The oxidation of the sample of iron is a serious drawback since, with the exception of magnetite (Fe_3O_4), all the iron oxides are not magnetic compounds. Iron NPs were prepared by thermal decomposition of the Fe(II) stearate complex obtained by mixing a solution containing 2.78 g of $FeSO_4 \cdot 7H_2O$ in 200 mL of degassed distilled water (10 mM) and 6.13 g of sodium stearate dissolved in 100 mL of the same solvent (25 mM). Letting the mixture react overnight, a precipitate of the complex Fe(II)-stearate was slowly separated. It was washed several time with degassed bidistilled water, was collected with a gooch filter and was dried under vacuum. The glassware used have been previously dried in an oven at 200°C for more than two hours. Under argon atmosphere, 1 g of Fe(II)-stearate was dispersed in 30 mL of octyl ether and heated for 2 hours at 300°C in a flask equipped with a reflux condenser. In the absence of oxygen, the decomposition of Fe(II)-stearate (*Td* = 285°C) provides the reduction of the ions Fe(II) to Fe(0). After vacuum drying 375 mg of superparamagnetic nanoparticles were obtained.

The coating of nanoparticles with a layer of $Cu^{(0)}$ has the purpose to protect the $Fe^{(0)}$ oxidation thus preserving its magnetic characteristics. The synthesis procedure was divided into two distinct phases: the first involves the direct redox reaction between the metallic iron of the NPs and Cu2+ ions in aqueous solution under Ar atmosphere. 90 mg of $CuSO_4$ were dissolved in 25 mL of double distilled H_2O and added under mechanical stirring to 10 mL of an aqueous suspension of 100 mg of iron NPs. The mixture was left to react for one hour to allow the redox reaction between the particles and the ions Cu^{2+}: $Fe^{(0)} + Cu^{2+} \rightarrow Fe^{2+} + Cu^{(0)}$ and/or $2Fe^{(0)} + 3Cu^{2+} \rightarrow 2Fe^{3+} + 3Cu^{(0)}$. In this case, the Fe NPs act both as a reagent for the reduction of Cu^{2+} and as a seed of crystallization, where is deposited a thin layer of metallic Cu which covers the surface of the NPs. The

obtained product was separated by magnetic decantation and repeatedly washed with distilled water. However, to increase the thickness of the Cu layer deposited, the NPs obtained from the first reaction were dispersed under mechanical stirring and Ar stream in 10 mL distilled water containing 106 mg of ascorbic acid. To this mixture were added drop by drop 5 mL of an aqueous solution of 30 mg of $Cu(NO_3)_2$. The ascorbic acid reduces Cu^{2+} to Cu^0 that crystallizes on the surface of the nanoparticles and ensures a complete and robust coating [254]. The mixture is left to react at a temperature of 50°C for one hour. The product obtained separated by magnetic decantation, was purified with 3-5 cycles of suspension in distilled water and magnetic decanting.

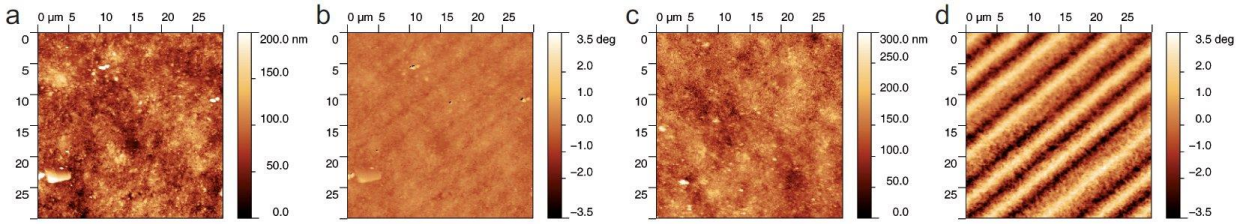

Figure 34 - Topography (a) and MFM image (b) of a standard floppy disks acquired with a not magnetized tip and topography (c) and MFM image (d) of the same sample acquired with a magnetized probe.

The weight ratio between iron and copper of the sample (Fe:Cu = 1:0.65) was obtained by ICP measurements. Actually, this is an average ratio between the whole amounts of iron and copper. Really, we do not have detailed information about the thickness of the Cu coating, which nevertheless is likely to be no thicker than a few nanometers, and we do not known if the thickness is dependent on the radius of the NPs. Unless c_s is directly proportional to d, the Fe:Cu ratio is dependent on the NP radius. Indeed, if we supposed c_s constant and independent from the NP diameter, the Fe:Cu ratio would linearly increase with the radius. Nevertheless, it should also be noted that bigger features observed in MFM images are actually agglomerates of smaller NPs, which would reduce the dependence of the Fe:Cu ratio on the actual size of the agglomerate. As for the effect of the nonmagnetic coating, VSM measurements confirmed that it is not responsible for any magnetic damping. Obviously, the presence of the coating increases the tip-sample distance reducing the magnetic field experienced by the MFM probe.

In addition, commercial Fe_3O_4 NPs with nominal average diameter of 20 nm (Sigma-Aldrich) were used. In order to perform MFM analysis, the NPs were deposited on clean Si substrates.

Instrumentation. MFM measurements were performed in air and at room conditions using two standard AFM setups (Solver, NT-MDT, Russia and Icon, Bruker Inc.) equipped with magnetic tips (MESP, Bruker Inc.) magnetized along the vertical axis *z* through a permanent magnet with stray field of about 220 mT. The effectiveness of the tip magnetization process was checked using a floppy disk reference sample. The same permanent magnet was mounted under the sample when performing in-field measurements. To calculate the magnetic phase shift and its uncertainty for each NP, a statistics was performed on data from a small area of the MFM image in correspondence of the top of the NP and on data corresponding to the substrate. The average MFM phase shift was calculated subtracting these two averaged values and the two uncertainties were used to calculate the uncertainty in the phase shift. In particular, the relative uncertainty is comprised between 5% and 10%.

5.4 - RESULTS AND DISCUSSION

5.4.1 - Effect of nonmagnetic coatings of nanoparticles

As an example to highlight the effect of long-range electrostatic forces in MFM, we report the analysis of super-paramagnetic Fe NPs with and without a Cu coating. Figure 31 shows an example of the topography and the MFM images of Fe NPs collected at different lift heights Δz. At small lift height ($\Delta z < 60$ nm), negative values of the phase contrast $\Delta\varphi$ were detected in correspondence of the NPs. This indicates a more intense attractive interaction of the tip with the NP than with the substrate, which is coherent with the magnetization of the NP induced by the magnetic stray field of the probe. The reduction of the contrast as Δz increases is (at least partially) due to the decay of the magnetic force with the distance but also to the fact that the magnetic stray field of the probe is not intense enough to induce a stable magnetization of the NPs. At larger lift height ($\Delta z > 60$ nm) a positive contrast is observed, reported also by other authors [157], which indicates that the tip is less attracted by the NP than from the substrate. This result cannot be explained taking into account only magnetic forces and also electrostatic tip-sample interactions must be invoked.

Thus, MFM images are affected also by differences in the electric properties of the NPs and the substrate. This is confirmed by the analysis of Cu-coated NPs shown in Fig. 32. These NPs exhibited a significant negative phase contrast in correspondence of all the tested lift-heights, indicating an attractive tip-sample interaction, which is coherent with

the expected orientation of the nanoparticles moments along the same direction of the tip magnetization.

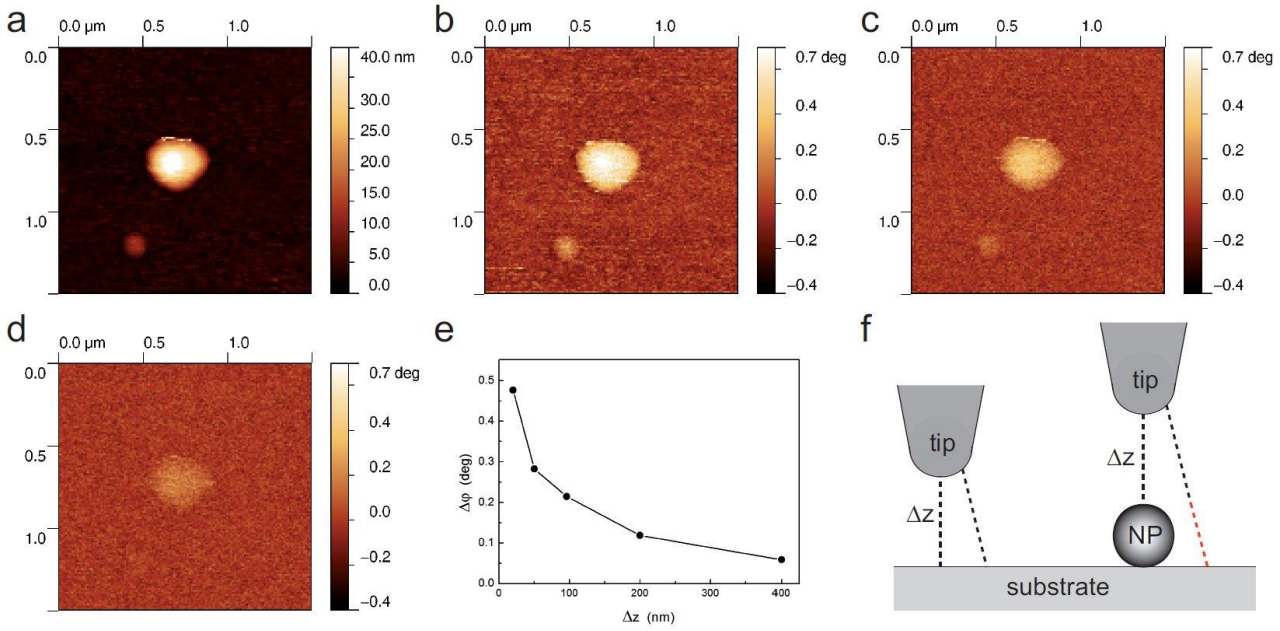

Figure 35 - Topography (a) and phase MFM images of an agglomerate of Fe3O4 NP with diameter *d* = 41 nm detected with a not magnetized probe at lift height Δ*z* 20 nm (b), 50 nm (c), 200 nm (d); (e) MFM phase contrast Δφ between the NP and the substrate as a function of Δ*z*; (f) sketch of the proposed mechanism leading to topography-induced artifacts: the additional distance is depicted in red.

The different signs in the contrast detected at high lift heights of NPs with the same magnetic properties indicate different long-range electrostatic tip-sample interactions which are attributable to the presence of the Cu coating. A second incongruence between experimental data and the model in Eq. (60) can be observed considering the dependence between $\Delta\varphi$ and d at fixed Δz, such as those reported in Fig. 33. These curves exhibit an almost linear trend, incompatible with Eq. (60), already reported but not rationalized yet [161], [209]. A possible explication could be the presence of significant electro-static interactions between the probe and the sample, which could produce an additional contrast in correspondence of the magnetic NPs.

5.4.2 - Tip-sample interactions

In order to better understand all the phenomena involved in the MFM contrast formation, we performed an analysis focused on the effects of the electrostatic forces and the application of an external magnetic field in MFM images. For this kind of analysis, commercial superparamagnetic Fe_3O_4 NPs were used.

5.4.2.1 - Nonmagnetic interactions.

To detect only electrostatic tip-sample interactions, we used a new MFM tip not previously magnetized. The magnetization state of the tip has been previously verified performing MFM measurements on a reference sample, consisting in a standard floppy disk [123]. The comparison between the obtained MFM images with those obtained using a magnetized probe (Fig. 34) confirms the negligible magnetization of the tip, which is thus only minimally sensitive to magnetic domains of the sample.

The not magnetized probe was used to acquire MFM images of (agglomerates of) magnetic NPs at different Δz (Fig. 35). The NPs exhibit positive contrast in respect to the substrate, which decreases as Δz increases (Fig. 35e). In general, the electrostatic contribution in MFM images of magnetic nanoparticles is thought to originate only from the different contact potential of the nanoparticles and the substrate, which involves different electrostatic interactions experienced by the tip [157]. Really, in our experience, in the absence of magnetic interactions (nonmagnetic samples and/or not magnetized tip) we commonly observe a positive (negative) contrast in correspondence of relieves (depressions) of the surface in different typologies of samples, e.g., in NPs, calibration gratings, vesicles, and cells [161], [255]. This suggests the presence of topography-induced artifacts in the MFM images. Indeed, a capacitive coupling exists between the tip and the sample which, to fix ideas, can be described as a plain capacitor $C_{ts} = \varepsilon_0 A_{eff}/z$, where ε_0 is the vacuum permittivity and A_{eff} is the effective area of the plates [116].

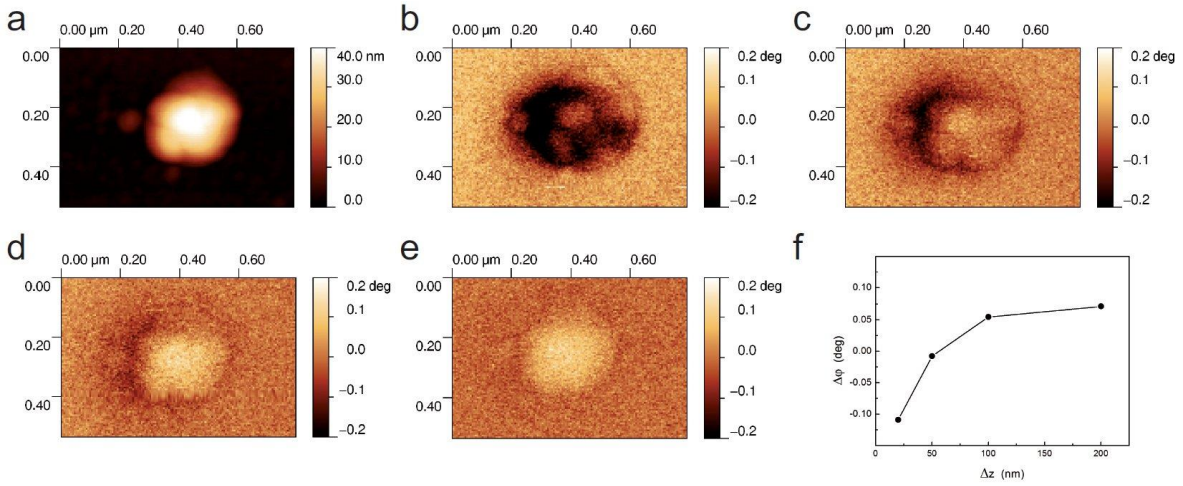

Figure 36 - Topography (a) and phase images of an agglomerate of Fe3O4 NP (*d* = 41 nm) detected with a standard magnetized probe at different Δz: 20 nm (b), 50 nm (c), 100 nm (d), 200 nm (e); (f) MFM phase contrast Δφ between the NP and the substrate as a function of Δz.

Thus, in the absence of electrostatic charges on the surface, the tip is attracted by the sample through a force $Fel = -1/2C_{ts}V_{ts}^2 = 1/2\varepsilon_0 V_{ts}^2 A_{eff}/z^2$ and thus $\Delta\varphi = -Q_c/k_c \partial F_{el}/\partial z = -\varepsilon_0 Q_c/k_c V_{ts}^2 A_{eff}/z^3$. In lift mode, the tip is at Δz from the point of the surface in correspondence of the tip vertical. When the tip is on a relief, all the other points of the surface are at a distance from the tip larger than when the tip is on the vertical of a point of the substrate. This extra distance is represented in red in the sketch in Fig. 36f. Thus, the effective tip-sample distance is larger when the tip is on a relief (like a NP) than when it is on the substrate. Therefore, the negative phase shift resulting from the capacitive coupling is larger on the substrate than in correspondence of the relief, leading to the positive contrast between the latter (e.g., a NP) and the substrate.

It is not surprising that this effect is visible not only on the features with size comparable with that of the tip but even on the much bigger ones. Indeed, it has been shown that not only the tip apex, but also the tip cone and the cantilever contributes to C_{ts} [210].

5.4.2.2 - Magnetic interactions.

After proper magnetization of the tip, the same Fe_3O_4 NPs were characterized. Figure 36 shows the characterization of one agglomerate of such NPs with diameter d = 41 nm. The result is analogous to the one obtained on Fe NPs (Fig. 31). The NP exhibits a negative phase contrast, indicative of an attractive tip-sample interaction, in correspondence of small tip-sample distances (Δz < 50 nm). Increasing the lift height the negative phase contrast decreases, becomes zero (Δz =50 nm) and then positive in

correspondence of high values of tip-sample separation (Δz > 50 nm). Taking into account the results obtained with the not magnetized tip on a NP with the same diameter (Fig. 35), we can now explain this trend as follows. In correspondence of low tip-NP distances a magnetic interaction occurs, which is due to the magnetization of the NP by the magnetic stray field of the probe. The NP is thus magnetized along the same direction of the tip magnetization, producing an attractive magnetic tip-sample force, which prevails over the repulsive electrostatic interactions, and, thus, produces a negative phase shift in MFM images.

Increasing the tip-sample distance, the intensity of the magnetic interactions decreases until becoming lower than the corresponding electrostatic tip-NP forces and, then, producing the inversion of the phase contrast. This could be due to the faster decay of the magnetic forces (z^4) in respect to the electrostatic ones (z^2) [256] as well as to the dependence of the NP magnetization on the distance from the tip, being it magnetized by the probe magnetic stray field. Comparing the values of $\Delta\varphi$ of NPs with similar size detected with the not-magnetized and the magnetized probe (Table 2), we observe that even when a magnetic signal can be detected by MFM the electrostatic contribution cannot be neglected to obtain an accurate quantitative data analysis.

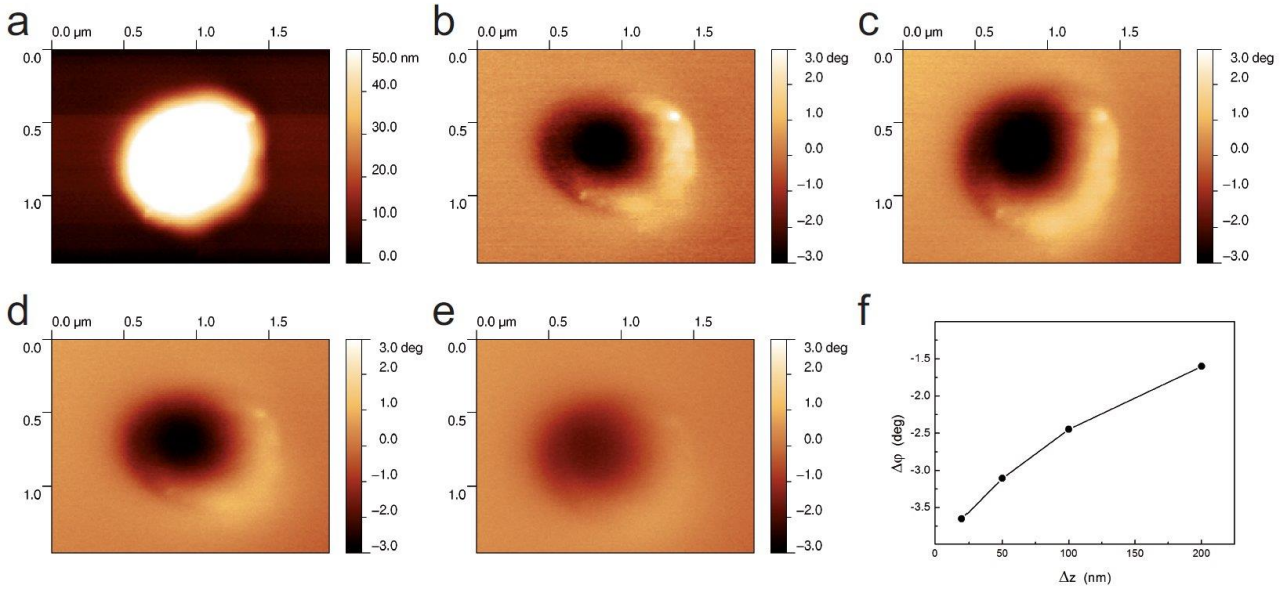

Figure 37 - Topography (a) and phase images of an agglomerate of Fe3O4 NPs (d = 85 nm) detected with a standard magnetized probe applying an external magnetic field at different Δz: 20 nm (b), 50 nm (c), 100 nm (d), 200 nm (e); (f) MFM phase contrast $\Delta\varphi$ between a NP and the substrate as a function of Δz.

Table 2 - Values of the phase shift detected in correspondence of NPs with similar diameter with the not magnetized probe ($\Delta\varphi_{el}$) and with the magnetized probe ($\Delta\varphi_{el}+\Delta\varphi_{mag}$) with and without the application of an external magnetic field

Δz (nm)	$\Delta\varphi_{el}$ (deg) (d_{NP}=41,28nm)	Out of field $\Delta\varphi_{el}+\Delta\varphi_{mag}$ (d_{NP}=41,16nm)	In field $\Delta\varphi_{el}+\Delta\varphi_{mag}$ (d_{NP}=41,16nm)
20	0,4768	-0,109	-1,0248
50	0,2828	-0,078	-0,6715

5.4.3 - Effects of an external magnetic field.

A further analysis has been carried out on the Fe_3O_4 NPs, applying an external magnetic field during the MFM measurements, in order to induce the saturation magnetization of the NPs independently from the probe magnetic stray field and, thus, from the tip-sample distance (Fig. 37). A negative phase contrast was detected even at large Δz. Also, comparing the values of the phase shift obtained with and without the external magnetic field on NPs agglomerate with similar diameter (Table 1), even at small Δz the in-field phase contrast results to be significantly higher than the phase contrast detected without applying any external magnetic field. This can be ascribed to a higher NP magnetization obtained by the application of the external magnetic field, demonstrating that the analyzed Fe_3O_4 nanoparticles were not saturated by the only magnetic stray field of the probe. Conversely, in presence of an external magnetic field, a contrast in MFM images is detected which is far bigger than that measured in out-of-field experiments, e.g., up to 10 times in measurements at small Δz. Comparing the in-field phase contrast to the electrostatic one, the electrostatic contribution results to be significant also when a high NP magnetization is achieved, suggesting that, also in this case, the evaluation of non-magnetic contribution in MFM images is needed to carry out quantitative analysis.

5.5 - CONCLUSIONS

In this work we reported the experimental MFM data acquired on different magnetic NPs in different experimental conditions (magnetized or not magnetized tip, in-field and out-of-field measurements). The results on the same superparmagnetic Fe NPs with and without a Cu coating highlighted the significant effect of tip-sample nonmagnetic interactions are likely to be responsible for a certain incompatibility between experimental MFM data and the simple theoretical model in which the tip and the NP are described as two magnetic dipoles. When characterizing small agglomerates (41 nm

in diameter) of commercial Fe_3O_4 NPs with not magnetized tips, we observed an apparently repulsive interaction between the tip and NP. Although this effect may result from the differences in the electric properties of the NPs and the Si substrate, on the basis of our other previous results on different kind of samples (magnetic and nonmagnetic NPs, calibration gratings, vesicles, and cells) we proposed a mechanism of topography-induced artifacts in the MFM images produced by the tip-sample capacitive coupling. Indeed, at fixed lift height, relieves on the surface correspond to larger tip-sample effective separation, leading to positive MFM contrasts in correspondence of the relieves with respect to the flat substrate. Conversely, a negative contrast is observed in correspondence of depression of the surface due to the reduced tip-sample effective separation. The comparison between the MFM contrast obtained on similar NPs in out-of-field and in-field measurements revealed that even small agglomerates of superparamagnetic NPs were not saturated by the sole magnetic stray field of the probe. Conversely, the presence of an external magnetic field which saturates the NPs magnetization allows one to detect far more intense magnetic signals, up to 10 times that obtained in out-of-field measurements at small lift height. The comparison of the pure electrostatic signal and the 'standard MFM signal' obtained in out-of-field and in-field MFM measurements revealed that the electrostatic tip-sample interactions produce a significant contribution, which, therefore must be taken into account in the quantitative interpretation of MFM data. Furthermore, when the NPs do not have a high and stable magnetic moment, which can occur when MFM measurements are carried out without applying an external magnetic field and at high lift height, electrostatic interactions can be prevalent on the magnetic ones. In this case, the necessity of removing electrostatic contributions in MFM images results to be essential not only for the quantitative data analysis but also for the simple verification of the nanoparticles magnetic character. Therefore, the development of experimental procedures and/or theoretical models able to eliminate and/or estimate these nonmagnetic contributions appears to be necessary in order to use MFM technique as a tool for the accurate quantitative magnetic characterization of materials at the nanoscale.

6. REMOVAL OF ELECTROSTATIC ARTIFACTS IN MAGNETIC FORCE MICROSCOPY BY CONTROLLED MAGNETIZATION OF THE TIP: APPLICATION TO SUPERPARAMAGNETIC NANOPARTICLES

Livia Angeloni[1,2], Daniele Passeri*[1], Melania Reggente[1], Diego Mantovani[2], and Marco Rossi[1,3]

[1]*Department of Basic and Applied Sciences for Engineering, SAPIENZA University of Rome, Via A. Scarpa 16, 00161 Rome, Italy*

[2]*Lab. for Biomaterials and Bioengineering (CRC-I), Dept. Min-Met-Materials Eng. & University Hospital Research Center, Laval University, Quebec City, Canada*

[3]*Research Center for Nanotechnology applied to Engineering of SAPIENZA University of Rome (CNIS), Piazzale A. Moro 5, 00185 Rome, Italy*

**Corresponding author: daniele.passeri@uniroma1.it*

Published in:
Scientific Reports
Received: 22 September 2015.
Accepted: 29 April 2016.
Published: 19 May 2016
DOI: 10.1038/srep26293

http://www.nature.com/articles/srep26293

Resumé

La microscopie à force magnétique (MFM) a été démontrée etre une technique utile pour la caractérisation des nanomatériaux magnétiques. Pour être analysés par les techniques MFM, les nanomatériaux sont généralement déposés sur des substrats plats, ce qui produce un contraste supplémentaire dans les images MFM en raison de l'inévitable hétérogèneité des interactions électrostatiques, qui ne peuvent pas être facilement distinguées de l'interaction magnétique.

Afin d'interpréter correctement les données MFM, une méthode pour supprimer les contributions électrostatiques des images MFM est nécessaire. Dans ce travail, nous proposons une nouvelle technique MFM, appelée MFM à magnetisation contrôlée (CM-MFM), basée sur le contrôle in situ de l'état de magnétisation de la sonde, qui permet d'évaluer et d'éliminer la contribution électrostatique dans les images MFM. L'efficacité de la technique à été démontrée par une étude de cas difficile, c'est-à-dire l'analyse de nanoparticules superparamagnétiques en absence d'un champ magnétique externe appliqué. Notre technique CM-MFM nous a permis d'acquérir des images magnétiques dépourvues des contributions électrostatiques, ce qui a révélé que le champ magnétique généré par la pointe est suffisant pour orienter complètement les nanoparticules superparamagnétiques et que l'interaction entre la pointe et l'echantillon magnétique peut être décrite par des modèles simples une fois que le les artefacts électrostatiques sont enlevés.

Abstract

Magnetic force microscopy (MFM) has been demonstrated as a valuable technique for the characterization of magnetic nanomaterials. To be analyzed by MFM techniques, nanomaterials are generally deposited on flat substrates, resulting in an additional contrast in MFM images due to unavoidable heterogeneous electrostatic tip-sample interactions, which cannot be easily distinguished from the magnetic one. In order to correctly interpret MFM data, a method to remove the electrostatic contributions from MFM images is needed. In this work, we propose a new MFM technique, called controlled magnetization MFM (CM-MFM), based on the in situ control of the probe magnetization state, which allows the evaluation and the elimination of electrostatic contribution in MFM images. The effectiveness of the technique is demonstrated through a challenging case study, i.e., the analysis of superparamagnetic nanoparticles in the absence of applied external magnetic field. Our CM-MFM technique allowed us to acquire magnetic images depurated of the electrostatic contributions, which revealed that the magnetic field generated by the tip is sufficient to completely orient the superparamagnetic nanoparticles and that the magnetic tip-sample interaction is describable through simple models once the electrostatic artifacts are removed.

6.1 - INTRODUCTION

The increasing interest in the study and the development of magnetic nanomaterials for different technological applications [245], [257], [258] has highlighted the need of new tools and procedures for the characterization of magnetic properties at the nanometer scale. Conventional techniques, such as superconducting quantum interference devices (SQUID) magnetometry [251] or vibrating sample magnetometry (VSM) [253], are widely used for the characterization of magnetic nanomaterials, but the magnetic characterization of single nanomaterials can be achieved only through the use of techniques which combine the capability of positioning and imaging at the nanometer scale with the probing of ultra-low magnetic fields. Accurate mapping of ultra-low magnetic field distribution has been demonstrated through the use of scanning magnetometry with Nitrogen-vacancy (N-V) color centers in diamond [259]–[262], which however requires a quite complex experimental setup. Therefore, despite the growing interest in these methods, the use of techniques based on simpler setups is still more widespread. Among them, magnetic force microscopy (MFM) is considered a promising technique thanks to its lateral resolution comparable to transmission techniques (10–20 nm), its applicability to all kinds of nanomaterials without any particular sample preparation, both in air and in liquid, its high magnetic sensitivity and its capability to map the magnetic evolution of a sample with respect to an applied field [263]–[266]. Nevertheless, despite the wide employment of MFM technique for the qualitative characterization of magnetic nanomaterials, only a few studies have been performed using MFM for the measurements of their magnetic properties [149], [156], [204], [267], [268]. The difficulty of obtaining reliable results is ascribable to a certain inconsistency between the experimental data and the theoretical models describing the magnetic tip-sample interactions. This incongruence has been mainly attributed to the not satisfactory description of the probe, generally assumed as a single magnetic point dipole [159], [269], and several attempts have been made to find more accurate mathematical approaches [158]. Such proposed models generally take into account only the magnetic tip-sample interactions, but different authors [216], [270] recently demonstrated that the signal detected by MFM contains also a significant contribution due to long-range electrostatic phenomena, which include the effect of fixed electric charges on the sample as well as of topography-modulated tip-sample capacitive coupling. Therefore, it should be more realistically described as the sum of a magnetic and an electrostatic contribution. Consequently, the evaluation of the effects of

electrostatic forces appears essential to obtain accurate magnetic measurements by MFM. Only a few studies have been carried out with the aim of distinguishing or eliminating the electrostatic signal in MFM images and a few methodologies have been proposed. For example, in the case of homogenous samples, the electrostatic contribution can be eliminated by compensating the tip-sample contact potential difference by the application of an appropriate bias voltage [215]. Nevertheless, if the analyzed sample is heterogeneous as in the case of magnetic nanomaterials deposited on flat substrates, the contact potential difference depends on the actual position of the probe on the sample surface and the electrostatic contribution cannot be removed by the application of a single, fixed, bias voltage value. In order to evaluate and eliminate the electrostatic contribution also in the case of heterogeneous samples, Jafaar et al [216] proposed the combined use of the Kelvin probe force microscopy (KPFM) and MFM techniques, the former allowing the measurement of the contact potential difference in each point of the scanned area and its compensation by opportunely adjusting the applied bias voltage during the scan. In switching magnetization MFM (SM-MFM), proposed by Cambel et al [217], [218], the analyzed surface is scanned twice in tapping mode, with opposite tip magnetization orientations, obtained by applying an opportune magnetic field before each scan. If the magnetization state of the sample is not affected by the external field applied to invert the probe magnetic moment and by the magnetic field induced by the tip during the measurements, reversing the probe magnetization results in the inversion of the detected magnetic contrast while the atomic and electrostatic contributions remain unchanged. Thus, adding the traces obtained with opposite tip moments the magnetic signal is annulled and only the contrast due to the atomic and electrostatic tip-sample interactions is visible. On the contrary, subtracting the same two traces the electrostatic signal is nullified and only the magnetic tip-sample interactions give rise to the contrast in the image. Differential MFM is an analogous method recently proposed by Wang et al [271], in which the two MFM images with reversed polarization are acquired subsequently to the topography with the tip maintained at a fixed distance (lift height) from the surface (lift mode). The applicability of these techniques for the evaluation of the electrostatic and magnetic signal is limited to hard ferromagnetic materials, having significant remanent magnetic moment and coercivity sufficiently high to ensure a constant magnetization of the sample even after the application of the external magnetic field necessary to invert the probe magnetization and under the magnetic stray field induced by the tip during the scan.

Due to this limitation, SM-MFM and differential MFM are not applicable to the most of magnetic nanomaterials, which exhibit magnetic characteristics near to the superparamagnetic limit (i.e., having low or zero coercivity).

In this work, we propose a new MFM technique, which we refer to controlled magnetization MFM (CM-MFM), which allows the evaluation and the elimination of electrostatic contribution in MFM images by controlling the tip magnetization state. The effectiveness of the technique is verified through its application to the investigation of superparamagnetic nanoparticles (NPs) in the absence of external field, which represents one of the most challenging targets of MFM. Magnetic images were acquired and rationalized describing both the tip and the NP as magnetic dipoles, demonstrating the suitability of this simple model when MFM data are depurated of the electrostatic contributions.

6.2 - MAGNETIC FORCE MICROSCOPY

Magnetic force microscopy (MFM) is a particular scanning probe microscopy (SPM) technique, which allows one to detect tip-sample magnetostatic interaction forces and to image them on the sample surface. This is obtained using an atomic force microscopy (AFM) setup equipped with a magnetic tip, generally consisting in a standard AFM Si probe coated with a magnetic layer with thickness of a few tens of nanometers. The cantilever is set into oscillation at a frequency f close to its first free resonance frequency f_0. When the probe is brought sufficiently close to the sample surface, the gradient along the z axis of the tip-sample force F produces a variation in the dynamic behavior of the cantilever, which can be described as a change in the phase shift:

$$\Delta\varphi = -\frac{Q_c}{k_c}\frac{\partial F_z}{\partial z} \qquad 61)$$

where Q_c and k_c are the cantilever quality factor and spring constant in air and with the tip not interacting with the sample, respectively, and $\partial F_z/\partial z$ is the gradient along the vertical axis z of the vertical component of the (magnetostatic) tip-sample interaction force (F_z) [116]. The actual expression of F_z depends on both the geometry and the magnetic domains configuration of both the tip and the sample. For example, on the basis of experimental data the former has been modeled using either a single point magnetic dipole, a cone with uniformly magnetized magnetic surface, or more exotic magnetic structures [155], [158], [161]. Also, different analytical expression for F_z are obtained in case the sample is a single magnetic dipole or a more complex structure

with periodic magnetic domains [122], [123], [155]. In particular, let us suppose that the sample is represented by a single small magnetic NP with diameter d uniformly magnetized with magnetization M_s, possibly coated with a nonmagnetic layer with thickness cs, which we describe as a single point magnetic dipole with magnetic moment $m_s = 1/6\pi M_s d^3$. If the tip can be modeled by a punctiform magnetic dipole with moment m_{tip}, the magnetic phase shift $\Delta\varphi$ observed when the tip is placed on the top of the NP, i.e., the symmetry axes of the tip and the NP coincide, can be described using a one dimensional analytical model which is justified by the symmetry of the problem. In this case, $\Delta\varphi$ is given by

$$\Delta\varphi = \mu_0 m_{tip} M_s \frac{Q_c}{k_c} \frac{d^3}{(\Delta z + c_s + \frac{d}{2} + A_{sp} + \delta_{tip})^5} \qquad 62)$$

where μ_0 is the permeability of free space, Δz is the lift height (the vertical distance between the tip apex and sample surface, i.e., the top of the NP), A_{sp} is the set-point amplitude during the first pass in tapping mode, and δ_{tip} is the position of the equivalent moment m_{tip} evaluated from the tip apex [155], [224]. MFM images are generally acquired in the so-called 'lift height mode'. In this two-pass modality, each line is scanned twice and two different images of the selected sample area are recorded. The first scan is performed in standard tapping mode to acquire and record the topography, while the second scan is performed in non-contact mode, in order to detect only long-range interaction forces (e.g., magnetic and electric forces) and obtain a magnetic map of the sample. During this second scan, the probe follows the trajectory of the previously recorded sample profile at a selected distance Δz (the lift height), which is maintained constant at each point (x, y) of the scanned area, in order to eliminate any possible artifact in the magnetic signal due to the variation in the long-range the tip-sample interaction forces produced by the modulation of the actual tip-sample distance.

6.3 - CONTROLLED MAGNETIZATION MFM

The experimental setup to perform controlled magnetization MFM (CM-MFM) consists in a standard MFM apparatus equipped with an electromagnet placed under the sample, which allows one to apply controllable out-of-plane static magnetic fields H in the range $-480\ Oe < H < +480\ Oe$ to the tip-sample system, without moving the probe from the scan area. Similar systems have been already applied to vary the magnetization state of the sample in order to study its magnetic evolution in response to magnetic fields [188]–

[191], [193]. Conversely, here the system is used to in situ control the magnetization state of the probe. The measurement procedure consists in two different phases: (i) the calibration of the remanent magnetic behavior of the MFM tip and (ii) the measurement of the 'only magnetic' MFM contrast by recording and opportunely post-processing two MFM images of the same sample area, acquired with two different magnetization states of the probe.

6.3.1 - Step I: Probe calibration

The calibration phase consists in the individuation of the characteristic parameters of the remanent hysteresis loop of the probe. This hysteresis curve is the plot, as a function of the value of magnetic field applied and then switched off, of the remanence corresponding to the in-field minor hysteresis loop where the maximum magnetization corresponds to the actual value of the magnetic field applied and then switched off [272]–[274]. The parameters to be determined to calibrate the tip are the remanent saturation magnetic field $H_{rs,tip}$ and the remanent coercivity $H_{rc,tip}$. Different calibration methods have already been developed for the characterization of the in-field magnetic characteristics of the MFM probes [221], [225], [228]. Here, we propose a simple method to measure the remanent hysteresis loop of the MFM probe. The procedure consists in the measurement of the MFM contrast detected on a high coercivity reference sample after the application and the subsequent switching-off of out-of-plane magnetic fields with different intensities. We use a commercial floppy disk as a reference sample. The out-of-plane coercivity of this kind of samples, significantly higher than the probe coercivity, allows us to ascribe the changes in the MFM contrast exclusively to the variation of the magnetization state of the sensor. At the same time, the well defined magnetic structure, consisting in a periodic pattern of in-plane domains alternatively oriented in opposite direction, allows us to easily measure the variations of the phase contrast in response to the changes in the magnetization state of the tip.

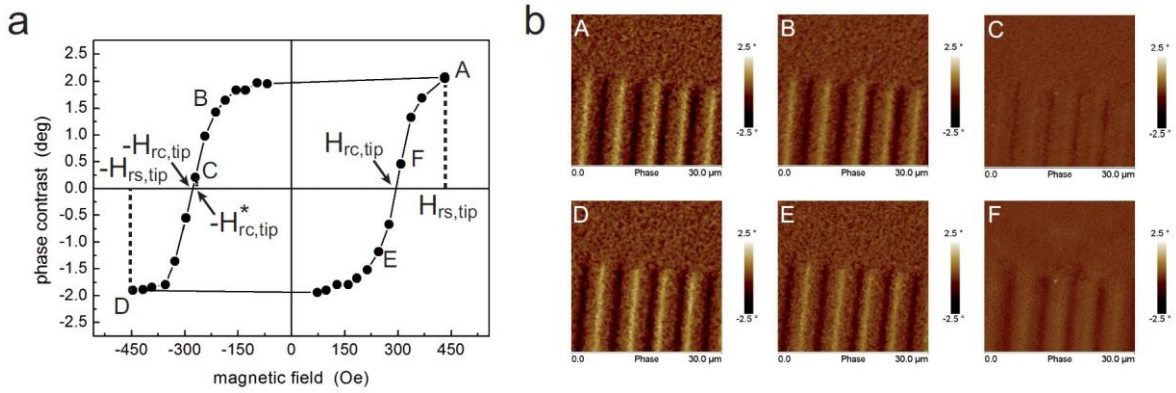

Figure 38 - Experimental characterization of the remanent magnetic properties of a standard MFM tip. (a) Hysteresis curve of the MFM phase contrast ($\Delta\varphi_{cont}$) as a function of the magnetic field *H* applied and subsequently switched off. (b) Examples of MFM images of the periodic magnetic domains of a standard floppy disk, from which the phase difference between two adjacent transition regions was measured in order to determine the points of the hysteresis curve. Points from A to F in panel (a) are obtained from images from A to F in panel (b).

When the tip magnetization is directed perpendicularly to the sample surface, the MFM contrast is maximum in correspondence of the domains transitions (positive or negative depending on the mutual direction of the involved tip and sample magnetic domains), where the magnetic field generated by the floppy has only vertical component [123]. Conversely, the MFM contrast is zero in correspondence of the internal domains regions, where the magnetic field generated by the floppy has only horizontal component [123]. Therefore, the (out-of-plane) remanent hysteresis loop of the probe can be obtained by plotting the MFM phase difference $\Delta\varphi^{cont}$ between two adjacent transition regions (i.e., the image contrast) as a function of the previously applied (and eventually switched-off) external magnetic field *H*. $\Delta\varphi^{cont}(H)$ is a function of the remanent magnetization of the tip and the sample ($M_{r,tip}$ and $M_{r,sample}$, respectively). $M_{r,tip}$ depends on the applied magnetic field *H*. Conversely, if a sample with high out-of-plane coercivity like the floppy disk is used, $M_{r,sample}$ is independent of *H*. Thus, the normalized remanent hysteresis curve of the MFM probe can be obtained

$$\frac{M_{r,tip}(H)}{M_{rs,tip}} = \frac{\Delta\varphi^{cont}(H)}{\Delta\varphi_s^{cont}} \qquad 63)$$

where $\Delta\varphi_s^{cont}$ is the MFM phase difference between two adjacent transition regions detected when the remanent magnetization of the tip reaches its saturation value ($M_{rs,tip}$). A typical remanent hysteresis loop of a standard MFM tip (MESP, Bruker Inc.) measured with this method is reported in Fig. 38a. Experiments were performed using a standard AFM apparatus (Icon, Bruker Inc.) provided with standard MFM imaging

technique and equipped with an in-house made CM-MFM setup. The latter is an electromagnet constituted by a coil (with inner diameter 1 cm, outer diameter 2.7 cm, and height 1.6 cm) supplied with direct electric current through a dc power supply and placed under the sample holder. The control of the power supply is external to and independent of the AFM electronics. Therefore, our technique can be implemented on every AFM apparatus, providing that enough room is available for the coil. At the beginning of the experiment, a magnetic field $H = 480\ Oe$ was applied. Switching off the magnetic field results in a partial demagnetization of the tip, which reaches a near-saturation state corresponding to its maximum remanent magnetization, i.e., its remanent saturation. An image of the magnetic domains of the floppy was acquired (image A in Fig. 38b, from which the value of $\Delta\varphi^{cont}$ marked with A in Fig. 38a is determined). Then, several MFM images were recorded after the application and the switching off of magnetic fields in the opposite direction with increasing intensities (e.g., images B and C in Fig. 38b corresponding to the point B and C in Fig. 38a) down to a magnetic field $H = -480\ Oe$ at which the saturation of $\Delta\varphi^{cont}$ in the opposite direction is observed (image D in Fig. 38b and point D in Fig. 38a). Then, positive values of H are applied to complete the hysteresis curve (e.g., images and points E and F). From the curve reported in Fig. 38a, it is possible to individuate both the saturation magnetic field $H_{rs,tip}$ necessary to obtain the saturation remanent magnetization of the probe, corresponding to its maximum magnetic sensitivity, and the coercive magnetic field $H_{rc,tip}$ necessary to annul the remanent magnetization of the probe [275].

6.3.2 - Step II: Determination of the magnetic signal

Once the remanent properties of the probe have been determined, the magnetic moment of the tip can be in situ controlled through the application and the subsequent switching off of appropriate magnetic fields. In particular, $+H_{rs,tip}$ must be applied to magnetize the tip, while $-H_{rc,tip}$ or $-H_{rs,tip}$ must be applied to annul or invert the tip magnetization, respectively.

In the CM-MFM procedure, a first scan of the area is performed at fixed Δz with the tip magnetized in its saturation state (having applied and then switched off a magnetic field $+H_{rs,tip}$) and a 'standard MFM image' is acquired. As previously discussed, such an image is affected by both magnetic and electrostatic tip-sample interactions. Indeed, the 'standard MFM signal' obtained with the magnetized tip ($\Delta\varphi_{MagnTip}$) is actually the

superimposition of both the 'true' magnetic signal ($\Delta\varphi_{mag}$) and the electrostatic signal ($\Delta\varphi_{el}$), i.e.,

$$\Delta\varphi_{MagnTip} = \Delta\varphi_{el} + \Delta\varphi_{mag} \qquad 64)$$

which is schematically represented in Fig. 39a. After the first scan, a magnetic field with intensity $-H_{rc,tip}$ is applied and switched off. A second image is acquired with the same instrumental parameters and the same lift height Δz, but with the probe having zero magnetization (Fig. 39c). In this case, the signal detected with the demagnetized tip $\Delta\varphi_{DemagnTip}$ is represented by the only electrostatic contribution, i.e.,

$$\Delta\varphi_{DemagnTip} = \Delta\varphi_{el} \qquad 65)$$

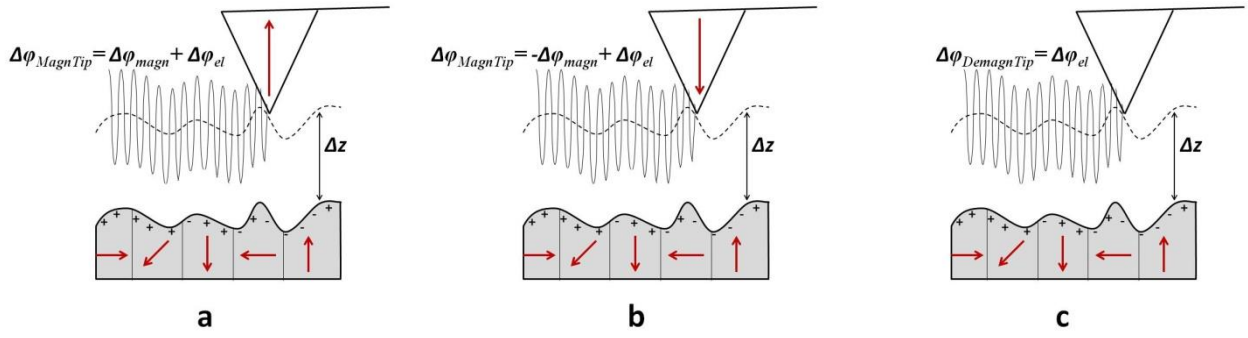

Figure 39 - Sketch of the tip-sample interactions in CM-MFM. The sample is assumed constituted by magnetic domains with different orientation (red arrows) and by distributed electric charges which are responsible for a tip-sample electrostatic interaction not uniform on the surface. The three configurations of the tip are characterized by different magnetization of the tip: (a) tip with saturated "up" magnetization; (b) tip with saturated "down" magnetization; (c) demagnetized tip.

Therefore, the magnetic contribution, which in the following we refer to as the CM-MFM signal $\Delta\varphi_{CM\_MFM}$, can be obtained by subtracting the second image to the first one, i.e.,

$$\Delta\varphi_{CM\_MFM} = \Delta\varphi_{MagnTip} - \Delta\varphi_{DemagnTip} = (\Delta\varphi_{el} + \Delta\varphi_{magn}) - \Delta\varphi_{el} = \Delta\varphi_{magn} \qquad 66)$$

The use of this mode, which we called zero probe magnetization (ZM) mode, allows the detection of the electrostatic and magnetic tip-sample interactions independently of the magnetization state of the sample, enabling the analysis of soft ferromagnetic, paramagnetic and superparamagnetic materials, to which the SM-MFM and differential

MFM are not applicable. The same CM-MFM instrumentation can be also used to distinguish the electrostatic and magnetic signals in MFM images of relatively hard ferromagnetic samples, the stray field of which could orient the domains of the tip, thus reducing the effectiveness of the tip demagnetization procedure. Indeed, a magnetic field with intensity $-H_{rs,tip}$ can be applied and switched off after the first scan, following a procedure analogous to that used in SM-MFM [217], [218] or in differential MFM [271]. A second MFM image is recorded with the probe magnetized along the opposite direction with respect to the first one (Fig. 39b) and the electrostatic and magnetic contributions can be evaluated by adding or subtracting the two images, respectively. An example of application demonstrating the effectiveness of the method is shown in Fig. 40, in which the characterization of a standard floppy disk using CM-MFM in ZM mode is reported. The topography (Fig. 40a) shows the presence of a particle (likely dust) with height of some hundreds of nanometers. The corresponding bright contrast ($\Delta\varphi$ = +1.42 deg) in standard MFM image (Fig. 40b) would suggest a repulsive tip-sample interaction, which however can hardly find a convincing physical rationalization. The same contrast $\Delta\varphi$ = +1.42 deg is observed in the electrostatic image acquired with the demagnetized tip (Fig. 40c), compatible with the presence of an electrostatic interaction produced by the tip-sample capacitive coupling [270]. After subtraction, the magnetic image is obtained (Fig. 40d), where the magnetic domains of the floppy are correctly visualized but no contrast ($\Delta\varphi$ = 0 deg) is observed in correspondence of the particle. This result experimentally demonstrates the potential capability of our method to compensate electrostatic phase shift signal resulting from the tip-sample capacitive coupling in magnetic images.

The value of $H_{rc,tip}$ can be easily determined with enough accuracy from the curve in Fig. 38a as the intersection with the horizontal axis of the linear curve fitting of the two points immediately below and above it. From a conceptual point of view, such a value can always be applied to completely demagnetize the MFM probe. The sensitivity of the dc power source used to generate the magnetic field, however, could prevent the application of the exact value of $H_{rc,tip}$, as it is discussed in details below. It is worth explicitly discussing the range of possible samples that can be investigated using CM-MFM. As detailed above, CM-MFM in ZM mode is particularly suitable for the analysis of superparamagnetic NPs, which cannot be investigated by SM-MFM and differential MFM as the NP magnetization is reversed together with that of the tip, preventing the inversion of contrast in the two magnetic images. The technique is also

effective on relatively hard magnetic samples, like the floppy disk, the magnetic domains of which are not affected by the magnetic fields applied during the magnetization and demagnetization procedures and which generate magnetic fields not sufficient to (even partially) polarize the demagnetized tip. In particular, the latter issue was explicitly verified in the case of floppy disk. If the magnetic field it generates could orient the demagnetized tip, no alternation between dark and bright stripes in correspondence of domain transitions would be observed in the phase shift images, resulting in a pattern of only dark (attractive) stripes with halved spatial period. Apart from these experimental evidences, the weakness of the field generated by the floppy is confirmed by its rough estimation from the phase contrast values it produces and using analytical models present in literature [123]. We calculated this field to be lower than 10−2 Oe at a lift height of 100 nm and thus negligible with the respect to $H_{rc,tip}$. The magnetization of the tip by the magnetic stray field of the sample, which has never been observed with the cantilevers we used in our experiments but it is likely to occur with low-coercive tips, limits the application of our technique on magnetic materials much harder that the floppy. In principle, these materials could be analyzed selecting different tip with higher coercivity. The magnetic field generated by these materials, however, would be so intense that electrostatic artifacts would be negligible. Really, even in the case of the standard floppy disk, the topography induced electrostatic artifacts modulate the standard MFM response but they are negligible with respect to the magnetic signal, so that the latter is well described by analytical models which consider only magnetic tip-sample interactions [123]. Also, it should be observed that MFM mainly targets to nanomaterials, which are unlikely to generate such intense magnetic fields, being more realistically near to the superparamagnetic limit. Conversely, materials with magnetic properties similar to those of the tip cannot still be analyzed with our technique. Indeed, even if the magnetic field they produce cannot polarize the demagnetized tip, the demagnetization/magnetization procedure could modify the orientation of their magnetic domains. This would not represent a limit if in-field measurement are required, but prevents the possibility of investigating their ‘pristine’ magnetic state.

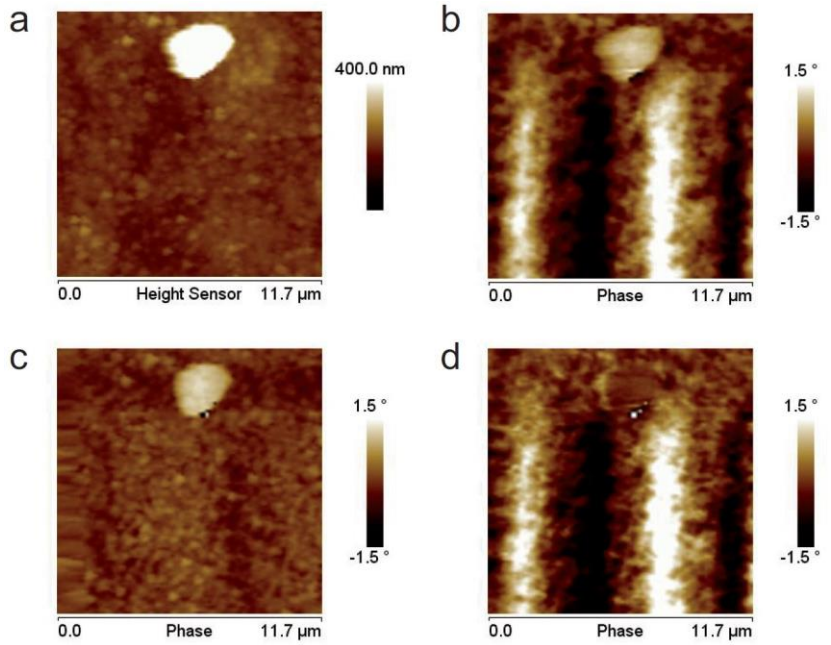

Figure 40 - CM-MFM characterization of a standard floppy disk. (a) Topography of an area where a particle (likely dust) is observable on the floppy surface and (b) corresponding standard MFM phase image acquired with the magnetized tip. (c) Phase image acquired with the demagnetized tip. (d) Magnetic phase image obtained by subtracting (c) from (b).

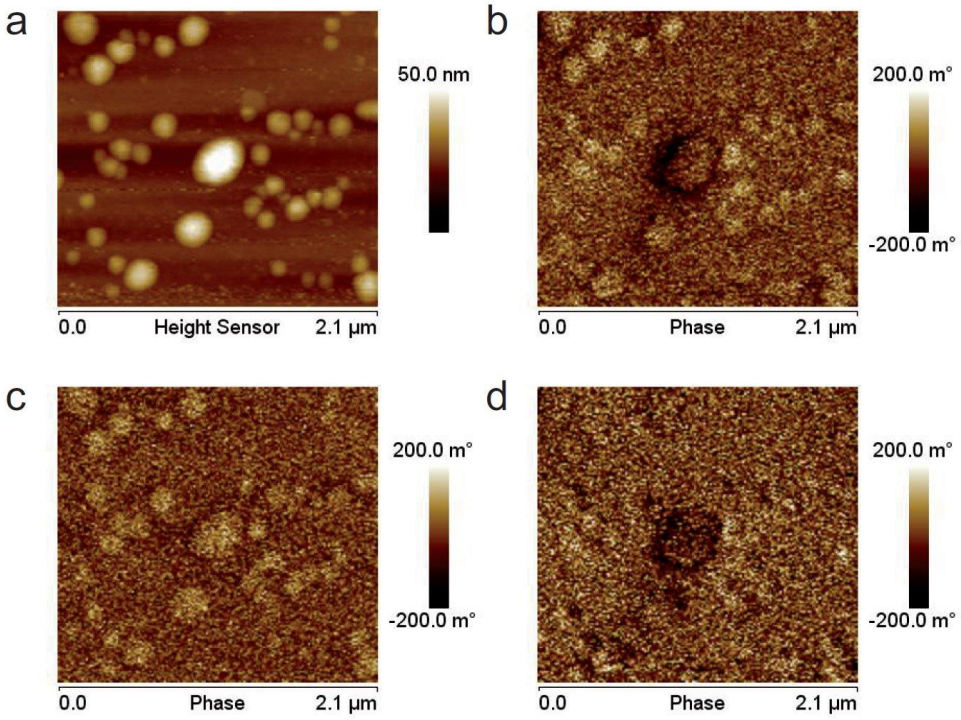

Figure 41 - CM-MFM characterization of superparamagnetic NPs. (a) Topography of an area where some NPs are visible and (b) corresponding standard MFM phase image acquired with the magnetized tip. (c) Phase image acquired with the demagnetized tip. (d) Magnetic phase image obtained by subtracting (c) from (b).

6.4 - CASE STUDY: ANALYSIS OF SUPERPARAMAGNETIC NANOPARTICLES

The effectiveness and the potentialities of the CM-MFM approach have been demonstrated through the study of superparamagnetic NPs, which probably represent the most challenging kind of sample for the sensitivity of standard MFM. Indeed, their nanometer size comparable with the MFM lateral resolution and their low magnetic moments make the magnetic tip-sample forces comparable with the corresponding electrostatic interactions [270]. Furthermore, because of their superparamagnetic character, if the MFM measurements are carried without applying any external magnetic field, the magnetization of the NPs is only due to the magnetic field induced by the probe during the scan and, thus, is always oriented along the same direction of the probe magnetization. The SM mode is thus inapplicable, while the ZM mode of CM-MFM can be used to decouple electrostatic artifacts from MFM images. The test sample was prepared depositing a colloidal solution of commercial Fe_3O_4 NPs (Sigma Aldrich) with nominal diameter of 20 nm on a clean monocrystalline Si substrate. The analysis was carried out using a MFM tip with a standard moment (MESP, Bruker Inc.). During the measurement session, both topographic and MFM images of the investigated areas were continuously acquired. Subsequent images of the same area could allow us to monitor possible gradual demagnetization of the tip as well as the occurrence of abrupt phenomena, e.g., destructive tip-sample contacts or snatching of NPs, which however have never occurred during the whole experiment.

The calibration of the tip was performed following the previously illustrated procedure, revealing a remanent saturation field $H_{rs,tip}$ = 440 Oe at which $\Delta\varphi_{cont}^{s}$ = 3,033 deg is measured. At the beginning of the experiment, the probe was magnetized through the application of a magnetic field with intensity $H_{rs,tip}$. The magnetic field was switched off and 'standard MFM' images of NPs were recorded, the sample being magnetized only through the magnetic field induced by the tip. Then, a magnetic field $-H_{rc,tip}$ was applied (and switched off) in order to annul the tip magnetization. Electrostatic images of the same sample area were then recorded with the demagnetized probe. CM-MFM images were obtained by subtracting the electrostatic images to the standard MFM images. An example of this CM-MFM characterization in ZM mode is reported in Fig. 41. In particular, Fig. 41a,b show the topography and the standard MFM image acquired at Δz = 20 nm, respectively, of an area of the sample where the biggest NP with diameter d = 30 nm is surrounded by smaller NPs with diameters d < 20 nm. In the

image recorded with the magnetized tip (Fig. 41b) a slight negative contrast was detected in correspondence of the biggest NP, indicating a weak attractive tip-NP interaction. Conversely, a positive contrast was detected in correspondence of smaller NPs, indicating a repulsive tip-sample interaction. Because of their superparamagnetic character, in the absence of an external magnetic field, NPs can be magnetized only by the tip magnetic stray field and, thus, only an attractive magnetic tip-sample interaction can occur. Consequently, the observed positive contrast cannot be attributable to magnetic phenomena. This result indicates the presence of a significant electrostatic contribution in standard MFM images, which results to be even higher than the magnetic one in correspondence of small NPs. In the phase image acquired with the demagnetized tip a positive contrast is observed in correspondence of all the NPs, i.e., also in the bigger one which exhibited a negative contrast in the images acquired with the magnetized tip. This confirms the presence of a significant positive electrostatic contribution in correspondence of all the analyzed NPs. Although the positive phase shift in correspondence of the NPs may indicate a difference between their electric properties and those of the substrate, it is more likely attributable to a topography-induced artifact due to the capacitive tip-sample coupling, i.e., to the reduction of the tip-sample attractive forces in correspondence of the NPs produced by the increasing of the average tip-sample distance [270].

Finally, Fig. 41d shows the image resulting form the subtraction of Fig. 41c (electrostatic contribution detected with the demagnetized tip) to Fig. 41b (standard MFM image acquired with the magnetized tip which is affected by both the electrostatic and the magnetic contribution). It represents the magnetic contribution, depurated of the electrostatic effects. A larger negative contrast is observable in correspondence of the NP which exhibits a negative contrast in standard MFM images (d = 30 nm). Conversely, only a slight negative contrast is observed in correspondence of small NPs (d < 20 nm) which can be hardly distinguished from the noise. This can be ascribed to the small volume of the NPs and, thus, to their magnetic stray field, lower than the probe sensitivity. In order to further confirm the magnetic nature of the tip-sample interaction detected in CM-MFM, we carried out an analysis of the phase contrast as a function of the tip-sample distance (i.e., lift height Δz) and of the NPs diameter d. Several images of the same sample area with different Δz have been recorded with both the magnetized and the demagnetized probe. For each image, the absolute value of the phase shift detected in correspondence of the NPs has been determined as the difference

between the mean values of the phase measured inside the NP and in correspondence of an adjacent region of substrate. The uncertainty in the measured values has been determined combining the statistics on a small area corresponding to the top of the NP and on the selected region of substrate. Figure 42a shows an example of standard MFM phase contrast $\Delta\varphi_{MagnTip}$ as a function of the lift height Δz obtained with the magnetized probe on a NP with d = 30 nm. In correspondence of small tip-sample separations (Δz < 50 nm), an attractive interaction with the NP is experienced by the tip (negative phase shift), which can be ascribed to the predominance of magnetic interactions in this region. Increasing the tip sample distance, the repulsive force decreases until becoming null and then attractive (Δz > 50 nm), indicating the predominance of electrostatic forces at large tip-sample separations. This is congruent with the faster distance-decay of magnetic forces (expected to be proportional to z^{-4}) with respect to the electrostatic ones (expected to be proportional to z^{-2})[256]. Nevertheless, although the general trend of the data is not difficult to justify, the actual $\Delta\varphi_{MagnTip}(\Delta z)$ data reported in Fig. 42a can be hardly rationalized through simple analytical models and their not monotonic behavior is apparently ascribable only to the occasional presence of a random bias in different MFM images. An analogous $\Delta\varphi_{DemagnTip}(\Delta z)$ curve on the same NP obtained with the demagnetized probe is reported in Fig. 42b, which represents the electrostatic signal. As expected, it is always positive, indicating a reduced tip-sample attractive force, and decreases with the increasing of the distance. Also in this case, data can be hardly rationalized through simple analytical models. Nevertheless, by subtracting the data acquired with the demagnetized probe (Fig. 42b) to those acquired with the magnetized probe (Fig. 42a) the CM-MFM signal $\Delta\varphi_{CM-MFM}$ is obtained (Fig. 42c). It turned out that a negative phase shift indicating an attractive (i.e., magnetic) tip-NP interaction exists also at distances larger than 50 nm. This was not detectable in standard MFM images because of the preponderance, at large tip-sample distances, of the electrostatic contribution with respect to the magnetic one. Thus, in the absence of any external magnetic field, the NP is magnetized by the tip stray field also when the probe is at distance larger than 50 nm. This produces an attractive magnetic interaction which, nevertheless, is not detectable by standard MFM measurements due to the predominant electrostatic contribution, but which can be revealed using CM-MFM in ZM mode. It is interesting to notice that while both the standard MFM data (Fig. 42a) and the electrostatic ones (Fig. 42b) cannot be described by simple models and seem affected by a remarkable uncertainty, the magnetic data (Fig. 42c) show a monotonic

trend. Moreover, the fit of $\Delta\varphi_{CM-MFM}(\Delta z)$ data reported in Fig. 42c using Eq. (62) demonstrates that they are very well described by the simple model in which both the tip and the NP are represented with punctiform magnetic dipoles. In particular, being performed the images with set-point amplitude A_{sp} = 28 nm, from the fit an experimental value of δ_{tip} = 39 ±4 nm is determined. This result indicates that, when the MFM signal is depurated of the effect of electrostatic tip-sample forces, a MFM tip acts as a single-point dipole. By averaging the results of an analogous analysis of data obtained on three NPs with different diameters, a value of δ_{tip} = 45 ± 7 nm has been obtained. Fig. 42d reports the $\Delta\varphi_{CM-MFM}(d)$ data measured at Δz = 20 nm together with the corresponding fit which has been obtained using Eq. (62) assuming δ_{tip} = 45 nm. Also in this case, the experimental curve is well described by Eq. (62) although the relatively narrow distribution of NP diameters does not allow us to present more efficacious results. Considering that in these experimental conditions the minimum value of phase shift we can reveal is 10^{-2} deg, we can evaluate that with the present settings and equipment our technique could allow the study of NPs with diameter not smaller than 10 nm. Interestingly, our results demonstrate that the weak magnetic field generated by the tip is sufficient to completely orient the magnetic domains of superparamagnetic NPs, which is a debated issue in the scientific community of MFM users [155], [276]. Moreover, as a result of the removal of electrostatic signal in MFM images through CM-MFM, the tip-sample interaction is found to be describable with the simple one dimensional model of two interacting magnetic dipoles.

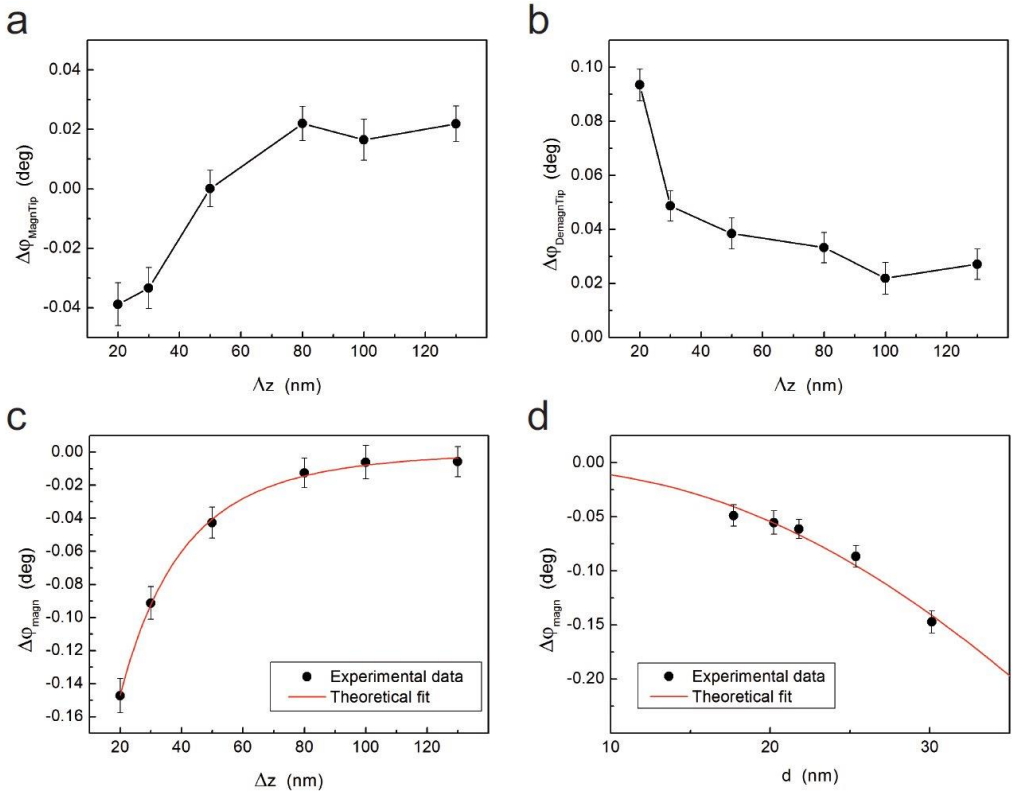

Figure 42 - Analysis of images collected using CM-MFM technique in ZM mode. (a) Standard MFM phase contrast (Δφ) as a function of the lift height (Δz) measured on a NP with diameter d = 30 nm using a magnetized probe, which is affected by both electrostatic and magnetic tip-sample interactions. (b) Phase contrast on the same NP as a function of the lift height acquired with the demagnetized tip, which is affected only by the electrostatic tip-sample interactions. (c) Magnetic phase contrast as a function of the lift height obtained by subtracting data in (b) from those in (a) with the corresponding fit using the simple model of two magnetic dipoles in Eq. (62). (d) Magnetic phase contrast as a function of the NP diameter obtained analyzing five NPs with the corresponding fit using the simple model of two magnetic dipoles in Eq. (62).

6.5 - CURRENT LIMITS AND FUTURE PERSPECTIVES

The results reported in this work demonstrate that, in principle, CM-MFM may represent a powerful technique to delete electrostatic artifacts resulting from tip-sample capacitive coupling in MFM images. Thus, CM-MFM images can be used to deduce information on local magnetic properties of materials, e.g., magnetic moment or magnetization, with nanometer lateral resolution. Despite the potentiality and the correctness of its working principle, however, we must point out some current limitations of our technique, mainly due to practical issues related to the experimental setup which basically lead to the incomplete demagnetization of the probe. Understanding and solving these limitations represent the main challenges of our current work of improvement of CM-MFM.

Obviously, being a two-pass technique, the correctness of topographic images is an essential prerequisite for the accuracy of CM-MFM. Artifacts in the reconstruction of the topography, e.g., due to incorrect choice of instrumental parameters like set-point, scan rate, or feedback gain, result in artifacts in the magnetic images which cannot be corrected. This problem is somewhat more severe in CM-MFM as two subsequent images of the same area have to be acquired, with the magnetized and the demagnetized tip, respectively. These issues affect CM-MFM as well as any other two-pass technique. In addition, since the MFM phase shift depends on the instrumental parameters (e.g., drive frequency and amplitude, set-point amplitude), the same parameters must be used in the calibration on the reference sample (e.g., the floppy) and in the analysis of the investigated sample (e.g., the NPs).

Other severe limitations can occur due to the incomplete demagnetization of the tip. Depending on the sensitivity of the power supply, indeed, the experimental setup is characterized by a minimum step allowed between two values of the applied magnetic field. In our case, for instance, the minimum allowed step between two values of magnetic field is 15 Oe. Apart from particular and occasional cases in which $-H_{rc,tip}$ coincides with one of applicable values of magnetic field, this demonstrates that with our experimental setup we cannot reach the complete demagnetized state of the tip. Indeed, referring to Fig. 38a, we determine $-H_{rc,tip} = -278.0 \pm 7.5$ Oe (which is in agreement with the (in-field) coercivity of about 400 Oe reported by the manufacturer) while the closest value of magnetic field we can apply is $-H^*_{rc,tip} = -270$ Oe. In correspondence of $-H^*_{rc,tip}$ we observe a contrast in the images equal to $\Delta\varphi^{cont}(-H^*_{rc,tip}) = 0.212$ deg, which is 10% of the saturation contrast $\Delta\varphi_s^{cont} = 2.081$deg. As $\Delta\varphi^{cont}$ is proportional to the tip magnetization, the signal detected with the (partially) demagnetized tip includes not only the electrostatic contribution but also a part of the magnetic one. Therefore, when subtracting the two signals obtained with the magnetized and (partially) demagnetized tip, respectively, the signal reflecting the magnetic tip-sample interaction is also modified. The extent of this effect can be evaluated, and the effect itself can be corrected, in the simple case of a sample the magnetization of which is independent from that of the tip. In this case, Eq. (65) can be rewritten as

$$\Delta\varphi_{DemagnTip} = \Delta\varphi_{el} + \varepsilon\Delta\varphi_{magn} \qquad 67)$$

where ε is a demagnetization ratio given by $\varepsilon = \Delta\varphi^{cont}(-H^{*}_{rc,tip})/\Delta\varphi_s^{cont}$. Notably, the value of ε can be determined from the MFM contrast on the floppy since on such a sample not only are electrostatic effects negligible with respect to the magnetic ones, but also because they are uniform over the surface. Therefore they are deleted when subtracting the maximum and minimum phase shifts in the MFM images to evaluate the phase contras [123]. In this case, instead of by Eq. (66), the CM-MFM signal is given by

$$\Delta\varphi_{CM\_MFM} = \Delta\varphi_{MagnTip} - \Delta\varphi_{DemagnTip} = (1 - \varepsilon)\,\Delta\varphi_{magn} \qquad 68)$$

Thus, despite the not complete demagnetization of the tip, the electrostatic contribution is completely deleted in $\Delta\varphi_{\mathrm{CM-MFM}}$, but the magnetic signal is underestimated or overestimated. This effect can be corrected since the magnetic signal can be obtained as

$$\Delta\varphi_{magn} = \frac{\Delta\varphi_{CM-MFM}}{1-\varepsilon} \qquad 69)$$

As ε can be easily determined from the MFM images of the floppy reference sample, our technique allows us to obtain the correct intensity of the magnetic signal depurated from the electrostatic contribution when the sample magnetization is independent of that of the probe. It is worth noting that the same result can be obtained even if $H^{*}_{rc,tip}$ is not chosen as close as possible to $H_{rc,tip}$ providing the corresponding value of ε is determined. Minimizing the residual magnetization of the tip (and thus ε), however, ensures the highest signal to-noise ratio.

The consistency of this correction method is demonstrated by data reported in Fig. 43. From the calibration of the probe on the floppy (Fig. 43a), the value of $H_{rs,tip}$ = 510 Oe is obtained at which the remanent magnetization of the tip can be considered saturated. Two values of magnetic field are determined at which the tip can be considered nearly demagnetized, i.e., $-H^{*}_{rc,tip}{}^{(1)} = -270$ Oe and $-H^{*}_{rc,tip}{}^{(2)} = -285$ Oe, respectively. These correspond to not null phase contrast values equal to $= \Delta\varphi^{cont}(-H^{*}_{rc,tip}{}^{(1)}) = 0.59$ deg and $\Delta\varphi^{cont}(-H^{*}_{rc,tip}{}^{(2)}) = -0.92$ deg (note that the the contrast is reversed in correspondence of $-H^{*}_{rc,tip}{}^{(2)}$), respectively. The values of phase contrast were determined from statistics on lines corresponding to maximum and minimum of the phase of the floppy domains in a certain area. Being $\Delta\varphi_s^{cont}$ = 2.52 deg, in correspondence of these two nearly demagnetized states of the tip the values $\varepsilon_1 = 0.23 \pm 0.01$ and $\varepsilon_2 = -0.36 \pm 0.01$ are determined, respectively, where the negative sign of ε_2 is due to the reversal of the contrast in correspondence of $-H^{*}_{rc,tip}{}^{(2)}$. In a different area of the sample, the contrast

between two selected points was used to determine the $\Delta\varphi_{\mathrm{CM–MFM}}$ signal as a function of the lift height Δz in the two cases of nearly demagnetized tip. As clearly shown in Fig. 43b, although $\Delta\varphi_{\mathrm{CM–MFM}}$ is supposed to represent the 'magnetic only' signal, two completely different curves are obtained. This is due to the fact that in the case characterized by ε_1 a fraction of the magnetic signal is actually subtracted and thus the latter is underestimated. Conversely, in the case characterized by ε_2 a fraction of the magnetic signal is added (due to reversal in sign of the phase contrast) and thus the latter is overestimated. After correction using Eq. (69), however, the same values of $\Delta\varphi_{magn}$ are obtained (Fig. 43c), which confirms the consistency of the method. The correction of CM-MFM data can effectively compensate the incomplete demagnetization of the tip in case of samples the magnetization of which does not depend on that of the tip, and can be applied not only to data obtained on selected points but on the whole CM-MFM images.

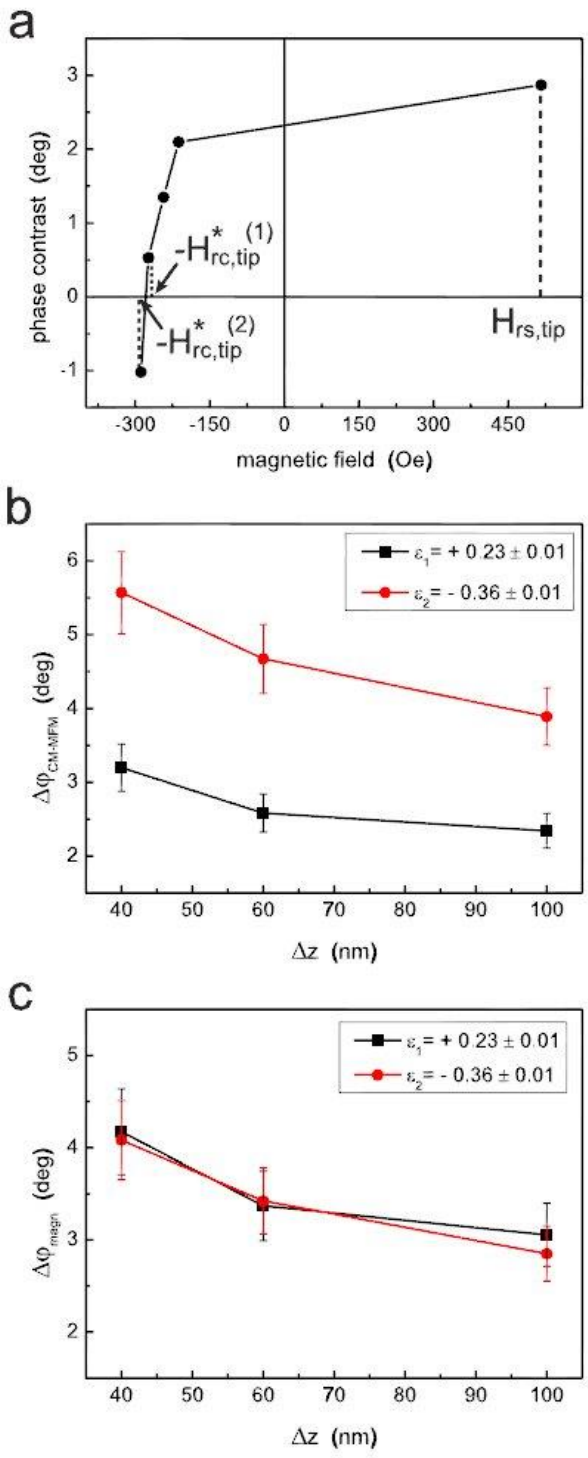

Figure 43 - (a) Tip calibration on the floppy, from which the remanent saturation magnetic field Hrs,tip and two values near the remanent coercive field are determined. (b) CM-MFM signal (ΔφCM−MFM) as a function of the lift height (Δz) measured on the floppy in two cases of nearly demagnetized tip, characterized by two values of the demagnetization factor ε. (c) Corrected magnetic signals (Δφmagn) as a function of the lift height (Δz), obtained using Eq. (69).

If the spin of the sample depends on that of the tip, like in superparamagnetic NPs, the incorrectly subtracted fraction of $\Delta\varphi_{magn}$ depends also on the magnetization states of the

NP when the tip is saturated and nearly demagnetized. For instance, if the magnetic moment of the NP is saturated neither when the tip is saturated nor nearly demagnetized, the magnetization of the NP is proportional to the magnetic field generated by the tip. This in turns is proportional to the tip magnetization. Therefore, Eq. (67) can be rewritten as

$$\Delta\varphi_{DemagnTip} = \Delta\varphi_{el} + \varepsilon^2\Delta\varphi_{magn} \qquad 70)$$

and thus the CM-MFM signal is given by

$$\Delta\varphi_{CM\text{-}MFM} = (1 - \varepsilon^2)\,\Delta\varphi_{magn} \qquad 71)$$

Thus, dividing $\Delta\varphi_{\mathrm{CM-MFM}}$ by $(1-\varepsilon^2)$, the corrected $\Delta\varphi_{magn}$ versus Δz curves can be obtained. Depending on the field generated by the tip, however, the magnetization of the NP can be saturated by the magnetized tip but not by the nearly demagnetized one. Moreover, depending on the residual magnetization of the tip, the magnetization state of the NP varies with the lift height. In this case, the ratio between the spin of the NP when the tip is fully magnetized and demagnetized is no longer proportional to ε. Thus, the correction factor cannot be easily estimated.

In order to demonstrate the effectiveness of this correction procedure in the case of the analyzed NPs, we acquired three sets of CM-MFM phase versus lift height curves using three different values of the demagnetization coefficient, i.e., $\varepsilon_1 = 0.17$, $\varepsilon_2 = 0.48$, and $\varepsilon_3 = 0.60$, determined on the reference floppy as previously described. In Fig. 44a, three of these curves, obtained on a NP with diameter d = 25 nm, are reported. The curves clearly show that the bigger ε the lower the $\Delta\varphi_{\mathrm{CM-MFM}}$ signal, which is obviously due to the bigger fraction of the subtracted magnetic signal a result of a bigger residual magnetization of the (nearly) demagnetized tip. Assuming that the magnetic stray field generated by the saturated tip is not much bigger than the saturation field of the NP, the CM-MFM signal can be corrected and the magnetic signal can be obtained as $\Delta\varphi_{magn} = \Delta\varphi_{\mathrm{CM-MFM}}/(1-\varepsilon^2)$. Thus, the curves shown in Fig. 44b are obtained, which demonstrate that the corrected $\Delta\varphi_{magn}$ values retrieved using the three different values of ε coincide within the experimental uncertainty.

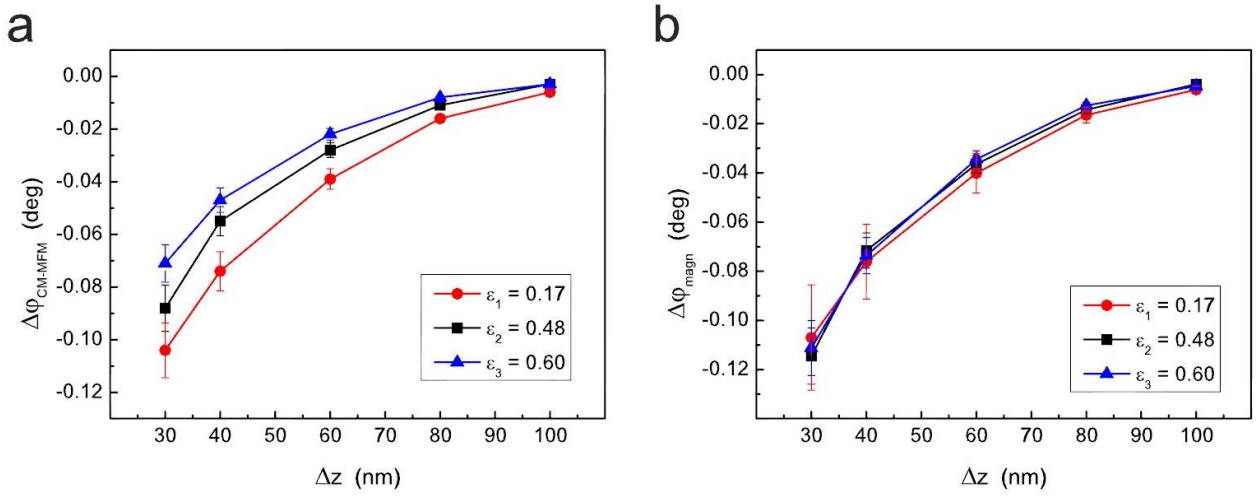

Figure 44 - (a) CM-MFM signal (ΔφCM−MFM) as a function of the lift height (Δz) measured on a NP with diameter d=25 nm in three cases of nearly demagnetized tip, characterized by three values of the demagnetization factor ε. (b) Corrected magnetic signals (Δφmagn) as a function of the lift height (Δz), obtained using Eq. (71).

Although potentially capable to correct CM-MFM data, the described procedures are admittedly a bit intricate and lengthen the whole CM-MFM procedure introducing additional sources of uncertainty. Also, the sample may contain different types of magnetic nanomaterials and the magnetic field generated by the tip may not uniformly affect them. In this case the correction procedure cannot be applied to the whole image but only to data collected in selected points. Also, even at fixed lift height the correction factor may be not constant over the sample surface. In addition, we note that the uncertainty in the value of the applied magnetic field results in an uncertainty in the values of the correction factors (which is included in the error bars in the graphics in Figs 43c and 44b). As the demagnetization is performed only at the beginning of the experiment and, thus, all the points in the curves are obtained with the very same value of ε, its uncertainty acts as a coefficient which multiplies all the points and therefore it must be considered when comparing curves obtained in different measurement sessions, i.e., after different demagnetization steps. Thus, not with standing the possibility of correcting CM-MFM data, the incomplete demagnetization of the tip represents a serious limitation to the accuracy of the technique. In order to overcome this limitation, if one wants to use the approach described in this work, an improved setup should be considered. Enhanced sensitivity of the power supply can ensure a smaller residual magnetization of the tip in its (nearly) demagnetized state. Also, a more effective

demagnetization procedure could be selected, e.g., through the use of damped oscillating magnetic fields.

Another current limit of CM-MFM is that the tip calibration procedure for the determination of the coercive field is performed using the floppy reference sample at a certain distance along the axis of the coil. The field generated by the coil, nevertheless, decreases as the distance from the coil along its axis increases. Therefore, if the sample is placed on the top of the coil, variations in the sample thickness result in variations in the distance between the tip and the coil and, thus, in the height at which the tip demagnetization procedure is performed. On samples much thinner or thicker than the floppy (including possible additional substrates), the demagnetization step is performed at height from the coil different from that at which calibration was performed. This leads to an incorrect demagnetization during the experiment with a residual magnetization of the probe significantly bigger than that estimated, dramatically affecting the accuracy of the measurement. In this work, great attention was paid to perform the tip demagnetization at the same height in both the calibration step on the floppy and in the analysis of the NPs. This strategy, however, may be hardly applicable in some specific cases, e.g., if the sample to be analyzed is particularly thick. In this case, no correction can be carried out. A solution to this limitation could consist in the ex situ demagnetization of the tip, using a 'demagnetization station'. Although modern AFM setups ensure a relatively accurate positioning even after macroscopic displacements of tip and sample (e.g., to shift between 'sample load' and 'sample scan' positions), this procedure may lead to drifts in the imaged area. This may result in more time-consuming experimental session especially when small areas and high resolutions are required. Another solution could be the use of a different demagnetization procedure, i.e., using oscillating damped magnetic field. Depending on the initial values of magnetic field, this procedure could allow a certain margin of variation of the tip-coil distance without compromising the accuracy of the tip demagnetization. Finally, another solution could be the use of a coil integral with the AFM head and, thus, with the tip. This would allow one to perform the demagnetization procedure at fixed and thus correct coil-tip distance. This however could not be implemented on every AFM setup due to the volume and weight of the coil. In particular, it could be hardly used in 'tip scan' AFM systems. Not with standing all the aforementioned limitations, CM-MFM has however the potential, which we have not fully explored yet, for accurate characterization of magnetic parameters of isolated nanomaterials. For example, the

curves reported in Fig. 44b can be fitted using Eq. (62) to roughly estimate the mass magnetization saturation of the analyzed NP. Indeed: k_c = 5 *N/m* and Q_c = 170 have been determined for the used cantilever; $m_{tip} = 1 \times 10^{-13}$ EMU can be assumed, although actually only its order of magnitude is indicated by the producer and thus we cannot be more accurate without its independent measurement; the values of the other parameters can be determined by the fit itself, even if the absence of proper statistics dramatically affects the accuracy of these values. With all these assumptions, M_s = 20 EMU/g is determined which, considering the uncertainty in m_{tip}, is compatible with but smaller than the values (about 60–70 EMU/g) obtained on macroscopic Fe_3O_4 NPs samples with similar diameters measured at room temperature by conventional techniques reported in literature [277]. Indeed, we must also add to the previously indicated sources of uncertainty the assumption that the NP is perfectly spherical and that its magnetization is uniform in the volume ignoring possible near-surface effects.

6.6 - CONCLUSIONS

In conclusion, we have addressed the issue of the effect of electrostatic tip-sample interactions in MFM, which generally prevent the acquisition of magnetic images and thus limit the accuracy of magnetic measurements at the nanometer scale. We developed a MFM-based approach in which the two subsequent images of the same area are collected, one with the magnetized and one with the quasi-demagnetized probe, which is possible after the determination of the remanent saturation and remanent coercivity magnetic fields of the actually used probe performed using a reference sample with periodically patterned magnetic domains. The effectiveness of our technique is demonstrated through a challenging case study, i.e., the characterization of superparamagnetic NPs in the absence of any applied external magnetic field. Images reflecting the magnetic properties of the sample have been obtained subtracting images acquired with the demagnetized tip to the standard MFM images, demonstrating the effectiveness of our techniques in the removal of electrostatic artifacts in MFM maps. Moreover, in addition to the demonstration of the technique, the analysis of our data demonstrated that the magnetic field produced by the magnetized tip is sufficient to completely orient the magnetic domains of superparamagnetic NPs even in the absence of any applied external magnetic field. Once the electrostatic artifacts are removed, the tip-sample interaction is well described by that of two single-point magnetic dipoles. The need for an accurate control of the instrumental parameters, the effect of the sample

thickness, and the incomplete demagnetization of the probe still represent serious limitations to CM-MFM which must be overcome to increase
the accuracy of the technique. Overall, our controlled magnetization MFM technique has been demonstrated to allow us to perform real magnetic characterizations at the nanometer scale.

7. SINGLE NANOPARTICLES MAGNETIZATION CURVES BY CONTROLLED TIP MAGNETIZATION MAGNETIC FORCE MICROSCOPY (CM-MFM)

Livia Angeloni[1,2], Daniele Passeri*[1], Davide Peddis[3],
Diego Mantovani[2], and Marco Rossi[1,4]

[1]*Department of Basic and Applied Sciences for Engineering, SAPIENZA University of Rome, Via A. Scarpa 16, 00161 Rome, Italy*

[2]*Lab. for Biomaterials and Bioengineering (CRC-I), Dept. Min-Met-Materials Eng. & University Hospital Research Center, Laval University, Quebec City, Canada*

[3]*Istituto di Struttura della Materia - CNR, 00016 Monterotondo Scalo, Rome, Italy*

[4]*Research Center for Nanotechnology applied to Engineering of SAPIENZA University of Rome (CNIS), Piazzale A. Moro 5, 00185 Rome, Italy*

**Corresponding author: daniele.passeri@uniroma1.it*

Submitted to:
Nanoscale

Resumè

Le développement de techniques de caractérisation magnétique à résolution spatiale élevée, capables de mesurer quantitativement les paramètres magnétiques de nanoparticules individuelles est un sujet brûlant dans le nanomagnétisme, en raison de l'application de plus en plus large de ces nanomatériaux dans plusieurs domaines technologiques et du conséquent besoin de comprendre et optimizer leurs propriétés magnétiques.

Parmi les autres techniques proposées, la microscopie à force magnétique (MFM), grâce à sa résolution latérale nanométrique et sa capacité d'étudier l'évolution magnétique d'un échantillon en réponse à un champ magnétique appliqué extérieurement, apparaît comme une méthode prometteuse pour la caractérisation magnétique à l'echelle nanometrique. Néanmoins, son applicabilité à la mesure quantitative de paramètres magnétiques de particules individuelles de taille inférieure à 100 nm est encore limitée par certains inconvénients, comme par example la présence d'artefacts électrostatiques. Récemment, ces limitations ont été surmontées par le développement d'une particulière technique MFM, appelée MFM (CM-MFM) à magnetization controlée, qui permet d'éliminer les effets électrostatiques et de mesurer la réelle interaction magnétique entre la pointe et la nanoparticule, en permettant une corrélation quantifiable entre le signal magnétique mesuré et l'aimantation de l'objet étudié.

Dans ce travail, nous proposons une procédure expérimentale basée sur l'utilisation de la technique CM-MFM et une methode d'analyse des données pour mesurer la courbe d'aimantation de nanoparticules magnétiques individuelles, c'est-à-dire pour obtenir leur magnétisation de saturation M_s, leur champ magnétique de saturation H_s et leur coercitivité H_c. L'utilisation de la méthodologie CM-MFM proposée nous a permis de mesurer, pour la première fois, les courbes d'aimantation de nanoparticules de Fe_3O_4 individuelles avec diamètres compris entre 21 et 32 nm, en utilisant un instrument MFM. Les résultats obtenus ont monté une très bonne concordance avec les données quantitatives obtenues par analyse SQUID sur un échantillon macroscopique du même type de nanoparticules. Ces resultats ont demontré la grande potentialité de la technique dans le domaine de la nanomagnétométrie.

Abstract

The development of high spatial resolution and element sensitive magnetic characterization techniques, able to quantitatively measure the magnetic parameters of individual nanoparticles (NPs) is a hot topic in nanomagnetism by reason of the wider and wider application of these nanomaterials in several technological fields and the consequent need of deeply understanding and tuning their magnetic properties. Among other proposed techniques, magnetic force microscopy (MFM), thanks to its high lateral resolution and the capability of studying the magnetic evolution of a sample in response to an externally applied magnetic field, appears as a promising method for the magnetic characterization of single nano-sized materials. Nevertheless, its applicability to the quantitative measurement of magnetic parameters of single particles with size lower than 100 nm is still limited by some drawbacks, above all the presence of electrostatic artifacts. Recently, these limitations have been overcome by the development of a particular MFM based technique, called controlled magnetization - MFM (CM-MFM), through the use of which the electrostatic effects are removed and the purely magnetic tip-NP interaction can be detected, allowing, in principle, a quantifiable correlation between the measured magnetic signal and the magnetization of the studied object.

In this work we propose an experimental procedure, based on the use of CM-MFM technique, and a post-processing data analysis to measure the magnetization curve of single magnetic nanoparticles, i.e., to individuate their saturation magnetization M_S, saturation magnetic field H_S, and their coercivity H_C. The use of the proposed CM-MFM methodology allowed us to measure, for the first time, the magnetization curves of individual Fe_3O_4 nanoparticles with diameters in the range of 21-32 nm by using a MFM instrument. The obtained results resulted in very good agreement with the quantitative data obtained by SQUID analysis on a macroscopic sample of the same kind of nanoparticles, showing the high potentiality of the technique in the field of nanomagnetometry.

7.1 - INTRODUCTION

The development of techniques for the magnetic characterization of nanoparticles (NPs) has become a fundamental need in nanomagnetism, because of the growing use of magnetic NPs (MNPs) in different technology fields, ranging from electronics (e.g., storage devices) [278] to environmental [279] and biomedicine applications [4], [5], [17], [18]. The design and the optimization of these systems require a deep understanding of the mechanisms regulating the magnetism at the nanoscale. For example, several efforts are oriented to the individuation of precise relationships between the magnetic properties and numerous influencing morpho-structural and chemical parameters of NPs (e.g., the size, the shape, the chemical composition, and the crystal structure) [280]–[282], as well as to the comprehension of the influence of the mutual dipolar interactions between individual NPs, which depend on the magnetization state of the individual elements, the distance between them, their spatial configuration, and which, at the same time, affect the overall magnetic behavior of NPs based systems [283]–[286]. Ensemble measurements, such as superconducting quantum interference device (SQUID) [35], vibrating sample magnetometer (VSM) [36], and alternative gradient field magnetometer (AGFM) [37], are conventional methods successfully used to investigate the magnetic properties of NPs ensemble, such as patterns and ferrofluids, but, because of their 'macroscopic' character, allow one to relate the magnetic properties to other physical parameters only statistically. Therefore, an exhaustive understanding of the magnetic behavior of NPs, which requires the disembroiling of the complex interplay of the numerous influencing factors, appears to be achievable only by the use of high spatial resolution and element sensitive techniques, able to quantitatively measure the magnetic parameters of individual NPs. For this reason several efforts are focused on the research and development of new techniques with more and more high resolution, able to study the magnetic behavior of single, smaller and smaller, isolated nano-objects. Several techniques have been explored, but a standard method to quantitatively measure the main magnetic parameters of isolated nanomaterials has not been individuated yet.

The magnetization reversal of single micro and nanostructures can be, for example, characterized by different techniques such as magnetoresistance techniques [42], spatially resolved Kerr effect (MOKE) [43], or magneto-optical scanning near field optical microscopy [44], but greater attention is paid to techniques having higher resolution and the capability of a more detailed study of the magnetization reversal of

nanometer-sized NPs, like transmission electron microscopy (TEM) based techniques, such as differential phase contrast mode (DPC) [63] or off-axis electron holography [65], [66], X-ray based techniques, such as soft X-ray spectroscopies, like X-ray holography [68] and transmission X-ray microscopy [69]–[71], ballistic Hall micro-magnetometry systems [56], [60], micro and nano-SQUID [49], [51], [52], and X-ray photoemission electron microscopy (XPEEM) [77], [83]. Nevertheless, all these techniques present some limitations, such as: the complex sample preparation procedures, typical of transmission electron techniques but also affecting nano-SQUID and ballistic Hall micro-magnetometry techniques, where the capability of measuring a single nano-object is related to the capability of placing that object in a determined area of the sensor, and, therefore, need additional instrumentation, such as nano-manipulators or atomic force microscopy (AFM) setups; the limited kind of analyzable materials as in the case of conventional X-ray microscopies, where only samples transparent to X-ray can be measured; the necessity of complex, expensive and not easily accessible instrumentation such as synchrotron facilities in XPEEM technique. For this reason research efforts are still addressed to the individuation of simple, user-friendly experimental setups which do not require complicated sample preparation, able to allow the study of any kind of magnetic nanomaterials and to furnish quantitative information about the magnetic parameters of the selected element.

Magnetic force microscopy (MFM) is a scanning probe microscopy technique, able to simultaneously acquire the morphology of a surface and map the magnetic interaction forces between the tip and the sample with nanometer spatial resolution. These capabilities, together with the possibility of equipping commercial MFM instruments with systems (electromagnets) able to produce adjustable magnetic fields both perpendicular (out-of-plane) and parallel (in-plane) to the sample surface, make MFM an effective and widely used tool for the qualitative study of the magnetic characteristics of single nanoparticles [155], [159], [161], [265], [287], also in response to the application of external magnetic fields [288]. Nevertheless, the potentialities of MFM in the measurement of quantitative magnetic parameters (such as the saturation magnetization M_s, the saturation magnetic field H_s, the coercivity H_c and the magnetization reversal curve) of single objects at the nanometer scale have still not been completely exploited and only few results are available. Indeed, currently, the only commonly used quantitative MFM procedure is the local statistical measurement of the switching field distribution and the remanent or ‘in field’ hysteresis curves of bit-

patterned recording media, consisting in arrays of nanodots [289] [290] [291], nanoislands [292], nanowires and nanotubes [193] [150], which is generally performed by applying controlled out-of-plane magnetic fields to the sample and counting the number of magnetically reversed entities.

Concerning the quantitative measurements of magnetic properties of single nanomaterials, the hysteresis loop of individual nanowires both under parallel and perpendicular magnetic fields has been measured by MFM [267]. Indeed, in the case of bistable magnetic nanomaterials with high magnetic moment (such as nanowires), the magnetization state of the sample can be easily visualized on MFM images as an alternation of 'bright' and 'dark' contrast (i.e., repulsive and attractive tip-NP interaction). Therefore, the magnetization curve (and the definition of quantitative magnetic parameters) of a single element can be obtained acquiring several images with different external magnetic fields [267] or by recording only one MFM image continuously varying the applied magnetic field during the scan [149] and then plotting the contrast between two points (dark/bright contrast) in a selected line or region as a function of the applied magnetic field. Similarly, the magnetization curve of single nanodots in response to out-of-plane and in-plane magnetic fields has been measured using MFM by plotting the nanodot average phase (or frequency/amplitude) shift as a function of the applied magnetic field [293] or by acquiring the MFM contrast in a single scan line while continuously varying the applied field [268]. These methods have been successfully applied to dots having size ranging from 200 nm to 20 μm. Nevertheless, in the case of superparamagnetic nanoparticles having size less than 100 nm, the magnetization reversal behavior of single NPs has been studied only qualitatively [288]. Only Sievers et al [156] and Schreiber et al [155] succeeded in retrieving the magnetic moment of nanoparticles from standard MFM images describing the tip-NP interaction as the force occurring between two magnetic dipoles, while other authors did not find any correlation between the experimental MFM data and the proposed 'dipole' model [158], [161], [209]. As already highlighted in the literature [287], these incongruities can be ascribed to several factors, which make magnetic nanoparticles with size lower than 100 nm a challenging sample to be quantitatively analyzed by MFM. These factors can be summarized as: i) the low magnetic moment, which produces a low magnetic tip-sample interaction, close to the sensitivity limit of the technique; ii) the presence, in MFM images, of an additional signal due to electrostatic tip-sample interactions (i.e., van der Waals, electric charge, capacitance

coupling), which has been demonstrated to be of the same order of magnitude in respect to the magnetic one [287]; iii) the lack of an unambiguous theoretical model describing the tip-sample (NP) interaction consistently with experimental data and the consequent difficulty in converting the detected MFM signal to the quantitative value of a physical parameter, such as the magnetic moment of a single nanoparticle. Some methods to remove the electrostatic effects in MFM images have been proposed, such as the combined use of Kelvin probe force microscopy and MFM, proposed by Jaafar et al [216], or the switching probe magnetization MFM and the differential MFM, proposed by Cambpel et al and Wang et al, respectively [215] [218] [271].

Recently, we proposed a new MFM technique, called controlled magnetization-MFM (CM-MFM), with the aim of depurating the MFM signal from the electrostatic artifacts and detecting the signal due to the sole magnetic tip-NPs interactions. The analysis of superparamagnetic nanoparticles through the use of CM-MFM showed that, once the electrostatic artifacts are removed from the MFM data and the 'pure magnetic signal' is detected, the tip-NP interaction can be simply described by the magnetic interactions between two single-point magnetic dipoles placed close to the geometrical center of the tip apex and the NP, respectively [294]. This result has confirmed the possibility of extrapolating quantitative information about the magnetic properties of nanoparticles from MFM measurements, but the elimination of the significant electrostatic effects is essential to this purpose.

In this work we propose a MFM based method to quantitatively retrieve the magnetization curve of single magnetic nanoparticles by in-field CM-MFM measurements. The procedure has been tested on Fe3O4 NPs and the obtained results have been compared with standard magnetometry to assess the effectiveness of the proposed technique.

7.2 - MATERIALS AND METHODS

7.2.1 - Controlled magnetization magnetic force microscopy

CM-MFM consists in the acquisition of two MFM images with two different magnetization state of the probe. Each MFM image is acquired using the standard MFM 'lift height mode', consisting in a double scan of the sample area: the first scan is performed in tapping mode in order to acquire and record the topography profile of the sample; the second scan is performed in dynamic non-contact mode with the tip

following a trajectory corresponding to the previously recorded sample profile, with the aim of recording the phase (or frequency) shift map due to the tip-sample long-range interaction forces F experienced in each point of the scanned area. In particular, the phase shift $\Delta\varphi$ is given by the relation

$$\Delta\varphi = -\frac{Q_c}{k_c}\frac{\partial F_z}{\partial z} \qquad 72)$$

where Q_c and k_c are the quality factor of the cantilever first resonance in air and the cantilever spring constant, respectively, and $\partial F_z/\partial z$ is the gradient along the z direction perpendicular to the surface plane of the component along z of the long-range interaction force F_z. In CM-MFM, a first standard MFM image ($\Delta\varphi_{MagnTip}$) is acquired with the probe magnetized in its saturation magnetization state ($M_{rs,tip}$). This image is given by the superimposition of the signals due to both magnetic ($\Delta\varphi_{magn}$) and electrostatic ($\Delta\varphi_{el}$) tip-sample interaction forces [294]. Then, the tip can be demagnetized through the application (and the switching off) of its coercive remanent field $-H_{rc,tip}$, previously determined by a probe calibration procedure, and a second image is acquired with zero probe magnetization and with the same scanning parameters ($\Delta\varphi_{DemagnTip}$), in order to detect only the electrostatic contribution ($\Delta\varphi_{el}$). Therefore the MFM signal due to only magnetostatic tip-sample interactions is obtained by subtracting the second image to the first one, being $\Delta\varphi_{magn} = \Delta\varphi_{MagnTip} - \Delta\varphi_{DemagnTip}$.

In this work, CM-MFM has been performed using a standard MFM instrumental apparatus (Icon, Bruker Inc.) equipped with a standard CoCr coated silicon cantilever (MESP, Bruker Inc.). From the analysis of the first free mode of the cantilever in air, the resonance quality factor $Q_c = 190$ and the cantilever spring constant $k_c = 1.0$ N/m were determined. The MFM setup was equipped with an electromagnet placed under the sample. This configuration allows the tuning of the magnetization state of the probe, through the application and the switching off of opportune out-of-plane magnetic fields as previously described [294], i.e., the implementation of CM-MFM technique, and the tuning of the 'in field' (out-of-plane) magnetization state of the sample through the application of controllable out-of-plane magnetic fields during the scan (and, therefore, the study of the magnetization state of the sample in response to an external magnetic field). The range of possible magnetic fields applicable with the used instrumentation is $-480\ Oe < H < +480\ Oe$, which has been demonstrated to be appropriate to saturate and nullify the magnetization of standard commercially available MFM probes [294]. The in situ demagnetization of the probe, necessary to perform CM-MFM, has to be obtained

by applying to the magnetized tip its previously measured remanent coercive field $H_{rc,tip}$. Therefore, a preliminary calibration phase has been necessary. Using a floppy disk as a reference sample, the remanent magnetization curve of the probe has been measured (and thus the saturation magnetic field $H_{rs,tip}$ and the coercive field $H_{rc,tip}$ have been determined) by plotting, as a function of the magnetic field, the phase contrast measured between two adjacent domains after applying and switching off magnetic fields with different intensities. The detailed 'probe calibration' procedure has been previously reported [294]. All the measurements reported in this work have been carried with the same probe for which the values of $H_{rs,tip} = 440\ Oe$ and $H_{rc,tip} = 230\ Oe$ have been found. In-field measurements have been performed by applying an out-of-plane external magnetic H_{ext} field in the range $-10\ Oe < H_{ext} < +65\ Oe$ and at $\Delta z = 100\ nm$.

7.2.2 - Materials and ancillary techniques

In order to validate the proposed measurement procedure, a sample of commercially available magnetite NPs (Sigma Aldrich) with nominal average diameter of 30 nm have been studied. The sample was diluted in distilled water and a drop of the resulting dispersion was placed on a silicon single crystal substrate. Measurements were performed after complete evaporation of the water.

The global magnetic characteristics of the sample were studied using SQUID. Macroscopic DC magnetization measurements were performed using a SQUID magnetometer equipped with a superconducting coil ($H_{max} = \pm 5T$). To avoid any movement of the NPs during the measurements, the samples, in the form of powders, were immobilized in epoxy resin. The obtained magnetization curve is reported in Fig. 45, from which the saturation magnetization $M_s = 78\ emu/g$ is calculated, reached at a saturation field of about $103\ Oe$.

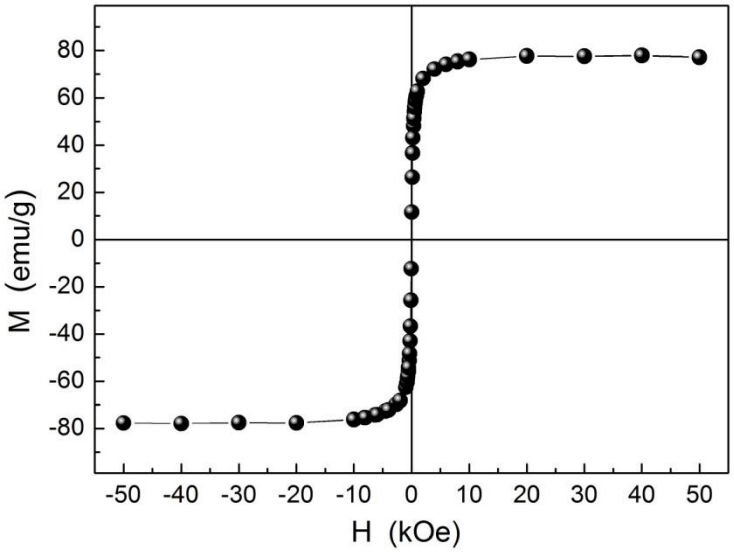

Figura 45 - Magnetization curve obtained on magnetite NPs by SQUID

7.3 - CM-MFM PROCEDURE FOR THE MEASUREMENT OF SINGLE NPS MAGNETIZATION CURVES

The CM-MFM procedure we propose to measure the magnetization curves of single magnetic nanoparticles consists in two phases: i) the acquisition of the magnetic phase signal as a function of the tip-sample distance (i.e., the lift height) on different NPs, in order to calibrate the magnetic parameters of the tip; ii) acquisition of the magnetic phase signal as a function of the applied magnetic field of isolated NPs and conversion of obtained curves into magnetization curves of each NP.

7.3.1 - Calibration of the magnetic parameters of the tip

Different CM-MFM images of NPs, resulting from the subtraction of the images obtained with the demagnetized probe to the corresponding standard MFM images, are acquired in correspondence of different lift heights (i.e., the distance between the probe and the sample). In Figure 46, an example of standard MFM images, the electrostatic images and CM-MFM (magnetic) images of a Fe_3O_4 NP having diameter of 31 nm acquired at different lift height values are shown.

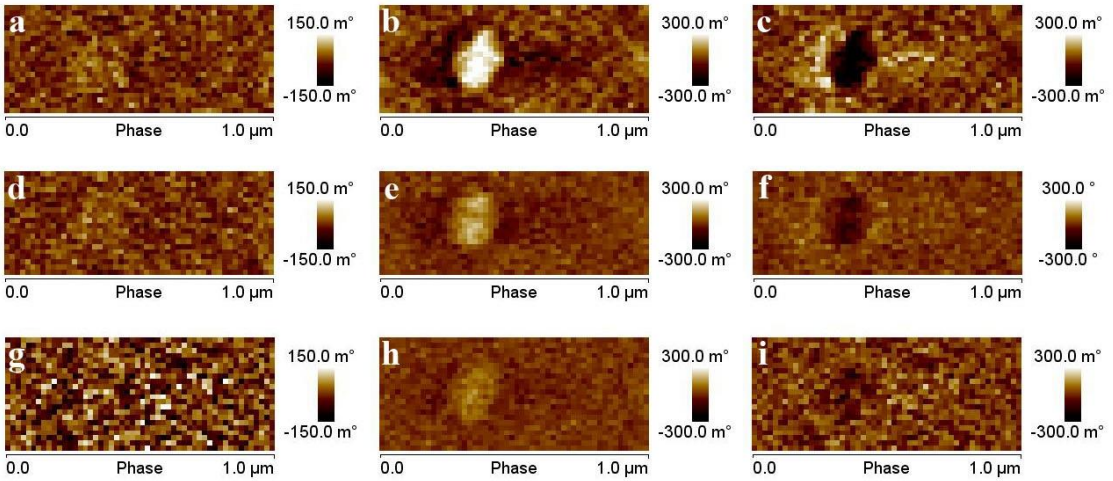

Figura 46 - Standard MFM images (a, d , g), electrostatic images (b, c, h) and CM-MFM images (c, f, i) at lift height Δz of 20 nm (a, b, c), 50 nm (d, e, f) and 80 nm (g, h, i) of a NP of 31 nm diameter.

As expected and already observed in previous works [294], [295], in electrostatic phase images, NPs exhibit positive phase contrast (in respect to the substrate), the intensity of which decreases with the increase of the tip-sample distance, pointing out the presence of detectable non-magnetic tip-NP interactions. The standard MFM images also show a positive contrast in correspondence of NPs, but lower than the corresponding electrostatic signal highlighting the presence of a magnetic effect (which, in the absence of an external magnetic field and in the case of superparamagnetic NPs, should give rise to a negative phase contrast contribution due to the attractive tip- NP interaction), which is 'hidden' by the predominant electrostatic signal and become visible only after its subtraction in CM-MFM images, which, indeed, exhibit negative contrast in correspondence of NPs, which decreases with the increase of the tip-sample distance. By measuring, for each tip-sample distance, the CM-MFM phase shift difference between the apex of the magnetic NP and the substrate and by plotting the obtained values as a function of the tip-sample distance (lift height), the magnetic phase-distance curve for each measured NP is obtained, an example of which is reported in Fig. 47a.

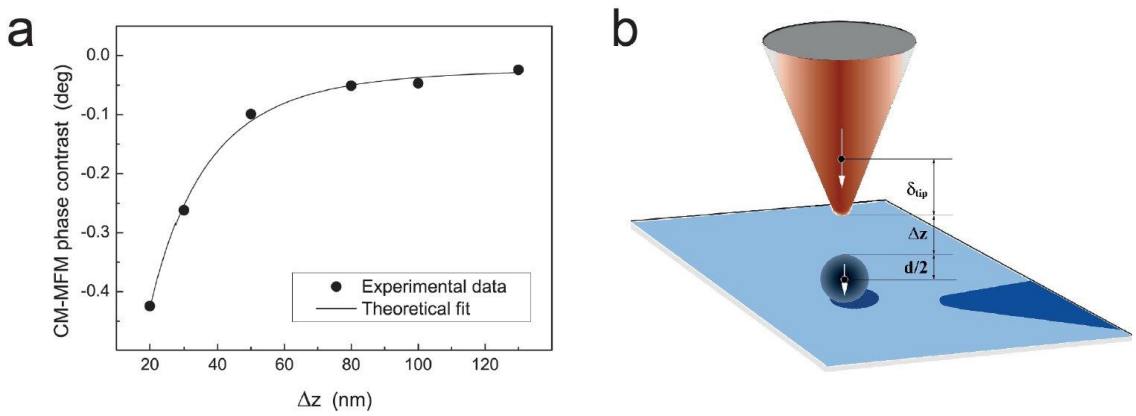

Figura 47 - (a) CM-MFM phase-distance curve (symbols) and theoretical fit (solid line); (b) sketch of the equivalent two-dipole model describing the tip- NP interaction.

In the absence of electrostatic artifacts, the tip-NP interaction can be described using the two-dipole model as sketched in Fig. 47b, where both the tip and the NP are described as two single point magnetic dipoles [294]. The magnetic phase shift can be obtained as

$$\Delta\varphi = \mu_0 m_{tip} M_{NP} \frac{Q_c}{k_c} \frac{d^3}{(\Delta z + c_s + \frac{d}{2} + A_{sp} + \delta_{tip})^5} \qquad 73)$$

where: μ_0 is the permeability of free space; Q_c and k_c are the quality factor and the spring constant of the used cantilever, respectively, which can be evaluated from the cantilever first free resonance in air; A_{sp} and Δz are the amplitude set point and the lift height selected for the specific measurement (and, therefore, are known); d is the NP diameter, measured as the NP height in topography images; c_s the thickness of the possible non-magnetic coating of the NP (which is 0 in the case of this work); M_{NP} is the magnetization of the NP; δ_{tip} is the position, in respect to the tip apex, of the equivalent magnetic dipole of the probe having moment m_{tip}. The tip moment m_{tip} and its equivalent position δ_{tip} are not known a priori and have to be determined. By fitting the $\Delta\varphi$ versus Δz experimental curves using Eq. 73, e.g., symbold and solid line in Fig. 47a, respectively, δ_{tip} can be evaluated. We repeated this procedure on 6 different NPs with different diameters, obtaining $\delta_{tip} + A_{sp} = 104 \pm 24$ *nm.*

7.3.1 - Magnetization curves measurement

After selecting an opportune lift height, different 'in-field' MFM images (using the magnetized probe) of an isolated NP are acquired in correspondence of different intensities of out-of-plane magnetic fields (H_{ext}) applied during the scan. At the same lift height, the pure electrostatic image corresponding to each NP is acquired with the demagnetized probe at $H_{ext} = 0$ and subtracted to the corresponding MFM image,

allowing the measurement of the 'pure' magnetic phase signal (corresponding to the apex of the NP) as a function of the applied magnetic field. As an example, in Fig. 48 a series of images obtained on a Fe_3O_4 NP of 31 nm diameter applying the described procedure, at lift height of 100 nm, is shown, and in particular: the topography (a), the electrostatic image at $H_{ext} = 0$ (b), the series of standard MFM images for different intensities of the applied magnetic field (c, e, g) and the series of corresponding CM-MFM images (d, f, h). The corresponding MFM and CM-MFM phase versus the applied magnetic field curves are reported in Fig. 49a and b, respectively. As visible in MFM images and in the MFM phase versus H_{ext} curves, in standard MFM images NPs exhibit a positive contrast, which is constant in correspondence of high magnetic fields (higher than 60Oe), decreasing with the decrease of the applied magnetic field, and reaches a constant value (close to zero) at about 20 Oe and lower magnetic fields intensities. Similar behavior has been observed inverting the direction of the applied magnetic fields. The reaching of a constant (saturation) value in correspondence of the highest and lowest magnetic fields values and the decrease/increase of the phase contrast with the decrease/increase of the applied magnetic field in the intermediate range indicates a relationship of the phase contrast trend with the magnetization reversal behavior, which can be also recognized observing the curve of the measured MFM phase contrast as a function of the applied field, reported, as an example, in Fig. 49a. Nevertheless, an inversion of the contrast (i.e., an inversion of the magnetization) should occur in correspondence of the reversal of the applied magnetic field. This is not observable in standard MFM images, which, indeed, give rise to a MFM phase versus applied magnetic field curve completely asymmetric in respect of both the two axes by reason of two phenomena. The first one, responsible for the fact that an inversion of the phase contrast is not visible at all in standard MFM images, is the presence of electrostatic artifacts, the effect of which is visible when comparing the MFM images with the correspondent electrostatic one. Indeed, the positive contrast detected in standard MFM images is higher than the electrostatic contrast in correspondence of high magnetic fields and lower than the electrostatic contrast in correspondence of low magnetic fields.

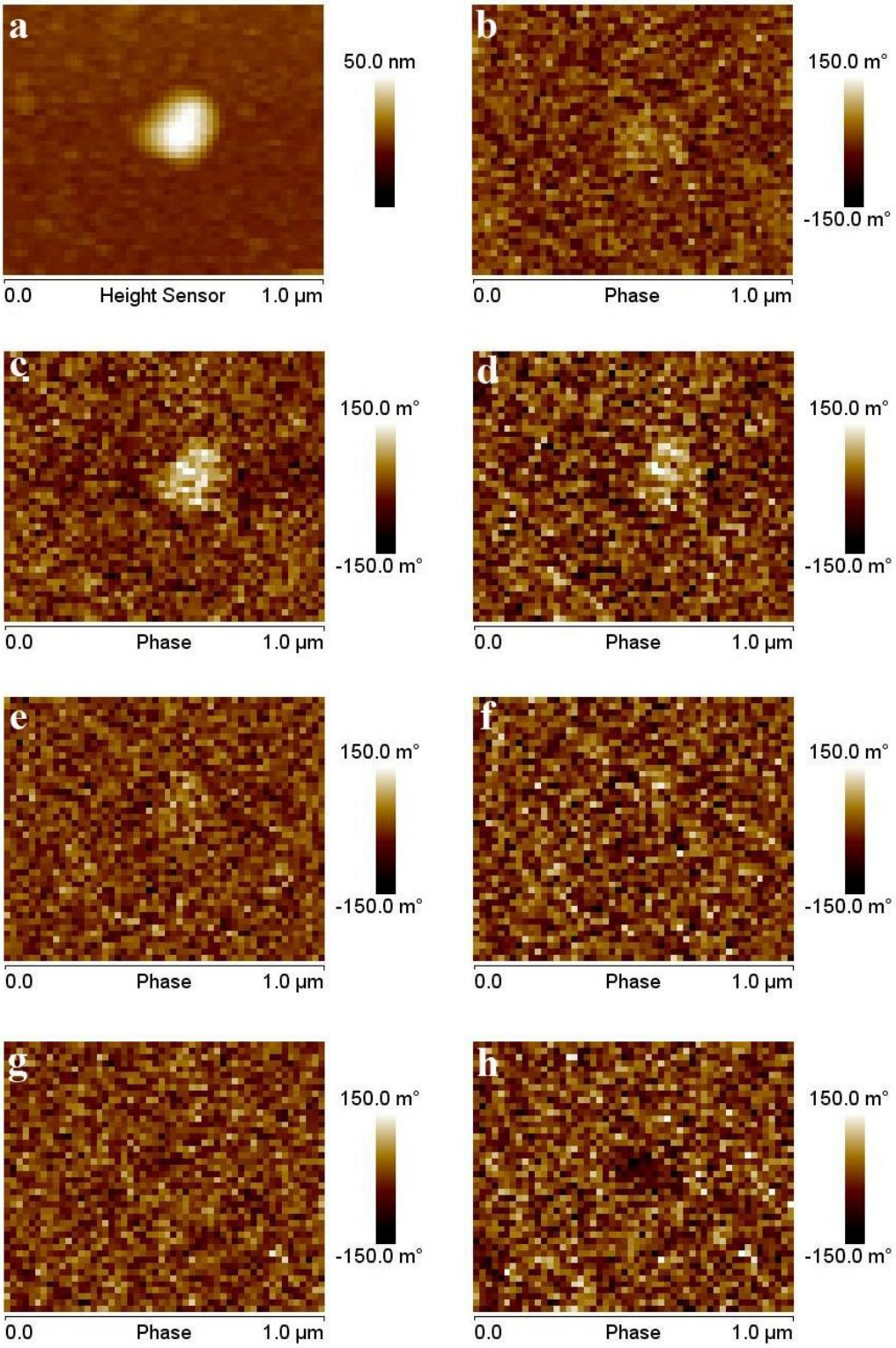

Figura 48 - Topography (a), electrostatic image at Δz=100nm and $H_{ext}=0$ (b), standard MFM images (c, e, g) and corresponding CM-MFM images (d, f, h) at H_{ext}= + 60Oe (c, d), H_{ext}= + 19Oe (e, f) and H_{ext}= -10Oe (g, h) of a NP of 31 nm diameter.

After subtracting the electrostatic effects to MFM images, an inversion of the contrast in correspondence of a value of magnetic field approximately intermediate between the

two ‘saturation’ magnetic field values is clearly visible in CM-MFM images, where the NP phase contrast is positive in correspondence of high magnetic fields and negative in images acquired at low magnetic fields. This confirms, not only the actual correspondence between the in-field CM-MFM data with the magnetization reversal curve of a NP, but also the accuracy of the measured electrostatic signal, indicated by the symmetry, in respect to the y-axis, of the curve obtained after the subtraction of the non-magnetic contribution, as shown in the curve reported in Fig. 49b. Nevertheless, as visible in both CM-MFM images and in the curve of the CM-MFM phase as a function of the applied magnetic field, the contrast inversion occurs in correspondence of magnetic field values very different from zero. This is due to the fact that the external magnetic field we apply is not the only one affecting the magnetization state of the sample, but also the magnetic stray field of the probe H_{tip} is present and produces an additional contribution to H_{ext}. This additional contribution can be, therefore, evaluated as the H_{ext} value corresponding to the center of the measured curve. From the value of H_{tip}, which we found as high as *33 ± 2 Oe*, the value of m_{tip} can be obtained from the relation

$$H_{tip} = \frac{1}{2\pi} \frac{m_{tip}}{(\Delta z + c_s + \frac{d}{2} + A_{sp} + \delta_{tip})^3} \qquad 74)$$

which gives m_{tip} = *(1.7 ± 0:4) x* 10^{-13} *emu*, in very good agreement with the (approximated) value of *1x*10^{-13} *emu* supplied by the producer. The single NP magnetization curve can be thus obtained converting the measured magnetic phase contrast in the corresponding magnetization values (M_{NP}) using Equation 73. As an example, Fig. 49c shows the calculated magnetization curve obtained from the CM-MFM phase versus H_{ext} curve reported in Fig. 49b.

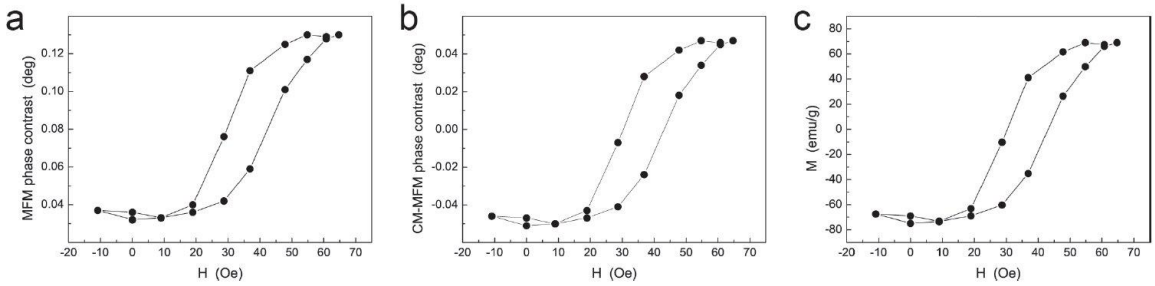

Figura 49 - (a) MFM phase versus applied magnetic field curve at Δz = 100 nm of a NP of diameter of 31 nm; (b) corresponding CM-MFM phase versus applied magnetic field curve; (c) corresponding magnetization versus applied magnetic field curve.

7.4 - RESULTS AND DISCUSSION

The described procedure has been applied to four Fe_3O_4 NPs. In Table 3, the obtained values of saturation magnetization (M_s) and coercive field (H_c) of the measured four magnetite NPs, with diameters in the range 21-32 nm, are reported.

Table 3 - Parameters obtained from the magnetization curves of four different NPs: for each NP with diameter d, the saturation magnetization Ms and the coercivity Hc are reported.

Diameter (nm)	M_s (emu/g)	H_c (Oe)
32	64±4	5.5±2
31	68±1	6.5±2
25	78±23	0
21	131±10	0

The values of Ms and the corresponding uncertainties are calculated from the two saturation magnetization values found for each curve, i.e., for positive and negative values of H_{ext}. All the values of M_s measured for the four NPs are in satisfyingly good agreement with the value of $M_s = 78$ *emu/g* measured with SQUID, considering that the latter is averaged on the whole population of NPs, and with the values of saturation magnetization of magnetite NPs reported in literature (55 - 92 emu/g) [277], [296]–[299]. Moreover, when calculating the weighted average value of saturation magnetization (using the mass of each NP as the weight in the average), *75±5 emu/g* is obtained which is in very good agreement with SQUID data.

Observing the values obtained in correspondence of the single NPs and their uncertainties, it is possible to note that the NPs with diameters around 30 nm (which is the nominal average diameter of the analyzed NPs) exhibit saturation magnetization

values close to the literature values [277], [296]–[298] and to the value obtained by SQUID. Furthermore, the small error indicates a high symmetry of the obtained curves (as also observable in Fig. 49, where the curve obtained for the NP with diameter of 31 nm is shown). These results seems to show the good operation of the technique for particles having diameter higher than 30 nm. The 25 nm sized NP shows a saturation magnetization in very good agreement with the value measured with SQUID and with the values reported in the literature. The high error indicates a significant asymmetry of the curve, which demonstrates a not accurate evaluation of the electrostatic signal in this case. A significantly higher value of saturation magnetization has been observed in correspondence of the smaller NP (21 nm). The significant and unexpected increasing of the saturation magnetization with the decreasing of the NP size could be due not to a real effect but to some limits of our procedure which could become particularly critical when the NP size decreases under a certain dimension. More specifically, in our previous works, we estimated that, with the present settings and equipment, our technique could be suitable for the study of NPs with diameter not smaller than 10 nm, being 10^{-2} *deg* the minimum value of detectable phase [294]. Nevertheless, also in correspondence of slightly higher dimensions, the magnetic sensitivity and the quantitative accuracy of the measurements are inevitably reduced. Furthermore, the volume of the NPs has been calculated considering the NPs having spherical size. This approximation, especially for very small NPs could be not realistic. Also, it is worth noting that from Fig. 49 the magnetic field H_{sat} required to saturate the magnetization of the NP is about 25 Oe. An analogous result is obtained for all magnetization curves we acquired. This result is somehow surprising if compared to the values of saturation field obtained by SQUID and commonly reported in literature, which are about 50 times bigger. Although this result deserves further investigation, we believe that a first attempt of rationalization can be done considering that NPs is our sample are much more diluted than in samples usually characterized with SQUID. Thus, the mutual interactions among NPs, which lead to a reduction of the effective magnetic field experienced by each NP, are negligible in our case. Therefore, we believe that saturation fields measured with 'global' techniques are actually overestimated due to not negligible magnetic interactions among magnetized NPs. Finally, the analysis of coercive field (H_c) of the measured NPs highlighted the presence of a certain hysteresis and thus a certain coercivity, in correspondence of bigger NPs (31 and 32 nm of diameter), while no coercivity has been detected in correspondence of NPs having

diameter lower than 25 nm, which therefore seem to exhibit a superparamagnetic behavior. Although additional and more accurate experiments are required also considering the relatively high uncertainty in the results here presented, the observation of a 'threshold effect' seems to confirm results already reported in literature, where an analogous effect was observed using standard 'global' techniques for the coercivity of magnetite NPs in the range between 25 and 15 nm [296]. Our results demonstrate that CM-MFM is a powerful technique for the magnetic characterization of single nanomaterials, allowing one to obtain the actual magnetization curve of the investigated nano-object. However, some issues still limiting the accuracy of our technique have to be addressed. Indeed, in addition to the limitation to the accuracy due to the experimental setup, e.g., the limited sensitivity of the power supply and the related possibility of not complete demagnetization of the tip [294], the analytical model used in the tip calibration should be improved, as the value of δ_{tip} retrieved from the fitting procedure shows a relatively high variation among different NPs.

Conversely, the estimation of H_{tip} is very accurate as it does not sensibly vary among different NPs. Nevertheless, the uncertainty in δ_{tip} results in an increased uncertainty in the values of m_{tip} estimated from H_{tip} using Eq. 74.

In addition, the incorrect evaluation of electrostatic forces, mainly due to a residual magnetization of the tip in its demagnetized state [294], may lead to asymmetric magnetization curves. This effect seems more dramatic in case of small NPs. Finally, the calculation of the magnetization is performed assuming a spherical geometry for the NPs which may be not correct in case of small NPs. This assumption may result in an incorrect calculation of the NP volume and thus of the magnetization. While the spherical assumption can be checked in case of bigger NPs from the topographical images, in case of smaller NPs the true geometry is difficult to assess due to the effect of tip convolution. Notwithstanding these current limitations which have to be addressed, however, CM-MFM has been proved a powerful technique for the local nanomagnetic characterization of single nanomaterials.

7.5 - CONCLUSIONS

An experimental procedure, consisting of a series of in-field CM-MFM measurements aimed to the reconstruction of the magnetic phase versus the tip-sample distance and versus the applied external magnetic field, and a data post-processing method for the quantitative magnetic characterization of single NPs have been proposed, described and

discussed in this work. The use of CM-MFM allowed us to obtain the signal originating from the sole magnetic tip-NP interaction, after subtracting the contributions due to any non-magnetic force. Consistently with previous results, the detected pure magnetic signal resulted well interpreted by the theoretical model describing the magnetic tip-NP interaction force as the interaction between two magnetic dipoles, confirming the correctness of the CM-MFM working principle. By fitting the measured magnetic phase versus distance curves and analyzing the information about the probe stray field retrieved from the measured magnetic phase versus applied magnetic field curves, we were able to calculate the unknown magnetic parameters of the used probe (i.e., the magnetic stray field H_{tip} and the magnetic moment m_{tip}), which showed a good consistency with the approximated values provided by the producer, demonstrating the efficiency of the procedure. The capability of accurately calibrating the magnetic behavior of the used probe allowed us to convert the magnetic phase values measured in correspondence of single NPs to the corresponding values of NP magnetization and to obtain the magnetization curves of single NPs as a function of the applied magnetic field, which represented one of the main open issues in the field of MFM-based characterization techniques. The proposed measurement and data analysis procedure has been tested on four Fe_3O_4 NPs having diameters in the range 21 - 32 nm, the measured saturation magnetization and coercivity values of which resulted in good agreement with the corresponding values found in the literature and with the values we measured, on the same NPs, through a SQUID analysis. It is therefore possible to conclude that, despite further analysis are needed to better evaluate the accuracy of the measured data, our CM-MFM technique has been demonstrated to be effective to perform real quantitative magnetic characterization at the nanometer scale and, in particular, on a challenging sample as single superparamagnetic nanoparticles, showing its high potentiality as a simple, not expensive, user-friendly and widely applicable nanomagnetometry tool.

8. MEASUREMENT OF THE NONMAGNETIC COATING THICKNESS OF CORE-SHELL MAGNETIC NANOPARTICLES BY CONTROLLED MAGNETIZATION MAGNETIC FORCE MICROSCOPY

L. Angeloni[1, 2, a)], D. Passeri[1, b)], F.A. Scaramuzzo[1], D. Di Iorio[3], M. Barteri[3,4],
D. Mantovani[2], M. Rossi[1,4]

[1]*Department of Basic and Applied Sciences for Engineering; University of Rome Sapienza; Via A. Scarpa 14, 00161 Rome, Italy.*
[2]*Department Min-Met-Materials Eng. & University Hospital Research Center; Laval University; Quebec City, Canada*
[3]*Department of Chemistry, SAPIENZA University of Rome, Piazzale A. Moro 5, 00185, Rome, Italy*
[4]*Research Center for Nanotechnology applied to Engineering of SAPIENZA University of Rome (CNIS), Piazzale A. Moro 5, 00185 Rome, Italy*

[a)] *Corresponding author: livia.angeloni@uniroma1.it*
[b)] *Corresponding author: daniele.passeri@uniroma1.it*

Published in:
AIP Conference Proceedings
21-24 September 2015
Location: Rome, Italy
Published: June 2016
DOI: 10.1063/1.4954489

http://aip.scitation.org/doi/abs/10.1063/1.4954489

Resumé

Les nanoparticules magnétiques (NPM) représentent un intéressant outil pour plusieurs applications biomédicales. Afin d'améliorer la stabilité de la dispersion, la biocompatibilité et la bio-fonctionnalité, les NPM doivent être revêtus de films non magnétiques. L'optimisation de ces systèmes nécessite la caractérisation detaillé non seulement du noyau magnétique, mais également des proprietés du revêtement. Outre les caracteristiques chimiques et physiques du revêtement, son épaisseur est une autre importante propriété qui peut influencer la taille, la forme et le comportement magnétique global du système. Dans ce travail, nous proposons une possible méthode pour mesurer l'épaisseur du revêtement non magnétique des NPM à l'aide de la technique de microscopie a force atomique à magnétisation contrôlée (CM-MFM). Une étude préliminaire sur l'applicabilité de la méthode proposée a été réalisée sur des NP de Fe_3O_4 revêtus d'un film de Cu.

Abstract

Magnetic nanoparticles (MNPs) represent an interesting tool for several biomedical applications. In order to improve the dispersion stability, the biocompatibility and bio-functionality, MNPs need to be coated with non-magnetic films. The optimization of these systems requires the deep characterization not only of the magnetic core, but also of the coating features. Beside the chemical and physical properties of the coating, its thickness is another important property which can influence the size, the shape and the overall magnetic behavior of the NPs system. In this work we propose a possible method to measure the thickness of the non-magnetic coating of core-shell MNPs through the use of controlled magnetization-magnetic force microscopy (CM-MFM). A preliminary study on the applicability of the proposed method has been performed on Fe_3O_4 NPs coated with a Cu film.

8.1 - INTRODUCTION

Magnetic nanoparticles (MNPs) are gaining increasing interest in many technological areas thanks to their particular magnetic properties and extremely small size. In recent years they have been extensively studied for their promising applications in biomedical field [300], such as drug delivery [301], immunoassay analyzer [302], magnetic resonance imaging (MRI) [303], and cancer hyperthermia [304].

In all of biomedicine related applications, MNPs need to be coated with non-magnetic films (e.g., SiO_2, surfactants, polymers, metals, etc.) in order to: (i) opportunely tune the surface charge to improve the dispersion stability and avoid agglomeration; (ii) prevent oxidation and corrosion phenomena; (iii) improve biocompatibility; (iv) provide functionality [282].

Therefore, several efforts are oriented to the development and the optimization of core-shell MNPs, and, in particular, on the optimization of coatings with suitable properties. To do that, appropriate characterization techniques must be used to determine and improve the relevant characteristics of the developed coating, such as the chemical composition, the structure, the surface energy, the permeability, the corrosion and oxidation resistance and the biocompatibility. Among these properties, also the coating thickness is a relevant factor to be taken into account, since it can influence, besides the total size of single MNPs, also other important properties, such as the permeability [305], i.e., the corrosion and oxidation resistance, and the overall magnetic properties of MNPs, such as the saturation magnetization [306], the NPs relaxivity (which determines the contrast agent efficacy for magnetic resonance imaging) [307] and the specific absorption rate (SAR) (which determines the efficacy for hyperthermia applications) [308], which are, of course, related to the actual fraction of non-magnetic material present in the system.

For this reason, the capability of tuning and, thus, characterizing the thickness of the coating is emerging as an essential need for the development and optimization of core-shell MNPs. Different techniques have been proposed and used to measure the MNPs coating thickness, but a standard method has not been individuated yet. For example the average thickness of the shell can be estimated through the statistical analysis of the size (i.e., diameter) of nanoparticles before and after the coating deposition, which can be performed by microscopy techniques having enough spatial resolution, such as scanning electron microscopy (SEM) or atomic force microscopy (AFM). If the dispersion of the size distributions is small in respect to the difference of their mean values, an average

evaluation of the coating thickness can be obtained by the half difference between the average diameters of the two NPs distributions. On the other hand, if the size distributions are overlapping, the estimation of coating thickness cannot be obtained with sufficient accuracy. Furthermore, these methods can be considered valid under the hypothesis that the size of the magnetic core does not change during the coating process, which is often not the case. In particular, a reduction of the volume of the magnetic core can occur during the surface modification process [309], which could result in the underestimation of the shell thickness.

An indirect evaluation of the coating thickness can be also obtained through the analysis of the magnetic properties of the uncoated and coated MNPs, which can be performed by magnetic techniques such as superconducting quantum interference devices (SQUID) magnetometry or vibrating sample magnetometry (VSM). Comparing the saturation magnetization values measured on the uncoated and coated samples, it is possible to estimate the concentration of the non-magnetic phase in the uncoated sample and, thus, deduce an average non-magnetic coating thickness value. Nevertheless, also with this method, the possible reduction of the magnetic phase resulting from the surface modification process cannot be taken into account.

A direct measurement of the coating thickness of single MNPs can be obtained by transmission electron microscopy (TEM), which, for example, has been widely used for the characterization of SiO_2 coated MNPs [310]. However, to perform TEM analysis may require a complex sample preparation and moreover not every material gives rise to a contrast high enough to allow a precise measurement of the coating thickness.

In this work, we propose an alternative method to measure the thickness of the non-magnetic coating of core-shell MNPs, based on the use of a recently introduced magnetic force microscopy (MFM) technique, called controlled magnetization MFM (CM-MFM) [311]. The proposed technique allows the measurement of the thickness of any non-magnetic coating on single MNPs, eliminating the intrinsic uncertainties of the statistical methods and avoiding the complex sample preparation procedures typical of TEM analysis. A brief description of MFM and CM-MFM working principles and of the CM-MFM procedure proposed to measure the non-magnetic coating thickness of MNPs is presented. A preliminary test of the operating principle of the technique has been carried out on Fe_3O_4 MNPs coated with a Cu film.

8.2 - THE TECHNIQUE

8.2.1 - Magnetic force microscopy

MFM is a scanning probe microscopy (SPM) technique the working principle of which is based on the detection of the magnetostatic interactions between a magnetic probe and a magnetic sample. In this technique, each line of the analyzed sample area is scanned twice. The first scan, performed in standard tapping mode, allows the reconstruction of the sample topography. The second scan is performed in dynamic non-contact mode at a selected tip-sample distance (Δz), with the probe following the trajectory of the previously recorded sample profile in order to maintain the tip-sample distance constant in each point of the scanned area. In this way, the dynamic behavior of the cantilever during the second scan is independent on the morphology of the surface and is affected only by the long-range (magnetostatic and electrostatic) interaction forces, allowing the reconstruction of a map of the magnetic domain configuration of the sample with the nanometric resolution typical of the SPM techniques. The magnetic map can be reconstructed from the amplitude, the frequency or the phase shift of the cantilever. In this work, the data were acquired using the phase shift signal, which is proportional to the first gradient of the tip-sample interaction force:

$$\Delta\varphi = -\frac{Q_c}{k_c}\frac{\partial F_z}{\partial z} \qquad 75)$$

where Q_c and k_c are, respectively, the quality factor and the elastic constant of the cantilever, and $\partial F_z/\partial z$ is the gradient along z of the detected tip-sample interaction force F_z, which, ideally, coincides with the magnetostatic interaction force between the probe and the sample and depends on the magnetic state of the tip and the sample.

MFM is a widely used technique for the mapping and the qualitative characterization of the magnetic domain configuration of magnetic materials [312], but its application to the quantitative measurement of physical parameters is still limited [313]. Indeed, also long-range electrostatic forces can be detected during the second scan, giving rise to an additional signal which makes the quantitative relationship between the detected MFM signal and the effective magnetization of the sample impossible [270]. A method to remove electrostatic artifacts is thus needed to perform quantitative measurements through MFM. In order to avoid artifacts due to the electrostatic tip-sample interactions and detect the signal exclusively due to the magnetic forces, different techniques have been proposed [314]. Among them, controlled magnetization MFM (CM-MFM), the

working of which is described in the following paragraph, is easy to be implemented and it has already been demonstrated to be effective in the detection of the real magnetic signal in correspondence of MNPs [311].

8.2.2 - Controlled magnetization MFM

In order to perform CM-MFM, a standard MFM apparatus must be equipped with an electromagnet, which allows the application of controllable out-of plane static magnetic fields to the tip-sample system, without moving the probe from the scan area. This system is used to tune the magnetization state of the probe (i.e. magnetize and demagnetize the probe), as described in the following.

Before the sample analysis, the probe is subjected to a calibration procedure aimed to the measurement of its remanent hysteresis curve, i.e. the individuation of the remanent saturation magnetic field ($H_{rs,tip}$) and the remanent coercive field ($H_{rc,tip}$). This can be obtained by using a reference sample with high coercivity and easily observable magnetic domains (e.g., a floppy disk). By acquiring MFM images after the application (and the switching off) of external magnetic fields with different intensities and plotting the detected magnetic contrast as a function of the applied (and switched off) magnetic field, the remanent magnetization curve (i.e., $H_{rs,tip}$ and $H_{rc,tip}$) of the probe is obtained.

Magnetic images of the sample, depurated of any electrostatic effect, are obtained by acquiring two images with two different magnetization state of the sample. A first standard MFM image, representative of the signal due to the sum of the electrostatic and magnetic interaction forces ($\Delta\varphi_{el}+\Delta\varphi_{magn}$), is acquired with the tip magnetized in its (remanent) saturation state. Then, the tip is demagnetized by the application (and switching off) of its remanent coercive field ($-H_{rc}$) (measured through the previously performed calibration procedure) and a second image, representative of the sole electrostatic signal ($\Delta\varphi_{el}$), is acquired using the same scanning parameters of the first image. Subtracting the second image to the first one, an image representing the sole magnetic signal is obtained, being ($\Delta\varphi_{el} + \Delta\varphi_{magn}$) - ($\Delta\varphi_{el}$) = $\Delta\varphi_{magn}$. Repeating the procedure for different values of lift height (Δz), it is thus possible to obtain a curve of the “pure” magnetic phase contrast as a function of the lift height distance, which, in the case of the analysis of MNPs, has been demonstrated to be well fitted by the theoretical model describing the tip and the MNP as two magnetic dipoles [311].

8.2.3 - Measurement of the thickness of the non-magnetic coating of MNPs by CM-MFM

Since the interaction between the tip and a coated nanoparticle can be modeled as that of two magnetic dipoles, the magnetic phase $\Delta\varphi$ is related to the thickness c of the coating and to the lift height Δz through the equation:

$$\Delta\varphi = A\frac{(d-2c)^3}{(\Delta z + \frac{d}{2} + \delta_{tip})^5} \quad 75)$$

where A is a coefficient which depends on the magnetic moment of the tip and on the magnetization of the magnetic core of the nanoparticle, δ_{tip} indicates the effective position of the magnetic moment which represents the tip, and d is the diameter of the NP [311]. The unknown parameters A and δ_{tip} can be determined by measuring the $\Delta\varphi$ versus Δz curve on the uncoated NPs and by fitting it with Eq. 75 imposing $c = 0$. Then, $\Delta\varphi$ versus Δz curve measured on the coated MNPs using the same tip and the same scanning parameters can be fitted with the values of A and δ determined on the uncoated MNPs, allowing the determination of the coating thickness c.

8.3 - MATERIALS AND METHODS

8.3.1 - Instrumentation

AFM and CM-MFM analysis have been performed through an Icon (Bruker Inc.) AFM apparatus, using a magnetic probe (MESP, Bruker). To implement CM-MFM technique, the standard instrumental apparatus was equipped with an electromagnet of 1050 coils, placed under the sample, which allows the application of controllable out-of plane static magnetic fields H in the range -480 Oe $< H < +480$ Oe to the tip-sample system. As reference sample for the probe magnetic calibration, a floppy disk has been used.

8.3.2 - Magnetic nanoparticles

Magnetic Fe_3O_4 and core-shell Fe_3O_4@Cu nanoparticles (NPs) were synthesized by chemical co-precipitation method according to a procedure optimized in our group [315]. Experimental details are reported below.

Synthesis of Fe_3O_4 NPs. 1.313 g (3.35 mmol) of Mohr salt ($(NH_4)_2Fe(SO_4)_2 \cdot 6H_2O$), 1.638 g (2.04 mmol) of $Fe_2(SO_4)_3$ and 0.919 g of polyvinylpyrrolidone (PVP) were

dissolved in 200 mL of distilled water. Under mechanical stirring and argon atmosphere, this Fe^{2+}/Fe^{3+} solution was added into 600 mL of a 0.7 M ammonia solution containing additional 0.911 g of PVP. The solution was left to react for 30 minutes at room temperature turning from orange to black, and then heated at 80 °C for 30 minutes. After cooling down, the reaction mixture was centrifuged at 3000 rpm for 10 minutes, the product was washed with NaCl (satured aqueous solution) and H_2O, separated by magnetic decantation, washed again with double distilled water, and finally dried under vacuum.

Synthesis of Fe_3O_4@Cu NPs. 295 mg (1.2 mmol) of ($Cu(NO_3)_2 \cdot 3H_2O$) were dissolved in 10 mL of distilled water. This solution was added to a dispersion of 405 mg of Fe_3O_4 NPs and 420 mg (2.4 mmol) of ascorbic acid in 300 mL of distilled H_2O, thermostated at 45°C and mechanically stirred. After 60 min reaction, the mixture was cooled down and washed several times with double distilled water. The precipitate was finally separated by magnetic decantation. In order to get a more homogeneous Cu layer, the procedure was repeated twice.

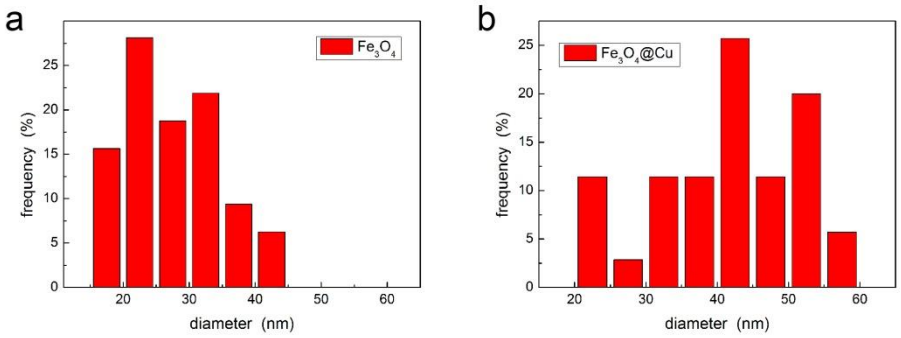

Figura 50 - Histogram of the diameters distribution of Fe_3O_4 NPs (a) and Fe_3O_4@Cu NPs (b) measured by AFM.

8.4 - RESULTS AND DISCUSSION

8.4.1 - Size (AFM) analysis

A preliminary analysis on the morphology and the size distribution of the Fe_3O_4 and Fe_3O_4@Cu NPs has been carried out by AFM. As an example, in Fig. 50 the histograms of the diameters of two samples of NPs deposited on a silicon wafer are reported. The Fe_3O_4 NPs exhibited diameters in the range 15-45 nm with an average diameter of 28 nm, while the Fe_3O_4@Cu NPs exhibited diameters in the range 20-60 nm with an

average diameter of 42 nm. An estimation of the coating thickness can thus be obtained by the half difference of the average diameters, which gives rise to an average coating thickness of 7 nm.

8.4.2 - CM-MFM analysis

CM-MFM measurements have been performed, without applying any external magnetic fields during the scans, following the standard procedure previously described.

Before analyzing the two samples of NPs, the calibration of the probe has been performed and the saturation field $H_{rs,tip}$= 440 Oe and the coercive field $H_{rc,tip}$= 285 Oe have been found.

"Magnetic" phase-distance curves have been obtained by acquiring standard MFM images, with the probe magnetized in its saturation state (through the application - and the switching off - of a magnetic field $H_{rs,tip}$ = 440 Oe), at different lift heights. Then, the magnetization of the probe has been nullified through the application of $-H_{rc,tip}$ = -285 Oe and "electrostatic images" of the same NPs have been acquired using the same scanning parameters and at the same lift-heights of the previously recorded standard MFM images. The "pure" magnetic images, for each lift-height, have been obtained by subtracting the "electrostatic images" to the standard MFM images. The phase signal, for each image, has been calculated as the difference between the phase measured in correspondence of the apex of the NP and the phase measured in correspondence of the silicon substrate.

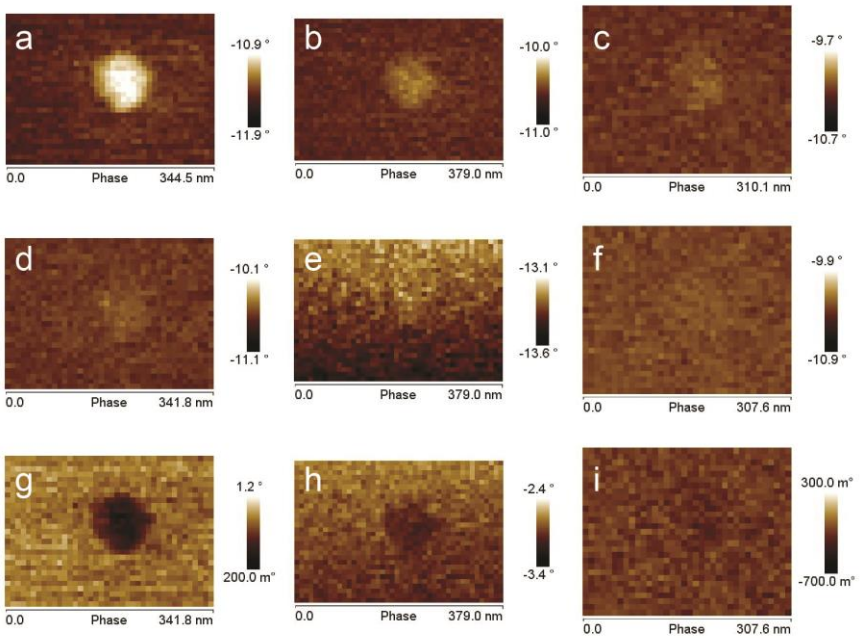

Figura 51 - - Phase images of a Fe_3O_4 NP obtained with the demagnetized probe at Δz = 30 nm (a), Δz = 50 nm (b) and Δz = 80 nm (c); phase images obtained with the magnetized probe (standard MFM images) at Δz = 30 nm (d), Δz = 50 nm (e) and Δz = 80 nm (f); phase images; phase images obtained by the subtraction of the images measured with the demagnetized probe to the images obtained with the magnetized probe at Δz = 30 nm (g), Δz = 50 nm (h) and Δz = 80 nm (i).

As an example, in Fig. 51, the standard MFM images (a, b, c), the electrostatic images (d, e, f) and the resulting "pure" magnetic images (g, h, i) obtained for a Fe_3O_4 NP in correspondence of different lift heights (30, 50, 80 nm) are shown. A positive phase contrast, representative of a repulsive tip-MNP interaction (or less attractive tip-MNP interaction in respect to the tip-silicon substrate interaction), has been observed in standard MFM images for each lift height. Being the measurements carried out without applying any external magnetic field and, thus, being the superparamagnetic nanoparticle magnetized by the only magnetic stray field of the probe, the detected MFM signal cannot be explained taking into account the only magnetic tip-NP interaction, which should give rise to a negative phase contrast (i.e., attractive tip-NP interaction). Therefore, the detected "standard MFM contrast" indicates the presence of significant non-magnetic tip-NP interactions in MFM measurements, as already observed in other works [270], which appear to be higher than the magnetic force in correspondence of each tested lift height.

The positive "standard MFM phase contrast" decreases with the increasing of the tip-sample distance, until becoming null in correspondence of high tip-sample separations ($\Delta z \approx 130$nm). As expected, the electrostatic images showed positive phase contrast in

correspondence of all the tested lift heights, confirming the presence of non magnetic interactions. Furthermore, the "electrostatic contrast" resulted higher than the correspondent contrast detected on standard MFM images, indicating the presence, in the latter, of a detectable magnetic signal produced by the magnetic attraction between the magnetic probe and the magnetized NP, by the probe stray field, in the same direction of the probe magnetization. This magnetic interaction appears clearly visible in the "pure" magnetic images (negative phase contrast) obtained after the subtraction of the electrostatic images to the MFM ones.

The CM-MFM analysis has been repeated for two Fe_3O_4 NPs and two Fe_3O_4@Cu NPs. Subtracting the phase values measured from the standard MFM and electrostatic images in correspondence of different lift heights, the trend of the pure magnetic signal (phase) as a function of the tip-NP distance has been obtained for each NP (shown in Fig. 52) and has been used to calculate the thickness of the coating of Fe_3O_4@Cu NPs.

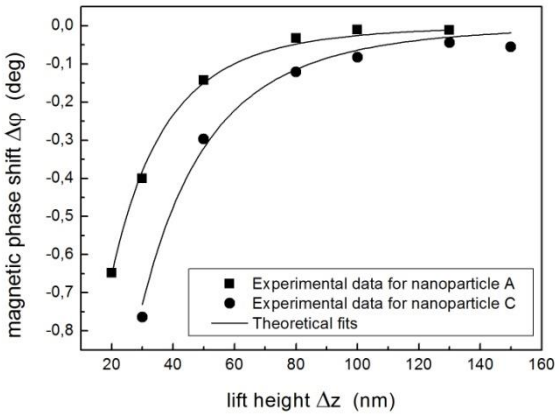

Figura 52 - Magnetic phase shift versus lift height for a uncoated (NP A) and a coated (NP C) nanoparticle, with the corresponding theoretical fits.

To determine the values of the unknown parameters A and δ_{tip}, the $\Delta\varphi$ versus Δz curves obtained on the uncoated Fe_3O_4 NPs (NPs A and B in Table 1) were fitted using Eq. 75 by imposing $c = 0$ to calibrate A and δ_{tip}, which were eventually used in the fitting of the $\Delta\varphi$ versus Δz curves obtained on the coated NPs (NPs C and D in Table 1), an example of which is the $\Delta\varphi$ versus Δz curve retrieved on a Fe_3O_4@Cu nanoparticle (NP C) reported in Fig 52. Thus, the values c of the thickness of the coating of each NP were determined, which are reported in Table 4. The values of c are coherent with the mean value of the thickness of the coating expected from statistics on AFM topographies. However, although the results reported in this work are not sufficient to fully validate

the method, our results demonstrates the potential of CM-MFM for the characterization of the thickness of the nonmagnetic coating of core-shell magnetic NPs.

TABLE 4. Summary table of the analyzed NPs, their outer diameter and non-magnetic coating thickness.

Analyzed NP	Type of NP	Outer diameter (AFM)	Coating thickness (CM-MFM)
A	Fe_3O_4	21 nm	-
B	Fe_3O_4	18 nm	-
C	Fe_3O_4@Cu	50 nm	11 ± 2 nm
D	Fe_3O_4@Cu	43 nm	8 ± 2 nm

8.5 - CONCLUSIONS

In this work we proposed a new method for the measurement of the thickness of the non-magnetic coating of magnetic nanoparticles, based on the use of CM-MFM technique. As a verification of the effectiveness of the technique we carried out a preliminary analysis on two Fe_3O_4 and two Cu-coated Fe_3O_4 NPs. CM-MFM has been successfully used to eliminate the significant electrostatic effects observed in standard MFM images and to detect the pure magnetic signal in correspondence of each analyzed NP. The pure magnetic signal versus the tip-sample distance curves detected in correspondence of all the analyzed NPs exhibited a trend which is well fitted by the theoretical model describing the tip-NP interaction as the interaction between two magnetic dipoles. The “dipole model” has thus been used to calculate the thickness of the coating of the core-shell NPs. The coating thickness obtained values presented good agreement with the average values obtained by the statistical analysis carried out by AFM on the two kinds of NPs. Nevertheless, further more statistically significant analysis need to be performed in order to assess the accuracy and the reproducibility of the technique.

9. CONCLUSIONS AND PERSPECTIVES

The objective of the presented study was to develop an AFM-based technique for the quantitative measurement of magnetic parameters (saturation magnetization M_s, coercivity H_c and magnetization reversal curve *M(H)*) of single magnetic nanoparticles to be used for biomedical purposes.

Indeed, as discussed in Chapter 1, ferromagnetic materials, when their dimensions are reduced to the nanoscale, exhibit very particular magnetic properties (superparamagnetic character), which can be exploited in several diagnostic and therapeutc applications, such as contrast agents for MRI, carriers for drug delivery and hyperthermia systems and markers for cell labeling. The development and optimization of these systems require a deep understanding of the magnetic behavior of the used nanomaterials, and, therefore, a detailed characterization of their main magnetic properties.

NPs systems are conventionally characterized by statistical techniques which allow the measurement of the overall magnetic parameters of numerous ensembles of NPs in the form of patterns or ferrofluids, which, however, do not allow the complete comprehension of all the mechanisms regulating the magnetic NPs system comportment, such as the dependence with other chemical and physical properties (e.g. the composition, the structure, the size, the shape) and the effects of the mutual inter-particles dipolar interactions. For this reason several efforts are focused on the development of high resolution and nano-element sensitive techniques able to measure the magnetic parameters of single nanoparticles and, thus, deepen the understanding of all the factors influencing the magnetic behavior of single elements and affecting the efficiency of the overall system.

Among other high resolution techniques, the working principles and the limitations of which have been briefly described and discussed in paragraph 1.3, Magnetic Force Microscopy, thanks to its nanometric lateral resolution, high sensitivity, applicability to all kind of magnetic nanomaterials without particular sample preparation and not expensive instrumental apparatus, is emerging as a potential tool for the characterization of single magnetic nanomaterials.

In Chapter 3, the working principle, the mechanisms of contrast formation and the theoretical models the basis of the interpretation of magnetic images, as well as the main application fields and the most recent advancements regarding MFM techniques

have been described and analysed. From the analysis of the state of the art, some opens issues have been identified as the main drawbacks limiting the application of the technique to the quantitative magnetic characterization of single magnetic nanoparticles, which can be summarize as follows:

i) The presence of non-magnetic tip-sample interactions, which produce an additional signal in MFM measurements, making difficult the extrapolation of the "pure" magnetic contribution and, therefore, the quantitative interpretation of the measured data;

ii) The effect of the mutual magnetic tip-sample interactions and, more specifically, in the case of magnetic nanoparticles, the presence of the probe magnetic stray field during the scan, which cannot easily be quantified and which can change the magnetization state of the sample during the measurement;

iii) The lack of a theoretical model describing the magnetic tip-NPs interactions consistently with experimental data and the consequent difficulty in "converting" the measured data in the values of real physical parameters such as the NP magnetization.

The significant presence of a non-magnetic contribution in MFM images has been demonstrated in the first preliminary experimental results presented in this thesis in Chapter 5, where an apparently repulsive interaction between the tip and the NP has been detected by performing "MFM" measurements with not magnetized probes and has been ascribed to the tip-sample capacitive coupling. The detected non-magnetic contrast, when compared with the contrast detected using standard magnetized probe in the absence and presence of an external magnetic field, resulted to be quantitatively significant and, thus, the possible main cause of the inconsistency between the experimental data and the theoretical model describing the tip-Np interactions as a "pure" magnetic interaction. Therefore, the development of experimental procedures and/or theoretical models able to eliminate and/or estimate these nonmagnetic contributions appeared to be necessary in order to use MFM technique as a tool for the accurate quantitative magnetic characterization of materials at the nanoscale. The preliminary results also showed the effect of the probe stray field, confirming the necessity of taking into account also the magnetic characteristics of the probe in order to quantitatively interpret MFM results.

The evidence of the necessity of a methodology to evaluate and to eliminate the electrostatic effects in MFM images retrieved from both the analysis of the literature

and from the preliminary results, led us to conceive the strategy which has been described in paragraphs 4.1 and 4.3 of this thesis and which has been followed to achieve the main goal of this research, i.e. the quantitative magnetic characterization of single MNPs by MFM, as well as the secondary result of measuring the thickness of the non-magnetic coating of single core-shell nanoparticles by MFM.

A new MFM-based approach, called Controlled Magnetization – MFM (CM-MFM), has been developed and described in Chapter 6, in which two subsequent images of the same area are collected, one with the magnetized and one with the "demagnetized" probe, and the "pure" magnetic signal is retrieved by subtracting the signal measured in the second image to the signal measured in the first one. This is possible through the determination of the remanent saturation and remanent coercivity magnetic fields of the actually used probe performed using a reference sample with periodically patterned magnetic domains. The effectiveness of CM-MFM technique has been demonstrated through the analysis of a non-magnetic agglomerate deposited on a floppy disk, the non-magnetic signal of which disappeared in CM-MFM images, after the subtraction of the signal detected in the measurements performed with the demagnetized probe, and through a challenging case study, i.e., the characterization of superparamagnetic NPs in the absence of any applied external magnetic field. Once the electrostatic artifacts are removed, the tip-NP interaction has been demonstrated to be well described by that of two single-point magnetic dipoles, indicating the effectiveness of the technique in the removal of electrostatic artifacts in MFM maps and the possibility of retrieving quantitative information about the magnetization state of single NPs through the use of the individuated theoretical model.

Once developed a method to remove the electrostatic artifacts in MFM images and determined the theoretical model relating the measured CM-MFM signal with the NP magnetization, it has been possible to quantitatively measure the magnetization reversal curve of single MNPs through an experimental procedure, consisting in a series of in-field CM-MFM measurements, and a data post-processing method, which has been proposed, described, discussed and tested in the work reported in Chapter 7 of this thesis. The proposed procedure allowed the calculation the unknown magnetic parameters of the used probe and to retrieve the magnetization values of single NPs as a function of an applied magnetic field. The technique has been tested performing the

analysis on four Fe_3O_4 NPs, the measured saturation magnetization and coercivity values of which resulted in good agreement with the corresponding values present in the literature and with the measured values, on the same NPs, through a SQUID analysis.
It is therefore possible to conclude that, despite the fact that further analysis are needed to better evaluate the accuracy of the measured data, controlled magnetization MFM technique has been demonstrated to be effective to perform real quantitative magnetic characterizations at the nanometer scale and, in particular, on a challenging sample as single superparamagnetic nanoparticles, which was the main objective of the PhD project.

Furthermore, the development of CM-MFM and the inviduation of the model describing the tip-NP interactions allowed us also to propose a new method for the measurement of the thickness of the non-magnetic coating of magnetic nanoparticles, based on the use of CM-MFM procedure described in Chapter 8 of this thesis. As a verification of the effectiveness of the technique a preliminary analysis on two Fe_3O_4 and two Cu-coated Fe_3O_4 NPs has been carried out. The “dipole model” has thus been used to calculate the thickness of the coating of the core-shell NPs. The coating thickness values obtained presented good agreement with the average values obtained by the statistical analysis carried out by AFM on the two kinds of NPs. Nevertheless, further more statistically significant analysis need to be performed in order to assess the accuracy and the reproducibility of the technique.

10. LIMITS OF CM-MFM

The obtained results demonstrated that, in principle, CM-MFM may represent a powerful technique to delete electrostatic artifacts resulting from tip-sample capacitive coupling in MFM images and to retrieve quantitative information about the main magnetic characteristics of single nanoparticles with diameter lower than 100 nm.

As described in detail in paragraph 6.5 of this thesis, despite the potentiality and the correctness of its working principle, the technique is characterized by some limitations, mainly due to practical issues related to the experimental setup, the understanding and solving of which represent the main challenges of the current and future work of improvement of CM-MFM.

First of all, being a two-pass technique, the correctness of topographic images is an essential prerequisite for the accuracy of CM-MFM. Artifacts in the reconstruction of the topography, e.g., due to incorrect choice of instrumental parameters like set-point, scan rate, or feedback gain, result in artifacts in the magnetic images which cannot be corrected. This problem is somewhat more severe in CM-MFM as two subsequent images of the same area have to be acquired, with the magnetized and the demagnetized tip, respectively. These issues affect CM-MFM as well as any other two-pass technique. In addition, since the MFM phase shift depends on the instrumental parameters (e.g., drive frequency and amplitude, set-point amplitude), the same parameters must be used in the calibration on the reference sample (e.g., the floppy) and in the analysis of the investigated sample (e.g., the NPs).

Another important limitation is represented by the method used to obtain the nullify the magnetization of the probe, which, in most cases, gives rise to a not complete demagnetization of the tip. Depending on the sensitivity of the power supply, indeed, the experimental setup is characterized by a minimum step allowed between two values of the applied magnetic field. In the case of the developed instrumental apparatus, for example, the minimum allowed step between two values of magnetic field is 15 Oe. Apart from particular and occasional cases in which $-H_{rc,tip}$ coincides with one of applicable values of magnetic field, this demonstrates that with our experimental setup it is not possible to reach the complete demagnetized state of the tip. In most cases, the effect of the incomplete demagnetization of the probe can be quantified and correct, as described and demonstrated in paragraph 6.5.

Although potentially capable to correct CM-MFM data, the described procedures are admittedly a bit intricate and lengthen the whole CM-MFM procedure introducing additional sources of uncertainty. Therefore, notwithstanding the possibility of correcting CM-MFM data, the incomplete demagnetization of the tip represents a serious limitation to the accuracy of the technique. Nevertheless, an improved setup, for example a power supply with higher sensistivity, could be considered in order to improve the technique accuracy. Also, a more effective demagnetization procedure could be selected, e.g., through the use of damped oscillating magnetic fields.

Another current limit of CM-MFM is that the tip calibration procedure for the determination of the coercive field is performed using the floppy reference sample at a certain distance along the axis of the coil. The field generated by the coil, nevertheless, decreases as the distance from the coil along its axis increases. Therefore, if the sample is placed on the top of the coil, variations in the sample thickness result in variations in the distance between the tip and the coil and, thus, in the height at which the tip demagnetization procedure is performed. On samples much thinner or thicker than the floppy (including possible additional substrates), the demagnetization step is performed at height from the coil different from that at which calibration was performed. This leads to an incorrect demagnetization during the experiment with a residual magnetization of the probe significantly bigger than that estimated, dramatically affecting the accuracy of the measurement. Therefore, great attention has to be paid to perform the tip demagnetization at the same height in both the calibration step on the floppy and in the analysis of the NPs. This strategy, however, may be hardly applicable in some specific cases, e.g., if the sample to be analyzed is particularly thick. In this case, no correction can be carried out. Also in this case, a possible solution could be the use of a different demagnetization procedure, i.e., using oscillating damped magnetic field. Depending on the initial values of magnetic field, this procedure could allow a certain margin of variation of the tip-coil distance without compromising the accuracy of the tip demagnetization.

11. FUTURE PERSPECTIVES

As highlighted in the previous paragraph describing the current open issues of CM-MFM, the main limitation of the technique is represented by the instrumental apparatus used and, in particular, by the procedure used to obtain the demagnetization of the probe.

The future works will, therefore, improve the instrumentation and, in particular, the development of a system able to in-situ demagnetize the probe by applying a damped oscillating magnetic field. This must allow one to improve the accuracy of the technique as well to reduce the time neccessary for the measurements, eliminating the necessary probe calibration procedure.

A systematic and statistically significant analysis should be performed on Fe_3O_4 NPs and other kind of nanoparticles with different characteristics in order to verify the accuracy and the applicability to all kind of samples of the technique.

Once verified the operation principle and the accuracy of the technique, CM-MFM could be used for the study of phenomena characterizing the nanomagnetism at the nanoscale, such as:

1) Study of the saturation magnetization, coercivity and magnetization reversal curve shape of NPs as a function of their size and their shape;
2) Study of the effect of the mutual inter-particle interactions, for example analyzing the saturation magnetization, coercivity and magnetization reversal curve shape in dependence of the conformation and spatial distributions of NPs (e.g. monomers, dimers, trimers, patterns with different inter-particles distances).

Future works will also concern the verification and validation of CM-MFM as a tool for the measurement of the non-magnetic coating of core-shell magnetic nanoparticles. More significant statistical analysis have to be performed on a higher number of nanoparticles and results could be compared with the results obtained by TEM measurements on the same kind of nanoparticles.

REFERENCES

[1] G. Herzer, «Chapter 3 Nanocrystalline soft magnetic alloys», in *Handbook of Magnetic Materials*, vol. 10, Elsevier, 1997, pagg. 415–462.

[2] K. J. Widder, A. E. Senyel, e G. D. Scarpelli, «Magnetic microspheres: a model system of site specific drug delivery in vivo», *Proc. Soc. Exp. Biol. Med. Soc. Exp. Biol. Med. N. Y. N*, vol. 158, n. 2, pagg. 141–146, giu. 1978.

[3] K. Mosbach e U. Schröder, «Preparation and application of magnetic polymers for targeting of drugs», *FEBS Lett.*, vol. 102, n. 1, pagg. 112–116, giu. 1979.

[4] Q. A. Pankhurst, J. Connolly, S. K. Jones, e J. Dobson, «Applications of magnetic nanoparticles in biomedicine», *J. Phys. Appl. Phys.*, vol. 36, n. 13, pagg. R167–R181, lug. 2003.

[5] Q. A. Pankhurst, N. T. K. Thanh, S. K. Jones, e J. Dobson, «Progress in applications of magnetic nanoparticles in biomedicine», *J. Phys. Appl. Phys.*, vol. 42, n. 22, pag. 224001, nov. 2009.

[6] K. J. Widder, R. M. Morris, G. A. Poore, D. P. Howard, e A. E. Senyei, «Selective targeting of magnetic albumin microspheres containing low-dose doxorubicin: total remission in Yoshida sarcoma-bearing rats», *Eur. J. Cancer Clin. Oncol.*, vol. 19, n. 1, pagg. 135–139, gen. 1983.

[7] J. Dobson, «Magnetic nanoparticles for drug delivery», *Drug Dev. Res.*, vol. 67, n. 1, pagg. 55–60, gen. 2006.

[8] J. Dobson, «Magnetic micro- and nano-particle-based targeting for drug and gene delivery», *Nanomed.*, vol. 1, n. 1, pagg. 31–37, giu. 2006.

[9] S. C. McBain, H. H. P. Yiu, e J. Dobson, «Magnetic nanoparticles for gene and drug delivery», *Int. J. Nanomedicine*, vol. 3, n. 2, pagg. 169–180, 2008.

[10] C. S. Brazel, «Magnetothermally-responsive Nanomaterials: Combining Magnetic Nanostructures and Thermally-Sensitive Polymers for Triggered Drug Release», *Pharm. Res.*, vol. 26, n. 3, pagg. 644–656, mar. 2009.

[11] A. D. Grief e G. Richardson, «Mathematical modelling of magnetically targeted drug delivery», *J. Magn. Magn. Mater.*, vol. 293, n. 1, pagg. 455–463, mag. 2005.

[12] R. T. Gordon, J. R. Hines, e D. Gordon, «Intracellular hyperthermia. A biophysical approach to cancer treatment via intracellular temperature and biophysical alterations», *Med. Hypotheses*, vol. 5, n. 1, pagg. 83–102, gen. 1979.

[13] R. K. Gilchrist, R. Medal, W. D. Shorey, R. C. Hanselman, J. C. Parrott, e C. B. Taylor, «Selective inductive heating of lymph nodes», *Ann. Surg.*, vol. 146, n. 4, pagg. 596–606, ott. 1957.

[14] R. W. Rand, M. Snyder, D. Elliott, e H. Snow, «Selective radiofrequency heating of ferrosilicone occluded tissue: a preliminary report», *Bull. Los Angeles Neurol. Soc.*, vol. 41, n. 4, pagg. 154–159, ott. 1976.

[15] H. Matsuki, T. Yanada, T. Sato, K. Murakami, e S. Minakawa, «Temperature-sensitive amorphous magnetic flakes for intratissue hyperthermia», *Mater. Sci. Eng. A*, vol. 181–182, pagg. 1366–1368, mag. 1994.

[16] R. E. Rosensweig, «Heating magnetic fluid with alternating magnetic field», *J. Magn. Magn. Mater.*, vol. 252, pagg. 370–374, nov. 2002.

[17] S. Laurent *et al.*, «Magnetic Iron Oxide Nanoparticles: Synthesis, Stabilization, Vectorization, Physicochemical Characterizations, and Biological Applications», *Chem. Rev.*, vol. 108, n. 6, pagg. 2064–2110, giu. 2008.

[18] Y. Jun, J. Seo, e J. Cheon, «Nanoscaling Laws of Magnetic Nanoparticles and Their Applicabilities in Biomedical Sciences», *Acc. Chem. Res.*, vol. 41, n. 2, pagg. 179–189, feb. 2008.

[19] A. Roch, R. N. Muller, e P. Gillis, «Theory of proton relaxation induced by superparamagnetic particles», *J. Chem. Phys.*, vol. 110, n. 11, pag. 5403, 1999.
[20] M. Corti *et al.*, «Magnetic properties of novel superparamagnetic MRI contrast agents based on colloidal nanocrystals», *J. Magn. Magn. Mater.*, vol. 320, n. 14, pagg. e320–e323, lug. 2008.
[21] A. Laghi, P. Paolantonio, F. Iafrate, F. Altomari, C. Miglio, e R. Passariello, «Oral contrast agents for magnetic resonance imaging of the bowel», *Top. Magn. Reson. Imaging TMRI*, vol. 13, n. 6, pagg. 389–396, dic. 2002.
[22] P. F. Hahn *et al.*, «First clinical trial of a new superparamagnetic iron oxide for use as an oral gastrointestinal contrast agent in MR imaging.», *Radiology*, vol. 175, n. 3, pagg. 695–700, giu. 1990.
[23] T. F. Jacobsen *et al.*, «Oral magnetic particles (ferristene) as a contrast medium in abdominal magnetic resonance imaging», *Acad. Radiol.*, vol. 3, n. 7, pagg. 571–580, lug. 1996.
[24] S. Saini *et al.*, «Blood-pool MR contrast material for detection and characterization of focal hepatic lesions: initial clinical experience with ultrasmall superparamagnetic iron oxide (AMI-227).», *Am. J. Roentgenol.*, vol. 164, n. 5, pagg. 1147–1152, mag. 1995.
[25] M. F. Bellin *et al.*, «Lymph node metastases: safety and effectiveness of MR imaging with ultrasmall superparamagnetic iron oxide particles--initial clinical experience.», *Radiology*, vol. 207, n. 3, pagg. 799–808, giu. 1998.
[26] M. G. Harisinghani, S. Saini, G. J. Slater, M. D. Schnall, e M. D. Rifkin, «MR imaging of pelvic lymph nodes in primary pelvic carcinoma with ultrasmall superparamagnetic iron oxide (Combidex): preliminary observations», *J. Magn. Reson. Imaging JMRI*, vol. 7, n. 1, pagg. 161–163, feb. 1997.
[27] S. Metz *et al.*, «Ferumoxtran-10-enhanced MR imaging of the bone marrow before and after conditioning therapy in patients with non-Hodgkin lymphomas», *Eur. Radiol.*, vol. 16, n. 3, pagg. 598–607, feb. 2006.
[28] A. Saleh, M. Schroeter, C. Jonkmanns, H.-P. Hartung, U. Modder, e S. Jander, «In vivo MRI of brain inflammation in human ischaemic stroke», *Brain*, vol. 127, n. 7, pagg. 1670–1677, lug. 2004.
[29] B. R. Smith *et al.*, «Localization to atherosclerotic plaque and biodistribution of biochemically derivatized superparamagnetic iron oxide nanoparticles (SPIONs) contrast particles for magnetic resonance imaging (MRI)», *Biomed. Microdevices*, vol. 9, n. 5, pagg. 719–727, ago. 2007.
[30] Q. L. Vuong, J.-F. Berret, J. Fresnais, Y. Gossuin, e O. Sandre, «A Universal Scaling Law to Predict the Efficiency of Magnetic Nanoparticles as MRI T2-Contrast Agents», *Adv. Healthc. Mater.*, vol. 1, n. 4, pagg. 502–512, lug. 2012.
[31] I. Šafařík e M. Šafaříková, «Use of magnetic techniques for the isolation of cells», *J. Chromatogr. B. Biomed. Sci. App.*, vol. 722, n. 1–2, pagg. 33–53, feb. 1999.
[32] Z. M. Saiyed, M. Parasramka, S. D. Telang, e C. N. Ramchand, «Extraction of DNA from agarose gel using magnetic nanoparticles (magnetite or Fe3O4)», *Anal. Biochem.*, vol. 363, n. 2, pagg. 288–290, apr. 2007.
[33] T. R. Sarkar e J. Irudayaraj, «Carboxyl-coated magnetic nanoparticles for mRNA isolation and extraction of supercoiled plasmid DNA», *Anal. Biochem.*, vol. 379, n. 1, pagg. 130–132, ago. 2008.
[34] D. W. Inglis, R. Riehn, J. C. Sturm, e R. H. Austin, «Microfluidic high gradient magnetic cell separation», *J. Appl. Phys.*, vol. 99, n. 8, pag. 08K101, 2006.
[35] M. M. Saari, K. Sakai, T. Kiwa, T. Sasayama, T. Yoshida, e K. Tsukada, «Characterization of the magnetic moment distribution in low-concentration

solutions of iron oxide nanoparticles by a high-Tc superconducting quantum interference device magnetometer», *J. Appl. Phys.*, vol. 117, n. 17, pag. 17B321, mag. 2015.
[36] J. Hu, I. Lo, e G. Chen, «Comparative study of various magnetic nanoparticles for Cr(VI) removal», *Sep. Purif. Technol.*, vol. 56, n. 3, pagg. 249–256, set. 2007.
[37] A. L. Urbano-Bojorge, N. Félix-González, T. Fernández, F. del Pozo-Guerrero, M. Ramos, e J. J. Serrano-Olmedo, «A Comparison of Magnetometry and Relaxometry Measures of Magnetic Nanoparticles Deposited in Biological Samples», *J. Nano Res.*, vol. 31, pagg. 129–137, apr. 2015.
[38] M. Tinkham, *Introduction to superconductivity*, 2. ed. Mineola, NY: Dover Publ, 2004.
[39] A. Barone e G. Paternò, *Physics and Applications of the Josephson Effect: BARONE:PHYSICS O-BK*. Weinheim, FRG: Wiley-VCH Verlag GmbH & Co. KGaA, 1982.
[40] L. Néel, «Théorie du traînage magnétique des substances massives dans le domaine de Rayleigh», *J. Phys. Radium*, vol. 11, n. 2, pagg. 49–61, 1950.
[41] A. H. Morrish e S. P. Yu, «Magnetic Measurements on Individual Microscopic Ferrite Particles Near the Single-Domain Size», *Phys. Rev.*, vol. 102, n. 3, pagg. 670–673, mag. 1956.
[42] M. Brands, R. Wieser, C. Hassel, D. Hinzke, e G. Dumpich, «Reversal processes and domain wall pinning in polycrystalline Co-nanowires», *Phys. Rev. B*, vol. 74, n. 17, nov. 2006.
[43] A. Fernández-Pacheco *et al.*, «Magnetization reversal in individual cobalt micro- and nanowires grown by focused-electron-beam-induced-deposition», *Nanotechnology*, vol. 20, n. 47, pag. 475704, nov. 2009.
[44] J. Schoenmaker *et al.*, «Local hysteresis loop measurements by magneto-optical scanning near-field optical microscope», *J. Appl. Phys.*, vol. 98, n. 8, pag. 086108, 2005.
[45] W. Wernsdorfer *et al.*, «DC-SQUID magnetization measurements of single magnetic particles», *J. Magn. Magn. Mater.*, vol. 145, n. 1–2, pagg. 33–39, mar. 1995.
[46] D. Mailly, C. Chapelier, e A. Benoit, «Experimental observation of persistent currents in GaAs-AlGaAs single loop», *Phys. Rev. Lett.*, vol. 70, n. 13, pagg. 2020–2023, mar. 1993.
[47] G. Cernicchiaro, K. Hasselbach, D. Mailly, W. Wernsdorfer, e A. Benoit, «How to Measure Persistent Currents in a Mesoscopic Ring», in *Quantum Transport in Semiconductor Submicron Structures*, B. Kramer, A c. di Dordrecht: Springer Netherlands, 1996, pagg. 207–219.
[48] V. Bouchiat, M. Faucher, C. Thirion, W. Wernsdorfer, T. Fournier, e B. Pannetier, «Josephson junctions and superconducting quantum interference devices made by local oxidation of niobium ultrathin films», *Appl. Phys. Lett.*, vol. 79, n. 1, pag. 123, 2001.
[49] S. K. H. Lam, «Noise properties of SQUIDs made from nanobridges», *Supercond. Sci. Technol.*, vol. 19, n. 9, pagg. 963–967, set. 2006.
[50] A. G. P. Troeman, H. Derking, B. Borger, J. Pleikies, D. Veldhuis, e H. Hilgenkamp, «NanoSQUIDs Based on Niobium Constrictions», *Nano Lett.*, vol. 7, n. 7, pagg. 2152–2156, lug. 2007.
[51] S. K. H. Lam, W. Yang, H. T. R. Wiogo, e C. P. Foley, «Attachment of magnetic molecules on a nanoSQUID», *Nanotechnology*, vol. 19, n. 28, pag. 285303, lug. 2008.

[52] C. Granata, E. Esposito, A. Vettoliere, L. Petti, e M. Russo, «An integrated superconductive magnetic nanosensor for high-sensitivity nanoscale applications», *Nanotechnology*, vol. 19, n. 27, pag. 275501, lug. 2008.
[53] A. G. P. Troeman *et al.*, «Temperature dependence measurements of the supercurrent-phase relationship in niobium nanobridges», *Phys. Rev. B*, vol. 77, n. 2, gen. 2008.
[54] D. D. Awschalom e M. E. Flatté, «Challenges for semiconductor spintronics», *Nat. Phys.*, vol. 3, n. 3, pagg. 153–159, mar. 2007.
[55] L. Bogani e W. Wernsdorfer, «Molecular spintronics using single-molecule magnets», *Nat. Mater.*, vol. 7, n. 3, pagg. 179–186, mar. 2008.
[56] L. Theil Kuhn *et al.*, «Magnetisation of isolated single crystalline Fe-nanoparticles measured by a ballistic Hall micro-magnetometer», *Eur. Phys. J. D*, vol. 10, n. 2, pag. 259, 2000.
[57] S. Wirth, M. Field, D. D. Awschalom, e S. von Molnár, «Magnetization behavior of nanometer-scale iron particles», *Phys. Rev. B*, vol. 57, n. 22, pagg. R14028–R14031, giu. 1998.
[58] A. D. Kent, S. von Molnár, S. Gider, e D. D. Awschalom, «Properties and measurement of scanning tunneling microscope fabricated ferromagnetic particle arrays (invited)», *J. Appl. Phys.*, vol. 76, n. 10, pag. 6656, 1994.
[59] E. Shung, T. F. Rosenbaum, e M. Sigrist, «Vortex Pinning and Stability in the Low Field, Superconducting Phases of UPt 3», *Phys. Rev. Lett.*, vol. 80, n. 5, pagg. 1078–1081, feb. 1998.
[60] A. K. Geim *et al.*, «Ballistic Hall micromagnetometry», *Appl. Phys. Lett.*, vol. 71, n. 16, pag. 2379, 1997.
[61] J. G. S. Lok, A. K. Geim, J. C. Maan, S. V. Dubonos, L. T. Kuhn, e P. E. Lindelof, «Memory effects in individual submicrometer ferromagnets», *Phys. Rev. B*, vol. 58, n. 18, pagg. 12201–12206, nov. 1998.
[62] Y. Li, P. Xiong, S. von Molnár, Y. Ohno, e H. Ohno, «Magnetization reversal of iron nanoparticles studied by submicron Hall magnetometry», *J. Appl. Phys.*, vol. 93, n. 10, pag. 7912, 2003.
[63] T. Uhlig e J. Zweck, «Recording of single-particle hysteresis loops with differential phase contrast microscopy», *Ultramicroscopy*, vol. 99, n. 2–3, pagg. 137–142, mag. 2004.
[64] W. J. de Ruijter e J. K. Weiss, «Detection limits in quantitative off-axis electron holography», *Ultramicroscopy*, vol. 50, n. 3, pagg. 269–283, ago. 1993.
[65] J. M. Thomas, E. T. Simpson, T. Kasama, e R. E. Dunin-Borkowski, «Electron Holography for the Study of Magnetic Nanomaterials», *Acc. Chem. Res.*, vol. 41, n. 5, pagg. 665–674, mag. 2008.
[66] E. Snoeck *et al.*, «Magnetic Configurations of 30 nm Iron Nanocubes Studied by Electron Holography», *Nano Lett.*, vol. 8, n. 12, pagg. 4293–4298, dic. 2008.
[67] H. A. Durr *et al.*, «A Closer Look Into Magnetism: Opportunities With Synchrotron Radiation», *IEEE Trans. Magn.*, vol. 45, n. 1, pagg. 15–57, gen. 2009.
[68] S. Eisebitt *et al.*, «Lensless imaging of magnetic nanostructures by X-ray spectro-holography», *Nature*, vol. 432, n. 7019, pagg. 885–888, dic. 2004.
[69] E. Amaladass, B. Ludescher, G. Schütz, T. Tyliszczak, e T. Eimüller, «Size dependence in the magnetization reversal of Fe⁄Gd multilayers on self-assembled arrays of nanospheres», *Appl. Phys. Lett.*, vol. 91, n. 17, pag. 172514, 2007.
[70] P. Fischer *et al.*, «Element-specific imaging of magnetic domains at 25 nm spatial resolution using soft x-ray microscopy», *Rev. Sci. Instrum.*, vol. 72, n. 5, pag. 2322, 2001.

[71] D.-H. Kim *et al.*, «Magnetic soft x-ray microscopy at 15 nm resolution probing nanoscale local magnetic hysteresis (invited)», *J. Appl. Phys.*, vol. 99, n. 8, pag. 08H303, 2006.
[72] E. Bauer, «Photoelectron spectromicroscopy: present and future», *J. Electron Spectrosc. Relat. Phenom.*, vol. 114–116, pagg. 975–987, mar. 2001.
[73] C. M. Schneider e G. Sch nhense, «Investigating surface magnetism by means of photoexcitation electron emission microscopy», *Rep. Prog. Phys.*, vol. 65, n. 12, pagg. 1785–1839, dic. 2002.
[74] H. Ohldag, A. Scholl, F. Nolting, S. Anders, F. U. Hillebrecht, e J. Stöhr, «Spin Reorientation at the Antiferromagnetic NiO(001) Surface in Response to an Adjacent Ferromagnet», *Phys. Rev. Lett.*, vol. 86, n. 13, pagg. 2878–2881, mar. 2001.
[75] C. T. Chen *et al.*, «Experimental Confirmation of the X-Ray Magnetic Circular Dichroism Sum Rules for Iron and Cobalt», *Phys. Rev. Lett.*, vol. 75, n. 1, pagg. 152–155, lug. 1995.
[76] A. Fraile Rodríguez, A. Kleibert, J. Bansmann, A. Voitkans, L. J. Heyderman, e F. Nolting, «Size-Dependent Spin Structures in Iron Nanoparticles», *Phys. Rev. Lett.*, vol. 104, n. 12, mar. 2010.
[77] F. Kronast *et al.*, «Element-Specific Magnetic Hysteresis of Individual 18 nm Fe Nanocubes», *Nano Lett.*, vol. 11, n. 4, pagg. 1710–1715, apr. 2011.
[78] R. Fink *et al.*, «SMART: a planned ultrahigh-resolution spectromicroscope for BESSY II», *J. Electron Spectrosc. Relat. Phenom.*, vol. 84, n. 1–3, pagg. 231–250, mar. 1997.
[79] J. Feng *et al.*, «An x-ray photoemission electron microscope using an electron mirror aberration corrector for the study of complex materials», *J. Phys. Condens. Matter*, vol. 17, n. 16, pagg. S1339–S1350, apr. 2005.
[80] F. Kronast *et al.*, «Depth-resolved soft x-ray photoelectron emission microscopy in nanostructures via standing-wave excited photoemission», *Appl. Phys. Lett.*, vol. 93, n. 24, pag. 243116, 2008.
[81] A. X. Gray *et al.*, «Standing-wave excited soft x-ray photoemission microscopy: Application to Co microdot magnetic arrays», *Appl. Phys. Lett.*, vol. 97, n. 6, pag. 062503, 2010.
[82] J. Kimling *et al.*, «Photoemission electron microscopy of three-dimensional magnetization configurations in core-shell nanostructures», *Phys. Rev. B*, vol. 84, n. 17, nov. 2011.
[83] O. Sandig *et al.*, «Imaging magnetic responses of nanomagnets by XPEEM», *J. Electron Spectrosc. Relat. Phenom.*, vol. 185, n. 10, pagg. 365–370, ott. 2012.
[84] R. Russo *et al.*, «Magnetic Nanoparticle Characterization Using Nano-SQUID based on Niobium Dayem Bridges», *Phys. Procedia*, vol. 36, pagg. 293–299, 2012.
[85] Y. Jun, J. Seo, e J. Cheon, «Nanoscaling Laws of Magnetic Nanoparticles and Their Applicabilities in Biomedical Sciences», *Acc. Chem. Res.*, vol. 41, n. 2, pagg. 179–189, feb. 2008.
[86] Q. A. Pankhurst, J. Connolly, S. K. Jones, e J. Dobson, «Applications of magnetic nanoparticles in biomedicine», *J. Phys. Appl. Phys.*, vol. 36, n. 13, pagg. R167–R181, lug. 2003.
[87] R. Kaur, A. Hasan, N. Iqbal, S. Alam, M. K. Saini, e S. K. Raza, «Synthesis and surface engineering of magnetic nanoparticles for environmental cleanup and pesticide residue analysis: A review: Sample Preparation», *J. Sep. Sci.*, vol. 37, n. 14, pagg. 1805–1825, lug. 2014.

[88] B. Stella *et al.*, «Design of folic acid-conjugated nanoparticles for drug targeting», *J. Pharm. Sci.*, vol. 89, n. 11, pagg. 1452–1464, nov. 2000.
[89] C. Wilhelm, F. Lavialle, C. Péchoux, I. Tatischeff, e F. Gazeau, «Intracellular Trafficking of Magnetic Nanoparticles to Design Multifunctional Biovesicles», *Small*, vol. 4, n. 5, pagg. 577–582, mag. 2008.
[90] R. Prassl *et al.*, «Ultrasmall superparamagnetic iron oxide (USPIO)-based liposomes as magnetic resonance imaging probes», *Int. J. Nanomedicine*, pag. 2349, mag. 2012.
[91] E. Roduner, «Size matters: why nanomaterials are different», *Chem. Soc. Rev.*, vol. 35, n. 7, pag. 583, 2006.
[92] G. Binnig e H. Rohrer, «Surface imaging by scanning tunneling microscopy», *Ultramicroscopy*, vol. 11, n. 2–3, pagg. 157–160, gen. 1983.
[93] H. Neddermeyer, A c. di, *Scanning tunneling microscopy*. Dordrecht ; Boston: Kluwer Academic Publishers, 1993.
[94] G. Binnig, C. F. Quate, e C. Gerber, «Atomic Force Microscope», *Phys. Rev. Lett.*, vol. 56, n. 9, pagg. 930–933, mar. 1986.
[95] A. L. Weisenhorn, P. K. Hansma, T. R. Albrecht, e C. F. Quate, «Forces in atomic force microscopy in air and water», *Appl. Phys. Lett.*, vol. 54, n. 26, pag. 2651, 1989.
[96] H.-J. Butt, B. Cappella, e M. Kappl, «Force measurements with the atomic force microscope: Technique, interpretation and applications», *Surf. Sci. Rep.*, vol. 59, n. 1–6, pagg. 1–152, ott. 2005.
[97] D. Passeri, A. Bettucci, e M. Rossi, «Acoustics and atomic force microscopy for the mechanical characterization of thin films», *Anal. Bioanal. Chem.*, vol. 396, n. 8, pagg. 2769–2783, apr. 2010.
[98] D. Passeri, M. Rossi, E. Tamburri, e M. L. Terranova, «Mechanical characterization of polymeric thin films by atomic force microscopy based techniques», *Anal. Bioanal. Chem.*, vol. 405, n. 5, pagg. 1463–1478, feb. 2013.
[99] F. Marinello, D. Passeri, e E. Savio, A c. di, *Acoustic scanning probe microscopy*. Berlin ; New York: Springer, 2013.
[100] U. Hartmann, «MAGNETIC FORCE MICROSCOPY», *Annu. Rev. Mater. Sci.*, vol. 29, n. 1, pagg. 53–87, ago. 1999.
[101] A. Majumdar, «SCANNING THERMAL MICROSCOPY», *Annu. Rev. Mater. Sci.*, vol. 29, n. 1, pagg. 505–585, ago. 1999.
[102] D. Passeri *et al.*, «Thermoacoustic Emission from Carbon Nanotubes Imaged by Atomic Force Microscopy», *Adv. Funct. Mater.*, vol. 22, n. 14, pagg. 2956–2963, lug. 2012.
[103] P. Girard, «Electrostatic force microscopy: principles and some applications to semiconductors», *Nanotechnology*, vol. 12, n. 4, pagg. 485–490, dic. 2001.
[104] E. Tamburri *et al.*, «Nanodiamond-mediated crystallization in fibers of PANI nanocomposites produced by template-free polymerization: Conductive and thermal properties of the fibrillar networks», *Polymer*, vol. 53, n. 19, pagg. 4045–4053, ago. 2012.
[105] D. V. Vezenov, A. Noy, e P. Ashby, «Chemical force microscopy: probing chemical origin of interfacial forces and adhesion», *J. Adhes. Sci. Technol.*, vol. 19, n. 3–5, pagg. 313–364, gen. 2005.
[106] Y. Martin e H. K. Wickramasinghe, «Magnetic imaging by ‘‘force microscopy’’ with 1000 Å resolution», *Appl. Phys. Lett.*, vol. 50, n. 20, pag. 1455, 1987.
[107] J. J. Sáenz *et al.*, «Observation of magnetic forces by the atomic force microscope», *J. Appl. Phys.*, vol. 62, n. 10, pag. 4293, 1987.

[108] D. Passeri *et al.*, «Effect of tip geometry on local indentation modulus measurement via atomic force acoustic microscopy technique», *Rev. Sci. Instrum.*, vol. 76, n. 9, pag. 093904, 2005.
[109] D. Passeri *et al.*, «Local indentation modulus characterization of diamondlike carbon films by atomic force acoustic microscopy two contact resonance frequencies imaging technique», *Appl. Phys. Lett.*, vol. 88, n. 12, pag. 121910, 2006.
[110] D. Passeri *et al.*, «Characterization of epoxy/single-walled carbon nanotubes composite samples via atomic force acoustic microscopy», *Phys. E Low-Dimens. Syst. Nanostructures*, vol. 40, n. 7, pagg. 2419–2424, mag. 2008.
[111] D. Passeri *et al.*, «Atomic force acoustic microscopy characterization of nanostructured selenium–tin thin films», *Superlattices Microstruct.*, vol. 44, n. 4–5, pagg. 641–649, ott. 2008.
[112] G. Bar, Y. Thomann, R. Brandsch, H.-J. Cantow, e M.-H. Whangbo, «Factors Affecting the Height and Phase Images in Tapping Mode Atomic Force Microscopy. Study of Phase-Separated Polymer Blends of Poly(ethene- *co* -styrene) and Poly(2,6-dimethyl-1,4-phenylene oxide)», *Langmuir*, vol. 13, n. 14, pagg. 3807–3812, lug. 1997.
[113] S. N. Magonov, J. Cleveland, V. Elings, D. Denley, e M.-H. Whangbo, «Tapping-mode atomic force microscopy study of the near-surface composition of a styrene-butadiene-styrene triblock copolymer film», *Surf. Sci.*, vol. 389, n. 1–3, pagg. 201–211, nov. 1997.
[114] B. Pignataro, L. Sardone, e G. Marletta, «Dynamic scanning force microscopy investigation of nanostructured spiral-like domains in Langmuir Blodgett monolayers», *Nanotechnology*, vol. 14, n. 2, pagg. 245–249, feb. 2003.
[115] J. J. Sáenz *et al.*, «Observation of magnetic forces by the atomic force microscope», *J. Appl. Phys.*, vol. 62, n. 10, pag. 4293, 1987.
[116] D. Schryvers, *Scanning force microscopy*, vol. 31. 1996.
[117] Y. Martin, C. C. Williams, e H. K. Wickramasinghe, «Atomic force microscope–force mapping and profiling on a sub 100-Å scale», *J. Appl. Phys.*, vol. 61, n. 10, pag. 4723, 1987.
[118] D. Rugar *et al.*, «Magnetic force microscopy: General principles and application to longitudinal recording media», *J. Appl. Phys.*, vol. 68, n. 3, pag. 1169, 1990.
[119] V. L. Mironov, D. S. Nikitushkin, C. Bins, A. B. Shubin, e P. A. Zhdan, «Magnetic Force Microscope Contrast Simulation for Low-Coercive Ferromagnetic and Superparamagnetic Nanoparticles in an External Magnetic Field», *IEEE Trans. Magn.*, vol. 43, n. 11, pagg. 3961–3963, nov. 2007.
[120] A. Wadas, P. Grütter, e H.-J. Güntherodt, «Analysis of in-plane bit structure by magnetic force microscopy», *J. Appl. Phys.*, vol. 67, n. 7, pag. 3462, 1990.
[121] F. Krause, F. Kaisinger, H. Starke, G. Persch, e U. Hartmann, «The influence of experimental parameters on contrast formation in magnetic force microscopy», *Thin Solid Films*, vol. 264, n. 2, pagg. 141–147, ago. 1995.
[122] I. G. Hughes, P. A. Barton, T. M. Roach, e E. A. Hinds, «Atom optics with magnetic surfaces: II. Microscopic analysis of the `floppy disk' mirror», *J. Phys. B At. Mol. Opt. Phys.*, vol. 30, n. 9, pagg. 2119–2132, mag. 1997.
[123] D. Passeri *et al.*, «Thickness measurement of soft thin films on periodically patterned magnetic substrates by phase difference magnetic force microscopy», *Ultramicroscopy*, vol. 136, pagg. 96–106, gen. 2014.

[124] D. W. Abraham, C. C. Williams, e H. K. Wickramasinghe, «Measurement of in-plane magnetization by force microscopy», *Appl. Phys. Lett.*, vol. 53, n. 15, pag. 1446, 1988.
[125] K. Ishikawa, R. Taguchi, E. Miyashita, J. Numazawa, e H. Ohshima, «Magnetic force microscopy image of Co–Cr–Ta layer in perpendicular magnetic tape at high linear recording density», *J. Appl. Phys.*, vol. 81, n. 8, pag. 4390, 1997.
[126] S. Porthun, L. Abelmann, e C. Lodder, «Magnetic force microscopy of thin film media for high density magnetic recording», *J. Magn. Magn. Mater.*, vol. 182, n. 1–2, pagg. 238–273, feb. 1998.
[127] M. R. Koblischka, B. Hewener, U. Hartmann, A. Wienss, B. Christoffer, e G. Persch-Schuy, «Magnetic force microscopy applied in magnetic data storage technology», *Appl. Phys. Mater. Sci. Process.*, vol. 76, n. 6, pagg. 879–884, apr. 2003.
[128] H. J. Reittu e R. Laiho, «Magnetic force microscopy of Abrikosov vortices», *Supercond. Sci. Technol.*, vol. 5, n. 7, pagg. 448–452, lug. 1992.
[129] A. P. Volodin e M. V. Marchevsky, «Magnetic force microscopy investigation of superconductors: first results», *Ultramicroscopy*, vol. 42–44, pagg. 757–763, lug. 1992.
[130] J. R. Kirtley, «Fundamental studies of superconductors using scanning magnetic imaging», *Rep. Prog. Phys.*, vol. 73, n. 12, pag. 126501, dic. 2010.
[131] A. Moser, «Magnetic force microscopy on high-Tc superconductors», *J. Vac. Sci. Technol. B Microelectron. Nanometer Struct.*, vol. 12, n. 3, pag. 1586, mag. 1994.
[132] A. Moser *et al.*, «Observation of Single Vortices Condensed into a Vortex-Glass Phase by Magnetic Force Microscopy», *Phys. Rev. Lett.*, vol. 74, n. 10, pagg. 1847–1850, mar. 1995.
[133] A. Volodin, K. Temst, C. Van Haesendonck, e Y. Bruynseraede, «Imaging of vortices in conventional superconductors by magnetic force microscopy», *Phys. C Supercond.*, vol. 332, n. 1–4, pagg. 156–159, mag. 2000.
[134] A. Volodin *et al.*, «Magnetic force microscopy of vortex pinning at grain boundaries in superconducting thin films», *Phys. C Supercond.*, vol. 369, n. 1–4, pagg. 165–170, mar. 2002.
[135] O. M. Auslaender *et al.*, «Mechanics of individual isolated vortices in a cuprate superconductor», *Nat. Phys.*, vol. 5, n. 1, pagg. 35–39, gen. 2009.
[136] F. Bobba *et al.*, «Vortex-antivortex coexistence in Nb-based superconductor/ferromagnet heterostructures», *Phys. Rev. B*, vol. 89, n. 21, giu. 2014.
[137] U. H. Pi, A. Schwarz, M. Liebmann, R. Wiesendanger, Z. G. Khim, e D. H. Kim, «Visualizing flux distribution of superconductors in external magnetic fields with magnetic force microscopy», *Phys. Rev. B*, vol. 73, n. 14, apr. 2006.
[138] E. W. J. Straver, J. E. Hoffman, O. M. Auslaender, D. Rugar, e K. A. Moler, «Controlled manipulation of individual vortices in a superconductor», *Appl. Phys. Lett.*, vol. 93, n. 17, pag. 172514, 2008.
[139] D. Buntinx, A. Volodin, e C. V. Haesendonck, «Combination of magnetic force microscopy with in situ magnetoresistance measurements», *J. Appl. Phys.*, vol. 92, n. 2, pag. 1014, 2002.
[140] Q. Lu, «Observation of Magnetic Domain Behavior in Colossal Magnetoresistive Materials With a Magnetic Force Microscope», *Science*, vol. 276, n. 5321, pagg. 2006–2008, giu. 1997.

[141] S. . Koch, R. . te Velde, G. Palasantzas, e J. T. . De Hosson, «Magnetic force microscopy on cobalt nanocluster films», *Appl. Surf. Sci.*, vol. 226, n. 1–3, pagg. 185–190, mar. 2004.
[142] C. T. Hsieh, J. Q. Liu, e J. T. Lue, «Magnetic force microscopy studies of domain walls in nickel and cobalt films», *Appl. Surf. Sci.*, vol. 252, n. 5, pagg. 1899–1909, dic. 2005.
[143] H. Z. Song *et al.*, «Influence of stress on the magnetic domain structure in Fe[sub 81]Ga[sub 19] alloys», *J. Appl. Phys.*, vol. 105, n. 1, pag. 013913, 2009.
[144] V. L. Mironov *et al.*, «Magnetic force microscope tip-induced remagnetization of CoPt nanodisks with perpendicular anisotropy», *J. Appl. Phys.*, vol. 106, n. 5, pag. 053911, 2009.
[145] J. Jalli *et al.*, «MFM studies of magnetic domain patterns in bulk barium ferrite (BaFe12O19) single crystals», *J. Magn. Magn. Mater.*, vol. 323, n. 21, pagg. 2627–2631, nov. 2011.
[146] H. S. Nagaraja, K. K. Nagaraja, F. Rossignol, F. Dumas-Bouchiat, C. Champeaux, e A. Catherinot, «Magnetic Domain Studies of Cobalt Nanostructures», *J. Supercond. Nov. Magn.*, vol. 25, n. 6, pagg. 1901–1906, ago. 2012.
[147] C. E. Vallet *et al.*, «Magnetic force microscopy of ferromagnetic nanoparticles formed in Al[sub 2]O[sub 3] and SiO[sub 2] by ion implantation», *J. Appl. Phys.*, vol. 92, n. 10, pag. 6200, 2002.
[148] S. Jain, A. O. Adeyeye, e N. Singh, «Spin re-orientation in magnetostatically coupled Ni_{80} Fe_{20} ellipsoidal nanomagnets», *Nanotechnology*, vol. 21, n. 28, pag. 285702, lug. 2010.
[149] M. Jaafar *et al.*, «Hysteresis loops of individual Co nanostripes measured by magnetic force microscopy», *Nanoscale Res. Lett.*, vol. 6, n. 1, pag. 407, 2011.
[150] M. R. Tabasum, F. Zighem, J. De La Torre Medina, A. Encinas, L. Piraux, e B. Nysten, «Magnetic force microscopy investigation of arrays of nickel nanowires and nanotubes», *Nanotechnology*, vol. 25, n. 24, pag. 245707, giu. 2014.
[151] A. J. Berger *et al.*, «Magnetization dynamics of cobalt grown on graphene», *J. Appl. Phys.*, vol. 115, n. 17, pag. 17C510, mag. 2014.
[152] V. Bliznyuk, S. Singamaneni, S. Sahoo, S. Polisetty, X. He, e C. Binek, «Self-assembly of magnetic Ni nanoparticles into 1D arrays with antiferromagnetic order», *Nanotechnology*, vol. 20, n. 10, pag. 105606, mar. 2009.
[153] J. Kim, H. Akinaga, e J. Kim, «Direct observation of the spin configurations of vertical Bloch line», *Appl. Phys. Lett.*, vol. 98, n. 5, pag. 052510, 2011.
[154] J. Kim, H. Akinaga, e J. Kim, «Observation of magnetic domain structures in epitaxial MnAs film on GaAs(001) with temperature hysteresis», *Appl. Phys. Lett.*, vol. 98, n. 10, pag. 102511, 2011.
[155] S. Schreiber *et al.*, «Magnetic Force Microscopy of Superparamagnetic Nanoparticles», *Small*, vol. 4, n. 2, pagg. 270–278, feb. 2008.
[156] S. Sievers *et al.*, «Quantitative Measurement of the Magnetic Moment of Individual Magnetic Nanoparticles by Magnetic Force Microscopy», *Small*, vol. 8, n. 17, pagg. 2675–2679, set. 2012.
[157] C. S. Neves *et al.*, «New insights into the use of magnetic force microscopy to discriminate between magnetic and nonmagnetic nanoparticles», *Nanotechnology*, vol. 21, n. 30, pag. 305706, lug. 2010.
[158] T. Häberle *et al.*, «Towards quantitative magnetic force microscopy: theory and experiment», *New J. Phys.*, vol. 14, n. 4, pag. 043044, apr. 2012.

[159] T. M. Nocera, J. Chen, C. B. Murray, e G. Agarwal, «Magnetic anisotropy considerations in magnetic force microscopy studies of single superparamagnetic nanoparticles», *Nanotechnology*, vol. 23, n. 49, pag. 495704, dic. 2012.
[160] J. Pacifico *et al.*, «Field gradient imaging of nanoparticle systems: analysis of geometry and surface coating effects», *Nanotechnology*, vol. 20, n. 9, pag. 095708, mar. 2009.
[161] D. Passeri *et al.*, «Magnetic force microscopy: Quantitative issues in biomaterials», *Biomatter*, vol. 4, n. 1, pag. e29507, gen. 2014.
[162] M. Miyasaka, Y. Saito, e H. Nishide, «Magnetic Force Microscopy Images of a Nanometer-Sized, Purely Organic High-Spin Polyradical», *Adv. Funct. Mater.*, vol. 13, n. 2, pagg. 113–117, feb. 2003.
[163] E. Fukuzaki e H. Nishide, «Room-temperature high-spin organic single molecule: nanometer-sized and hyperbranched poly[1,2,(4)-phenylenevinyleneanisylaminium]», *J. Am. Chem. Soc.*, vol. 128, n. 3, pagg. 996–1001, gen. 2006.
[164] H. Yanagi e A. Manivannan, «Epitaxial growth of molecular magnetic thin films of lithium phthalocyanine», *Thin Solid Films*, vol. 393, n. 1–2, pagg. 28–33, ago. 2001.
[165] M. Cavallini *et al.*, «Magnetic Information Storage on Polymers by Using Patterned Single-Molecule Magnets», *Angew. Chem. Int. Ed.*, vol. 44, n. 6, pagg. 888–892, gen. 2005.
[166] N. A. Zaidi, S. R. Giblin, I. Terry, e A. P. Monkman, «Room temperature magnetic order in an organic magnet derived from polyaniline», *Polymer*, vol. 45, n. 16, pagg. 5683–5689, lug. 2004.
[167] M. K. Jaiswal, R. Banerjee, P. Pradhan, e D. Bahadur, «Thermal behavior of magnetically modalized poly(N-isopropylacrylamide)-chitosan based nanohydrogel», *Colloids Surf. B Biointerfaces*, vol. 81, n. 1, pagg. 185–194, nov. 2010.
[168] D. Nyamjav, J. M. Kinsella, e A. Ivanisevic, «Magnetic wires with DNA cores: A magnetic force microscopy study», *Appl. Phys. Lett.*, vol. 86, n. 9, pag. 093107, 2005.
[169] M. Jaafar *et al.*, «Structural Insights into Magnetic Clusters Grown Inside Virus Capsids», *ACS Appl. Mater. Interfaces*, vol. 6, n. 23, pagg. 20936–20942, dic. 2014.
[170] C.-W. Hsieh, B. Zheng, e S. Hsieh, «Ferritin protein imaging and detection by magnetic force microscopy», *Chem. Commun.*, vol. 46, n. 10, pag. 1655, 2010.
[171] R. V. Martinez, M. Chiesa, e R. Garcia, «Nanopatterning of ferritin molecules and the controlled size reduction of their magnetic cores», *Small Weinh. Bergstr. Ger.*, vol. 7, n. 20, pagg. 2914–2920, ott. 2011.
[172] C. Dietz, E. T. Herruzo, J. R. Lozano, e R. Garcia, «Nanomechanical coupling enables detection and imaging of 5 nm superparamagnetic particles in liquid», *Nanotechnology*, vol. 22, n. 12, pag. 125708, mar. 2011.
[173] T. M. Nocera, Y. Zeng, e G. Agarwal, «Distinguishing ferritin from apoferritin using magnetic force microscopy», *Nanotechnology*, vol. 25, n. 46, pag. 461001, nov. 2014.
[174] R. Hergt *et al.*, «Magnetic properties of bacterial magnetosomes as potential diagnostic and therapeutic tools», *J. Magn. Magn. Mater.*, vol. 293, n. 1, pagg. 80–86, mag. 2005.
[175] R. B. Proksch, T. E. Schäffer, B. M. Moskowitz, E. D. Dahlberg, D. A. Bazylinski, e R. B. Frankel, «Magnetic force microscopy of the submicron

magnetic assembly in a magnetotactic bacterium», *Appl. Phys. Lett.*, vol. 66, n. 19, pag. 2582, 1995.
[176] M. Albrecht, V. Janke, S. Sievers, U. Siegner, D. Schüler, e U. Heyen, «Scanning force microspy study of biogenic nanoparticles for medical applications», *J. Magn. Magn. Mater.*, vol. 290–291, pagg. 269–271, apr. 2005.
[177] D. Eberbeck *et al.*, «Blocking of magnetic moments of magnetosomes measured by magnetorelaxometry and direct observation by magnetic force microscopy», *J. Magn. Magn. Mater.*, vol. 289, pagg. 70–73, mar. 2005.
[178] J. D. Wei, I. Knittel, C. Lang, D. Schüler, e U. Hartmann, «Magnetic properties of single biogenic magnetite nanoparticles», *J. Nanoparticle Res.*, vol. 13, n. 8, pagg. 3345–3352, ago. 2011.
[179] H. Gojzewski, M. Makowski, A. Hashim, P. Kopcansky, Z. Tomori, e M. Timko, «Magnetosomes on surface: an imaging study approach: Magnetosomes on surface», *Scanning*, vol. 34, n. 3, pagg. 159–169, mag. 2012.
[180] J. R. Dunn *et al.*, «Magnetic material in the human hippocampus», *Brain Res. Bull.*, vol. 36, n. 2, pagg. 149–153, 1995.
[181] J. Dobson, «Nanoscale biogenic iron oxides and neurodegenerative disease», *FEBS Lett.*, vol. 496, n. 1, pagg. 1–5, mag. 2001.
[182] Y. Amemiya, T. Tanaka, B. Yoza, e T. Matsunaga, «Novel detection system for biomolecules using nano-sized bacterial magnetic particles and magnetic force microscopy», *J. Biotechnol.*, vol. 120, n. 3, pagg. 308–314, nov. 2005.
[183] A. V. Moskalenko, P. L. Yarova, S. N. Gordeev, e S. V. Smirnov, «Single Protein Molecule Mapping with Magnetic Atomic Force Microscopy», *Biophys. J.*, vol. 98, n. 3, pagg. 478–487, feb. 2010.
[184] H. Shen *et al.*, «Magnetic force microscopy analysis of apoptosis of HL-60 cells induced by complex of antisense oligonucleotides and magnetic nanoparticles», *Biophys. Chem.*, vol. 122, n. 1, pagg. 1–4, giu. 2006.
[185] Y. Zhang, M. Yang, M. Ozkan, e C. S. Ozkan, «Magnetic force microscopy of iron oxide nanoparticles and their cellular uptake», *Biotechnol. Prog.*, vol. 25, n. 4, pagg. 923–928, lug. 2009.
[186] T. Ouchi, Y. Arikawa, T. Kuno, J. Mizuno, S. Shoji, e T. Homma, «Electrochemical Fabrication and Characterization of CoPt Bit Patterned Media: Towards a Wetchemical, Large-Scale Fabrication», *IEEE Trans. Magn.*, vol. 46, n. 6, pagg. 2224–2227, giu. 2010.
[187] J. Butler *et al.*, «Reconfigurable and non-volatile vertical magnetic logic gates», *J. Appl. Phys.*, vol. 115, n. 16, pag. 163903, apr. 2014.
[188] T. Wang *et al.*, «A magnetic force microscopy study of the magnetic reversal of a single Fe nanowire», *Nanotechnology*, vol. 20, n. 10, pag. 105707, mar. 2009.
[189] A. V. Davydenko, E. V. Pustovalov, A. V. Ognev, e L. A. Chebotkevich, «Magnetization Reversal in the Single Epitaxial Co(111) Nanowires With Step-Induced Anisotropy», *IEEE Trans. Magn.*, vol. 48, n. 11, pagg. 3128–3131, nov. 2012.
[190] C. C. Chen *et al.*, «Investigation on the Magnetization Reversal of Nanostructured Magnetic Tunnel Junction Rings», *IEEE Trans. Magn.*, vol. 45, n. 10, pagg. 3546–3549, ott. 2009.
[191] M. Aniya *et al.*, «Magnetization Reversal Process of Hard/Soft Nano-Composite Structures Formed by Ion Irradiation», *IEEE Trans. Magn.*, vol. 46, n. 6, pagg. 2132–2135, giu. 2010.
[192] M. Tekielak *et al.*, «The effect of magnetostatic coupling on spin configurations in ultrathin multilayers», *J. Appl. Phys.*, vol. 110, n. 4, pag. 043924, 2011.

[193] M. R. Tabasum, F. Zighem, J. De La Torre Medina, A. Encinas, L. Piraux, e B. Nysten, «Magnetic force microscopy study of the switching field distribution of low density arrays of single domain magnetic nanowires», *J. Appl. Phys.*, vol. 113, n. 18, pag. 183908, 2013.
[194] M. Ranjbar *et al.*, «Antiferromagnetically Coupled Patterned Media and Control of Switching Field Distribution», *IEEE Trans. Magn.*, vol. 46, n. 6, pagg. 1787–1790, giu. 2010.
[195] Y. Chen *et al.*, «Switching Probability Distribution of Bit Islands in Bit Patterned Media», *IEEE Trans. Magn.*, vol. 46, n. 6, pagg. 1990–1993, giu. 2010.
[196] J. K. W. Yang *et al.*, «Fabrication and characterization of bit-patterned media beyond 1.5 Tbit/in ^{2}», *Nanotechnology*, vol. 22, n. 38, pag. 385301, set. 2011.
[197] W. L. Pei *et al.*, «Incoherent magnetization reversal in Co–Pt nanodots investigated by magnetic force microscopy», *Acta Mater.*, vol. 59, n. 12, pagg. 4818–4824, lug. 2011.
[198] J. Jin Park, M. Reddy, B. J. H. Stadler, e A. B. Flatau, «Hysteresis measurement of individual multilayered Fe-Ga/Cu nanowires using magnetic force microscopy», *J. Appl. Phys.*, vol. 113, n. 17, pag. 17A331, 2013.
[199] M. Brands, R. Wieser, C. Hassel, D. Hinzke, e G. Dumpich, «Reversal processes and domain wall pinning in polycrystalline Co-nanowires», *Phys. Rev. B*, vol. 74, n. 17, nov. 2006.
[200] A. Fernández-Pacheco *et al.*, «Magnetization reversal in individual cobalt micro- and nanowires grown by focused-electron-beam-induced-deposition», *Nanotechnology*, vol. 20, n. 47, pag. 475704, nov. 2009.
[201] J. Schoenmaker *et al.*, «Local hysteresis loop measurements by magneto-optical scanning near-field optical microscope», *J. Appl. Phys.*, vol. 98, n. 8, pag. 086108, 2005.
[202] L. Theil Kuhn *et al.*, «Magnetisation of isolated single crystalline Fe-nanoparticles measured by a ballistic Hall micro-magnetometer», *Eur. Phys. J. D*, vol. 10, n. 2, pag. 259, 2000.
[203] M. Coïsson *et al.*, «Local field loop measurements by magnetic force microscopy», *J. Phys. Appl. Phys.*, vol. 47, n. 32, pag. 325003, ago. 2014.
[204] M. V. Rastei, R. Meckenstock, e J. P. Bucher, «Nanoscale hysteresis loop of individual Co dots by field-dependent magnetic force microscopy», *Appl. Phys. Lett.*, vol. 87, n. 22, pag. 222505, 2005.
[205] M. Coïsson *et al.*, «Local hysteresis loops measurements on irradiated FeSiB patterned dots by magnetic force microscopy», *J. Magn. Magn. Mater.*, vol. 373, pagg. 250–254, gen. 2015.
[206] M. Coïsson, G. Barrera, F. Celegato, A. Manzin, F. Vinai, e P. Tiberto, «Magnetic vortex chirality determination via local hysteresis loops measurements with magnetic force microscopy», *Sci. Rep.*, vol. 6, pag. 29904, lug. 2016.
[207] C. Moya, Ó. Iglesias-Freire, N. Pérez, X. Batlle, A. Labarta, e A. Asenjo, «Direct imaging of the magnetic polarity and reversal mechanism in individual Fe $_{3-x}$ O $_4$ nanoparticles», *Nanoscale*, vol. 7, n. 17, pagg. 8110–8114, 2015.
[208] E. Pinilla-Cienfuegos *et al.*, «Imaging the Magnetic Reversal of Isolated and Organized Molecular-Based Nanoparticles using Magnetic Force Microscopy», *Part. Part. Syst. Charact.*, vol. 32, n. 6, pagg. 693–700, giu. 2015.
[209] G. Cordova, S. Attwood, R. Gaikwad, F. Gu, e Z. Leonenko, «Magnetic Force Microscopy Characterization of Superparamagnetic Iron Oxide Nanoparticles (SPIONs)», *Nano Biomed. Eng.*, vol. 6, n. 1, mar. 2014.

[210] L. Fumagalli *et al.*, «Nanoscale capacitance imaging with attofarad resolution using ac current sensing atomic force microscopy», *Nanotechnology*, vol. 17, n. 18, pagg. 4581–4587, set. 2006.
[211] I. Casuso, L. Fumagalli, G. Gomila, e E. Padrós, «Nondestructive thickness measurement of biological layers at the nanoscale by simultaneous topography and capacitance imaging», *Appl. Phys. Lett.*, vol. 91, n. 6, pag. 063111, 2007.
[212] R. Schmidt, A. Schwarz, e R. Wiesendanger, «Hydrogen-related contrast in atomic force microscopy», *Nanotechnology*, vol. 20, n. 26, pag. 264007, lug. 2009.
[213] R. Engel-Herbert, T. Hesjedal, J. Mohanty, D. M. Schaadt, e K. H. Ploog, «Magnetization reversal in MnAs films: Magnetic force microscopy, SQUID magnetometry, and micromagnetic simulations», *Phys. Rev. B*, vol. 73, n. 10, mar. 2006.
[214] A. Asenjo, D. García, J. García, C. Prados, e M. Vázquez, «Magnetic force microscopy study of dense stripe domains in Fe-B/Co-Si-B multilayers and the evolution under an external applied field», *Phys. Rev. B*, vol. 62, n. 10, pagg. 6538–6544, set. 2000.
[215] A. Schwarz e R. Wiesendanger, «Magnetic sensitive force microscopy», *Nano Today*, vol. 3, n. 1–2, pagg. 28–39, feb. 2008.
[216] M. Jaafar, O. Iglesias-Freire, L. Serrano-Ramón, M. R. Ibarra, J. M. de Teresa, e A. Asenjo, «Distinguishing magnetic and electrostatic interactions by a Kelvin probe force microscopy–magnetic force microscopy combination», *Beilstein J. Nanotechnol.*, vol. 2, pagg. 552–560, set. 2011.
[217] V. Cambel *et al.*, «Magnetic elements for switching magnetization magnetic force microscopy tips», *J. Magn. Magn. Mater.*, vol. 322, n. 18, pagg. 2715–2721, set. 2010.
[218] V. Cambel *et al.*, «Switching Magnetization Magnetic Force Microscopy — An Alternative to Conventional Lift-Mode MFM», *J. Electr. Eng.*, vol. 62, n. 1, gen. 2011.
[219] A. Hubert, W. Rave, e S. L. Tomlinson, «Imaging Magnetic Charges with Magnetic Force Microscopy», *Phys. Status Solidi B*, vol. 204, n. 2, pagg. 817–828, dic. 1997.
[220] R. D. Gomez, E. R. Burke, e I. D. Mayergoyz, «Magnetic imaging in the presence of external fields: Technique and applications (invited)», *J. Appl. Phys.*, vol. 79, n. 8, pag. 6441, 1996.
[221] K. L. Babcock, V. B. Elings, J. Shi, D. D. Awschalom, e M. Dugas, «Field-dependence of microscopic probes in magnetic force microscopy», *Appl. Phys. Lett.*, vol. 69, n. 5, pag. 705, 1996.
[222] P. B. Fischer e S. Y. Chou, «10 nm electron beam lithography and sub-50 nm overlay using a modified scanning electron microscope», *Appl. Phys. Lett.*, vol. 62, n. 23, pag. 2989, 1993.
[223] L. Kong e S. Y. Chou, «Study of magnetic properties of magnetic force microscopy probes using micronscale current rings», *J. Appl. Phys.*, vol. 81, n. 8, pag. 5026, 1997.
[224] J. Lohau, S. Kirsch, A. Carl, G. Dumpich, e E. F. Wassermann, «Quantitative determination of effective dipole and monopole moments of magnetic force microscopy tips», *J. Appl. Phys.*, vol. 86, n. 6, pag. 3410, 1999.
[225] A. Carl, J. Lohau, S. Kirsch, e E. F. Wassermann, «Magnetization reversal and coercivity of magnetic-force microscopy tips», *J. Appl. Phys.*, vol. 89, n. 11, pag. 6098, 2001.

[226] C. Liu *et al.*, «Calibration of magnetic force microscopy using micron size straight current wires», *J. Appl. Phys.*, vol. 91, n. 10, pag. 8849, 2002.
[227] T. Kebe, «Calibration of magnetic force microscopy tips by using nanoscale current-carrying parallel wires», *J. Appl. Phys.*, vol. 95, n. 3, pag. 775, 2004.
[228] M. Jaafar, A. Asenjo, e M. Vazquez, «Calibration of Coercive and Stray Fields of Commercial Magnetic Force Microscope Probes», *IEEE Trans. Nanotechnol.*, vol. 7, n. 3, pagg. 245–250, mag. 2008.
[229] Y. Wu, Y. Shen, Z. Liu, K. Li, e J. Qiu, «Point-dipole response from a magnetic force microscopy tip with a synthetic antiferromagnetic coating», *Appl. Phys. Lett.*, vol. 82, n. 11, pag. 1748, 2003.
[230] H. Saito *et al.*, «Simulation of high-resolution MFM tip using exchange-spring magnet», *J. Magn. Magn. Mater.*, vol. 310, n. 2, pagg. e939–e940, mar. 2007.
[231] N. Amos, R. Ikkawi, R. Haddon, D. Litvinov, e S. Khizroev, «Controlling multidomain states to enable sub-10-nm magnetic force microscopy», *Appl. Phys. Lett.*, vol. 93, n. 20, pag. 203116, 2008.
[232] S. N. Piramanayagam, M. Ranjbar, E. L. Tan, H. K. Tan, R. Sbiaa, e T. C. Chong, «Enhanced resolution in magnetic force microscropy using tips with perpendicular magnetic anisotropy», *J. Appl. Phys.*, vol. 109, n. 7, pag. 07E326, 2011.
[233] H. Li, D. Wei, e S. N. Piramanayagam, «Micromagnetic studies on resolution limits of magnetic force microscopy tips with different magnetic anisotropy», *J. Appl. Phys.*, vol. 111, n. 7, pag. 07E309, 2012.
[234] S. Porthun, L. Abelmann, S. J. L. Vellekoop, J. C. Lodder, e H. J. Hug, «Optimization of lateral resolution in magnetic force microscopy», *Appl. Phys. Mater. Sci. Process.*, vol. 66, n. 7, pagg. S1185–S1189, mar. 1998.
[235] H. J. Hug *et al.*, «Quantitative magnetic force microscopy on perpendicularly magnetized samples», *J. Appl. Phys.*, vol. 83, n. 11, pag. 5609, 1998.
[236] A. van den Bos, I. Heskamp, M. Siekman, L. Abelmann, e C. Lodder, «The CantiClever: a dedicated probe for magnetic force microscopy», *IEEE Trans. Magn.*, vol. 38, n. 5, pagg. 2441–2443, set. 2002.
[237] H. Dai, J. H. Hafner, A. G. Rinzler, D. T. Colbert, e R. E. Smalley, «Nanotubes as nanoprobes in scanning probe microscopy», *Nature*, vol. 384, n. 6605, pagg. 147–150, nov. 1996.
[238] T. Arie, H. Nishijima, S. Akita, e Y. Nakayama, «Carbon-nanotube probe equipped magnetic force microscope», *J. Vac. Sci. Technol. B Microelectron. Nanometer Struct.*, vol. 18, n. 1, pag. 104, 2000.
[239] H. Kuramochi *et al.*, «Material dependence of magnetic force microscopy performance using carbon nanotube probes: Experiments and simulation», *J. Appl. Phys.*, vol. 115, n. 9, pag. 093907, mar. 2014.
[240] F. Wolny *et al.*, «Iron filled carbon nanotubes as novel monopole-like sensors for quantitative magnetic force microscopy», *Nanotechnology*, vol. 21, n. 43, pag. 435501, ott. 2010.
[241] F. Wolny *et al.*, «Magnetic force microscopy measurements in external magnetic fields—comparison between coated probes and an iron filled carbon nanotube probe», *J. Appl. Phys.*, vol. 108, n. 1, pag. 013908, 2010.
[242] M. U. Lutz *et al.*, «Magnetic properties of α-Fe and Fe_3C nanowires», *J. Phys. Conf. Ser.*, vol. 200, n. 7, pag. 072062, gen. 2010.
[243] D. Kim, N.-K. Chung, S. Allen, S. J. B. Tendler, e J. W. Park, «Ferritin-Based New Magnetic Force Microscopic Probe Detecting 10 nm Sized Magnetic Nanoparticles», *ACS Nano*, vol. 6, n. 1, pagg. 241–248, gen. 2012.

[244] Q. A. Pankhurst, J. Connolly, S. K. Jones, e J. Dobson, «Applications of magnetic nanoparticles in biomedicine», *J. Phys. Appl. Phys.*, vol. 36, n. 13, pagg. R167–R181, lug. 2003.
[245] R. Kaur, A. Hasan, N. Iqbal, S. Alam, M. K. Saini, e S. K. Raza, «Synthesis and surface engineering of magnetic nanoparticles for environmental cleanup and pesticide residue analysis: A review: Sample Preparation», *J. Sep. Sci.*, vol. 37, n. 14, pagg. 1805–1825, lug. 2014.
[246] M. Liberatore *et al.*, «Effect of External Magnetic Field on IV 99mTc-Labeled Aminosilane-Coated Iron Oxide Nanoparticles: Demonstration in a Rat Model», *Clin. Nucl. Med.*, vol. 40, n. 2, pagg. e104–e110, feb. 2015.
[247] B. Stella *et al.*, «Design of folic acid-conjugated nanoparticles for drug targeting», *J. Pharm. Sci.*, vol. 89, n. 11, pagg. 1452–1464, nov. 2000.
[248] S. Mornet, S. Vasseur, F. Grasset, e E. Duguet, «Magnetic nanoparticle design for medical diagnosis and therapy», *J. Mater. Chem.*, vol. 14, n. 14, pag. 2161, 2004.
[249] R. Prassl *et al.*, «Ultrasmall superparamagnetic iron oxide (USPIO)-based liposomes as magnetic resonance imaging probes», *Int. J. Nanomedicine*, pag. 2349, mag. 2012.
[250] «Smart magnetic nanovesicles for theranostic application: Preparation and characterization», *Il Nuovo Cimento C*, n. 2, pag. 103, mag. 2013.
[251] K. Enpuku *et al.*, «Detection of Magnetic Nanoparticles with Superconducting Quantum Interference Device (SQUID) Magnetometer and Application to Immunoassays», *Jpn. J. Appl. Phys.*, vol. 38, n. Part 2, No. 10A, pagg. L1102–L1105, ott. 1999.
[252] N. L. Adolphi *et al.*, «Characterization of single-core magnetite nanoparticles for magnetic imaging by SQUID relaxometry», *Phys. Med. Biol.*, vol. 55, n. 19, pagg. 5985–6003, ott. 2010.
[253] J. Hu, I. Lo, e G. Chen, «Comparative study of various magnetic nanoparticles for Cr(VI) removal», *Sep. Purif. Technol.*, vol. 56, n. 3, pagg. 249–256, set. 2007.
[254] K. Sun, J. Qiu, J. Liu, e Y. Miao, «Preparation and characterization of gold nanoparticles using ascorbic acid as reducing agent in reverse micelles», *J. Mater. Sci.*, vol. 44, n. 3, pagg. 754–758, feb. 2009.
[255] Passeri D., Angeloni L., Reggente M., e Rossi M., «Magnetic Force Microscopy», in *Magnetic characterization techniques for nanomaterials*, Springer Berlin Heidelberg.
[256] S. Belaidi, P. Girard, e G. Leveque, «Electrostatic forces acting on the tip in atomic force microscopy: Modelization and comparison with analytic expressions», *J. Appl. Phys.*, vol. 81, n. 3, pag. 1023, 1997.
[257] null Sun, null Murray, null Weller, null Folks, e null Moser, «Monodisperse FePt nanoparticles and ferromagnetic FePt nanocrystal superlattices», *Science*, vol. 287, n. 5460, pagg. 1989–1992, mar. 2000.
[258] Q. A. Pankhurst, N. T. K. Thanh, S. K. Jones, e J. Dobson, «Progress in applications of magnetic nanoparticles in biomedicine», *J. Phys. Appl. Phys.*, vol. 42, n. 22, pag. 224001, nov. 2009.
[259] C. L. Degen, «Scanning magnetic field microscope with a diamond single-spin sensor», *Appl. Phys. Lett.*, vol. 92, n. 24, pag. 243111, 2008.
[260] L. T. Hall, J. H. Cole, C. D. Hill, e L. C. L. Hollenberg, «Sensing of Fluctuating Nanoscale Magnetic Fields Using Nitrogen-Vacancy Centers in Diamond», *Phys. Rev. Lett.*, vol. 103, n. 22, nov. 2009.

[261] L. Rondin *et al.*, «Nanoscale magnetic field mapping with a single spin scanning probe magnetometer», *Appl. Phys. Lett.*, vol. 100, n. 15, pag. 153118, 2012.
[262] S. Hong *et al.*, «Nanoscale magnetometry with NV centers in diamond», *MRS Bull.*, vol. 38, n. 02, pagg. 155–161, feb. 2013.
[263] A. de Lozanne, «Application of magnetic force microscopy in nanomaterials characterization», *Microsc. Res. Tech.*, vol. 69, n. 7, pagg. 550–562, lug. 2006.
[264] C. Moya, Ó. Iglesias-Freire, X. Batlle, A. Labarta, e A. Asenjo, «Superparamagnetic versus blocked states in aggregates of $Fe_{3-x}O_4$ nanoparticles studied by MFM», *Nanoscale*, vol. 7, n. 42, pagg. 17764–17770, 2015.
[265] C. Moya, Ó. Iglesias-Freire, N. Pérez, X. Batlle, A. Labarta, e A. Asenjo, «Direct imaging of the magnetic polarity and reversal mechanism in individual $Fe_{3-x}O_4$ nanoparticles», *Nanoscale*, vol. 7, n. 17, pagg. 8110–8114, 2015.
[266] P. Ares, M. Jaafar, A. Gil, J. Gómez-Herrero, e A. Asenjo, «Magnetic Force Microscopy in Liquids», *Small Weinh. Bergstr. Ger.*, vol. 11, n. 36, pagg. 4731–4736, set. 2015.
[267] J. Jin Park, M. Reddy, B. J. H. Stadler, e A. B. Flatau, «Hysteresis measurement of individual multilayered Fe-Ga/Cu nanowires using magnetic force microscopy», *J. Appl. Phys.*, vol. 113, n. 17, pag. 17A331, 2013.
[268] M. Coïsson *et al.*, «Local field loop measurements by magnetic force microscopy», *J. Phys. Appl. Phys.*, vol. 47, n. 32, pag. 325003, ago. 2014.
[269] U. Hartmann, «MAGNETIC FORCE MICROSCOPY», *Annu. Rev. Mater. Sci.*, vol. 29, n. 1, pagg. 53–87, ago. 1999.
[270] L. Angeloni *et al.*, «Experimental issues in magnetic force microscopy of nanoparticles», 2015, pag. 020010.
[271] Y. Wang, Z. Wang, J. Liu, e L. Hou, «Differential magnetic force microscope imaging: Differential magnetic force microscope imaging», *Scanning*, vol. 37, n. 2, pagg. 112–115, mar. 2015.
[272] F. J. Castaño, C. A. Ross, A. Eilez, W. Jung, e C. Frandsen, «Magnetic configurations in 160–520-nm-diameter ferromagnetic rings», *Phys. Rev. B*, vol. 69, n. 14, apr. 2004.
[273] D. Farrell, Y. Cheng, R. W. McCallum, M. Sachan, e S. A. Majetich, «Magnetic Interactions of Iron Nanoparticles in Arrays and Dilute Dispersions», *J. Phys. Chem. B*, vol. 109, n. 28, pagg. 13409–13419, lug. 2005.
[274] D. Hasegawa *et al.*, «Angular-dependent remanent magnetization curve for perpendicular magnetic recording media determined by precise polar-Kerr detection system», *J. Magn. Magn. Mater.*, vol. 320, n. 22, pagg. 3027–3031, nov. 2008.
[275] C. Kittel, «Theory of the Structure of Ferromagnetic Domains in Films and Small Particles», *Phys. Rev.*, vol. 70, n. 11–12, pagg. 965–971, dic. 1946.
[276] M. Savla, R. P. Pandian, P. Kuppusamy, e G. Agarwal, «Magnetic Force Microscopy of an Oxygen-Sensing Spin-Probe», *Isr. J. Chem.*, vol. 48, n. 1, pagg. 33–38, set. 2008.
[277] G. F. Goya, T. S. Berquó, F. C. Fonseca, e M. P. Morales, «Static and dynamic magnetic properties of spherical magnetite nanoparticles», *J. Appl. Phys.*, vol. 94, n. 5, pag. 3520, 2003.
[278] S. Karmakar, S. Kumar, R. Rinaldi, e G. Maruccio, «Nano-electronics and spintronics with nanoparticles», *J. Phys. Conf. Ser.*, vol. 292, pag. 012002, apr. 2011.

[279] S. C. N. Tang e I. M. C. Lo, «Magnetic nanoparticles: Essential factors for sustainable environmental applications», *Water Res.*, vol. 47, n. 8, pagg. 2613–2632, mag. 2013.
[280] J. L. Dormann, D. Fiorani, e E. Tronc, «Magnetic Relaxation in Fine-Particle Systems», in *Advances in Chemical Physics*, vol. 98, I. Prigogine e S. A. Rice, A c. di Hoboken, NJ, USA: John Wiley & Sons, Inc., 1997, pagg. 283–494.
[281] A. Kolhatkar, A. Jamison, D. Litvinov, R. Willson, e T. Lee, «Tuning the Magnetic Properties of Nanoparticles», *Int. J. Mol. Sci.*, vol. 14, n. 8, pagg. 15977–16009, lug. 2013.
[282] Z. Karimi, L. Karimi, e H. Shokrollahi, «Nano-magnetic particles used in biomedicine: Core and coating materials», *Mater. Sci. Eng. C*, vol. 33, n. 5, pagg. 2465–2475, lug. 2013.
[283] L. C. Branquinho *et al.*, «Effect of magnetic dipolar interactions on nanoparticle heating efficiency: Implications for cancer hyperthermia», *Sci. Rep.*, vol. 3, ott. 2013.
[284] S. Mørup, M. F. Hansen, e C. Frandsen, «Magnetic interactions between nanoparticles», *Beilstein J. Nanotechnol.*, vol. 1, pagg. 182–190, dic. 2010.
[285] D. Peddis, P. E. Jönsson, S. Laureti, e G. Varvaro, «Magnetic Interactions», in *Frontiers of Nanoscience*, vol. 6, Elsevier, 2014, pagg. 129–188.
[286] D. Fiorani e D. Peddis, «Understanding dynamics of interacting magnetic nanoparticles: from the weak interaction regime to the collective superspin glass state», *J. Phys. Conf. Ser.*, vol. 521, pag. 012006, giu. 2014.
[287] L. Angeloni *et al.*, «Experimental issues in magnetic force microscopy of nanoparticles», 2015, pag. 020010.
[288] E. Pinilla-Cienfuegos *et al.*, «Imaging the Magnetic Reversal of Isolated and Organized Molecular-Based Nanoparticles using Magnetic Force Microscopy», *Part. Part. Syst. Charact.*, vol. 32, n. 6, pagg. 693–700, giu. 2015.
[289] M. Ranjbar *et al.*, «Antiferromagnetically Coupled Patterned Media and Control of Switching Field Distribution», *IEEE Trans. Magn.*, vol. 46, n. 6, pagg. 1787–1790, giu. 2010.
[290] J. K. W. Yang *et al.*, «Fabrication and characterization of bit-patterned media beyond 1.5 Tbit/in ^{2}», *Nanotechnology*, vol. 22, n. 38, pag. 385301, set. 2011.
[291] W. L. Pei *et al.*, «Incoherent magnetization reversal in Co–Pt nanodots investigated by magnetic force microscopy», *Acta Mater.*, vol. 59, n. 12, pagg. 4818–4824, lug. 2011.
[292] Y. Chen *et al.*, «Switching Probability Distribution of Bit Islands in Bit Patterned Media», *IEEE Trans. Magn.*, vol. 46, n. 6, pagg. 1990–1993, giu. 2010.
[293] M. V. Rastei, R. Meckenstock, e J. P. Bucher, «Nanoscale hysteresis loop of individual Co dots by field-dependent magnetic force microscopy», *Appl. Phys. Lett.*, vol. 87, n. 22, pag. 222505, 2005.
[294] L. Angeloni, D. Passeri, M. Reggente, D. Mantovani, e M. Rossi, «Removal of electrostatic artifacts in magnetic force microscopy by controlled magnetization of the tip: application to superparamagnetic nanoparticles», *Sci. Rep.*, vol. 6, pag. 26293, mag. 2016.
[295] L. Angeloni *et al.*, «Measurement of the nonmagnetic coating thickness of core-shell magnetic nanoparticles by controlled magnetization magnetic force microscopy», 2016, pag. 020006.
[296] H. Iida, K. Takayanagi, T. Nakanishi, e T. Osaka, «Synthesis of Fe3O4 nanoparticles with various sizes and magnetic properties by controlled hydrolysis», *J. Colloid Interface Sci.*, vol. 314, n. 1, pagg. 274–280, ott. 2007.

[297] H. M. Lu, W. T. Zheng, e Q. Jiang, «Saturation magnetization of ferromagnetic and ferrimagnetic nanocrystals at room temperature», *J. Phys. Appl. Phys.*, vol. 40, n. 2, pagg. 320–325, gen. 2007.
[298] M. Andrés Vergés *et al.*, «Uniform and water stable magnetite nanoparticles with diameters around the monodomain–multidomain limit», *J. Phys. Appl. Phys.*, vol. 41, n. 13, pag. 134003, lug. 2008.
[299] G. Muscas *et al.*, «Magnetic Properties of Small Magnetite Nanocrystals», *J. Phys. Chem. C*, vol. 117, n. 44, pagg. 23378–23384, nov. 2013.
[300] S. Laurent *et al.*, «Magnetic Iron Oxide Nanoparticles: Synthesis, Stabilization, Vectorization, Physicochemical Characterizations, and Biological Applications», *Chem. Rev.*, vol. 108, n. 6, pagg. 2064–2110, giu. 2008.
[301] M. Talelli *et al.*, «Superparamagnetic Iron Oxide Nanoparticles Encapsulated in Biodegradable Thermosensitive Polymeric Micelles: Toward a Targeted Nanomedicine Suitable for Image-Guided Drug Delivery», *Langmuir*, vol. 25, n. 4, pagg. 2060–2067, feb. 2009.
[302] J. E. Smith, K. E. Sapsford, W. Tan, e F. S. Ligler, «Optimization of antibody-conjugated magnetic nanoparticles for target preconcentration and immunoassays», *Anal. Biochem.*, vol. 410, n. 1, pagg. 124–132, mar. 2011.
[303] H. E. Daldrup-Link *et al.*, «MRI of Tumor-Associated Macrophages with Clinically Applicable Iron Oxide Nanoparticles», *Clin. Cancer Res.*, vol. 17, n. 17, pagg. 5695–5704, set. 2011.
[304] S. Laurent, S. Dutz, U. O. Häfeli, e M. Mahmoudi, «Magnetic fluid hyperthermia: Focus on superparamagnetic iron oxide nanoparticles», *Adv. Colloid Interface Sci.*, vol. 166, n. 1–2, pagg. 8–23, ago. 2011.
[305] S. L. C. Pinho *et al.*, «Relaxometric Studies of γ-Fe $_2$ O $_3$ @SiO $_2$ Core Shell Nanoparticles: When the Coating Matters», *J. Phys. Chem. C*, vol. 116, n. 3, pagg. 2285–2291, gen. 2012.
[306] Y.-H. Deng, C.-C. Wang, J.-H. Hu, W.-L. Yang, e S.-K. Fu, «Investigation of formation of silica-coated magnetite nanoparticles via sol–gel approach», *Colloids Surf. Physicochem. Eng. Asp.*, vol. 262, n. 1–3, pagg. 87–93, lug. 2005.
[307] L. E. W. LaConte *et al.*, «Coating thickness of magnetic iron oxide nanoparticles affects R2 relaxivity», *J. Magn. Reson. Imaging*, vol. 26, n. 6, pagg. 1634–1641, dic. 2007.
[308] M. A. Gonzalez-Fernandez *et al.*, «Magnetic nanoparticles for power absorption: Optimizing size, shape and magnetic properties», *J. Solid State Chem.*, vol. 182, n. 10, pagg. 2779–2784, ott. 2009.
[309] Y. Yuan, D. Rende, C. L. Altan, S. Bucak, R. Ozisik, e D.-A. Borca-Tasciuc, «Effect of Surface Modification on Magnetization of Iron Oxide Nanoparticle Colloids», *Langmuir*, vol. 28, n. 36, pagg. 13051–13059, set. 2012.
[310] M. Coşkun e M. Korkmaz, «The effect of SiO2 shell thickness on the magnetic properties of ZnFe2O4 nanoparticles», *J. Nanoparticle Res.*, vol. 16, n. 3, mar. 2014.
[311] L. Angeloni, D. Passeri, M. Reggente, D. Mantovani, e M. Rossi, «Removal of electrostatic artifacts in magnetic force microscopy by controlled magnetization of the tip: application to superparamagnetic nanoparticles», *Sci. Rep.*, vol. 6, pag. 26293, mag. 2016.
[312] D. Passeri *et al.*, «Thickness measurement of soft thin films on periodically patterned magnetic substrates by phase difference magnetic force microscopy», *Ultramicroscopy*, vol. 136, pagg. 96–106, gen. 2014.

[313] C. Dong *et al.*, «Visualization and quantification of magnetic nanoparticles into vesicular systems by combined atomic and magnetic force microscopy», 2015, pag. 020011.
[314] A. Schwarz e R. Wiesendanger, «Magnetic sensitive force microscopy», *Nano Today*, vol. 3, n. 1–2, pagg. 28–39, feb. 2008.
[315] D. Passeri *et al.*, «Magnetic force microscopy: Quantitative issues in biomaterials», *Biomatter*, vol. 4, n. 1, pag. e29507, gen. 2014.